The interaction of an internal solitary wave with surface gravity waves

Alexandra Elizabeth Thomas

Doctor of Philosophy
The University of Edinburgh
2002

Abstract

Solitary waves are nonlinear, non-oscillatory disturbances of permanent form. Recent advances in synthetic aperture radar imaging and analysis techniques have confirmed *in situ* observations and measurements that the passage of oceanic internal waves, including internal solitary waves, is associated with modulations in sea surface roughness. Such measurements have not only revealed the ubiquity of this phenomenon but also demonstrated the existence of large amplitude, tidally induced, internal solitary waves. It appears that little laboratory-based research has been carried out in this field. This work, therefore, focusses on the study of the velocity and density fields resulting from the interaction between a surface wave train and an internal solitary wave, propagating in a two-layer fluid. Digital Particle Image Velocimetry (DPIV) and Planar Laser Induced Fluorescence (PLIF) were employed to provide two-dimensional instantaneous velocity and density information, respectively. Previous studies in this field have been performed using intrusive probe techniques. Results from a preliminary DPIV investigation on single internal solitary waves concurred with previous research and highlighted the constraints of the DPIV system. The results were also compared to a recently developed and validated fully nonlinear numerical method. In the interaction investigations, both wavelength and amplitude modulations of the surface waves were observed. In some cases, the shape of the internal wave was distorted. Velocity profiles were compared to the linear superposition of surface wave linear theory and the fully nonlinear numerical method predictions. In addition, the PLIF analysis showed that, for the wave and stratification parameters investigated, there was no evidence for the compression and expansion of the density interface during the interaction.

Acknowledgements

My thanks must firstly go to my supervisor Clive Greated for all his encouragement and support. Special thanks must also go to Peter Davies at the University of Dundee for all his invaluable help and advice.

I would also like to thank those without whom this thesis really would not have been possible. In no particular order these are: Frank Morris, for his help in the lab. and also for being a good mate, members of the technical staff in the department Andrew and Arthur, Colin for his patience and help with all things electronic and likewise, Jim. A particular note of thanks must go to Prof. John Grue for allowing me to use the Internal Wave Program, developed at the University of Oslo [1]. My gratitude also goes to Per-Olav Rusås for his endless patience and help in running the Internal Wave Program. I must also thank Maarten for helping me to set it up and run it here. Thank you to Lucien Murray-Pitts for helping me configure the conductivity probe. I must thank Jimbo, John and Dave for their support, friendship and advice and likewise Ted for all his help with image processing routines. Thanks must also go to the rest of the Fluids and Acoustics group, both present and ex-members, Scott, Sooz, Ant, Jonathan, Mark, Tom, Dawn, Orlando, Alan, who have been a good laugh and great colleagues over the past three years.

I also owe a debt of thanks to all my Edinburgh friends who have helped me a great many ways, cheering me up, cooking me nice food, and generally being great company; Lotte, Mark, Katy, Ruth, Jantze, Barrie, Miriam, Alan... Billions

[1] documented in: J. Grue et al. "Properties of large-amplitude internal waves", JFM 1999, Vol. 380.

of hugs and thanks to Nicolas whose relentless enthusiasm and quality cuisine has helped me persevere to the end. Last, but not least, thanks to Mum and Dad for supporting me throughout.

This project was funded by EPSRC. Their support is greatly acknowledged.

Declaration

I do hereby declare that this thesis was composed by myself and that the work described therein is my own, except where explicitly stated otherwise.

Alexandra Thomas

December 2001

Table of Contents

List of Figures

List of Tables

Chapter 1

Introduction

This laboratory-based study investigates the interaction processes resulting from a small amplitude surface wave train passing over an internal solitary wave of depression. It is now well-known that internal waves are a ubiquitous natural phenomenon, occurring in the stratified medium of either the atmosphere or the ocean. Internal solitary waves are localised pulse-like disturbances, of either elevation or depression. They occur due to a balance of nonlinear wave-steepening effects and linear wave dispersion [27] and consequently can maintain their shape over considerably long distances.

Many observations of solitary waves have been reported over the past 40 years. As in the case of other gravity waves, they have been detected in the atmosphere [95, 84, 67] and, of particular relevance in the present work, in the ocean [70], in both shallow water and deep sea regions. Here, many are tidally induced,

occurring due to a change in bottom topography [11, 69]. In some cases, their amplitudes have been measured to be from 20m to in excess of 100m and with characteristic length scales of 200 to 3000m, the longer length scales associated with the larger waves. They have also been associated with strong currents.

In situ measurements of these waves are difficult to obtain. As a result, their space - time evolution is difficult to follow. However, recent progress in satellite technology and in associated imaging techniques has revealed that the passage of oceanic internal waves is linked to changes in sea surface roughness [4, 7, 12, 13]. In some cases, the surface wave modulation has been so intense it has lead to surface wave breaking [70]. These advances in detection techniques have enabled a considerably better understanding of the nature of these waves.

The global occurrence of internal solitary waves has promoted much interest within all branches of research. For example, their passage can affect marine nutrient and animal distributions [70] and induce large hydrodynamic forces on surface and sub-surface structures [11, 29].

The increase in interest in these waves in oceanographic and other fields has given an impetus for solitary wave laboratory-based investigations [51, 44, 65, 29]. Most previous work has been concerned with validations of shallow and deep water theories. In particular, the weakly nonlinear Korteweg - de Vries (KdV) approximation has been found to be capable of predicting small amplitude solitary wave characteristics only. In contrast, a recently developed fully nonlinear

numerical model [30, 28] has been shown to successfully model large amplitude solitary wave properties [30, 28, 29, 34].

Although there is now much evidence of surface wave modulation as a result of internal wave propagation, little laboratory or theoretical work appears to have been carried out on the subject. Most previous laboratory work has been performed using oscillatory surface and internal wave trains [23, 58, 52]. A recent investigation, involving small amplitude solitary waves of depression [33, 32], was performed using resistive and capacitative probes. Such measurement techniques have the disadvantage of disturbing the flow and only providing measurements at single points within the fluid. Most comparisons with theory in such work have been made using derivations of a theory initially presented by Longuet-Higgins and Stewart (LHS) [61, 33, 63]. As in the case of prior laboratory investigations, this predicts amplitude and wavelength modulations of small amplitude oscillatory surface waves riding on an oscillatory internal wave train.

The present work intends to further the laboratory study of surface wave modulation by the passage of an internal solitary wave in two ways. Firstly, two non-intrusive laser measurement techniques, as opposed to the previously used intrusive probe methods, will be applied; namely Digital Particle Image Velocimetry (DPIV) and Planar Laser Induced Fluorescence (PLIF). These optical measuring techniques have the advantage of providing instantaneous two-dimensional velocity and concentration information, respectively, within a plane of the flow

under study. This will allow entire velocity and concentration fields, defined by the laser light sheet dimensions, to be investigated. Furthermore, in contrast to previous studies, this work will investigate primarily the surface wave - solitary wave interaction processes for large amplitude solitary wave flow. As earlier work has shown that existing analytical models cannot adequately predict these waves' properties, the fully nonlinear numerical method [30, 28] will be appealed to, to provide a comparison with the DPIV measurement results. In addition, the results will be compared to the theory originally presented by LHS[61] and adapted to the case of solitary waves.

In the first instance, an introduction to the subject is given in chapter 2. Previous laboratory and field-based work on solitary waves is reviewed. Relevant theories and their assumptions, pertaining to the propagation of surface waves and to the propagation of internal solitary waves, are given. Lastly, a development of the LHS theory [61] to determine surface wave amplitude and wavelength modulation for surface wave trains riding over an internal solitary wave is presented.

Chapter 3 presents the theory and practical application of the measurement techniques to be used throughout the course of the study; namely Digital Particle Image Velocimetry (DPIV) and Planar Laser Induced Fluorescence (PLIF). The experimental facilities are presented and the method of generating both internal solitary waves and a surface wave train are explained.

Chapters 4 and 5 present the results of the investigation using each of the mea-

surement techniques, DPIV and PLIF, respectively. The layout of each chapter is similar. First, the parameter space of the investigation is assessed within the context of the available experimental facilities and the application of the appropriate technique to two-layer fluid flow. Each is applied in the first instance to the study of single internal solitary waves of depression, and, in the case of DPIV, to the study of small amplitude surface wave trains, before being employed to investigate the interaction between an internal solitary wave and a train of surface waves. All the internal waves are generated at a brine - fresh water interface.

Lastly, chapter 6 draws together the main points raised throughout the discussion sections. The experimental set-up and procedure and the main results of the investigation are summarised. The advantages and drawbacks of the techniques used are identified. Suggestions for further work are presented.

In summary, therefore, the overall aims of this work are as follows:

- to apply Digital Particle Image Velocimetry (DPIV) to a laboratory study of a surface wave train - internal solitary wave interactions
- to apply Planar Laser Induced Fluorescence (PLIF) to a laboratory study of internal solitary waves
- to apply PLIF to a surface wave train - internal solitary wave interaction
- to assess the effect of the interaction on the resulting flow fields using both the DPIV and PLIF measurement techniques

- to identify any surface wave or internal wave modulations resulting from the interaction process

Chapter 2

Internal Solitary Wave and Surface Wave Dynamics

The main objective of this study is to investigate the interaction processes that occur between an internal solitary wave and a train of surface water waves. In order to understand the motivation for this work, it is necessary to gain an appreciation of the concept of a solitary wave and the historical background of previous research in this field, both in the laboratory and the ocean. This chapter first introduces solitary and internal solitary waves and presents the main results from the Korteweg de Vries equation; a weakly nonlinear, weakly dispersive long wave approximation to solitary wave propagation. The work to date assessing the validity of the KdV theory is reviewed in the context of both oceanic and laboratory-generated solitary waves. Finally, a theory describing the inter-

action and ensuing amplitude and wavelength modulations of short waves riding on an internal solitary wave is presented. The motivation for this study and the proposed approach is then justified within the context of previous publications.

2.1 Gravity Waves and Stratified Fluids

2.1.1 Gravity waves

Gravity waves are characterised by a balance between gravity and fluid inertia [59]. Under gravity, the fluid, when disturbed, has a tendency to return to a state of stable equilibrium. The associated restoring force allows waves to be supported. These waves can exist at the interface between different fluids or within the body of a single fluid. For the latter case, the undisturbed variation in density can be represented as either a discontinuous or continuous function of distance from the fluid surface. Such a density variation with depth is known as a stratification, in either a multi-layer or continuously varying configuration.

Often quoted examples of continuously stratified media are the atmosphere and the ocean. In contrast, a discontinuous stratification is step-like, the discontinuity arising at the horizontal boundary between two homogeneous fluids of different, but constant, density. Effectively, any stratification can be considered to consist of discrete layers of fluid. The density variation is then confined to the surface

separating two adjacent layers and gravity acts to restore the "flatness" of this surface when disturbed.

Waves propagating upon an air - water surface are referred to as surface gravity waves. Immiscible fluid systems, such as those composed of oil and water, have a similar step-like density profile. Now, however, with any disturbances confined to the surface between the adjacent, immiscible fluids, the waves are said to be internal. The waves generated within this configuration are isotropic. This is a much simpler stratified configuration than the continuous case and as a result, continuous stratifications are, wherever possible, represented by a discrete layer system. Some situations where this simplification may apply are discussed in section 2.4.1.

2.1.2 Buoyancy frequency and the Richardson number

In experimental fluid dynamics, researchers are often required to investigate a full-sized object or system, in order to investigate its dynamical characteristics and properties. In many cases, this is impractical so the apparatus must be modelled and scaled appropriately. As the dimensions of the test piece or test facilities have been altered, the resulting properties of the flow may not necessarily match those of the original. In order to ensure that the model properties and behaviour can be transferred to full scale, conditions of geometric and dynamical similarity must be satisfied. This constraint ensures that the problem under investigation

is posed in terms of a set of dimensionless groupings, the values of which should match their corresponding full-scale counterparts. Non-dimensional numbers rely on relevant quantities such as length and velocity scales that characterise the flow system under consideration. A well known non-dimensional number is the Reynolds number, which relates the inertial and viscous forces in a fluid. It is defined as

$$Re = \frac{UL}{\nu}, \tag{2.1}$$

where U is a velocity scale, L is a length scale and ν is the kinematic viscosity of the fluid (the ratio of the dynamic viscosity, μ, to the fluid density, ρ).

Dimensionless numbers are also useful in classifying fluid flow systems. The Reynolds number is often used to provide a guide as to whether a flow is laminar or turbulent. Such numbers are used as "bench marks", enabling particular dynamical set-ups to be compared to other systems, situations or models. Dimensional analysis is therefore also applicable to theoretical studies, allowing theoretical results to be compared to experimental work or other theoretical models.

In stratified fluids, the static stability of the system requires that the density of the fluid, ρ, increases with depth from the fluid surface, such that $\frac{\partial \rho}{\partial z} < 0$, where the vertical coordinate z increases positively upwards from the quiescent fluid free surface. Consider a particle of fluid in a continuously stratified, statically stable medium. If this fluid particle moves a small distance vertically upwards from a reference point z to $z + \delta z$, where the density is slightly reduced from that

at the reference position, ρ_0, the particle has an excess density over that of the surrounding fluid. As a result, the particle experiences a downwards gravitational restoring force proportional to this density difference. It then overshoots its equilibrium level and experiences an upward force due to a buoyancy deficit. As a result, the displaced particle oscillates vertically until its motion is sufficiently damped for the motion to cease. The buoyancy frequency, $N(z)$, is the natural frequency of oscillation associated with the above simple harmonic motion of a neutrally buoyant fluid parcel, moving vertically in a water column, when it is given a small displacement from its equilibrium position. Effectively, it provides a measure of the stability of a stratified water column against small vertical perturbations. In the laboratory set-up presented in this work, it can be written to a good approximation as [59]

$$N^2(z) = -\left[g\frac{(\frac{\partial \rho}{\partial z})}{\rho_0}\right], \tag{2.2}$$

where g is the acceleration due to gravity.

The vertical distribution of $N(z)$ is one of the most important dynamical characteristics of the ocean, classifying its static stratification. The corresponding period can vary from a few minutes to several hours in the deep ocean.

The Froude number, Fr, relates the inertial forces to the gravitational forces in a suitable non-dimensional ratio and is a guide to the relative importance of the

inertial and gravity terms, where a liquid free surface is involved. It is defined as

$$Fr = \frac{U}{(gL)^{1/2}}. \tag{2.3}$$

where the length scale, L, usually represents the water depth or wavelength.

The corresponding non-dimensional parameter, for stratified fluid systems, is the internal Froude number, $Fr_{int} = U/(g'L)^{1/2}$, where $g' = g\Delta\rho/\rho$. It is sometimes expressed in terms of the bulk Richardson number, Ri. Both Fr_{int} and Ri relate the inertial forces to the buoyant forces within a fluid with $Ri = (1/Fr_{int})^2$. It is sometimes useful to describe the flow in terms of the gradient Richardson number, Ri_g, defined as

$$Ri_g = -\frac{N^2(z)}{\left(\frac{\partial u}{\partial z}\right)^2}, \tag{2.4}$$

where $\frac{\partial u}{\partial z}$ is a characteristic velocity gradient within the fluid.

In some circumstances in stratified media, there may exist a primary parallel shear flow in which a horizontal velocity varies with depth, $u(z)$. When such a system is subject to small disturbances, the static stability requirement of $\frac{\partial \rho}{\partial z} < 0$ may not be sufficient to prevent instability. Howard [40] suggests that a sufficient condition for dynamic stability of a stratified shear flow is that $Ri_g \geq 0.25$ everywhere within the flow field. This criterion is referred to, amongst others, by Grue *et al.* [29] and Kao *et al.* [44] where it is investigated as a characterisation of instability in the propagation of internal waves.

2.1.3 Density profile and interface thickness

The shape of a static two-layer density gradient is often described empirically by a hyperbolic tangent profile [64, 44]. The profile is given by

$$\rho(y) = \frac{\Delta\rho}{2} \tanh\left(\frac{y}{\Delta h}\right) + \overline{\rho}, \tag{2.5}$$

where $\Delta\rho = \rho_1 - \rho_2$ is the density difference across the lower and upper layers of densities ρ_1 and ρ_2 respectively, $\overline{\rho}$ is the average density of the stratification and Δh describes the interface thickness. The vertical coordinate y increases positively upwards away from the interface. Figure 2.1 shows a typical density profile, ρ against y, encountered throughout the course of the experimental work carried out in this study (chapters 4 and 5). The corresponding "tanh" profile fit is also shown. The stratification consists of a fresh water layer ($y > 0$) separated from a denser saline layer ($y < 0$) by a very thin region over which the density varies continuously such that the profile is almost step-like. The density profile was obtained using a microconductivity probe [36], the details of which are described in section 3.2.5.

The quantity Δh, derived from the best fit tanh profile, provides a convenient measure of the interfacial width, though other methods could be employed. For example, two isopycnals, or constant density contours, of a particular value can be located within the flow field, say $0.8 \times \overline{\rho}$ and $1.2 \times \overline{\rho}$, and tracked over time

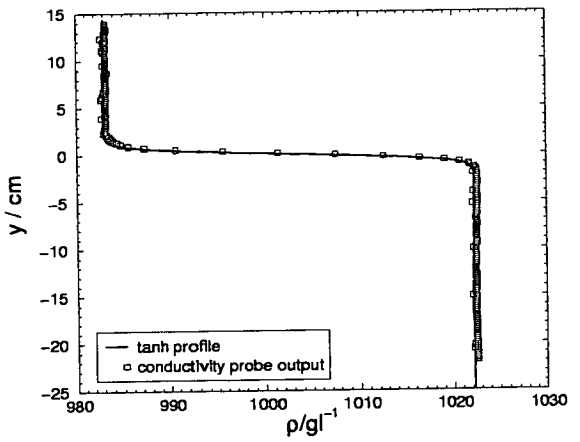

Figure 2.1: A typical density profile of the stratifications used throughout this work and the hyperbolic tangent fit using (2.5).

[21]. A measure of the instantaneous thickness of the interface is then defined empirically as the vertical distance between the two reference isopycnals at any time. A measure of the interface thickness can also be obtained from the vertical profile of either the density gradient or the buoyancy frequency, since there is a peak in the graph of density gradient with depth at the point of inversion. The width of the interface can then be taken empirically to be the width of the peak at, say, its half height.

2.2 Small Amplitude Surface Waves: Linear Theory

In this section, an overview of first order surface wave theory is given. This will be useful both in section 2.5.1 where a theoretical description of the interaction

of a soliton and a train of surface waves is described and in section 4.4.2 where linear theory is used to validate the results of surface wave train experiments.

Small amplitude, linear, surface gravity wave theory describes the two-dimensional propagation of small surface waves in a homogeneous inviscid fluid of constant depth. Such waves may also be known as "first order Stokes' waves" or "Airy waves", named after the first two researchers, in the mid 1800's, to derive the expressions presented below.

The subscript S in the following sections and throughout the remainder of this work is used to refer to surface wave characteristics. Linear theory is pertinent to periodic surface waves whose amplitude, a_S, is much smaller than their wavelength, λ_S, and the water depth, H. The wave steepness, defined as $2a_S/\lambda_S$, is therefore much less than 1, a condition which also applies to the surface waves used throughout this investigation. As a result, these waves are sometimes referred to as infinitesimal or small waves. This constraint allows the boundary conditions of the problem to be linearised. The fluid is assumed to be incompressible, inviscid and irrotational. In this instance, the flow is referred to as potential flow. The motion is also assumed to be "steady" in an inertial frame of reference, such that the waves are of constant period. The effect of surface tension may also be neglected, provided that the wavelength is sufficiently long (section 4.2.2).

One problem of surface wave dynamics is that the position of the free surface

is not known *a priori*. However, as the wave amplitude is small, the linearised boundary conditions are applied at the mean water level (MWL) (see figure 2.2), which is the level at which the area above the wave trough is equal to the area under the wave crest. A consequence of this property is that the expressions below are valid within the main body of the fluid; from the bottom, $z = -H$, to the level of the wave trough. Hence, the main errors in velocity predictions for the fluid motion (equations (2.12) and (2.13)) are likely to arise in the region $z = \pm\eta_S$, above the height of the wave trough.

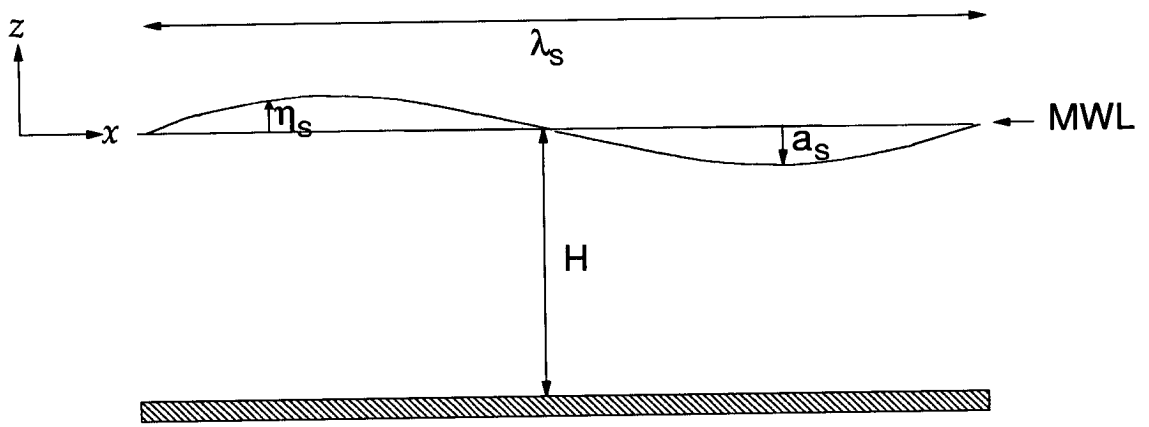

Figure 2.2: Diagram illustrating the surface wave terminology and coordinate system used in this work for a homogeneous fluid.

Surface gravity waves are dispersive; the speed of wave propagation increases with wavelength. The dispersion relation is written as [77]

$$\omega_S^2 = gk_S \tanh(k_S H), \tag{2.6}$$

where ω_S is the angular frequency and k_S is the wave number, given by

$$k_S = \frac{2\pi}{\lambda_S}. \tag{2.7}$$

Hence as $\omega_S = c_S k_S$, c_S, the phase velocity of the wave, can be written as

$$c_S = \sqrt{\frac{g\lambda_S}{2\pi} \tanh\left(\frac{2\pi H}{\lambda_S}\right)}. \tag{2.8}$$

The group velocity, c_{gS}, or energy transport velocity of a wave group or packet, is given by

$$c_{gS} = \frac{d\omega_S}{dk_S}. \tag{2.9}$$

Hence,

$$c_{gS} = \frac{1}{2} c_S \left(1 + \frac{2k_S H}{\sinh(2k_S H)}\right). \tag{2.10}$$

The surface elevation of the wave motion, η_S, is written as

$$\eta_S(x,t) = a_S \cos(\omega_S t - k_S x), \tag{2.11}$$

where a_S is the amplitude, t is time, and x is the horizontal coordinate.

The horizontal and vertical fluid particle velocity components at a fixed point (x, z) are respectively [77]

$$u_S(x,z,t) = \omega_S a_S \frac{\cosh[k_S(z+H)]}{\sinh(k_S H)} \cos(\omega_S t - k_S x), \tag{2.12}$$

and

$$v_S(x,z,t) = -\omega_S a_S \frac{\sinh[k_S(z+H)]}{\sinh(k_S H)} \sin(\omega_S t - k_S x). \tag{2.13}$$

The fluid particle trajectories are elliptical. The longer the wave relative to the water depth, the more elongated the ellipse. The ellipse also becomes "flatter" with depth, being reduced to a purely horizontal motion at the bottom boundary.

2.3 Interfacial Solitary Waves

In this section, the concept of an internal solitary wave is presented. The Korteweg - de Vries (KdV) theory, known to describe the propagation of small amplitude solitary waves, is examined. Previous laboratory-based studies are discussed in order to compare and contrast this theory with other, more recently developed approximations. Finally, the range of validity of the KdV theory, investigated in previous research, is reviewed.

2.3.1 Background

In 1834, John Scott Russell made the first recorded observation of what he termed "a great primary wave of translation" whilst walking along the banks of the Union canal, in Scotland. He published his findings in 1845 [78]: "*I was observing the motion of a boat which was rapidly drawn along a narrow channel [...] when the*

boat suddenly stopped – not so the mass of water in the channel which it had put in motion: it accumulated around the prow of the vessel in a state of violent agitation, then suddenly leaving it behind, rolled forward with great velocity, assuming the form of a solitary elevation, a rounded smooth and well defined heap of water, which continued its course apparently without change of form or diminution of speed". He later characterised this wave as a *solitary wave.*

2.3.2 Surface solitary waves

Russell's systematic series of experiments was the first step in the development of today's widely accepted solitary wave, shallow water, theory. He performed a set of detailed investigations, firstly in the mouths of the rivers Dee and Clyde. His later experiments in artificial channels, however, enabled him to deduce much clearer conclusions.

Following his discovery of the solitary wave, he went on to classify water waves into four distinct orders [80]:

1. Waves of translation
2. Oscillating waves
3. Capillary waves
4. Corpuscular waves

It is in the first of these categories, also referred to as waves of first order, that he classed solitary waves. He remarked that these waves are characterised by the fact that the total fluid mass is moved from one place to another and that the motion of the fluid does not correspond to the motion of the wave, that itself has a uniform velocity. He noted that the new waves had certain properties. These are listed below.

- The solitary wave travels without distortion of form. Viscous action and friction with the channel sides and bottom cause an attenuation of height but not a change of form.
- The wave reflects off a wall and continues to move in the opposite direction without change of form.
- On collision, the waves maintain their form.
- The wave breaks when wave height exceeds water depth.

He also verified experimentally that the speed of the wave, c, in a flat channel of depth H, was related to its amplitude, a, by the relationship

$$c = \sqrt{g(H+a)}. \tag{2.14}$$

In order to generate a solitary wave in his laboratory, Russell used a channel of rectangular cross section and tried various generation mechanisms. One of these

was to use a vertical plate to hold back a volume of water. Upon it's release, the wave took shape. A similar system is used in this work to generate internal solitary waves (section 3.2.6). Another method was to drop a mass, such as a brick, into the channel. This displaces a mass of water that then develops into a solitary wave. A vertical plate, placed at one end of the channel, which is then suddenly moved towards the other end, was also successful. Russell also recognised that it was almost impossible to generate a solitary wave perfectly. He remarked that if a very large volume of water is displaced, the initial wave will separate into an ensemble of solitons, a leading solitary wave followed by a series of other smaller waves. These latter waves, being smaller in height, have a correspondingly reduced velocity. In some circumstances, he noticed an oscillatory wave train tail follows the wave or waves. Russell acknowledged that not all initial disturbances evolve into solitary waves. This was confirmed later in the subsequently developed theory.

2.3.3 The Korteweg - de Vries theory

The set of experimental observations made by Russell represent a milestone in the subsequent mathematical evolution of wave theories. It wasn't until over 50 years after Russell's first publication that a theory of solitary wave propagation was developed, published by Korteweg and de Vries in 1895. Although the first description of a wave of permanent form was discovered by Boussinesq in 1871,

it was Korteweg and de Vries' work [53] that yielded more accurate results to describe the waveform and to determine the maximal possible wave height. They aimed initially to settle the, at-the-time-controversial, issue of whether the shape of advancing surface solitary waves in a rectangular channel behaved, as surface sinusoidal waves do, by becoming steeper at the front and less steep behind, even when friction is neglected. They considered the effect that both nonlinearity and dispersion would have on the speed of long wavelength surface waves in a irrotational, inviscid and incompressible fluid. Long water waves are described as such if $H/\lambda \ll 1$ where λ is the wavelength, or a characteristic length scale associated with the wave, and H is the mean water depth.

Their work resulted in an equation, now known as the Korteweg-de Vries (KdV) equation, describing the long time evolution of small, but finite amplitude, long dispersive water waves down a channel of rectangular cross section. This equation is given to first order in a/H, where a is the maximal amplitude of the wave, in equation (2.15).

$$\eta_t + c_0\,\eta_x + c_1\eta\eta_x + c_2\eta_{xxx} = 0, \tag{2.15}$$

where η is the surface elevation as a function of time, t, and distance down the channel, x, c_0 is the associated linear long wave phase speed and c_1 and c_2 are constant coefficients. The subscripts refer to partial derivatives with respect to the variable concerned.

The type of solution resulting from this equation depends on the importance of the

term $c_2\eta_{xxx}$ relative to the nonlinear, dispersive term $c_1\eta\eta_x$. This is determined by the non-dimensional parameter $a\lambda^2/H^3$, where a is the maximal amplitude of the wave. When this parameter is large enough, the nonlinear effects cause the wave front to steepen as the waves advance. In contrast, if $a\lambda^2/H^3 = O(1)$, then there is a balance between wave steepening and dispersion and the periodic waves retain their form as they propagate. When $a\lambda^2/H^3 \to 0$, the wave profile approaches that of a sinusoidal wave, as the nonlinear term has only a small contribution.

Cnoidal waves are a set of steady periodic wave train solutions to the KdV equation and were so-called because they follow the form of the square of the Jacobian elliptic function, cn. As the period of the wave, T, is increased such that $T \to \infty$ and therefore that the wavelength also tends to infinity, the cnoidal waveforms degenerate into a series of isolated "humps". Between them, the water surface is almost undisturbed. It is in this limiting configuration of the cnoidal wave, when the nonlinear and dispersion terms balance, that the solitary wave solution occurs. The solution represents a non-periodic, non-oscillatory, single isolated mass of water, propagating without change of form. The limiting solution, describing the wave profile $\eta(x,t)$, is given by

$$\eta(x,t) = a\,\mathrm{sech}^2[(x - c_{\mathrm{KdV}}t)/\lambda]. \tag{2.16}$$

Hence, according to KdV theory, the form of a shallow water solitary wave follows

a "sech squared" profile. λ is now a characteristic length associated with the solitary wave and c_{KdV} its speed.

It must be noted that the equations given here refer to mode 1 solitary waves. For each wave mode, there exists a corresponding KdV equation. The waves are more energetic with increasing mode number. As only first mode waves are investigated in this study, wherever a solitary wave is mentioned, it is assumed that the wave is of the first mode type.

Following Korteweg and de Vries' work, there was little further investigation of the subject. However, interest in solitary waves was revived in the 1960's. Nearly 70 years after their discovery, Zabusky and Kruskal [97] made a computer simulation of the KdV equation to simulate the collision of two solitary waves. Contrary to expectations, the waves did not undergo a strong nonlinear interaction. Instead, the waves retained their shapes and propagation velocities after the collision. Due to their particle-like properties, the researchers coined the phrase "soliton" to describe them. Solitons are therefore often used to describe a solitary wave when it is infinitely separated from any other soliton [17]. In 1967, Gardner *et al.* developed a method to solve the KdV equation as an initial value problem. This allowed an analytical prediction of the evolution in time of an arbitrary initial waveform, $\eta(x, 0)$. If the waveform is sufficiently localised, it will evolve into a finite set of rank-ordered solitons followed by a dispersive wave train. Since these developments, the KdV equation has been used in a variety of applications across

many areas of science involving solids, liquids, gases and plasmas [66, 56].

2.3.4 Internal solitary waves and the extension of KdV theory to two-layer fluids

The KdV shallow water wave theory, where the wave motion is weakly nonlinear and the waves are long relative to the depth of fluid, can be extended to cover internal solitary waves propagating at the interface between two fluids of different density. Throughout the course of this study, ρ refers to fluid density and the subscripts 1 and 2 refer to the bottom and top fluid layers respectively.

For a single fluid, the waves can occur either as waves of elevation, a bump of fluid rising above the free surface, which are gravity dominant, or as waves of depression, where capilliarity dominates. The wave type, in this case, depends on whether the water depth, H, is less than or greater than a critical depth, $H_{cr} = (3\sigma/\rho g)^{\frac{1}{2}}$ where σ is the surface tension coefficient and ρ is fluid density [92]. For water, in which $\sigma = 0.073\text{N/m}$, this critical depth is $H_{cr} = 0.47\text{cm}$.

Keulegan [48] found that, in the case of a statically stable two-layer fluid, such that $\rho_2/\rho_1 < 1$, and neglecting capilliarity, it can be predicted that the solitary wave will be a wave of elevation if $h_1/h_2 \ll 1$, where h is fluid layer depth. Conversely, if $h_1/h_2 \gg 1$, the wave will be one of depression. The critical value of the depth ratio dividing the two wave regimes is, however, very sensitive to

the upper boundary condition; that is whether the upper surface is a rigid lid or a free surface. Walker [92] investigated the relationship between waves of elevation and depression and expanded the theoretical work to include the effect of interfacial surface tension in both the rigid lid and free surface formalism. For the parameters used in this experimental study, the interfacial surface tension effects are not significant and the solitary waves generated are all gravity driven. As the values of lower layer depth to upper layer depth ratios, h_1/h_2, used in this work are greater than 1 in all cases, only solitary waves of depression are investigated.

In the same way as for a single fluid, the internal wave motion can be described by balancing nonlinear and dispersive effects. This leads to the two-layer fluid KdV equation which, to first order in (a/h_2), has the same form as equation (2.15). However, $\eta(x,t)$ is now the interfacial displacement between the two fluids and the constants take on a slightly different form. The coordinate system and the relevant parameters are shown in figure 2.3. Various KdV theoretical models have been developed in the past [48, 60, 51, 68, 82, 44] to describe the evolution of weakly nonlinear interfacial gravity waves. A theory, as originally proposed by Long [60] and detailed by Grue *et al.* [29], is presented below.

The constants c_0, c_1 and c_2, in (2.15), are defined as

$$c_0^2 = \frac{g h_1 h_2 (\rho_1 - \rho_2)}{\rho_2 h_1 + \rho_1 h_2}, \tag{2.17}$$

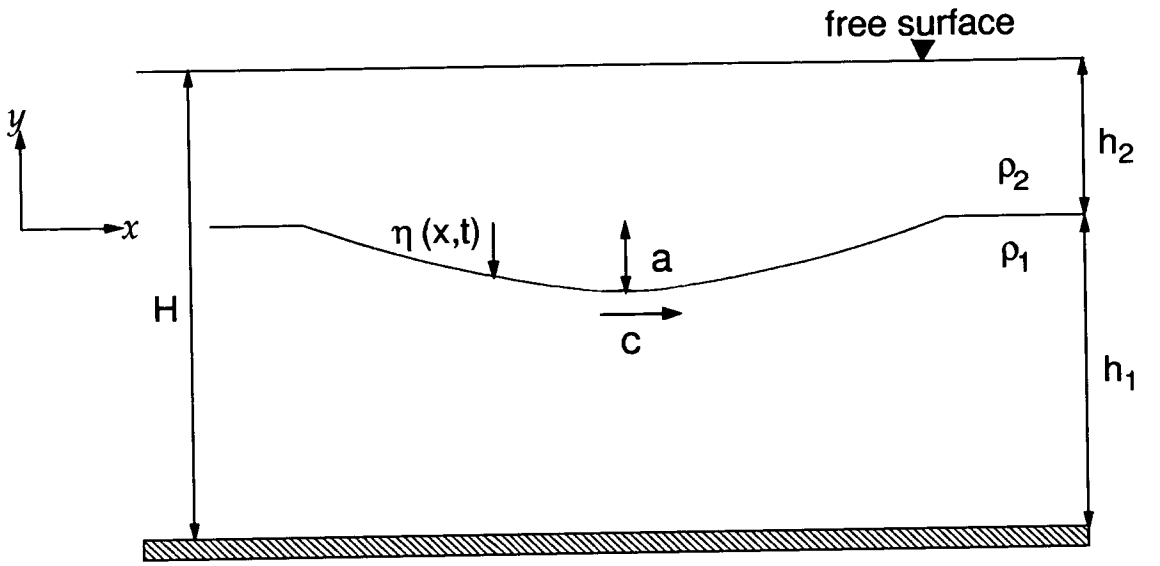

Figure 2.3: Coordinate system used in the KdV two-layer fluid approximation.

$$c_1 = (c_0/h_2) \times \left[\frac{1 - \frac{\rho_1/\rho_2}{h_1/h_2}}{2\left(1 + \frac{\rho_1/\rho_2}{h_1/h_2}\right)} \right], \tag{2.18}$$

and

$$c_2 = (c_0 h_2^2) \times \frac{h_1}{h_2} \left[\frac{\rho_1/\rho_2 + \frac{1}{h_1/h_2}}{6\left(1 + \frac{\rho_1/\rho_2}{h_1/h_2}\right)} \right]. \tag{2.19}$$

The wave speed, c_{KdV} is written as

$$c_{\mathrm{KdV}} = c_0 \left(1 + \frac{a(\rho_2 h_1^2 - \rho_1 h_2^2)}{2h_2 h_1 (\rho_2 h_1 + \rho_1 h_2)} \right). \tag{2.20}$$

The form of an internal KdV soliton also follows a "sech-squared" profile and the characteristic wavelength, λ is defined as

$$\frac{1}{\lambda^2} = \frac{3a[1 - (\rho_1 h_2^2)/(\rho_2 h_1^2)]}{4 h_2^2 h_1 (\rho_1/\rho_2 + h_2/h_1)} \tag{2.21}$$

and the horizontal particle velocity profiles, in the upper layer where $0 < y < h_2$ and in the lower layer where $-h_1 < y < 0$, are written to second order in (a/h_2) as

$$u_2(x,y,t) = c_0 \left\{ \frac{\eta}{h_2} \left[1 + \frac{a(\rho_2 h_1^2 - \rho_1 h_2^2)}{2h_1 h_2(\rho_2 h_1 + \rho_1 h_2)} \right] - \frac{\eta^2}{h_2^2} - \frac{h_2 \eta_{xx}}{6} + \frac{\eta_{xx}(y-h_2)^2}{2h_2} \right\}, \tag{2.22}$$

$$u_1(x,y,t) = c_0 \left\{ -\frac{\eta}{h_1} \left[1 + \frac{a(\rho_2 h_1^2 - \rho_1 h_2^2)}{2h_1 h_2(\rho_2 h_1 + \rho_1 h_2)} \right] - \frac{\eta^2}{h_1^2} - \frac{h_1 \eta_{xx}}{6} + \frac{\eta_{xx}(y+h_1)^2}{2h_1} \right\}, \tag{2.23}$$

where η_{xx} is the second derivative of the interfacial displacement with respect to x. There is a flow reversal in the bottom layer such that there exists a velocity shear across the interface, separating the two fluids, with the velocity having a zero value at a location within this layer.

Other internal solitary wave theories

Aside from the shallow water internal wave theory, characterised by the KdV equation, other analytical models have been developed to classify and describe internal waves in both the deep water regime, where the wavelength is much smaller than the overall water depth, and in fluids of finite extent, where the wavelength is of the same order as the fluid depth. The first of these theories, the deep water theory, was developed by Benjamin [10] and the governing equation is known in the literature as the Benjamin-Ono equation. The total fluid depth is infinite, and the density variations only extend over a limited depth. The internal

wave is long relative to the intrinsic length scale of the stratification. These waves are more dispersive than the shallow water wave type. Benjamin [10] found the resulting solitary wave solution to have a Lorentzian profile. In the finite depth theory, presented by Kubota *et al.* [54], the pycnocline is much smaller than the total fluid depth. The finite depth evolution equation has been shown to reduce to the KdV equation and the Benjamin-Ono equation in the shallow and deep water limits respectively. Joseph [43] found the solitary wave solution to this equation.

Laboratory validations of internal wave theories

The range and validity of KdV theory for internal solitary waves propagating in a two-layer fluid system has been investigated by a large number of researchers. Here, some of the most recent and pertinent investigations to the present study are reviewed.

In [51], Koop and Butler investigate the domain of validity of both the shallow water, deep water and KdV theories, extending the KdV equation to second order such that the effect of including higher order terms may be assessed. An immiscible two fluid system consisting of Freon and fresh water was used, generating solitary waves by means of an electronically controlled sub-surface paddle. Measurements were made using capacitance gauges along the length of the wave tank in order to determine interfacial displacement. They found, from experiments

performed in both the deep and shallow water configurations, that the Korteweg - de Vries theory agrees relatively well quantitatively with both the wave shape and the amplitude - wavelength scaling for solitons in the shallow water regime. In addition, they found that extending the KdV equation to second order substantially increases the range of validity of the theory and concluded that the KdV analysis is capable of satisfactorily modelling small amplitude solitons in fluids of limited vertical extent. The KdV equation, to second order in a/h_2 becomes [51]

$$\eta_t + c_0\,\eta_x + c_1\eta\eta_x + c_2\eta_{xxx} + c_3\eta_{5x} + c_4(\eta\eta_{xx})_x + c_5(\eta^3)_x + c_6(\eta_x^2)_x = 0, \quad (2.24)$$

and the solitary wave solution to this extended equation is given by

$$\frac{\eta(x,t)}{h_2} = \frac{a}{h_2}\,\mathrm{sech}^2[(x-ct)/\lambda]\left\{1 + \frac{a}{h_2}C\,\tanh^2[(x-ct)/\lambda]\right\} + O\left[\left(\frac{a}{h_2}\right)^3\right], \quad (2.25)$$

where the constants c_2, c_3, c_4, c_5, c_6 and C are given in appendix B. For the deep water case, Koop and Butler argue that the range of validity of this theory is limited and that their results fall outside this range. In the case of the finite depth theory, where the experimental conditions are suitable however, they remark that the discrepancies are not easily explained. Similar conclusions were also drawn by Hammack, Leone and Segur [82].

Kao *et al.* [44] and Grue *et al.* [29] also investigated experimentally the range

of validity of the KdV theory for internal solitary waves. Kao *et al.* [44] used a two-fluid fresh water - brine configuration. To generate the solitons, they used a guillotine-style gate system, a method also used by Grue *et al.* [29] and in the work presented here. This system is described in section 3.2.6. Four different measurement techniques were employed to characterise the waves. Direct flow visualisation by photography was used and an interface follower tracked a particular density contour of the pycnocline. Hot-film anemometry and the hydrogen bubble technique were employed to measure wave particle velocities and study the vertical shear structure respectively. They ran a series of experiments varying both the volume of water trapped behind the gate and the depth ratio of the two layers. They found, in agreement with Koop and Butler [51], that the KdV theory provides a suitable description of small amplitude solitons in a finite depth fluid. They observed the existence of a systematic deviation of the experimental results from the theory as the amplitude of the solitary wave was increased.

Grue *et al.* [29] extended their investigations to cover large amplitude solitary waves. In a series of laboratory experiments, they used a salt water - fresh water system, using a density difference of around 2% with a sharp pycnocline. Measurements were performed using an optical particle tracking technique, capable of determining wave particle velocities. The results supported those of Kao *et al.* [44], demonstrating that first order KdV theory provides a good description of small amplitude solitary waves, for a wide range of layer depth ratios, h_2/h_1, up to non-dimensional amplitudes of around $a/h_2 \sim 0.4$. In particular, the re-

sults validated their new fully nonlinear numerical model, capable of correctly modelling large amplitude solitary waves [28]. This model, used to validate solitary wave generation experiments performed in this study, is further described in section 4.3.2.

The KdV equation neglects the effect of dissipation. Russell [78] noticed that a surface solitary wave propagates without change of form, but that it does experience amplitude attenuation due to friction. Grue *et al.* [29] also noted in their experimental work on internal solitons that the velocity in the lower layer is reduced with distance travelled and is exhibited by the resultant decay in amplitude. The viscous decay of surface solitons was investigated by Keulegan [47] and by Hammack and Segur [41] who presented a procedure for estimating the decay of a leading soliton within a train of solitary waves. Koop and Butler [51] discussed how existing theories could be extended to include viscous effects for internal solitons. Leone *et al.* [57] derived a formula for the decay of a long internal solitary wave propagating in a quiescent two-layer fluid. In this experimental study, however, amplitude attenuation by viscous dissipation is not considered to be an important factor given the distance over which the investigated solitary waves are measured (section 3.2.4).

Main assumptions of the Korteweg de Vries theory

In summary, the main assumptions leading to the KdV equation, which is weakly nonlinear and weakly dispersive, are

- The motion is 2D
- The fluid is incompressible and irrotational
- The waves are long relative to total fluid depth
- The wave amplitudes are small but finite so that

$$\frac{\overline{\eta}}{h_1 + h_2} \ll 1 \tag{2.26}$$

- Viscous effects are weak and can therefore be ignored

2.4 Internal Solitary Waves in the Ocean and the Atmosphere

2.4.1 The ocean and the atmosphere as stratified fluids

Both the ocean and atmosphere are well-known examples of stratified media. The structure of the ocean is concentrated upon here, although some references and examples of atmospheric stratification are also given.

In the ocean, the density of sea water is a function of pressure, salinity and temperature. Temperature variations are responsible for density variations of around 0.5% whereas salinity changes can affect changes in density of about 0.2%. Ocean dynamics are heavily influenced by these latter two variables and their effects are generally much more important than that of pressure. In general, there is a decrease in temperature with depth from the surface and an increase in salinity.

In the deep ocean, particularly in equatorial and tropical regions, there exists a surface zone of approximately uniform density. Changes in temperature and salinity, initiated at the surface, become well-mixed by surface waves and instabilities within this upper layer. This area is therefore known as the "mixed layer" and can be from approximately 25m to 250m in depth. Figure 2.4 illustrates a typical temperature distribution within the deep ocean in tropical and mid-latitude regions. Below the mixed layer, there lies a zone in which the density increases rapidly with depth, before the density gradient decreases. This middle region, where the temperature gradient is greatest, is called the thermocline. Correspondingly, it is in this region that the buoyancy frequency, N, is at a maximum. The thermocline can be thought of as the interface between two layers of water of different temperature. In the summer months, the mixed layer can become stratified due to heating at the surface, hence a seasonal thermocline can develop. Although the ocean is certainly an example of a continuously stratified fluid, the thermocline can be viewed as a relatively thin layer when compared

to the overall depth. Internal waves can become trapped within the thermocline zone. The oscillations are restricted to this region and can only propagate in a horizontal direction [59].

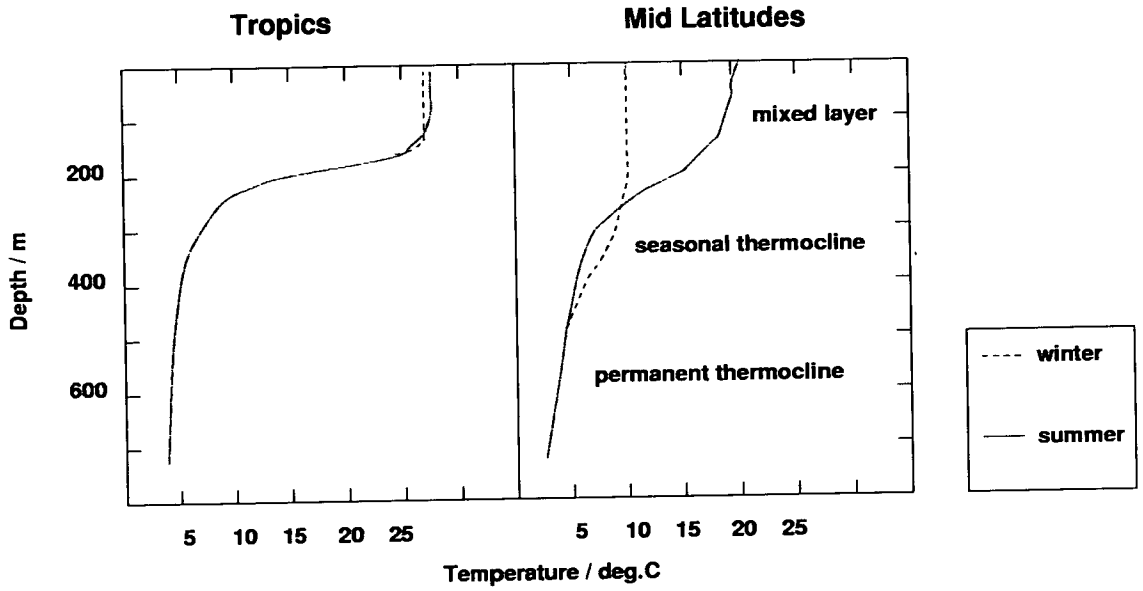

Figure 2.4: Typical temperature distributions in the deep ocean, which lead to changes in density with depth. Graphs of temperature change with depth are shown for the Mid Latitudes and tropical regions [72].

In the open ocean, most variations in density are continuous and can be linked to variations in temperature. In shallow seas and coastal shelf regions, the stratification often has a pronounced two layer profile. The mixed layer is still present but represents a substantially greater proportion of the total depth. A temperature gradient can gradually be restored within this region in calm conditions. Insolation from the surface and an influx of cooler water from the open ocean can result in a sharp thermocline being established either near the surface, or close to the sea floor. The density gradient is almost exclusively determined by variations in temperature and the salinity is approximately constant with depth [70]. This

density gradient may be referred to as a shelf thermocline.

In contrast, in fjords [28] and estuaries, and in some polar regions, salinity is often the controlling stratification factor. Sharp stratifications are also observed in such areas. Fresh water, moving seaward, overlies the heavier, salt water. If the sea surface remains relatively calm, the tidal motions are too weak to overcome the buoyancy force of the stratification and so the density gradient is preserved. The two fluids are then separated by a thin region over which the density changes continuously. In such circumstances, internal waves can propagate along the density gradient region, as in the deep ocean example above. Such a system can be simplified to that of the discontinuous stratification case if the interface is considered as a thin surface. Any effects of diffusion of salt into the fresh water are neglected.

The structure of the stratification inherent in the atmosphere is somewhat different from the oceanic density profile. The density decreases rapidly with altitude. As a result, the buoyancy frequency is not sharply peaked as in the thermocline, but varies more gradually. Internal waves in the atmosphere can have wavelengths of the order of kilometres, upon which scale $N(z)$ varies slowly. In addition, winds interact with and can modify the characteristics of waves in the atmosphere. Stationary atmospheric waves can occur over large topographic features such as mountains in a steady wind. They can often be identified by flat lenticular-shaped clouds to the lee of the obstacle.

2.4.2 Oceanic and atmospheric solitary waves

Observations of internal solitary waves in nature are widely documented in both the ocean [70] and the atmosphere [84, 67, 95]. This section introduces oceanic and atmospheric internal waves and discusses the motivation behind their continued study. Some of the quantitative studies of oceanic solitary waves that have been published in the last 20 years are then reviewed.

Internal gravity waves in the oceans and the motivation for their study

Unsurprisingly, over the past century, many observations of internal gravity waves have been reported in both the ocean and the atmosphere. In 1896, Fridtjov Nansen, a Norwegian explorer on an expedition to the Arctic, noticed that his ship was experiencing some resistance to forward motion, even though the water surface was calm [28]. His ship had experienced what is now called the "dead water phenomenon". Although no waves were visible at the water surface, internal waves, propagating at the interface between a surface layer of fresh water and a lower, more dense, saline layer beneath it, inhibited the ship's velocity.

Oceanic internal gravity waves are oceanic motions which occur, typically, on a characteristic scale of between 10m and 10km [70]. As the temperature or salinity gradients tend to be quite sharp, any disturbance to the thermocline or pycnocline will usually propagate away from the region of generation as an internal wave.

The seasonal variability of the density structure of the ocean is reflected in the variability of internal wave characteristics, affecting for instance the direction of propagation and the size of the waves. Oceanic internal waves may propagate in a direction different or opposed to the general surface wave direction and can be generated by a variety of mechanisms [6]:

- tidal flows of stratified water over and around topographical features (illustrated in figure 2.5), such as islands and continental shelf edges
- atmospheric forcing via pressure changes and surface stress
- other mechanisms displacing the pycnocline from its equilibrium position

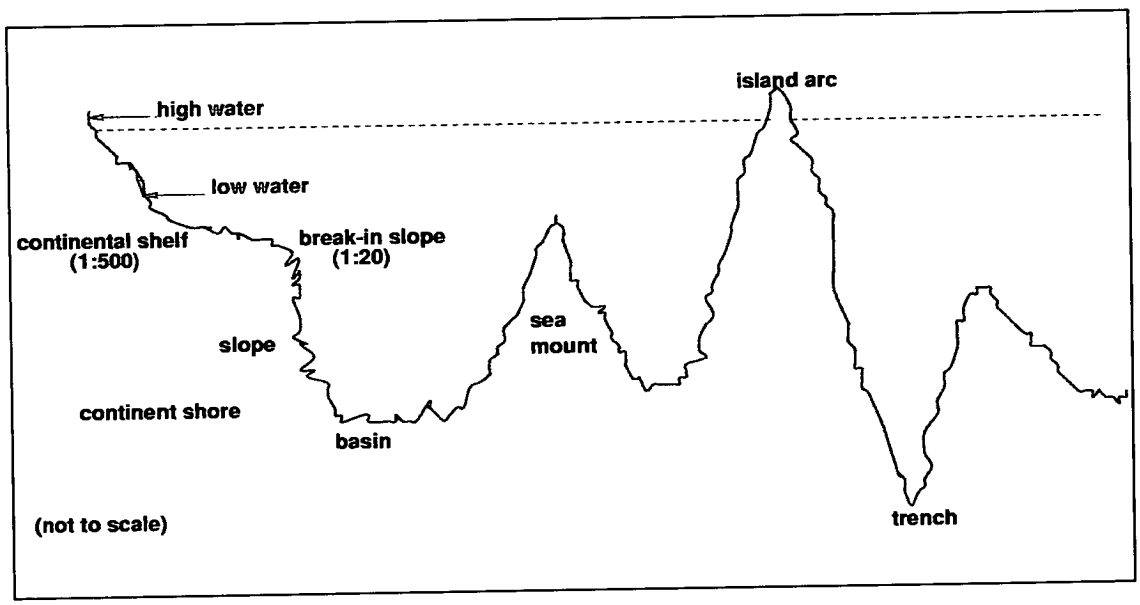

Figure 2.5: Some features of coastal and deep water oceans.

The study of internal waves is relevant to many fields of research. As internal waves carry with them considerable momentum and energy, their propagation can

dramatically influence the characteristics of both the local and global oceanic environment. Changes in currents, caused by internal waves, can induce large forces on both static and floating marine structures such as oil platforms and risers. As a result, the study of internal waves is very pertinent to some areas of engineering. One particular example where knowledge of such hydrodynamic loading is important is in the recently projected construction of a submerged floating tunnel in Rogaland, Norway [28, 29].

Knowledge of the properties of internal waves is interesting from a biological viewpoint. The vertical displacement of the thermocline, as a result of internal wave propagation, can also affect temperature and therefore marine nutrient distributions within the ocean [20]. This, in turn, can affect marine animal populations [6].

There also exists widespread interest in internal wave propagation in meteorological fields. Ocean - atmospheric coupling is known to play a role in both local and global climate changes [25, 6]. An often-quoted example of the effects of this interaction is the El Niño - Southern Oscillation (ENSO) phenomenon whereby a large-scale equatorial internal wave travels eastwards across the Pacific ocean. The resulting deepening of the thermocline, in the vicinity of the South American coast causes a significant warming of the surrounding waters and a dramatic change in the region's climate marked by torrential rains and a drop in the marine fish population. These climatic changes are strongly linked to a reversal of

the Trade winds, known as the Southern Oscillation. Global short term changes in climate have also been observed as a result and much research is continually being focused on understanding the dynamics, causes and consequences of the phenomenon [35, 88, 42].

Within the oceanic environment, however, obtaining accurate measurements and a complete description of internal wave trains is a difficult task. It is difficult to track a wave over both long periods of time and long distances in order to build up a picture of how the wave evolves. Until recently, information could only be gathered at a series of closely spaced points at the water surface, using underwater acoustics and hydrographic sensors. Such *in situ* techniques can only provide localised measurements which do not yield all the hydrodynamical information, for instance, the mean flow field.

However, the passage of internal waves may create a "signature" on the water surface, caused by a straining of the shorter surface waves. These patterns are indicated by the appearance of areas of increased surface roughness and, in some cases, breaking waves, which subsequently dissipate [69, 13]. Such surface wave manifestations can be detected by optical and radar devices from aircraft or satellites, as the resulting change in sea surface pattern can alter the reflectivity of surface waves [5, 70, 7, 13]. The leading edge of a wave train appears as a bright streak on a radar image, corresponding to a region of enhanced surface roughness. In particular, the synthetic aperture radar (SAR) has been shown

to be very sensitive to small variations in surface reflectivity [4]. It is a further understanding of the manifestation of these surface wave signatures that provides the principal motivation for this work.

Observations of atmospheric and oceanic solitary waves

There have been many observations of oceanic solitary waves. A sudden disturbance to the density distribution, for example at a tidal sill, can lead to the formation of solitons or solitary wave packets, rank-ordered in amplitude, wave spacings and crest lengths. There seems to be two possible generation mechanisms of solitary wave trains; either by evolution from an initial waveform over water of constant depth or by fission of an initially stable soliton propagating over water of decreasing depth [5]. They are usually solitary waves of depression as the stratification is generally strongest near the surface. They also exhibit remarkable coherence and permanence [11], travelling for long distances without appreciable attenuation, and having strong associated currents. They are often observed on a 12 hour cycle, suggesting that they are associated with changes in the diurnal tide [69, 11, 7]. Only recently has it become possible to identify with certainty the occurrence of solitary wave trains in the ocean due to the introduction of the use of SAR, used in combination with older *in situ* methods.

Solitary waves have also been detected in the atmosphere [95]. One of the most famous examples manifests itself over the northern coast of Australia, and due to

its most common appearance at sunrise is known as "the Morning Glory" [84]. It is associated with a single long horizontal roll , or series of rolls, of low cloud which appears on the eastern skyline, usually in calm cloudless conditions. It advances rapidly bringing with it sudden, short lived, wind squalls, easily identified by a sudden jump in atmospheric pressure. There is rarely any precipitation associated with the squalls. Although the dynamical mechanism behind the generation of Morning Glories, in some cases, is still not fully understood, they are identified as large amplitude solitary waves. The roll cloud appears as a result of warm, moist sea air being entrained upwards and condensing along the leading edge of the cloud [14]. They are most frequently observed in the spring months. The Morning Glory can extend for considerable distances, sometimes over 1000km, travelling inland at a speed of around 10ms^{-1} [67]. The cloud base is usually rather low, at around 300m above the land surface. A photograph of the Morning Glory is shown in figure 2.6.

The applicability of KdV theory to solitary wave occurrences in the ocean

KdV theory has been validated by field work results in coastal areas, the deep sea, lakes and enclosed seas, such as the Mediterranean. There also exists a large quantity of well documented evidence that the passage of internal waves affect the shape of waves at the surface. Ostrovsky and Stepanyants [70] provide an

Figure 2.6: The Morning Glory phenomenon, off the coast of North Australia in the Gulf of Carpentaria [1].

overview of some accounts of field work observations of solitary waves most relevant to this work. Three examples [5, 7, 13] of such accounts are reviewed here both in the context of the applicability of the KdV theory to internal oceanic solitary waves and the change in surface roughness due to the passage of such disturbances. A summary of the parameters used in the three publications mentioned is given in table 2.1. The variable ρ_0 refers to a reference density.

Authors	h_1 (m)	h_2 (m)	a (m)	h_1/h_2	a/h_2	$\Delta\rho/\rho_0$
Osborne & Burch (1980)	863	230	60	3.75	0.26	N/A
Alpers & Salusti (1983)	450	40	15	11.25	0.375	0.0013
Brandt *et al.* (1999)	976	24	32	30.5	1.33	0.0023

Table 2.1: Summary of the data collected in fieldwork [5, 7, 13] and used for comparison with KdV theory.

In 1980, Osborne and Burch [5] undertook a series of measurements in the An-

daman Sea, south-east of the Bay of Bengal. In this area, regions of short, choppy, breaking surface waves, known as tide rips, had been previously observed and were thought to be associated with the passage of long internal waves. The internal waves are caused by strong tidal currents flowing over a varying bottom topography and through inlets that oppose surface wave propagation. The ocean density structure in this region is quite stable during the late summer months, when this study was carried out. Sea water temperature was measured at various depths at one location. A well mixed surface layer extends to around 60m, the subsequent temperature variation with depth then provides a significant vertical density stratification. Large, rank-ordered increases in temperature were attributed to packets of solitary waves of depression. Analysis of the results was supported by satellite photographs of the sea surface, taken above the experiment location. It was deduced that the internal waves could have amplitudes as large as 60m. The internal wave packets occurred approximately in 12 hour cycles, indicating that the waves were tidal in origin. A KdV two-layer model was used to interpret the data. Although better agreement was found with a continuous stratification model, the authors remark that the first order KdV theory adequately predicts two important characteristics; firstly, there exists no particle velocity decay with depth below approximately 600m; secondly, the ratio of horizontal particle speeds in the two layers is close to the depth ratio of the layers. They justify the use of this theory as these properties are not predicted by the Benjamin - Ono equation.

The strait of Messina in the Mediterranean, separating the Italian peninsula and the island of Sicily, has always been associated with strong currents and vortices. The sill, located at the strait, acts as a submarine barrier to water flowing through the channel. Legends claim that the currents were caused by two monsters, Scylla and Charybdis, but they are now known to occur as a result of tidal action. In the strait, lighter water from the North converges with denser, more saline water from the South, yielding a density difference of around 0.1%. Tidal currents are superimposed on these "stationary" currents, which lead to the formation of tidal bores at the sill. These develop into solitary wave trains further away from the strait. Alpers and Salusti [7] compare KdV theory to data collected from satellite images taken over the area. For the purpose of implementing the theory, they used *in situ* measurements obtained two years prior to when the satellite images were taken. The magnitude of these parameters can be seen in table 2.1. They argue that results obtained from the KdV equation for wave propagation velocity compare favourably with those obtained from the SAR images, once differences in the environmental conditions between the two data collection periods were taken into account.

More recently, Brandt, Romeiser and Rubino [13] used a two-layer KdV low order theory to validate two methods of interpreting SAR images in order to detect sea surface patterns of internal solitary waves. The images were taken over the Strait of Messina, off the East coast of Sicily. The data compared favourably with the theoretical results for which wave parameters were estimated from hydrographic

measurements taken at the sea surface.

2.5 The Interaction of an Internal Solitary Wave and a Train of Oscillatory Surface Waves

The investigations discussed in the previous section show that the passage of oceanic internal waves is characterised by a change in the sea surface roughness. In some cases, the distortion is great enough to cause the surface waves to break. In fact, when gravity waves of short wavelength ride upon the surface of much longer waves, the wavelength of the shorter waves tend to become shorter and steeper at the crests of the longer waves. Conversely, the short waves become longer and lower in the troughs. In addition, there is a corresponding increase in the amplitude of the shorter waves. This phenomenon was initially investigated by Unna [89] and later expanded by Longuet-Higgins and Stewart (LHS) [61]. In this section, the theory presented by LHS [61] is discussed in the context of short surface waves interacting with internal solitary waves.

2.5.1 The theory of the interaction following Longuet - Higgins and Stewart

Longuet-Higgins and Stewart (LHS) [61] present a rigorous and complete method to calculate the changes in amplitude and wavelength arising from the nonlinear interactions between two oscillatory wave trains, one with a much longer wavelength than the other. The theory is based on an evaluation of the wave motion following a classical Stokes' expansion. The general results, derived using Stokes' nonlinear surface wave approximation, are extended to cover various wave configurations, including progressive wave trains in water of both infinite and finite depth and trains of standing waves.

In order to arrive at the derivations, LHS [61] assume that

- the fluid is irrotational
- the fluid is inviscid
- one of the waves is much shorter than the other such that $k_{\mathcal{L}} \ll k_{\mathcal{S}}$ where k is the wave number and $\mathcal{S}$ and $\mathcal{L}$ refer to the short and long waves respectively
- the shorter waves are superimposed on the longer waves
- the waves satisfy Stokes' nonlinear surface wave approximation

In the same publication [61], the same expressions were also derived by an alternative reasoning using the same assumptions, by considering the effect that

the long waves have at the fluid free surface. This approach is pertinent to the present study as it does not depend on the long waves being sinusoidal in nature, only on them being progressive. LHS assume that the orbital motion of the longer waves stretch the free surface, thus expanding proportionally the wavelength of the shorter waves. If the long wave is sufficiently long relative to the wavelength of the shorter waves, then it can be assumed that the orbital velocity of the long wave, $u_{\mathcal{L}}$, does not change considerably over one period or wavelength of the short waves and so can be considered to be constant. Thus, in this limit, the effect the long waves have on the shorter waves can be thought of as analogous to that of a current.

By considering the rate at which two fluid particles at the water surface separate, with an initial separation dx, they find that the relative change in short wave wavelength $\lambda'_{\mathcal{S}}/\lambda_{\mathcal{S}}$ can be written as

$$\frac{\lambda'_{\mathcal{S}}}{\lambda_{\mathcal{S}}} = 1 + \int \frac{\partial u_{\mathcal{L}}(x,t)}{\partial x} dt. \tag{2.27}$$

In order to obtain an expression for the change in amplitude of the short waves, LHS assume that:

- the energy density of the short waves is given by

$$E'_{\mathcal{S}} = \frac{1}{2}\rho g a_{\mathcal{S}}^2 \left(1 + \frac{1}{2g}\frac{\partial v_{\mathcal{L}}}{\partial t}\right), \tag{2.28}$$

where a'_S is the modified amplitude of the short waves, $\frac{\partial v_L}{\partial t}$ is the vertical acceleration at the free surface due to the presence of the long internal wave, ρ is the density of the fluid and g is the gravitational acceleration

- the rate of transfer of short wave energy, E, is given by

$$E = E'_S c_{gS} + E'_S u_L + S_x u_L, \tag{2.29}$$

where S_x is the radiation stress of the short waves and u_L is horizontal velocity associated with the long waves, near the free surface. The three terms, in order of appearance, represent

1. the bodily transport of energy by the group velocity of the surface waves
2. the bodily transport of energy by the horizontal fluid velocity associated with the long wave
3. the work done by the horizontal fluid velocity of the long wave against the radiation stress of the waves

- the short wave energy is conserved

They subsequently find that the relative increase in short wave amplitude, a'_S/a_S can be written as

$$\frac{a'_S}{a_S} = 1 + \left(\frac{c_{gS}}{c_S} + \frac{1}{4}\right)\frac{u_L}{c_L} - \frac{1}{4g}\frac{\partial v_L}{\partial t}, \tag{2.30}$$

where c_S is the phase speed of the short waves given by equation (2.8) and $v_\mathcal{L}$ is the vertical particle velocity of the long wave near the free surface.

As equations (2.27) and (2.30) do not depend on the long waves being sinusoidal in nature, they may be adapted to apply to the case of short waves riding upon an internal solitary wave. In previous sections (2.3.4 and 2.4.2), it has been shown that the range of validity of the KdV theory is far reaching, providing a good approximation of deep and shallow water, small to medium amplitude, solitary wave characteristics in both laboratory and oceanic situations. KdV theory is, therefore, applied to provide the relevant expressions for the solitary wave horizontal particle speeds and wave velocity. The KdV notation from section 2.3.4 is used such that $u_\mathcal{L} = u_2$, where u_2 is the horizontal particle velocity at the free surface $y = h_2$ given by equation (2.22). c_{KdV} refers to the speed of the solitary wave.

In equation (2.30), the term $1/g(\partial v_\mathcal{L}/\partial t)$, a normalised vertical acceleration due to the long wave fluid motion, is small when compared to $u_\mathcal{L}/c_\mathcal{L}$ and can therefore be neglected, such that the relative change in amplitude for a train of surface waves riding on an internal solitary wave becomes,

$$\frac{a'_S}{a_S} = 1 + \left(\frac{c_{gS}}{c_S} + \frac{1}{4}\right)\frac{u_2|_{y=h_2}}{c_{\mathrm{KdV}}}, \tag{2.31}$$

where now the subscript S refers to the surface wave notation introduced in section 2.2. Similarly, the expression for the relative increase in wavelength can

be written as

$$\frac{\lambda_S'}{\lambda_S} = 1 - \frac{c_0}{ch_2}\eta(x,t)\left(1 + a\frac{(\rho_2 h_1^2 - \rho_1 h_2^2)}{2h_1 h_2(\rho_2 h_1 + \rho_1 h_2)}\right). \tag{2.32}$$

Here, only the first term of $u_2|_{y=h_2}$ in equation (2.22), is used such that the approximation to the velocity at the fluid free surface due to the solitary wave is to first order. Neglecting terms 2 and 3 greatly reduces the complexity of the resulting expression. The characteristic shape of the functions in equations (2.31) and (2.32) is shown in figure 2.7. The graphs of relative change in amplitude (figure 2.7 (a)) and wavelength (figure 2.7 (b)) are plotted against solitary wave "phase", or non-dimensional distance, x/λ, from the maximum depression of the solitary wave shape. It can be seen that whilst the amplitude of the surface wave rises, its wavelength decreases. In both cases, the greatest change is located about the maximum amplitude of the solitary wave.

2.5.2 Laboratory investigations of internal wave - surface wave interactions

The Longuet-Higgins and Stewart (LHS) theory and the development of the radiation stress concept has been the motivation and basis for subsequent studies and investigations [62, 23, 58, 49, 52, 33]. These studies are reviewed here so as to provide a context for the present work.

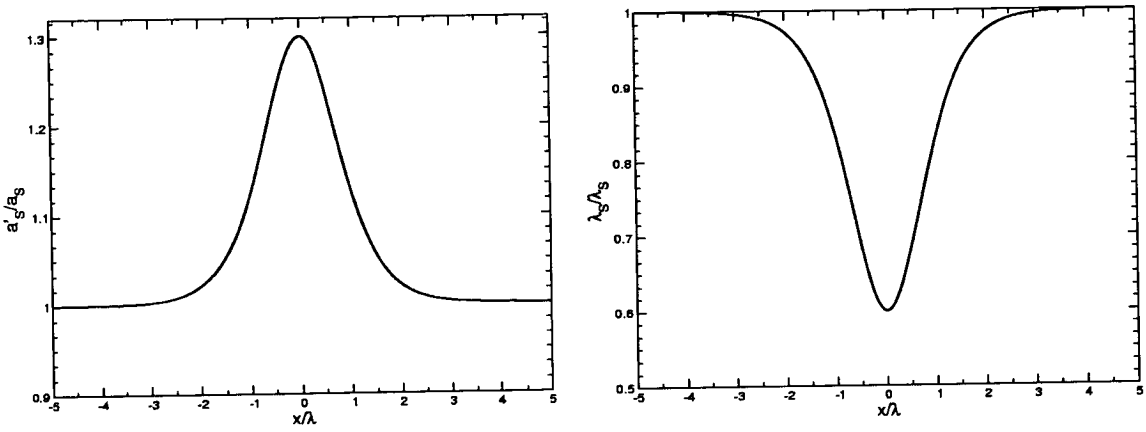

(a) a'_S/a_S (b) λ'_S/λ_S

Figure 2.7: Relative change in surface wave amplitude and wavelength, calculated from equations (2.31) and (2.32), against solitary wave "phase", or non-dimensional distance from the maximum depression of the solitary wave, x/λ.

Gargett and Hughes [23] investigated the interaction between short surface waves and a periodic mean current propagating in a direction oriented at an angle ϕ_0 to the surface waves, using an approach based on LHS. Their theory is compared to field work measurements of wind-generated surface waves. Over the crests of the internal wave, they found that if the component of the speed of the surface wave in the same direction as the internal wave train is smaller than the speed of the internal wave, the surface wave is turned away and its amplitude decreased. Over the internal wave troughs, the opposite occurred.

Lewis *et al.* [58] presented the results of a series of experiments investigating the interaction of monochromatic internal and surface waves, propagating in the same direction, such that the angle between the direction of propagation of the two wave trains was $\phi = 0$. A two-layer fluid system, composed of water and a

kerosene and Freon mix, was used to measure modulations of wave characteristics. The density variation was of the order of 1% across the interfacial region. Two resistance wave gauges were used to measure internal and surface wave profiles and a specially designed optical device measured the wave slope directly. A theory was also developed, based on the LHS approach and was found to agree with the experimental results. The authors found that the magnitude of the modulations depended strongly on the relative wave speeds, the maximum interaction effect occuring when the phase speed of the internal wave and the group velocity of the surface wave were matched. They referred to this regime as the resonant case.

Koop and Redekopp [52] presented a theory and supplementary experimental results, investigating the generation of a low frequency long internal wave modulated by a high frequency internal wave train. The dynamic coupling and exchange of energy between the two wave trains was investigated. They used a three-layer immiscible fluid system using fresh water, a kerosene and Freon mix and a saline lower layer. The high frequency wave propagated at the upper interface and the low frequency wave at the lower interface. Waves were generated along the upper pycnocline and the response to this forcing was studied at the lower interface. An infrared optical interfacial wave gauge was used to measure interfacial displacements. They found that good agreement between the theory and the experimental results was obtained.

In [32], Guizien and Barthelemy investigated the interaction between an internal

solitary wave of depression and a monochromatic surface wave train in a salt water - fresh water stratification. Internal and surface waves could be produced such that they either propagated in the same or opposite directions. Hence, $\phi = 0$ or π. Different layer depth ratios were used such that $h_1/h_2 \sim 2.5$ to 4. The density gradient used was of the order of 2 - 3% and the pycnocline thickness was approximately 0.15 times the depth of the top layer. Small amplitude surface waves, with a frequency of around 2Hz, were generated using a plunger-type wave maker and scaled as shallow water waves. Measurements of the surface wave amplitude modulation were taken using a series of capacitance probes. The range of solitary wave amplitudes was limited to small amplitudes such that $|a|/h_2 \sim 0.3 - 0.4$. The solitary wave characteristics were calculated using a low order KdV approach. Table 2.2 provides a summary of the parameters used. Clear amplitude modulations were detected by the measurement probes. They noted that any surface wave phase modulation, however, proved difficult to quantify [32]. In [33], they compare their results to those of Lewis *et al.* [58] whose theory assumed that the horizontal velocity profile of the internal wave did not vary with depth. This is not true in the case of small amplitude solitary waves for which horizontal velocity in the upper layer increases with distance from the interface. They concluded that short wave energy may not be conserved when the wavelength of the surface wave train is not much smaller than that of the internal wave. They added that such wave energy conservation may only apply to wind generated surface waves in the deep ocean, whose wavelength is sufficiently small

when compared to typical internal wave length scales.

Characteristics	
Density difference, $\Delta\rho$	2 - 3%
Layer depth ratios, h_1/h_2	2.5 - 4
Surface wave frequencies (Hz)	2 - 2.5
Surface wave amplitude, a_S (m)	0.006 - 0.008
Surface wave steepness, $2a_S/\lambda_S$	$\sim$ 0.03
Soliton wavelength (m)	1.2
Soliton amplitude, $\|a\|/h_2$	0.3 - 0.4

Table 2.2: Summary of main parameters used by Guizien *et al.* [32]

2.6 Motivation for the Study and Review of Chapter 2

In this chapter, phenomena involving stratified fluids and internal gravity waves were introduced. Stokes' linear surface wave approximation was presented. The concept of a solitary wave was then put forward, from its initial discovery by Russell in the late 19th century, to observations of internal solitary wave trains in the ocean made by synthetic aperture radar, as recently as two years ago.

The development of the KdV theory, a weakly nonlinear, weakly dispersive approximation, which describes the propagation of solitary waves in a rectangular channel, was outlined. The applicability of this theory to the propagation of both laboratory generated internal solitons in a two-layer fluid and oceanic solitary

wave measurements was reviewed. In general, KdV theory adequately predicts the form and amplitude - wavelength scaling of small amplitude solitons in a range of depth regimes, but breaks down in the large amplitude limit. It was also seen that extending the KdV equations to second order in a/h_2 increased the range of validity of the theory. However, the numerical fully nonlinear model presented by Grue *et al.* [30, 28, 29] is successful in predicting large amplitude soliton characteristics where the KdV model fails.

It was shown (section 2.5.1) that the assumptions of the Longuet - Higgins and Stewart (LHS) theory [61] can be applied to the interaction of an internal soliton in a two-layer fluid with a train of short wavelength surface waves. The use of the KdV theory in the approximation is also justified. So far, there seems to have been little investigation of the applicability of the LHS interaction theory. The few studies, which have already been undertaken, have mainly been done in the field of oscillatory internal waves, and have been discussed in section 2.5.2. Although the work presented by Guizien and Barthelemy [33] is concerned with surface wave amplitude modulations as a result of internal solitary wave - surface wave interactions, the range of wave characteristics of both wave types were rather limited. Only two surface wave frequencies were used and only small amplitude solitary waves were generated. The LHS theory is referred to but only an approximation to the LHS results seems to have been used. The data sets were therefore somewhat restricted. As a result, it is evident that there exists plenty of scope for further work in this field.

The laboratory experiments on internal solitary waves propagating in a two-layer fluid, carried out to date by other researchers and reported in this chapter (sections 2.3.4, 2.4.2 and 2.5.2), have, with the exception of Grue *et al.* [29], been performed using non-quantitative flow visualisation methods and intrusive probes, which can obstruct the flow and yield only temporally- and spatially-averaged information. In this respect, this study differs. Here, full field, instantaneous, non-intrusive flow visualisation will be used, namely Digital Particle Image Velocimetry (DPIV) and planar laser induced fluorescence (PLIF), to provide quantitative velocity and density maps of the flow respectively. Both techniques are described in the next chapter.

This work firstly enables the suitability of these techniques to be assessed in the context of two-layer fluid solitary wave investigations. In addition, as these methods are non-intrusive, there will be no distortion of any observed surface wave modulation, or of any soliton modulation. The full field nature of the techniques also allow the surface and internal effects of the interaction to be observed simultaneously. Grue *et al.* [29] also mention that the exact density structure of the interfacial region remains unknown when the gate generation method (section 3.2.6) is used. This question could possibly be resolved using PLIF.

The motivation of this study is therefore two-fold. The first goal is to successfully apply DPIV and PLIF measuring techniques to the investigation of laboratory

generated internal solitary waves propagating at a brine - fresh water interface. The aim is to then extend this work to investigate surface wave - internal solitary wave interactions and compare the results with a theory initially developed by Longuet - Higgins and Stewart [61] and adapted to the case of internal solitary waves following KdV theory.

Chapter 3

Experimental Measurement Techniques and Facilities

This chapter details the experimental measuring techniques used throughout this work, in addition to the experimental facilities and apparatus. Emphasis is put on the theory behind the techniques and their general application to experimental fluid dynamics. Inherent errors in the techniques are also considered. Specific aspects of the techniques pertaining directly to the study of surface waves and stratified flows are reserved for chapter 4 where they are discussed in the context of the experimental apparatus and facilities.

3.1 Experimental Measurement Techniques

In this section, the measurement techniques used throughout this work are introduced and discussed. The techniques employed are Digital Particle Image Velocimetry (DPIV) and Planar Laser Induced Fluorescence (PLIF). Both applications are non-intrusive, planar flow visualisation techniques. In this study, they both rely on a laser light sheet to illuminate a vertical plane of the flow in order to obtain velocity information, in the case of the former, and density distribution information, in the case of the latter. There are, in effect, two stages to each technique; the data acquisition process and the analysis. The principles, the applications of the techniques and the acquisition and analysis methods of each are considered. The specific set-up and relevant parameters for each technique are then discussed in the chapters 4 and 5 as the experimental work they were applied to is presented.

3.1.1 Digital Particle Image Velocimetry

In the field of experimental fluid mechanics, particle image velocimetry (PIV) is now a well established optical measurement technique. It is an optical velocity information acquisition technique, allowing instantaneous quantisation of two-dimensional velocity characteristics within a plane of the flow, without the intrusion of measurement probes, which obstruct the fluid motion. It has been

used successfully in turbulent, laminar or high speed regimes. As the methods of data acquisition for PIV have been both extensively developed and employed over the past few decades, many detailed descriptions and discussions of the measurement technique have been published [76, 93, 2]. The aim here is to give a general overview of the technique with particular reference to how Digital Particle Image Velocimetry (DPIV) can be used to yield accurate and reliable flow measurements in stratified fluid flow experiments.

The general principles of particle image velocimetry

Raw PIV data are obtained by imaging the flow under investigation. The area of interest in the flow is exposed to a planar light sheet. The light scattered by seeding particles introduced into the fluid prior to starting the measurement is then recorded using an imaging system. Successive recordings of the flow at known time intervals, δt, can be made, either on the same frame or consecutive frames. This yields a series of tracer particle "patterns" which are then subjected to a statistical analysis routine to determine the average particle displacement.

The entire image is divided up following a regular lattice pattern, into small, usually square, areas, known as interrogation spots. A spatial correlation routine is then performed over each image. In an interrogation area of $N \times N$ pixels, the

maximum spatial frequency, f_s, that can be measured is

$$f_s = \frac{1}{N} \tag{3.1}$$

In order to sample this frequency correctly, according to the Shannon (or Nyquist) sampling theorem, the images must be sampled at twice that spatial frequency, $2f_s$. This is equivalent, in real space, to a spatial interval of $1/2f_s$ pixels. Imposing a regular sampling grid of spacing $\frac{N}{2} \times \frac{N}{2}$ pixels on each image will give a 50% overlap between interrogation areas in the correlation routine.

$$\text{grid spacing} = \frac{1}{2f_s} \equiv \frac{N}{2} \tag{3.2}$$

Any smaller overlap will result in the data being oversampled. The statistical measurements of the particle displacements are distributed across the image plane upon a regular two-dimensional lattice, determined by the dimensions of the sampling grid. The result is, therefore, a two-dimensional velocity vector map for every image pair of the flow.

The correlation routine can either be performed on consecutive images, each containing one exposure of the tracer particles or on a single image, containing multiple exposures of the flow. In the former case, the process is that of cross correlation, in the latter, that of auto-correlation. The work presented here only concerns itself only with cross-correlation as this method has two very

useful advantages. Figure 3.1 show schematically the principles of both the auto-correlation and cross-correlation analyses respectively.

Whereas the auto-correlation process yields a series of peaks in the correlation plane, consisting of a self-correlation peak in the centre and smaller peaks, symmetrically either side of the centre peak, the cross-correlation technique gives only one significant peak corresponding to the average displacement of the particles within the interrogation area. In the auto-correlation plane, the symmetrical nature of the secondary peaks relative to the central one highlights the issue of 180° directional ambiguity. This ambiguity, however, is removed in cross correlation. In addition to this, the dynamic velocity range of the system is increased; that is, that small velocities close to zero, which would result in overlapping particles in a multiply exposed image, can be detected as there is no self correlation peak to mask the displacement peaks [18].

The development to digital image capture and analysis: Digital Particle Image Velocimetry

In the earlier years of PIV development and measurements, images of the flow were captured using wet-film photography. Computational speed and memory limitations meant that the mean displacement evaluation was performed optically using double or multiple exposures of particle patterns on a single frame. With the advent of digital imaging systems, now more readily available due to

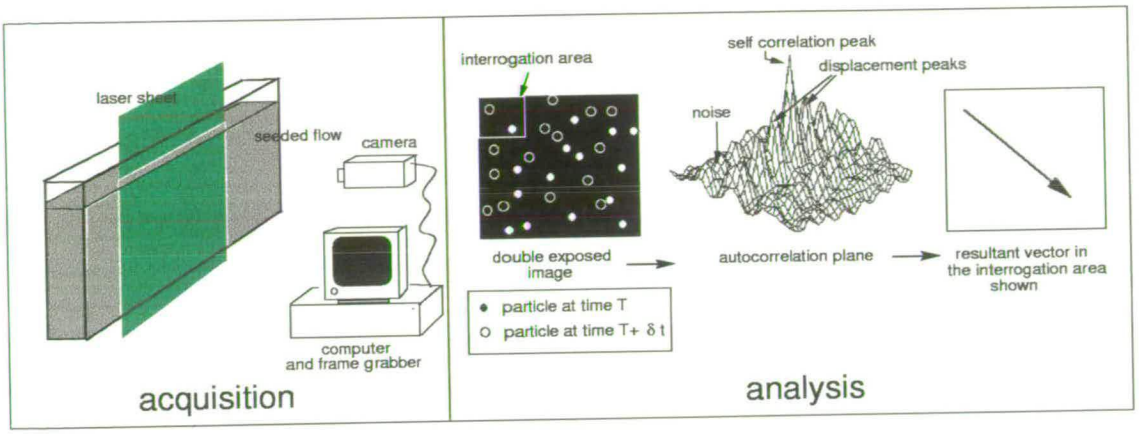

(a) Auto-correlation

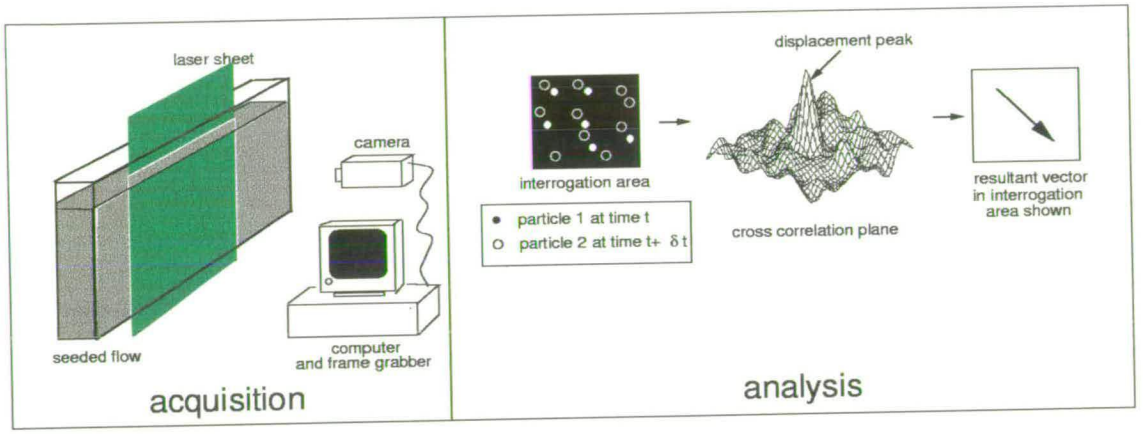

(b) Cross-correlation

Figure 3.1: The stages of PIV auto-correlation (a) and cross-correlation (b). In (a) the image is multiply exposed, whereas in (b) two separate exposures are cross correlated.

decreases in cost and increases in computing power, sequences of images are usually captured electronically. As the analysis can also be performed digitally, the rapidity with which results can be calculated means that digital PIV (DPIV) is now the favoured technique and is employed here. The operation of a digital camera and a description of the system used in this work is presented in section 3.2.7.

Digital Particle Image Velocimetry analysis; peak detection and bias error

In cross-correlation, used throughout this work, individual exposures of the tracer particles are captured on separate consecutive images. Nevertheless, it is useful to think in terms of particle image pairs where a pair refers to the image of a particle captured at a time t on a first exposure and the image of the same particle on a second subsequent exposure, at a time $t + \delta t$ later.

Although the overall accuracy of DPIV measurements is the result of a combination of experimental design and analysis factors, one key aspect is the location of the correlation peak. Particle image size, the seeding density and the presence of strong velocity gradients all influence the overall quality of the peak detection and hence the displacement estimate. The resulting effects of these combine to bias the measurement in various ways and are collectively known as bias error.

The particle images are not ideal; their spatial intensity distribution, known as their point spread function, is not a δ-function but can be well approximated by a normalised Gaussian curve [76]. Consequently, the signal peak in the correlation plane is a displacement function rather than a sharp peak. Each particle image pair in the interrogation area contributes to the overall shape of the resultant correlation signal. It is therefore useful to ensure that the individual contributions are as well defined as possible. If a velocity gradient exists over the interrogation spot, the shape of the displacement function will also broaden and small

displacements will contribute more to the height of the peak than larger ones. It is, therefore, also desirable that the velocity gradient over the interrogation area is small.

As the image is captured electronically, on a CCD array, locating the correlation peak to the nearest array element position, or pixel, is not satisfactory as this will result in a large error in the estimation of the displacement. Therefore, sub-pixel accuracy must be achieved. In digital imaging where the particle images are of the order of 2 - 3 pixels in diameter, this can be done by interpolation; fitting a "three point estimator" to the peak. This finds the highest point of the peak to within $\pm 1/10$ to 1/20pxl [93, 76, 94]. One of the most common routines to be employed for this purpose is the Gaussian peak fit [94] where the displacement correlation peak is assumed to be Gaussian in shape since the particle image intensity distribution can be well represented by such a curve. In the case where the particle image diameter is rather small, there may not be sufficient information to fit the curve well, as adjacent values to the peak can be hidden within the background noise. Conversely, if the particle image diameter is too big, the correlation peak increases in width and decreases in height and the same problem arises, thus leading to spurious peaks being detected.

Finally, there exists a finite probability that a peak from the background noise in the correlation plane may be detected as the highest peak in the plane and therefore as the signal peak. This will lead to an erroneous velocity vector known

as an outlier. This probability can be reduced if the peak is substantially larger than the background noise. Keane and Adrian [38] suggest that the height of the signal peak should be between 1.2 and 1.5 times larger than any other. In this work, the factor used has a value of 1.2. If this condition is not met, then a gap in the vector map will appear. This can be interpolated at a later stage in the analysis.

DPIV set-up optimisation

In addition to the consequences of digital analysis and location of the correlation peak, there exist other aspects of the DPIV set-up which can also substantially affect the quality and accuracy of the results. A key requirement of any PIV set-up is that the seeding particles can be assumed to faithfully follow the flow, without altering the fluid properties and also without interacting with each other. The smaller the particles, the more likely it is that they do follow the flow motion. Here, there must be a trade-off between the ability of the particles to scatter light effectively and to track the flow accurately. Experiments in water require either larger particles than those in air or brighter illumination, as particles in water scatter approximately ten times less effectively than those in air [2]. In the work presented here, conifer pollen, a common seeding material for PIV experiments [75, 18], is used.

A number of recommendations, aimed at optimising the PIV set-up, are sum-

marised by Adrian [3] and Westerweel [94]. These recommendations are often referred to as "design rules". The seeding density across each interrogation area should be uniform and such that each area contains many particle images. This also implies that the particle images must be small. The estimation error in the displacement is a minimum when

$$d_t/d_\tau \sim 2, \tag{3.3}$$

where d_t is the particle image diameter and d_τ is the pixel length.

For the velocity gradients over an interrogation area to be small, it is important that the velocity variations, $|\Delta u|$, are also small. If

$$|\Delta u|\, \delta t \ll d_t/M, \tag{3.4}$$

where δt is the time interval between two correlated images and M is the magnification of the imaging system, then the displacement field can be considered to be locally uniform [94].

The homogeneity of the seeding over the measurement area is also important. The greater the particle density, the greater the probability of a valid displacement detection. The number of particle pairs over an interrogation area depends on the overall particle density, $\mathcal{N}$ and the amounts of in plane and out-of-plane displacement, F_I and F_O respectively. If there is no in or out of plane displacement,

the values of both F_I and F_O are unity.

F_O is expressed as the normalised correlation of the intensities of two consecutive image intensities in terms of the out-of-plane displacement, δZ [46], and can be interpreted as the loss of particle image pairs due to motion perpendicular to the plane of the light sheet [93]. It is given by [45]

$$F_O(\delta Z) = \frac{\int I_O(Z) I_O(Z + \delta Z) dZ}{\int I_O^2(Z) dZ}, \tag{3.5}$$

where I_O is the intensity distribution of the light sheet and δZ is the displacement of the particles out of the light sheet, perpendicular to the (X, Y) image plane.

The in-plane displacement is denoted F_I and is defined as the normalised correlation of the interrogation area intensity [46]

$$F_I(\mathbf{s}) = \frac{\int I_1(\mathbf{X}) I_1(\mathbf{X} + \mathbf{s}) d\mathbf{X}}{\int I_1^2(\mathbf{X}) d\mathbf{X}}, \tag{3.6}$$

where I_1 is the intensity over the interrogation area centred at coordinates $\mathbf{X_1} = (X_1, Y_1)$ and $\mathbf{s}$ is the spatial frequency coordinate in the Fourier transform plane [80].

The product of these three parameters is a measure of the effective particle image pair density. It was shown [46], using Monte Carlo simulations, that for the cross-correlation technique, the product $\mathcal{N} F_I F_O$ must be greater than 10 to yield valid measurements in around 95% of the interrogation areas. Particle image density

also directly affects the measurement uncertainty. The more correlation pairs in the interrogation area there are, the stronger the correlation peak signal will be. Thus, if a flow can be densely seeded, then a high detection rate and low measurement uncertainty can be achieved.

Overall, over an interrogation area of 32pxl×32pxl, the relative error on a DPIV measurement is of the order of 1% for a displacement equal to about one quarter of the interrogation area [94].

Post processing of PIV measurements and data validation

It is almost inevitable that, in some instances, a tall background noise peak will be incorrectly selected as the displacement peak leading to an erroneous velocity vector, commonly known as an outlier. In most cases, these can be easily detected by eye in the vector map, as their magnitude and direction are often considerably different from the surrounding flow field and they appear as single anomalous vectors. They are also more common at the edge of the illuminated area under study. Although the outliers could be detected manually, it is useful, especially in the case of large data sets containing many vector maps, to employ a data validation algorithm which can identify these data drop-out points. Interpolation or extrapolation can then be used to fill the gaps left by the validation routine. There are various routines which can be implemented [76, 93]. The method of validation and interpolation used here is that of a local median filter.

Median filtering is often applied in image processing to remove binary noise. The principle behind this routine is that the 8 nearest neighbours of a single vector $v(i,j)$ at position (i,j) are linearly ordered with respect to either their magnitude or their i and j components. The median value v_{med}, that is the middle value of the ordered set, is then compared to the value under scrutiny. If

$$\frac{|v_{\text{med}} - v(i,j)|}{v(i,j)} > \epsilon_{\text{thresh}} \tag{3.7}$$

where ϵ_{thresh} is some pre-determined threshold, then the value $v(i,j)$ is replaced by the value of the median.

There are two advantages to using a median as opposed to a mean filter [93]. The first is that the median filter technique is non-linear. A spurious vector will have a much larger or smaller value which distinguishes it from those of the valid vectors around it. Computing the median will place the spurious vector at the beginning or end of the ordered set. The median value, therefore, does not depend on the value of the outlier. In contrast, the outlier will strongly influence the value of the mean, deviating it from the expected value. The second advantage is that the median filter preserves edges, that is that gradients are not smoothed out. This is useful in internal solitary wave studies in a two-layer fluid, where a discontinuity in the velocity profile exists at the density interface.

3.1.2 Planar Laser Induced Fluorescence

Planar Laser Induced Fluorescence (PLIF) is a measuring technique also based on laser sheet visualisation and digital image processing. Following a calibration procedure, the fluorescence intensity of a passive tracer that is excited by the laser light, is measured to yield the concentration of the tracer over the illuminated area of the flow. The tracer can either be a species already present in the flow or added for the purpose of the measurement.

PLIF in stratified flows

In the past, mixing processes and stratified flow characteristics have been investigated in a variety of situations using a variety of experimental techniques. They either involve probing the flow in some way, to measure variables such as conductivity [65, 92] or by observing the flow with an optical flow visualisation technique.

Optical techniques include direct visualisation whereby a marker, either a dye, bubbles or solid particles, are followed along with the fluid motion. In the case of stratified flows, for instance, a dye can be used to indicate one of the fluid layers [44, 37] or a constant density contour, known as an isopycnal [15]. Alternatively, a measurement of the change in refractive index of the medium can be made. These methods include Schlieren techniques [16], shadowgraph and interferomet-

ric techniques, all of which can be used to relate changes in refractive index to changes in density in transparent media.

There exist, however, drawbacks with both investigative methods. Probes are intrusive in nature and can therefore disturb the fluid motion and upset the stratification. They can also only provide spatially and temporally averaged quantitative information. Shadowgraph and Schlieren techniques are most commonly used to provide only qualitative flow visualisation [26]. Interferometric methods give space-averaged information, masking many aspects of any fine mixing structures present in the flow and are also difficult to construct for large scale experimentation.

Laser Induced Fluorescence (LIF) and its two-dimensional counterpart, Planar LIF (PLIF), have been successfully used over the past twenty years or so in a variety of applications to investigate velocity [55, 79], temperature [79] and density [21, 55, 9] fields as well as concentration and mixing [50, 24]. In contrast to probe or other optical experimental techniques, PLIF is particularly attractive for the investigations of mixing in stratified flows. As it is non-intrusive, the layers are not disturbed by the measurement procedure. The fast response time of the dye allows rapid changes in concentration to be observed and the sensitivity of the fluorescence to small changes in dye concentration mean that very small scale concentration fluctuations can be studied. Lastly, it enables a large region of a flow to be observed at one time.

Fluorescence

The fluorescence spectrum of a compound results from the emission of radiation that has been absorbed by the compound. A molecule absorbs energy in the form of light at one frequency and emits this energy a short time later of the order of nanoseconds, in the form of light, at a lower frequency. The wavelength of the emitted fluorescence is thus longer than that of the absorbed light. The emission and absorption spectra of the fluorescent molecule is broad. A full description of this phenomenon can be found in [31].

There are various aspects of fluorescence that, when used as an analytical tool, could pose disadvantages if they are not taken into consideration. Firstly, the fluorescence of a compound can increase with viscosity; as the number of molecular collisions is reduced, the energy transfer is also reduced . The fluorescence of a species can also be affected by photo-decomposition. The incident light on the compound can affect the ability of the compound to fluoresce, thus reducing the emission intensity with time [8]. Lastly, fluorescence can undergo a process known as quenching. This is where there is a reduction of fluorescence due to deactivating effects, sometimes from other substances in the solution. Three causes are mentioned briefly here:

- quenching due to temperature increases
- oxygen quenching, whereby concentrations of oxygen present in the fluo-

rescing solution reduce the fluorescence

- concentration quenching

The last of these three cases is most pertinent to the work undertaken here. As fluorescence occurs by absorption of light at a certain wavelength, if the concentration of dye is too large, the tracer nearest the light source absorbs most of the radiation. As a result, less incident light can reach the solution at greater distances away. In the case of PLIF, where attenuation of the laser light sheet with distance from the source inevitably leads to inhomogeneous fluorescence, the solution is used only at low initial dye concentrations.

Fluorescent dyes

Various dyes have been investigated over the years for their suitability as fluorescent tracers for concentration measurements. Arcoumanis *et al.* [8] discuss this in some detail, comparing three dyes commonly employed in this technique, namely fluorescein, rhodamine 6G and rhodamine B. They compare the performance of the dyes with increasing dilution in tap water. The dye characteristics are set out in table 3.1 below. Considerations taken into account include

- the absorption and emission spectra of the dyes for the range of wavelengths available in modern instrumentation
- the requirement that the overlap between these spectra is small

- the quantum efficiency such that there is a high signal to noise ratio
- the solubility of the dye in the medium of the flow and the susceptibility of the dye to factors such as temperature, pH number, concentration and oxygen

Whilst in the earlier years of laser induced fluorescence development, fluorescein dye was one of the more common tracers to be used [91, 50], Arcoumanis *et al.* [8] find it to have significant disadvantages over rhodamine. In the case of fluorescein, there exists a reduction of fluorescence intensity with time, the rapidity of which increases with increased laser power. This quenching also increases with dye concentration. Overall, rhodamine B and 6G are more stable, and rhodamine B is the most cost effective. In addition, the response of rhodamine B fluorescence to the laser light was linear at concentrations of less than 0.08 mg/l in tap water; the intensity of the light emitted is a measure of the concentration of the dye at any point in the measurement plane. For these reasons and because its emission spectrum is almost completely separate from the absorption spectrum, rhodamine B is used throughout this work. Also, the molecular diffusivities of rhodamine and salt are equivalent [21]. Changes in the concentration of dye can, therefore, be linked to changes in the concentration of salt. In this way, constant light intensity contours yield constant density contours in the flow field. This is pertinent to the work described here, where solitary waves are generated in a brine - fresh water two-layer stratification.

dye	absorption spectrum (nm)			emission spectrum (nm)		
	lower	upper	maximum	lower	upper	maximum
fluorescein	430	520	490	490	600	510
rhodamine B	460	590	550	550	680	590
rhodamine 6G	460	560	530	540	660	560

Table 3.1: The absorption and emission spectra of fluorescein, rhodamine B and rhodamine 6G, taken from [8].

PLIF experimental design and optimisation

Having suitably introduced a fluorescent, the area of the flow under study must be illuminated using a laser light sheet of a suitable wavelength to excite the dye and recorded. As in the case of PIV, a sequence of images can be acquired either digitally using a CCD camera, or using conventional photography or video with subsequent digitisation. The scattered light from the laser is filtered out using a high pass filter placed in front of the camera lens such that only the intensity of the fluorescence is recorded.

In optical measuring techniques using CCD imaging, each pixel in the image corresponds to a small volume of the illuminated cross-section of the flow. The number of photons reaching each pixel is inversely proportional to the square of the camera lens f-number [90]. In performing PLIF measurements, it is therefore advantageous to use a low f-number lens. When imaging large regions of a flow, the signal is ultimately limited by the low light intensity per pixel.

Houcine *et al.* [39] show that, to a good approximation, the pixel greylevel value is independent of the distance between the laser sheet and the front lens of the camera. They also find that the relationship between greylevel and tracer concentration is linear provided that the initial concentration used is low and the laser power is high, such that the intensity of fluorescence of even small concentrations of dye are still detectable by the CCD sensors. This concurs with the results of Arcoumanis *et al.* [8].

In summary, a PLIF set-up can be optimised as follows:

- by increasing the intensity of the laser beam
- by choosing a tracer dye with characteristics most suitable for the experimental set-up
- by ensuring the relationship between dye concentration and fluorescence intensity is linear, i.e. the dye is used in its optimal dynamic range
- by reducing the *f*-number of the camera lens
- by maximising the CCD camera signal to noise ratio

Post processing of PLIF images

Post processing of the PLIF images is important if quantitative information about density distribution in the flow is to be retrieved. Normalisation of the concen-

tration intensities with respect to a background intensity field has the effect of removing any non-uniformities in the greylevel distribution on the image that are due to non-uniformities in the laser light sheet rather than due to changes in concentration. It also removes the effects of laser light dissipation within the fluid, which causes a reduction in the fluorescence intensity with distance from the laser light source.

A background intensity can be obtained by imaging the flow field where the dye has been homogeneously mixed over the measurement volume. For a raw image taken at time t, the greylevel value of each pixel $G_r(i,j,t)$, at image coordinates (i,j), is divided by the corresponding pixel's greylevel value, $G_B(i,j)$, in the background image. This ratio is then scaled up by a appropriate factor, S, such that the resulting greylevel value, $G_N(i,j,t)$, is [73]

$$G_N(i,j,t) = \frac{G_r(i,j,t)}{G_B(i,j)} \times S. \tag{3.8}$$

In order to relate changes in fluorescence intensity to changes in salinity in a quantitative manner, a calibration must be carried out. A series of solutions which are increasing dilutions of the initial dye concentration are exposed to the same laser light intensity, under the same experimental conditions. This procedure has several goals. Firstly, it allows the relationship between fluorescence intensity and concentration to be determined. It is advantageous to ensure not only that the response of the emitted light intensity to concentration is linear, but also that the

dynamic range of the set-up is maximised. The gradient of the response should be high, such that small changes in concentration produce big changes in intensity. Secondly, the procedure maps each dilution of the initial concentration to an average pixel greylevel value such that at zero dye concentration, there should be no fluorescence. The filter should successfully remove the incident laser light, thus resulting in a measured emitted light intensity of zero and therefore a pixel greylevel value of zero.

Having obtained normalised intensity images of the flow field, the greylevel values can be mapped to concentration levels using results from the calibration procedure that have been normalised in a similar way. A schematic of a two-layer fluid PLIF set-up, similar to that used in this investigation and presented in chapter 5, is shown in figure 3.2.

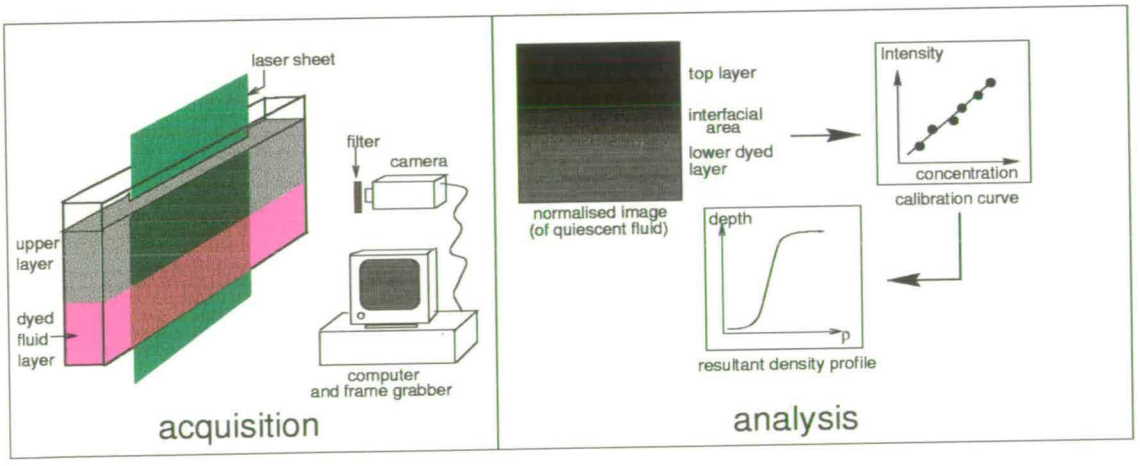

Figure 3.2: The two stages of the digital PLIF experimental procedure for stratified flows; the data collection and analysis. In the analysis, once the image is normalised, the greylevel pixel values can be related to density using the calibration curve

3.2 Experimental Facilities

In this section, the experimental facilities are described and the experimental set-up is explained. The operational range of the facilities are given. Any necessary calibrations of the equipment are also summarised.

3.2.1 The wave tank

All the laboratory experiments in this work are carried out in a wave flume, designed and built at the University of Edinburgh [83]. The flume, built in four sections, is 7.5 m long and 0.4 m wide. The sides are constructed from glass 25mm thick. The tank supports are made from box section mild steel. A hinged wave paddle is built into the flume at one end. The still water level (SWL) is designed to be 0.71m, such that the wave maker (section 3.2.2) operates correctly. A diagram of the tank is shown in figure 3.3.

3.2.2 Generating surface waves

The surface waves can be generated in the flume by means of a hinged absorbing wave paddle manufactured by Edinburgh Designs Ltd. It comprises a force and velocity transducer that measures the reflected wave component on the wave maker and subtracts this from the outgoing wave signal. The paddle can produce sinusoidal wave trains in the frequency range of $\sim$ 0.8 to $\sim$ 1.4Hz, when the water

level in the flume is equal to the SWL.

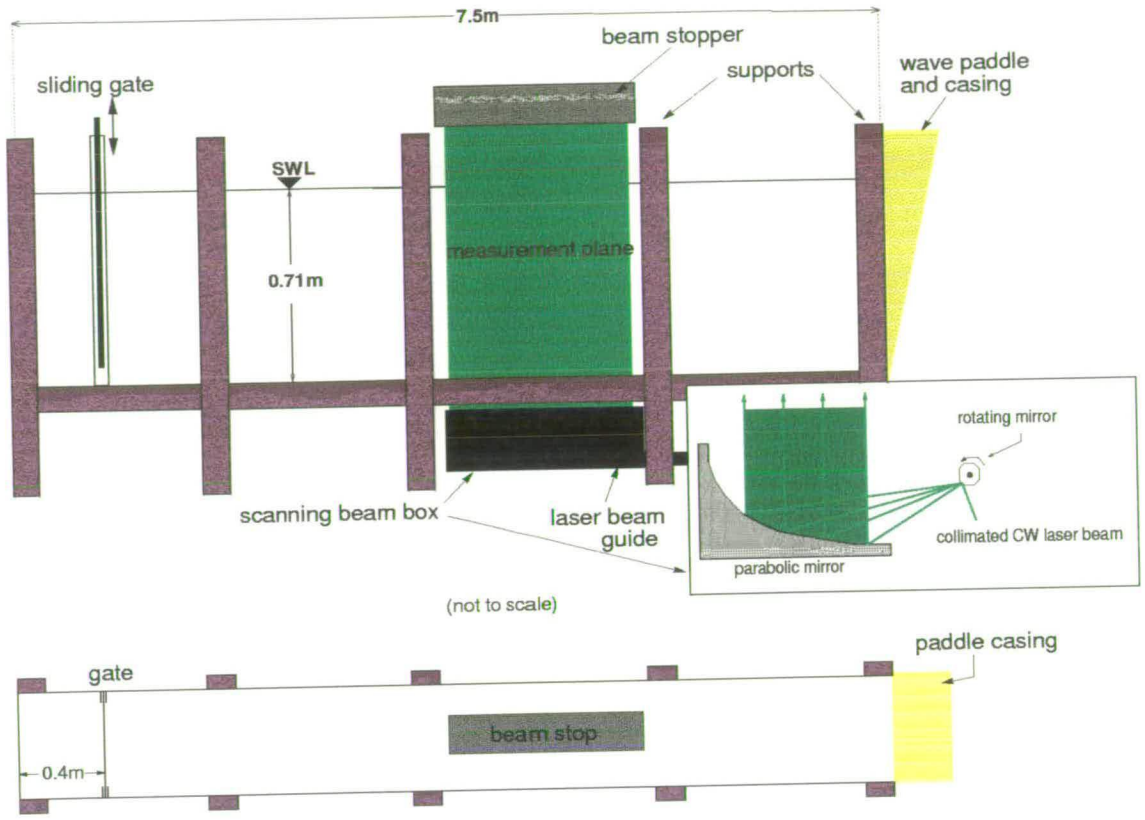

Figure 3.3: The wave flume and scanning beam system; an front elevation and plan view.

3.2.3 Wave gauges

Wave gauges allow the free surface elevation and the frequency of the surface waves to be measured. The gauges each consist of two parallel steel rods and a sinusoidal carrier signal is supplied to them. The output signal, in volts, is a measure of the conductivity and depends linearly on the submersion of the gauges in fresh water. Following a calibration (figure 3.4), achieved by sampling the gauge output at a series of submersion depths when the water surface is

quiescent, the output voltage can be related to the free surface elevation, in units of length.

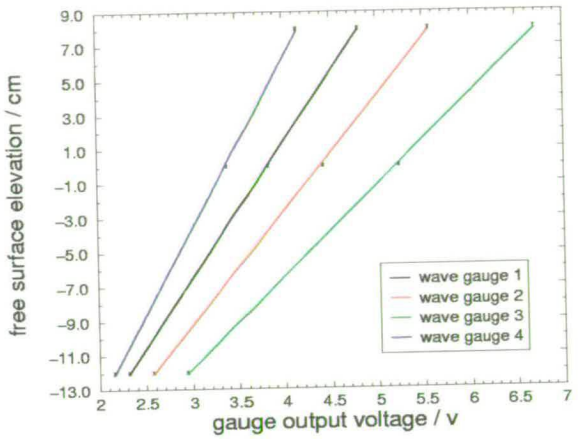

Figure 3.4: Free surface elevation from the SWL in cm against the wave gauge output voltage. The relationship is linear when fresh water is used.

In the present study, when required, the gauges were fixed vertically at regular space intervals in the flume such that they were equidistant from the front and back glass panels of the tank. The wavemaker hardware controls the operation and sampling time of the gauges. Sampling, set at a rate of 16Hz, is triggered to start at a user-defined instant within the wave paddle control software. The data are stored on the wave paddle personal computer (PC) for subsequent analysis.

3.2.4 The scanning beam illumination system

In large scale experimental fluid dynamics, two types of illumination system are commonly used; pulsed laser systems and scanning beam systems. While the pulsed laser system is useful in rapid flows, delivering short bursts of laser light,

the scanning beam alternative is more suitable for flows with velocities of the order of a metre per second and is therefore employed here.

A collimated beam from an argon ion 15W continuous wave laser, of wavelength 514nm, is shone onto a rapidly rotating octagonal mirror. The frequency of rotation can be accurately adjusted in the range 50 to 200rps. The mirror scans the beam across a parabolic mirror, creating a pseudo-light sheet, the extent of which is determined by the dimensions of the parabolic mirror. The system, encased in a box, is situated below the glass bottomed wave flume such that the light sheet is directed vertically upwards through the fluid, as illustrated in figure 3.3. Although to the human eye, it appears that a plane of light is directed through the base of the flume, in fact the beam illuminates a volume of the fluid, the width and breadth of the laser beam, for a very small time interval. Each region is then re-illuminated on every subsequent scan. The total measurement volume is about 0.7m wide and 2mm thick.

In multiply exposed images, the scan rate determines the time between exposures. It will be seen in section 3.2.7 that, in the case of the DPIV single frame exposures sequences obtained throughout this investigation, the scan rate is also an important consideration. In the PLIF experiments, however, presented in chapter 5, the scan period does not affect the time interval between exposures, but can affect image quality. If the exposure time of the images and scan rate are not chosen carefully, the images may be unevenly illuminated. This irregular

illumination will vary with consecutive frames.

3.2.5 Setting up a stratification

A two-layer brine - fresh water stratification can quite easily be achieved. Salt water, of the desired density, is pre-prepared and stored in two large reservoirs of dimensions 1.5m by 0.9m by 0.8m. These tanks are situated in the laboratory such that the brine reaches ambient room temperature. To ensure that the salt is homogeneously mixed, once dissolved, it is stirred using a submersible pump placed inside each reservoir. The salt water is then pumped into the wave flume to the desired level. The fresh (tap) water is put into a series of plastic storage boxes placed above the wave flume, each with a small outlet from which the flow can carefully be controlled. In this way, the fresh water can reach the same ambient temperature as the brine. A sharp stratification can be obtained by allowing the fresh water to drip very slowly through floating sponges initially placed on the salt water surface.

In the experiments performed for this study, the density of the saline layer and the density profile of the stratification is obtained using a microconductivity probe [36]. The probe is driven vertically through the fluid by a stepper motor which can be accurately controlled and is interfaced by a PC. The output from the probe is an analogue voltage, digitised by an analogue to digital converter card in the PC. Once calibrated, the data, in volts, can then be interpreted as a measurement

of density. Figure 3.5 shows the linear relationship between the probe output and density of salt water. The graph shows two independent calibration runs (black and red data points respectively). A line of best fit has been fitted to each data set.

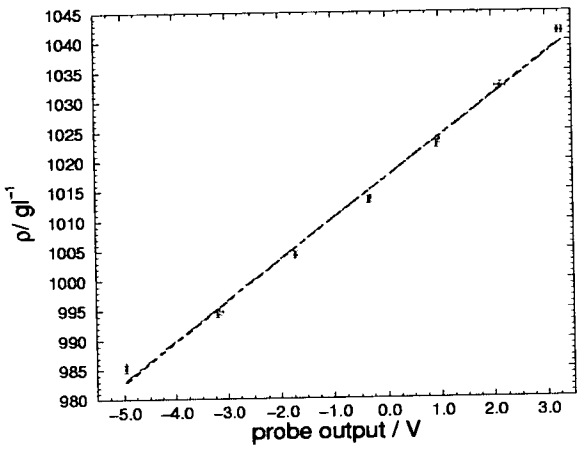

Figure 3.5: Calibration of the microconductivity probe: the relationship between output voltage and density of salt water is linear.

3.2.6 Generating single internal solitary waves

Internal solitary waves are generated by means of a sliding "gate" system, similar to that used by Kao *et al.* [44] and Grue *et al.* [28, 29]. The gate frame is fitted at a distance of 0.4m from the back wall of the tank, at the opposite end from the wave paddle, and sealed in place. Once a two-layer stratification has been set up, the gate, a heavy duty, made-to-measure sheet of perspex, is slotted into the frame until there is but a small gap between the tank base and the bottom edge of the gate. An additional known volume of fresh water is then added, again

using a floating sponge, behind the gate. The gap at the base of the gate allows a corresponding mass of salt water to move to the other side such that hydrostatic balance is maintained. A schematic of the resulting stratification is shown in figure 3.6.

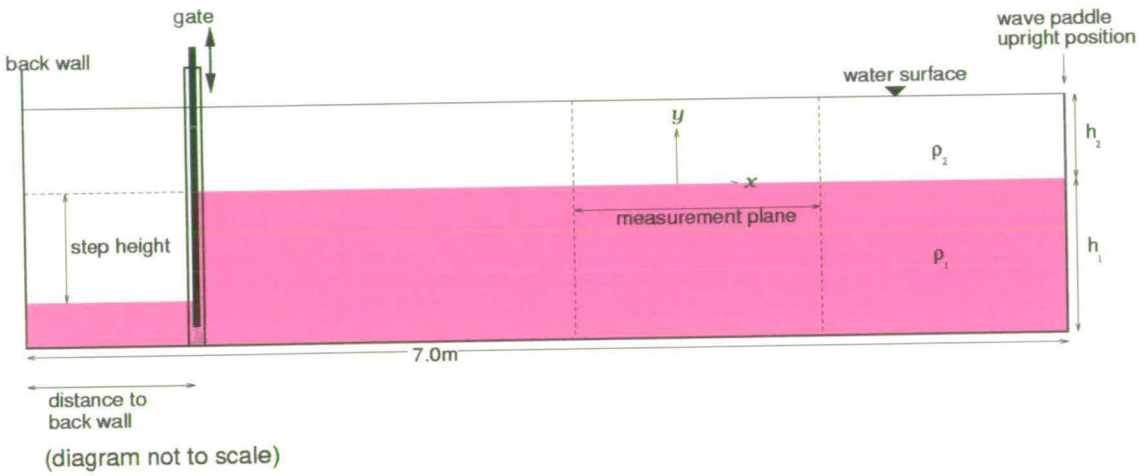

Figure 3.6: Diagram showing the stratification configuration for generating an internal solitary wave.

Upon removal of the gate, achieved by sliding the perspex sheet upwards and out of the frame, the extra volume of fresh water is released and develops into a solitary wave a short distance down the tank, before reaching the measurement region. By carefully choosing the volume of water added, a single solitary wave can be generated. Any disturbance caused by fluid motion around the sliding gate supports will have damped out by the time the fully-formed solitary wave reaches the measurement region. Previous work [34] had not noted that such disturbances affected the results [96], as good agreement with numerical simulations [30, 84] were found. However, a recent development in the experimental facilities in Oslo University has meant that a sliding gate support is now no longer necessary.

This new sliding gate mechanism relies on a tight fitting sheet of strong plastic material which is released using a compressed air controlled system. This also means that there is no manual intervention in opening the gate. Such a system was not available for the present work.

3.2.7 Imaging the flow

Charged couple device cameras

As planar flow visualisation techniques have moved away from the use of conventional photography to digital imaging due to the overwhelming decrease in acquisition and processing times, it is useful to briefly describe how a digital camera operates.

A charged coupled device (CCD), in a digital camera, is a two-dimensional array of sensors that convert quanta of light into electric charge. Each element in the array is called a pixel. The array consists of a semi-conducting substrate with a series of metal conductors on the surface with an insulating oxide layer below. An incident photon on the semi-conductor generates an electron-hole pair, the hole is absorbed whilst the electron is stored in a potential well. This process is illustrated in figure 3.7. The output voltage signal is directly proportional to the charge stored. There is, therefore, a linear relationship between the scattered light from the flow under study and the output voltage from each pixel. The voltage is

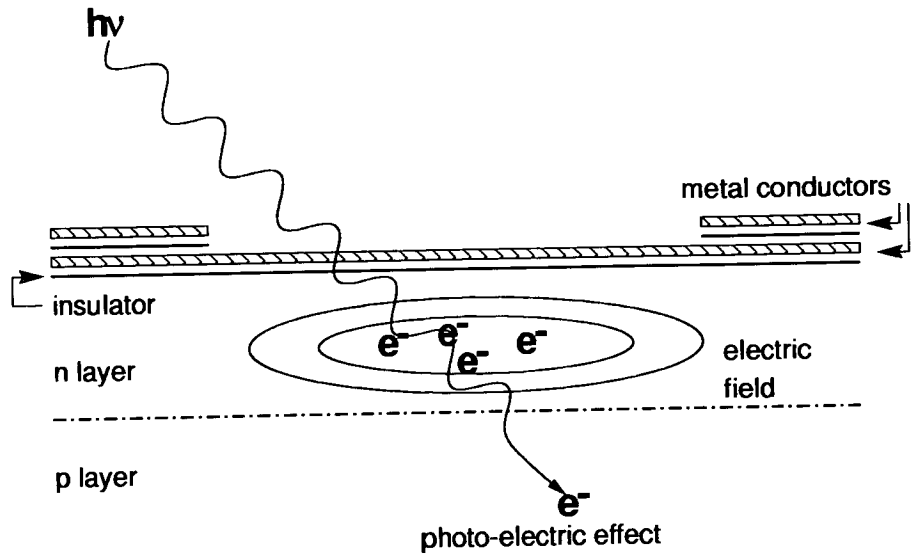

Figure 3.7: A basic model of how a pixel works (taken from [76]).

then converted to a grey scale pixel value by an analogue to digital converter. In this study, an 12-bit camera is used. This implies that there exist a possible 4096 ($=2^{12}$) grey scales for each pixel. This allows a much finer contrast resolution to be achieved. More conventionally, however, 8-bit cameras and computer displays are used, which allow 256 ($=2^{8}$) greylevels in an image. A pixel value of 0 thus corresponds to black and one of 255 to white.

Properties of the CCD array can affect the quality of any acquired images. The pixel sensitivity and it's spectral response vary with the wavelength of light incident on the array. The dynamic range of the sensors must also be optimised. This range is a measure of the full well capacity and the background current noise. This noise increases with temperature of the array, it is therefore important that the CCD array is kept at a cool and constant temperature. Another important consideration is the physical size of the pixels and the size of the pixel array, as

this determines the resolution of the camera.

Digital imaging systems use frame grabbing hardware to capture and store the images prior to them being transferred to the hard drive of the computer, for storage and analysis. The memory available on the frame grabber board limits the number of images that can be taken in one run or experiment, whilst the frequency at which the images can be captured and then transferred to the board, from the camera, puts a limit on the minimum time interval between images. In the case of conventional digital imaging, photography or video, this time interval is fixed. For certain systems, however, it is now possible to set two different time intervals. The images are downloaded to the frame grabber in pairs such that the time interval between the two images of a single pair, δt, and the time interval between successive image pairs, Δt, can be defined separately. This is particularly useful in the particle image velocimetry cross-correlation technique, described in section 3.1.1, where the analysis is performed over pairs of consecutive exposures. As ideally, $\delta t \ll \Delta t$, a series of image pairs can be taken over a longer time period than using a fixed time separation between every exposure without either jeopardising the optimisation of the PIV technique, or requiring a considerable amount of computer memory to store a large number of images. Such a system is used in the work presented here.

Operation of the camera system

In all the experiments, the flow was imaged using a digital CCD "Sensicam" camera made by PCO Optics GmbH. This 12-bit camera has a scan area of 8.6mm by 6.9mm, with an array size of 1280 by 1024 pixels. This gives actual pixel dimensions of 6.7μm by 6.7μm. The spectral sensitivity and quantum efficiencies of the CCD sensors is almost optimal in the range of the wavelengths of light of interest, that is between 514nm and 570nm [71]. The camera is designed to capture a series of image pairs, operating under software written by the manufacturers. The images are downloaded in pairs to a PC, via a standard BNC connection. The 2^{12} greyscale levels are mapped to the more conventional 2^8=256 greylevels, or 8-bit display, by a linear look-up table. The characteristics of the look-up table are user-defined within the software package, prior to grabbing a series of images. The mapping used for these experiments is shown in figure 3.8.

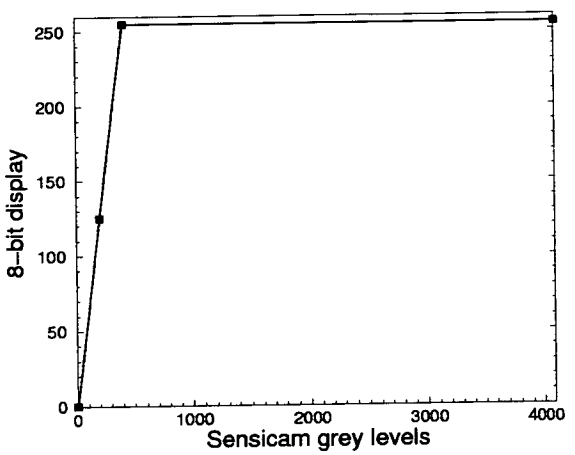

Figure 3.8: The look-up table used in the experiments to map the 2^{12} greylevels of the "Sensicam" camera to the 8-bit computer display.

As the camera can capture pairs of images, the system is particularly useful for DPIV experimentation. The middle section of the schematic in figure 3.9 shows the stages of the image capture process. The first integration time, I_1, is user-defined and is determined by the duration of an input TTL pulse from an external timing box to the frame grabbing board. Reception of the rising edge of the TTL signal triggers the capture of every image pair. The subsequent and second integration time, I_2, is completely determined by the readout time of the first image and is set at 125ms. By default, however, there exists only a very short time interval, of the order of 200ns, between two exposures of a pair. This interval is referred to in figure 3.9 as the "dead time". The interval, Δt, between image pairs is determined by the frequency with which the TTL pulse is sent to the board. The frequency of image pair capture is limited by the overall time it takes to download each image pair to the board from the CCD array. In the case of the system presented here, this results in a minimum time interval between image pairs of 0.55 seconds.

A mechanical shutter allows both the exposure time of the second image, ΔE_2, and the time interval between the two exposures, δt, to be controlled. The shutter is fitted to the camera, behind the camera lens and is also operated by sending a TTL signal of suitable width from a pulse generator to the shutter control box. It is set to be leading edge active, opening for the duration of the pulse it receives. Figure 3.10 shows a schematic of the camera and shutter set-up and the triggering mechanism.

There are two possible ways in which this camera - shutter system can be used. The synchronisation of the TTL pulses sent to the camera and shutter depend on the method chosen. The shutter can either be opened and closed once (method 1) or twice (method 2) for each image pair. In the former case, the scan rate of the laser beam determines both the exposure of the second image and the time between them, δt. In the latter case, where the shutter opens twice, δt is the time over which the shutter remains closed between the two exposures. The schematic in figure 3.9 shows the TTL pulse synchronisation for the camera and shutter for both shuttering techniques. The application of these two alternative methods to the DPIV study of internal solitary waves and surface wave trains is discussed in sections 4.3.1 and 4.4.2.

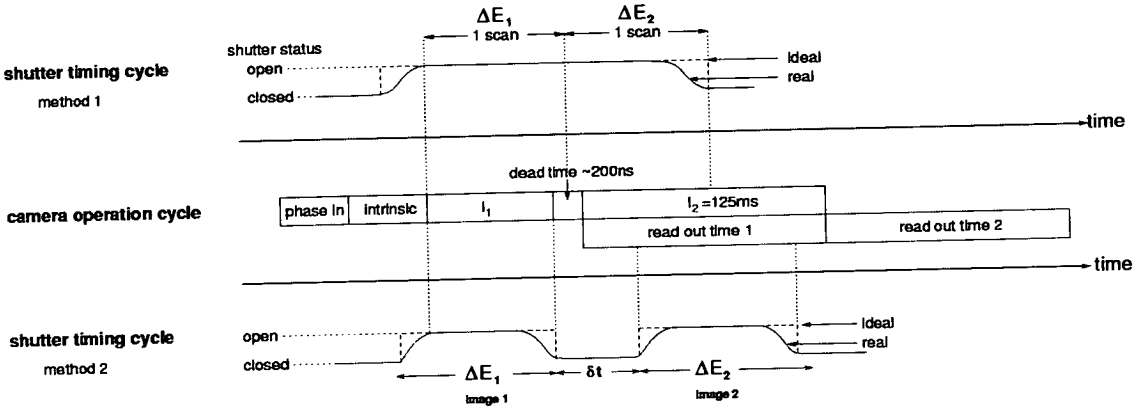

Figure 3.9: The "Sensicam" camera. The schematic shows both the operation of the CCD array in the camera and that of the mechanical shutter (two possible methods), used to define the interval δt and the exposure time ΔE_2.

The shutter and the camera are selected to be leading edge active, such that both are triggered on the rising edge of the input pulses. The shutter used throughout this work is the VS25 model made by Vincent and Associates. It is 25mm in

diameter and allows a Nikon lens to be attached to the front. All experiments described in this work use a 28mm Nikon lens at f 2.8. Table 3.2.7 summarises the main details of camera and shutter system used.

Camera properties	
Camera type	PCO Sensicam, double shutter version, 12-bit
Array size (pxl)	1280 × 1024
Pixel size (μm)	6.7 × 6.7
Lens	Nikon 28mm, f 2.8
Trigger mechanism	TTL pulse, rising edge active
Minimum Δt (s)	0.55
Shutter properties	
Shutter type	Vincent and Associates VS25
Diameter (mm)	25
Trigger mechanism	TTL pulse, rising edge active

Table 3.2: The main characteristics of the camera and shutter system used throughout the course of this work

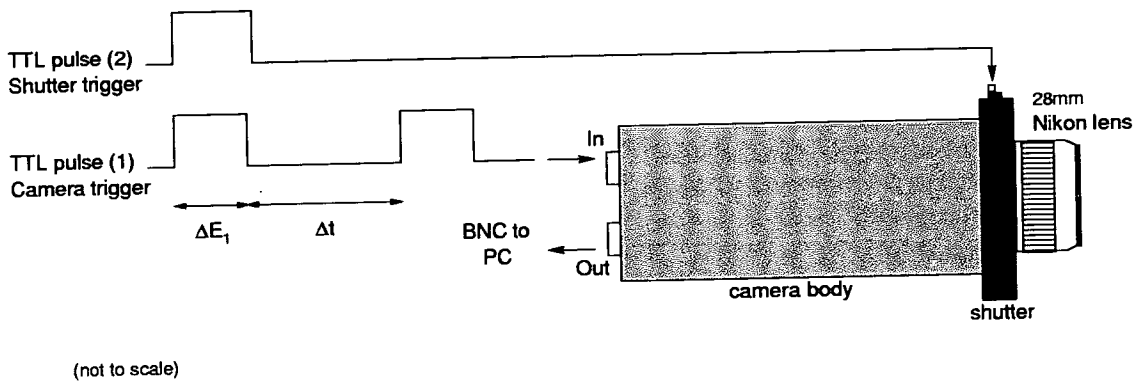

Figure 3.10: The camera system used in the experiments presented in this work.

Ultimately, the camera system is limited by the maximum number of bitmap images the frame grabber can store. This puts an upper bound on the number of images that can be taken in one experiment and is limited to approximately

60 image pairs in the set-up used here.

3.2.8 Scaling the images

In order to determine the magnification of the optical set-up, a grid was placed at the position of the laser light sheet inside the full wave flume. The grid is a sheet of 6mm thick perspex with a 5cm by 5cm square lattice etched onto one side and fixed onto a perspex stand. It was ensured that the base and sides of the grid were square with the tank base and front and rear panels. The lattice is highlighted when exposed to a low power laser light sheet. The camera can then be focused on the grid and the illuminated area is imaged. This procedure also ensures the proper alignment of the camera with the light sheet. Misalignment of the camera can result in errors in the measurements taken, caused by a reduction in image quality. By carefully ensuring that the camera is correctly positioned, these errors can be minimised. The magnification of the system in all experiments was of the order of $M \sim 0.01$. The actual measurement area that could therefore be viewed by the camera, given the lens system and magnification used, was approximately $60 \times 50\text{cm}^2$.

3.2.9 The complete laboratory set-up

A plan view of the complete laboratory set-up is shown below (figure 3.11). The camera is aligned with the measurement plane, defined by the laser light sheet and is situated at approximately 2m in front of the front glass panel. This distance is limited by the size of the laboratory.

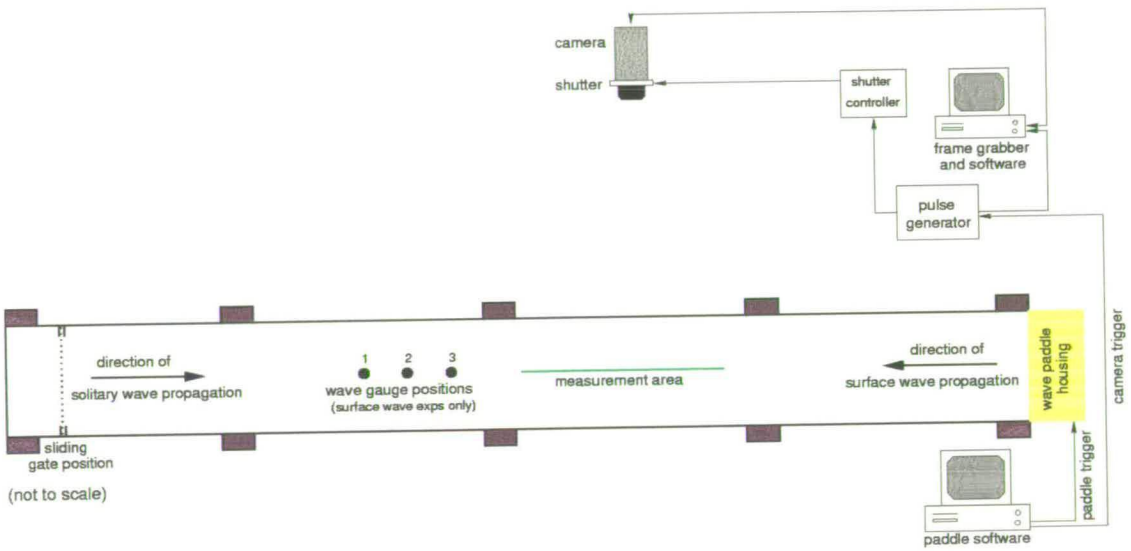

Figure 3.11: A plan view of the complete laboratory set-up.

3.3 Review of chapter 3

In this chapter, the experimental techniques used, namely Digital Particle Image Velocimetry (DPIV) and Planar Laser Induced Fluorescence (PLIF), were introduced. Their general application to experimental fluid dynamics was discussed. A specific description of their application to the interaction of a solitary wave with a train of surface waves is left to chapters 4 and 5. In addition, the ex-

perimental facilities were introduced and described. Particular set-up details will be described in the relevant results sections, 4.3 and 4.4, for the case of DPIV measurements, and 5.2 and 5.3 for the PLIF measurements.

Chapter 4

The Interaction of a Surface Wave Train and an Internal Solitary Wave: A DPIV Investigation

4.1 Introduction

The underlying motivation of the present study is to investigate the interaction processes that occur when an internal solitary wave of depression passes under a train of progressive surface waves in a two-layer brine - fresh water fluid. In

this chapter, an investigation of the interaction using Digital Particle Image Velocimetry (DPIV) (section 3.1.1) is presented. To the author's knowledge, such an investigation has not been performed before. Previous studies [33, 32] have employed only intrusive probe techniques to determine surface wave amplitude modulation. This study, in contrast, is intended to reveal the velocity structure of the flow as the interaction occurs, in addition to any wave modulation.

In the first instance, the aim of the work presented in this chapter is to provide a reference data set of characteristics for both non-interacting wave types, which can be then compared with the interaction experiment results. Hence, DPIV experiments are performed separately on both single internal solitary waves of depression and small amplitude surface waves (sections 4.3 and 4.4), before an investigation of their interaction is made (section 4.5). Before discussing the experimental procedure and results for the two wave types, the limitations of the experimental apparatus are identified in the context of generating a brine - fresh water two-fluid system (section 4.2.1). An investigation into the suitability of the chosen seeding material (pollen) used for all DPIV measurements performed in this study, is also made (section 4.2.2).

DPIV measurements are performed on a set of four solitary waves of depression; two of small amplitude and two of large amplitude, each generated by means of a sliding gate mechanism (section 3.2.6). The experimental method is outlined in section 4.3.1 whilst the results and analysis are presented in section 4.3.2. The

wave characteristics; amplitude and wave shape, are obtained from the measurements and compared to KdV theory (section 2.3.4) and a recently developed and validated fully nonlinear numerical method [30, 28]. Vector maps and velocity profiles of the flow are presented. Drawbacks of the available camera - shutter system (section 3.2.7) and their effect on the dynamic range of the measurement technique are discussed. The repeatability of the sliding gate generation mechanism is also investigated.

The experimental set up for the DPIV investigation of small amplitude surface wave trains and the results are presented in sections 4.4.1 and 4.4.2 respectively. The choice of surface wave amplitudes and wavelengths are justified within the context of the operational range of the wave paddle (section 3.2.2). Surface wave trains are generated in three fluid configurations; homogeneous fresh water and two two-layer fluid regimes. In all three cases, profiles of maximum velocity are presented and surface wave profiles are obtained from the DPIV images. A comparison of surface wave characteristics propagating in different fluid configurations appears not to have been made before. The results are compared to linear theory predictions (section 2.2).

Lastly, interaction processes resulting from progressive surface waves passing over a large amplitude internal solitary wave are investigated (section 4.5). Amplitude and wavelength modulation of the surface wave train is identified. Surface wave profiles are compared to surface wave linear theory. Amplitude and wavelength

modulations are compared to the predictions of the Longuet - Higgins and Stewart theory (section 2.5.1). DPIV measurements yield quantitative velocity information about the interaction flow field. Velocity profiles at surface wave crests and troughs are obtained. The results (section 4.5.2) are compared to the linear superposition of the non-interacting flow fields obtained from the previous DPIV experiments on the individual wave types (sections 4.3.2 and 4.4.2).

The aims of this chapter can thus be summarised as follows:

- to assess the parameter space of the experimental system for the generation of internal solitary waves and their interaction with surface wave trains in a brine - fresh water stratification
- to determine the repeatability of both wave generation mechanisms; the sliding gate mechanism (section 3.2.6) and surface wave paddle (section 3.2.2)
- to compare the results from both surface waves and internal solitary wave measurements to the appropriate theory and also, in the case of the solitary waves, a nonlinear model [30, 28]
- to obtain reference data sets for both wave types for comparison with the interaction experimental results (section 4.5)
- to provide instantaneous, quantitative velocity information for the flow field resulting from the interaction between an internal solitary wave of large

amplitude and a train of progressive surface waves

- to assess any surface wave amplitude and wavelength modulation resulting from the interaction process

4.2 Investigating Two-Layer Fluid Flow using DPIV

In this section, the constraints imposed on generating a two layer fluid stratification, given the available experimental facilities (section 3.2), are considered. The effect on the parameter space of the investigation is determined. Finally, the DPIV measuring technique, when applied to stratified flows, is discussed.

4.2.1 Experimental facility constraints: Choosing the stratification parameters

A two-layer stratification can be characterised in terms of the density difference, $\Delta\rho/\rho_2 = (\rho_1 - \rho_2)/\rho_2$, and the layer depth ratio, h_1/h_2, of the two fluids where the subscripts 1 and 2 refer to the lower and upper layers of the stratification respectively. These are key defining parameters in determining the resulting characteristics of the solitary waves generated. The density difference across the salt water - fresh water interface determines the speed of the waves; the larger

the density difference, the greater their speed. The layer depth ratio determines the extent, or wavelength, of the solitary wave [28]. The smaller the depth layer ratio, the broader the wave.

The values of both $\Delta\rho/\rho_2$ and h_1/h_2, selected for this investigation, are justified in terms of the limitations imposed by the available experimental facilities. As one of the aims of the work on single solitary waves presented in this section is to identify the characteristics of the solitary waves to be used in the subsequent surface wave train - internal wave interaction experiments (section 4.5), a consideration of the requirements of these experiments was also necessary. This imposed additional constraints on the stratification parameter space, which are also discussed below.

The available water storage facilities imposed a maximum and minimum value upon the quantity h_1/h_2. The bottom layer fluid depth, h_1, was restricted by the maximum volume of brine that could be held in the two large reservoirs in the laboratory. Similarly, the upper layer depth, h_2, was limited by the maximum volume of fresh water that could be kept in the storage containers above the wave flume. To generate calibrated surface wave trains (section 3.2.2), the fluid free surface was required to be level with the still water level (SWL) of the built-in wave paddle. This is equivalent to a total fluid depth of 0.71m. All experiments were therefore carried out such that $H = h_1 + h_2 = 0.71\text{m}$. To investigate the effect of the top layer fluid depth on the surface wave - internal wave interaction, it was desirable to use two different layer depth ratios, h_1/h_2. Consequently, the

two extremes of the range of possible layer depth ratios were chosen, $h_1/h_2 \approx 4$ and $h_1/h_2 \approx 6$.

The value of $\Delta\rho/\rho_2$ used in the present work can be explained by, again, considering the principal aim of this work, namely to investigate the interaction between an internal solitary wave and a train of surface waves. The limited range of the layer depth ratio resulted in very broad solitary waves. Neither the width of the measurement volume, defined by the laser light sheet (section 3.2.4), nor the field of view of the single camera were sufficient to image the whole length of the internal wave instantaneously. In addition, surface wave generation using the in-built wave paddle was inhibited by the length of the wave flume of 7.5m. Standing waves were set up quite quickly after the paddle had been put in motion (section 4.4.1). For the interaction to be successfully observed over the entire length of the solitary wave, the internal wave needed to have completely passed the measurement area before the standing waves developed. As the density difference across the interface determines the speed of the wave, a larger density difference than that used in previous studies [44, 28, 29] was necessary, such that the density difference, $\Delta\rho/\rho_2 \sim 5\%$.

As the brine had to be prepared in two separate reservoirs (section 3.2.5), there was a possibility that the salt water in each was of a slightly different density. To ensure that the saline water was uniform in density once it had been pumped to the desired water depth in the wave flume, the submersible pumps were used to

thoroughly mix the brine, before adding the fresh water layer. Advantage of this was taken to introduce either the pollen, for the DPIV experiments (sections 4.3.1, 4.4, 4.5), or the rhodamine dye, in the case of the PLIF experiments (chapter 5), so as to ensure that these too were homogeneously mixed along the length of the flume and throughout the depth of the saline fluid.

4.2.2 Considerations of the DPIV technique in stratified fluids

Although previous work, reviewed in section 2.3.4, has already investigated in some detail internal solitary waves in a two-layer fluid, some aspects of the present work are different. Firstly, there appears to be little published research into internal solitary waves using DPIV [29]. Particle Tracking Velocimetry (PTV), which relies on similar principles, has been more extensively employed [29, 34]. In particular, pollen, the seeding material used in the present work, was not used in these earlier investigations. This section, therefore, discusses the suitability of pollen as a seeding material for use in the two-layer flows encountered in this study.

In the case of the all DPIV experiments carried out in this work, the flow was uniformly seeded with conifer pollen. When wet, the pollen, which has an average diameter of around 60μm, has approximately the same density as fresh water and therefore has only a small tendency to float. It was, however, necessary to ensure

that the pollen was not only approximately neutrally buoyant in fresh water but also in a salt water stratification with an appropriate density change across the interface.

A small glass tank of dimensions 50cm×35cm and 65cm in height was placed inside the wave flume on a stand that allowed the laser light sheet to shine up through the base. A stratification, where $\Delta\rho/\rho_2 \sim 5\%$, was set up in the manner described in section 3.2.5. The bottom layer was over-seeded with pollen before slowly adding the upper fresh water layer. The pollen rises through the fluid as the upper layer is introduced, such that, if the quantity of pollen is carefully chosen, the particle density is approximately uniform throughout the fluid on completion of the filling procedure. The experiment must then be performed shortly after this. A long delay will result in inhomogeneous seeding, the majority of the pollen settling at and just below the free surface. All subsequent DPIV two-layer fluid investigations were seeded in the same way.

The camera set-up was typical of all the experiments presented in this work. A spatial calibration (section 3.2.8) was performed to determine both the magnification of the imaging system and to align the camera with the measurement volume determined by the laser light sheet. Having allowed time for currents induced by the filling process to dissipate, a series of image pairs of the undisturbed fluid were captured. The rise time of the particles was found to be of the order of 0.25mms^{-1}, a result which is in agreement with that stated by Quinn [75]. In

addition, the magnitude of the velocities were found to be of the same order in the lower and upper layers of the stratification.

Although a few more outliers were present in the interfacial region, they were suitably interpolated by the post processing local median routine (section 3.1.1). It was noted that there was no noticeable deflection of the laser beam as it passed through the interfacial region.

Once the stratification had been set up, it was impossible to introduce more pollen into the bottom layer. Under-seeding the flow would lead to a poor correlation in the DPIV analysis. Over-seeding, on the other hand, would result in a large quantity of pollen accumulating, over time, at the free surface. Selecting a volume of pollen that would minimise the risk of either of these situations was therefore advantageous. The quantity of pollen depended on the time taken to fill the tank to the still water level, which, in turn, depended both on the layer depth ratio, h_1/h_2, and on the additional volume, V, of fresh water introduced behind the gate. A smaller layer depth ratio and large volume, V, substantially increased the filling time and hence a larger quantity of pollen was required. Typical filling times for the top fresh water layer in the experiments described in this work were of the order of 2 to 3 hours. For a given h_1/h_2 ratio, the faster the filling time, the thicker the interface became. The brine was made up using 75kg of salt for each experiment. Table 4.1 shows the volume of pollen used for each solitary wave set-up. This was optimised according to the time taken to fill the top fluid

Solitary wave amplitude	depth ratio $h_1/h_2 \approx 4$	depth ratio $h_1/h_2 \approx 6$
small amplitude $a/h_2 \sim -0.5$	80ml	70ml
large amplitude $a/h_2 < -1$	170ml	150ml

Table 4.1: Optimal pollen volumes for the investigations involving internal solitary waves.

layer.

As the pollen accumulates at the fluid free surface, it creates a surface film, which may act to reduce the surface tension. The first order dispersion relation [17]

$$\omega_S^2 = \left(g k_S + \frac{\sigma k_S^3}{\rho} \right) \tanh k_S H \tag{4.1}$$

describes the orbital frequency, ω_S, of waves on a free surface, where g is the acceleration due to gravity, k_S is the wave number, σ is the surface tension, ρ is the fluid density and H is the total fluid depth. Plots of phase velocity, c_S, against wavelength, λ_S, are shown in figure 4.1, where both equation (4.1) (red line) and the dispersion relation neglecting the surface tension term (equation (2.6), black line) are plotted. At small wavelengths, the surface tension term dominates. At larger wavelengths, gravity is the significant restoring force and the effect of surface tension is negligible. Svensen [85] states that for $\lambda_S > 3$cm, surface tension will have no significant effect on the wave motion. Pullen [74]

also investigated the effect of surface films on paddle-generated surface waves. His findings also concurred with existing theories. The range of wavelengths that can be produced by the surface wave paddle is also marked in the graph in figure 4.1. It can be seen that, as this lies outwith the range of wavelength values that will be affected by changes in surface tension, the pollen is expected to have no significant influence in the characteristics of the generated waves.

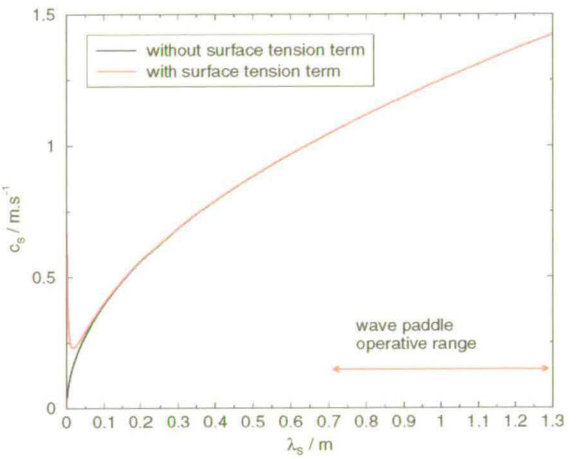

Figure 4.1: Graph of phase velocity, c_S, of deep water waves against wavelength, λ_S, both neglecting surface tension (black line) and including the surface tension term in equation (4.1) (red line).

It is important to assess the ability of the pollen to follow accurately the fluid motion under investigation. The particle Reynolds number, Re_p, is given by

$$Re_p = \frac{(v_f - v_p)\, d_p}{\nu}, \tag{4.2}$$

where ν is the kinematic viscosity such that $\nu = \mu_f/\rho_f$, μ_f being the dynamic viscosity of the fluid and ρ_f its density, d_p refers to the diameter of the particle and $|v_f - v_p|$ is the instantaneous relative velocity between the particle and the

fluid. If $Re_p \ll 1$, then the particles can be considered to closely follow the flow and viscous effects dominate. In this regime, the Stokes' drag, D, approximates the force acting on each particle, such that

$$D = 6\pi\, \rho_f \nu^2\, Re_p. \tag{4.3}$$

The balance of momentum of a particle in the flow can thus be written as

$$6\pi\, \rho_f \nu^2\, Re_p = (\frac{4\pi}{3})\rho_p\, d_p^3\, |\dot{v}_p|. \tag{4.4}$$

Following the scheme detailed by Grue *et al.* [29], $\dot{v}_p \sim |v_{p(max)}|/T$, where T is the time over which a seeding particle is accelerated from rest to $|v_{p(max)}|$, its maximum particle velocity. Substituting for $\dot{v}_p$ and Re_p (equation (4.2)), equation (4.4) can be rearranged:

$$|v_f - v_p| \sim \frac{2d_p^2}{9\nu T}\, |v_{p(max)}|. \tag{4.5}$$

In these experiments, for solitary waves, $T \approx 5$s, $|v_{p(max)}| \approx 0.2\text{ms}^{-1}$ and for pollen, $d_p = 6 \times 10^{-5}$m. Substituting the result of equation (4.5) into equation (4.2), the particle Reynolds number is much less than unity, with a value of the order of 10^{-4}. The particles, therefore, can be assumed to follow the flow closely. The accuracy, determined by the ratio $\frac{|v_f - v_p|}{|v_{p(max)}|}$ [29], is in the case of the

experiments performed here much less than 1%.

In conclusion, therefore, despite the pollen not being completely neutrally buoyant in the fluids used for this study, the rise time is sufficiently low and the particles track the flow sufficiently well, for the seeding material to be used in the DPIV investigations that follow in sections 4.3.1, 4.4 and 4.5.

4.3 A DPIV Investigation of Single Internal Solitary Waves in a Two-Layer Fluid

This section presents and discusses results from the DPIV investigation on single internal solitary waves of depression. The experimental set-up is described. Limitations of the data acquisition system are discussed. The results are compared to theoretical predictions and to previous work.

4.3.1 DPIV experimental set-up and method for the investigation of single internal solitary waves

This section focusses on the details of the experimental set-up for the investigation of single internal solitary waves of depression propagating at a brine - fresh water interface. The experimental method is outlined. Use of the camera system is explained and justified within the context of both its operating limitations and

those of the illumination system available.

For every solitary wave experiment described, the total fluid depth, $H = h_1 + h_2$, was equal to that of the wave paddle still water level (SWL), such that $H = 0.71$m. The two-layer fluid was set-up in the way described in section 3.2.5, the pollen being mixed into the saline layer prior to the fresh water being introduced. A reference density profile was obtained in the quiescent stratification using the microconductivity probe (section 3.2.5) prior to each experiment. The depth of the upper layer was determined by locating the point of inflection on the profile. The solitary waves were generated as described in section 3.2.6.

In the first instance, suitable values of V, the extra volume of fresh water introduced behind the gate, and D, the distance to the sliding gate from the end wall of the wave flume, were selected such that a single large amplitude ($a/h_2 < -1$) internal solitary wave of depression and a single small amplitude ($a/h_2 \sim -0.5$) internal solitary wave could be generated respectively in each of the two stratification configurations $h_1/h_2 \approx 4$ and $h_1/h_2 \approx 6$. This trial experimentation allowed the optimal amount of pollen to be found for each set of DPIV measurements. It was ensured that the wave had formed completely before reaching the measurement volume, which was determined by the position of the laser light sheet. In both stratification regimes, the maximum amplitude wave was determined by the maximum volume of water which could be introduced behind the gate, whilst still only generating a single solitary wave. The position of the gate

	Configuration $h_1/h_2 \approx 4$		**Configuration** $h_1/h_2 \approx 6$	
	$a/h_2 < -1$	$a/h_2 \sim -0.5$	$a/h_2 < -1$	$a/h_2 \sim -0.5$
H (m)	0.71	0.71	0.71	0.71
V (l)	79	20	80	20
D (m)	0.4	0.4	0.4	0.4

Table 4.2: Summary of the parameters used to generated the four solitary waves investigated in this study.

was fixed at $D = 0.4$m for every solitary wave investigated. Overall, therefore, DPIV measurements were performed on four separate internal solitary waves. Table 4.2 summarises the parameters pertaining to the initial experimental set-up used for each. The characteristics obtained from the DPIV measurements are fully detailed in table 4.4 and are discussed in the next section.

Although the general ideas underlying the DPIV measuring technique have been described in the previous chapter, here, the details of the DPIV data acquisition procedure used in this study are presented. The Nikon 28mm lens was set at $f2.8$, using a magnification of $|M| \sim 0.01$ (sections 3.2.7 and 3.2.8).

In section 3.2.7, two methods of controlling the exposures for the PCO Sensicam camera were introduced. The first system (figure 3.9, method 1) relies on the scan rate of the laser beam across the parabolic mirror to determine the interval between the two exposures, δt, whilst a mechanical shutter, placed behind the camera lens, prevents the second image from over-exposing. Given that the second exposure commences 200ns after the first integration time of the CCD array is

completed, if the exposure time of each image of a pair is exactly equal to the scan rate of the laser beam, then the time between the two consecutive exposures is equal to the scan rate also. This is because although the laser beam appears to be a sheet of light permanently illuminating the measurement volume, it is in fact illuminating a very small portion equal to the width of the beam at any one instant. Therefore, on any subsequent scan, the particle has moved on and will be illuminated a time δt later, equal to the scan rate of the laser beam. So, the time interval between exposures is constrained by the slowest speed of the rotating mirror in the scanning beam box. The slower the speed, the longer the time interval δt. Hence, for the set-up described here, if the first method was used, the maximum time interval possible between two images of a pair was $\delta t = 2.5$ms.

In the second method (figure 3.9, method 2), the mechanical shutter was used to control both the time interval between exposures and the length of the second exposure, by opening and closing twice for each image pair. This method, however, is constrained by the rapidity with which the shutter can open and close. The larger the shutter, the slower it is. This imposes a minimum second exposure time, $\Delta E_2 \sim 11$ms, which, in the case of the large amplitude solitary waves, gave blurred particle images. Whilst the first exposure is completely determined by software control of the camera CCD array, the second exposure depends on the length of time the shutter remains open. As the array is still active during this latter period, the intensity of the second image is affected by the additional time necessary for the shutter to both fully open and to fully shut. In contrast to

the first shuttering method, this set-up presented no practical limit for the time interval, δt, so long as the CCD was still active for the second exposure. This interval could therefore be optimised to yield a sufficient particle displacement between particle images.

In this study, particle velocities within the large amplitude solitary wave ($a/h_2 < -1$) flow field are about 6 times larger than those in the small amplitude solitary wave flows, with $a/h_2 \sim -0.5$. It was found that the first shuttering set-up was most suitable for use with the large amplitude solitary waves as, although the time interval between the images was small (giving small particle displacements), the images remained in focus. In contrast, the second system was used in the small amplitude solitary wave experiments, as the longer time interval between two images of a pair gave greater seeding particle displacements for the DPIV analysis.

Exposure control could also have been achieved by placing a shutter across the laser beam path. In this case, the diameter of the shutter could be reduced as it needs only to accommodate the diameter of the laser beam. This would, therefore, be capable of much shorter exposures. However, the laser power used to illuminate the flow in these experiments is around 16W and would burn straight through any such device. Though an opto-acoustic light modulator could be used in a similar way to shut off the laser beam between exposures, this option was not available for this study and is therefore not discussed here.

	solitary wave $a/h_2 \sim -0.5$ exposure time / delay	**solitary wave** $a/h_2 < -1$ exposure time / delay
ΔE_1 (ms)	9	2.5
δt (ms)	57	2.5
ΔE_2 (ms)	11	2.5
Δt (ms)	550	550

Table 4.3: Table showing the timings used in the image capture of DPIV images for the single solitary wave experiments.

It is important to note that in both cases, the DPIV camera - shutter system was used at the limits of the range of timings available for it. The camera timings used in both the large and small amplitude wave sets are summarised in table 4.3. In all cases, the time between image pairs, Δt was 0.55s. This is equivalent to the maximum grabbing frequency of the camera system, allowing the maximum possible number of velocity maps to be obtained as each wave passed the measurement volume.

In all of the experiments, the camera was first aligned with the laser light sheet in the manner described in section 3.2.8. Frame grabbing was activated on the opening of the sliding gate so as to ensure that the entire progression of the solitary wave was recorded. This also allowed the time taken for each wave to reach the measurement region to be determined. A maximum of 60 image pairs could be acquired by the camera in one run. This gave an overall experiment run-time of 33s.

The DPIV cross-correlation analysis was performed on a grid of 16pxl×16pxl and with an interrogation area of 32pxl×32pxl. Spurious vectors on all the resulting vector maps were interpolated using a median filter routine. They were then scaled using the results from the spatial calibration.

4.3.2 DPIV results and discussion of the single internal solitary wave experiments

The analysis of the measurements presented in this section focusses on the assessment of both the solitary wave generation mechanism and the ability of the DPIV measurement facility to measure the velocity fields of the solitary waves produced. The ultimate aim of the analysis was to provide quantitative information about the velocity fields, against which the experimental results obtained from the interaction investigation (section 4.5.2) could be compared. In particular, the defining characteristics of the waves, namely their amplitude and their shape, are obtained from the resulting scaled vector maps of the flows. These results are compared to KdV theory (section 2.3.3) and to a previously validated fully nonlinear numerical model [30, 28].

Table 4.4 summarises the characteristics of the four solitary waves investigated here using the DPIV measuring technique. Similar waves were subsequently used for the surface wave - internal solitary wave interaction investigations (sections 4.5 and 5.3). The values of the non-dimensional density difference, $\Delta\rho/\rho_2$, be-

depth ratio h_1/h_2	volume V (l)	amplitude a/h_2	density difference $\Delta\rho/\rho_2$ (%)	KdV linear wave speed c_0 ($cm.s^{-1}$)	nonlinear wave speed c ($cm.s^{-1}$)
4.0	79	-1.24	5.5	24.57	30.34
3.93	20	-0.48	4.0	21.13	23.98
6.25	80	-1.95	4.94	20.15	28.61
6.1	20	-0.68	4.2	18.71	24.33

Table 4.4: Table showing the characteristics of the 4 single solitary waves investigated using DPIV.

tween the two fluid layers are obtained from the calibrated conductivity probe measurements taken prior to each experiment. The wave amplitudes, a/h_2, were found from analysis of the DPIV vector maps and will be discussed further. The KdV linear wave speed, c_0, is calculated following equation (2.17). The nonlinear wave speed, c, is the nonlinear method prediction [30, 28] calculated with initial conditions a/h_2, h_1/h_2 and $\Delta\rho/\rho_2$, as detailed in the table.

The preparation of each experiment was very lengthy due to the time needed to prepare the salt solution and also set up the two-layer fluid. At least 24 hours were needed to ensure that the salt had thoroughly dissolved, before starting the filling process. A large volume of fluid, approximately 2000l, was required to fill the tank to the correct level (SWL) and the top layer needed to be introduced very gradually. As a result, only one experiment could be performed in a day. Once the stratification was in place, the measurements were carried out within one hour, before the seeding particles became too sparse in the lower layer.

In addition to the above considerations, each stratification could only be used once. The wave motion took over one hour to damp out completely. During this time, the pollen continued to rise. When the fluid was once again quiescent, the interface had thickened considerably and little seeding remained in the lower layer of the stratification. As a result, it was not possible to re-use the brine - fresh water set-up. The graphs in figure 4.2 show both a plot of non-dimensional fluid density $(\rho - \rho_2)/\rho_2$ versus y/h_2 and the corresponding plot of $N(y/h_2)$, before and after the passage of a large amplitude internal solitary wave in the quiescent $h_1/h_2 \approx 4$ regime. The initial conditions of the set-up were the same as those summarised in table 4.4, although the density difference was slightly smaller. The broadening of the buoyancy frequency peak and the reduction in the peak height indicate that the interface has widened. The centre of the interface can also be seen to have been pushed down by the mixing process, following repeated reflection of the decaying solitary wave from each end of the wave flume.

Re-use of the salt water was attempted by pumping the brine out from the bottom of the wave flume through a filter to remove the pollen, back into the laboratory reservoirs. However, not all of the pollen was removed by the filter and, in the ambient temperature of the laboratory, turned the salt water cloudy. This cloudiness reduced substantially the contrast in the raw DPIV images in the subsequent experiment. This, in turn, reduced the quality of the resulting vector maps.

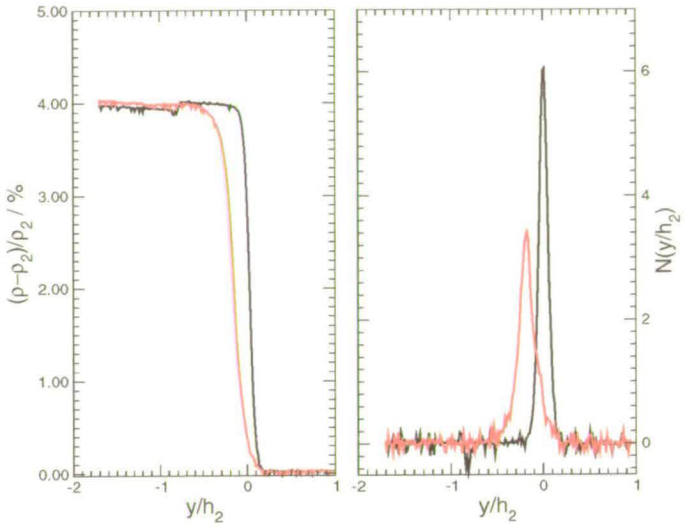

Figure 4.2: Density profiles (left hand graph) and the corresponding buoyancy frequency, $N(y/h_2)$ (right hand graph) of the stratification before (black line) and after (red line) a large amplitude solitary wave passed the measurement area. The profiles were taken when the fluid was quiescent.

A sequence of three consecutive vector maps of each solitary wave (table 4.4) are shown in figures 4.3, 4.5, 4.7 and 4.9. The times refer to the elapsed time from when the gate is opened at $t = 0$s. The coordinates of the plots are given in terms of y, the distance from the interface and x, the distance across the measurement area (figure 2.3). Plots of isovelocity contours, where the blue contours indicate u, horizontal velocity, and the red contours indicate v, vertical velocity, have also been shown. The velocities are in units of cm.s^{-1} such that the horizontal velocity contours are plotted in intervals of 4cm.s^{-1}, and vertical velocity contours are plotted every 2cm.s^{-1}. The same vector maps are shown in the adjacent plots in figures 4.4, 4.6, 4.8 and 4.10 for the same waves, however, here contours of absolute vorticity, $|w|$, have been included. The vorticity is defined as the curl of the velocity vector and for the two-dimensional velocity plots presented here is

given by the vertical component

$$w = \frac{\partial v}{\partial x} - \frac{\partial u}{\partial y}, \tag{4.6}$$

such that it is directed normal to the plane defined by the laser light sheet.

As the waves are very broad, each vector map only displays a portion of the waveform. The two layers of fluid can be distinguished by the horizontal velocity shear across the interface. The horizontal velocities in the top fluid layer are positive (in the direction of increasing x), where as those in the bottom layer are negative. The interface can be easily distinguished on the absolute vorticity plots as a broad band of high vorticity. This is also true of the fluid free surface, above which $(u, v) = (0, 0)$. The isovelocity plots show that the horizontal velocities tend to zero in the interfacial region. Thus, locating the position of zero horizontal velocity, $u = 0$, can provide an indication of the interface position, $\eta(x)$, across each map. By tracking the location of zero horizontal velocity at a particular vector column over a sequence of velocity maps, a profile of interface position against time can be obtained. Hence, both the wave shape and the maximum amplitude $\eta(x)/h_2 = a/h_2$ of each wave can be determined from the DPIV measurements.

Previous work has found first order KdV theory (section 2.3.4) to be successful in describing small amplitude solitary waves where $a/h_2 \gtrsim -0.4$. Extending the theory to second order was seen to slightly increase its range of validity. There

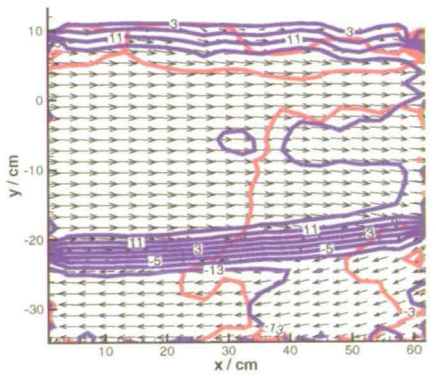

(a) $t = 21.45$s

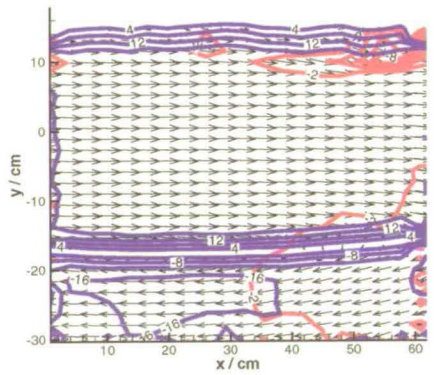

(b) $t = 22$s

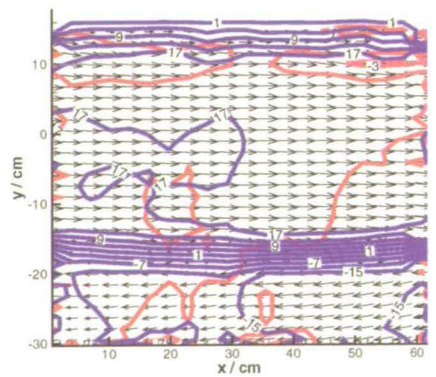

(c) $t = 22.55$s

Figure 4.3: Vector maps and isovelocity contours for a solitary wave ($h_1/h_2 = 3.4$ and $a/h_2 = -1.24$).

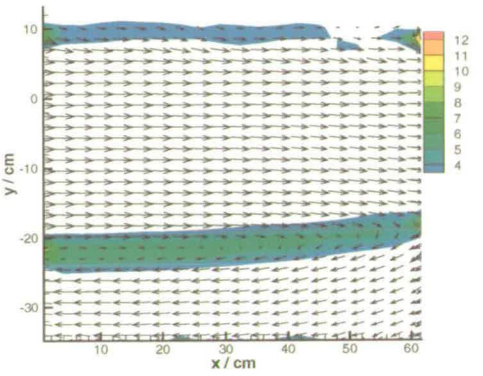

(a) $t = 21.45$s

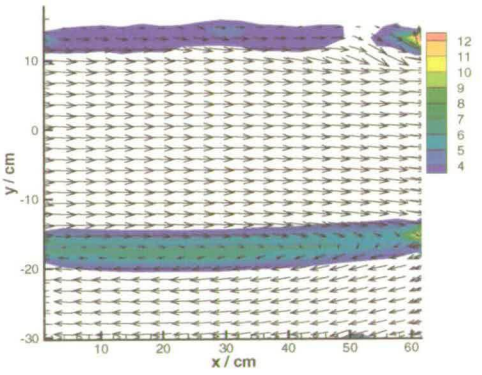

(b) $t = 22$s

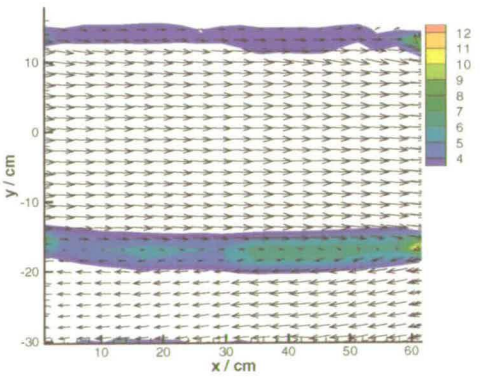

(c) $t = 22.55$s

Figure 4.4: Vector maps with vorticity contours for the solitary wave in figure 4.3.

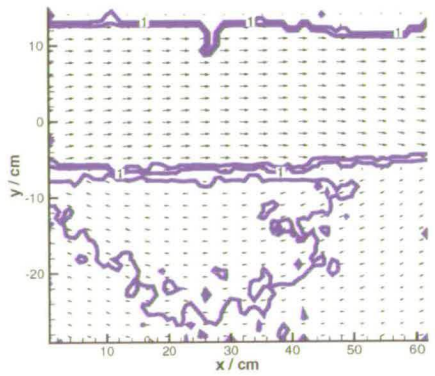

(a) $t = 24.75$s

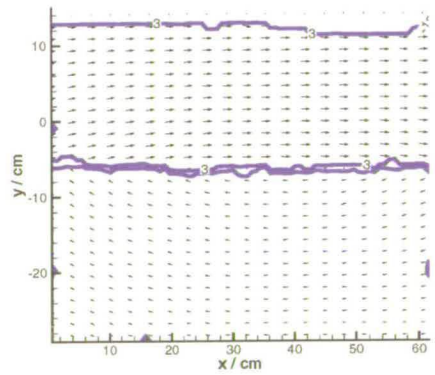

(b) $t = 25.3$s

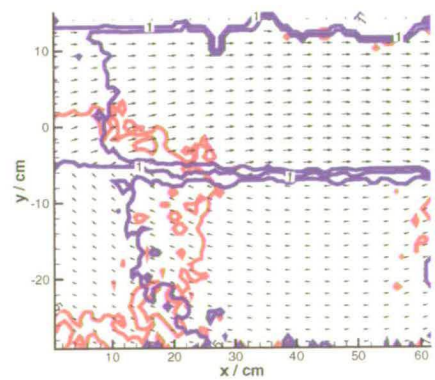

(c) $t = 25.85$s

Figure 4.5: Vector maps and isovelocity contours for a solitary wave ($h_1/h_2 = 3.9$ and $a/h_2 = -0.48$).

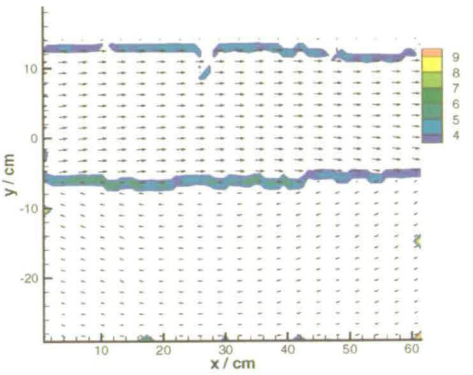

(a) $t = 24.75$s

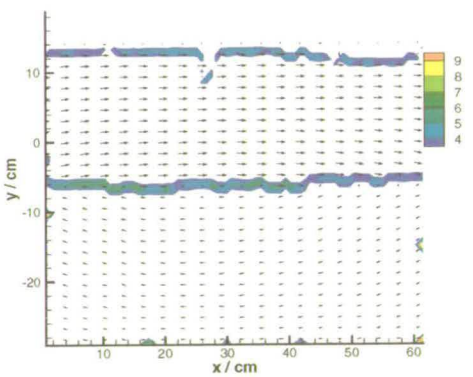

(b) $t = 25.3$s

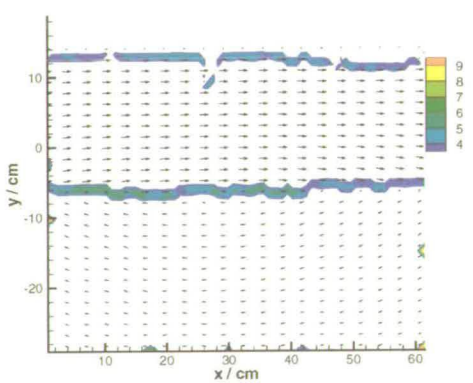

(c) $t = 25.85$s

Figure 4.6: Vector maps and vorticity contours the solitary wave in figure 4.6.

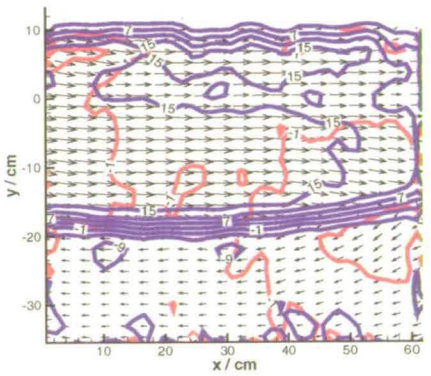

(a) $t = 22.55$s

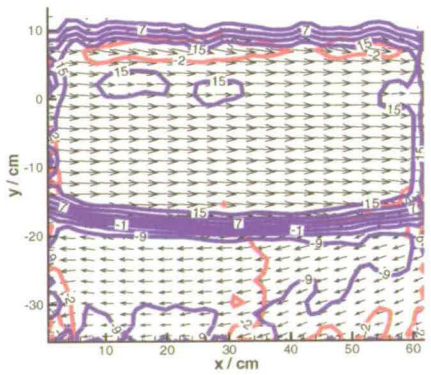

(b) $t = 23.1$s

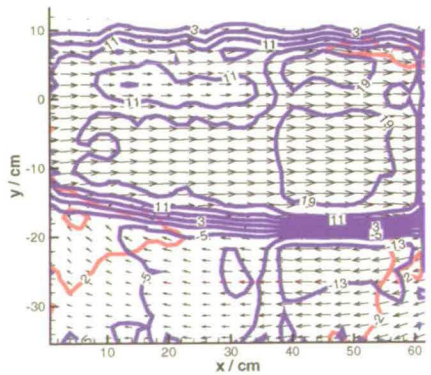

(c) $t = 23.65$s

Figure 4.7: Vector maps and isovelocity contours for a solitary wave ($h_1/h_2 = 6.25$ and $a/h_2 = -1.95$).

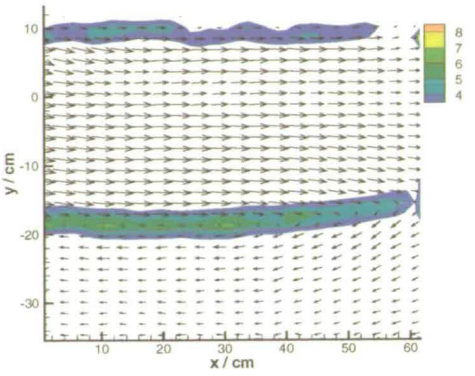

(a) $t = 22.55$s

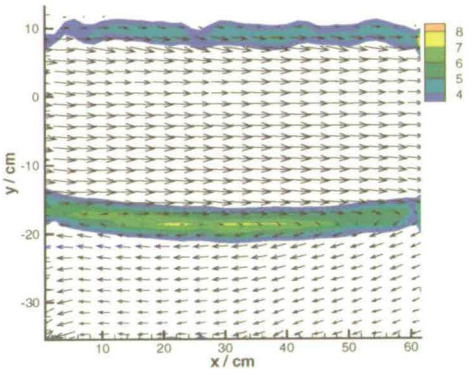

(b) $t = 23.1$s

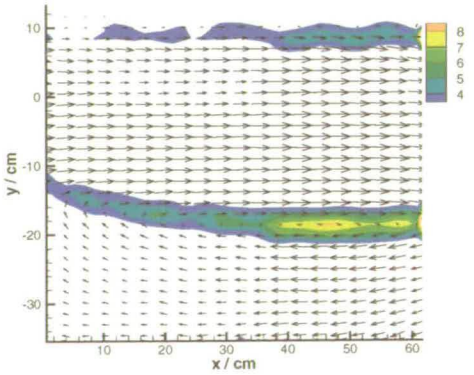

(c) $t = 23.65$s

Figure 4.8: Vector maps with vorticity contours for the solitary wave in figure 4.7.

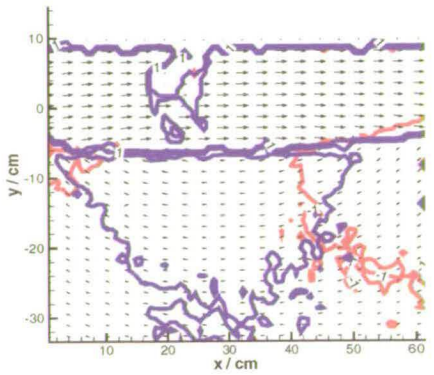

(a) $t = 25.3$s

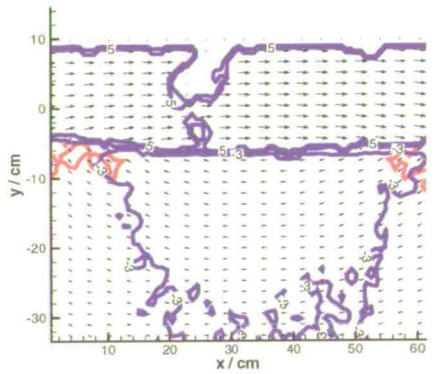

(b) $t = 25.85$s

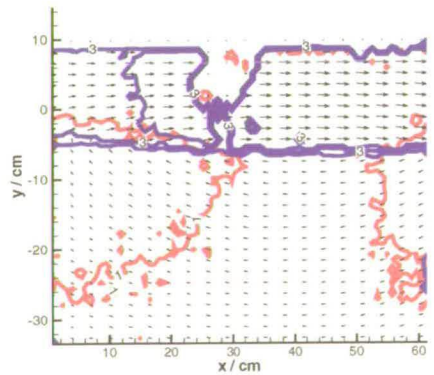

(c) $t = 26.4$s

Figure 4.9: Vector maps and isovelocity contours for a solitary wave ($h_1/h_2 = 6.1$ and $a/h_2 = -0.68$).

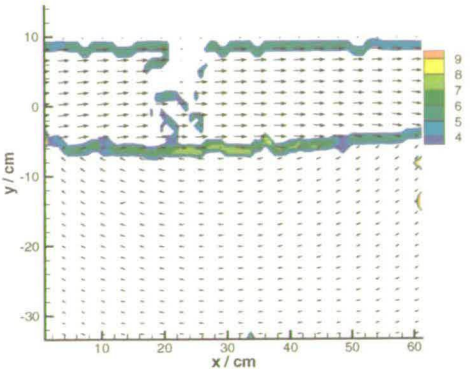

(a) $t = 25.3$s

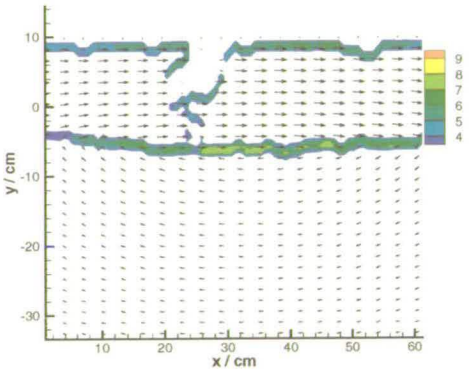

(b) $t = 25.85$s

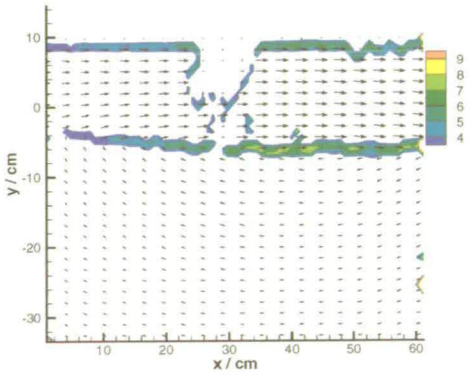

(c) $t = 26.4$s

Figure 4.10: Vector maps and vorticity contours for the solitary wave in figure 4.9.

lacks, however, an analytical model that can describe suitably large amplitude solitary waves for which $a/h_2 \leq -1$. Recently (section 2.3.4), a fully nonlinear time-stepping model [30, 28] has been developed and validated successfully against experimental data [30, 28, 29, 34] for both small and large amplitude interfacial solitary waves. An overview of the model method and assumptions, followed by a brief review of the literature, is given here.

The method models solitary waves of permanent form in a two-layer fluid of infinite horizontal extent, but of finite depth, in a frame of reference moving with the wave speed, c. A boundary integral method representation based on Cauchy's theorem is used. Boundary-Integral Methods (BIM), first proposed by Svensen [86], have been found to be very accurate in modelling nonlinear free-surface flows [22]. The underlying assumption of the BIM is that the fluid is homogeneous and incompressible and the fluid motion is irrotational, such that the velocities are found from potential theory. The motion of a fluid in potential flow is completely determined by the fluid velocities around the fluid boundary. Consequently, only the fluid motion at the boundaries needs to be resolved and only the boundary itself needs to be discretised. This has significant computational advantages, reducing both the complexity of the problem (the number of variables) and the computational time [22].

For the model discussed here, the behaviour of the two-layer fluid, where $\rho_1 > \rho_2$, under the action of gravity is considered. The interface separating the layers is

taken to be infinitely thin. The pressure in each of the fluids is determined from the Bernouilli equation such that the pressure is continuous over the interface. As the speed of the internal waves is small, there is little vertical motion of the fluid in the vicinity of the free surface. As a result, the application of a rigid lid condition at the free surface is justified [28, 29] such that $v_2|_{y=h_2} = 0$. In addition, the kinematic boundary condition along the bottom of the lower fluid layer is $v_1|_{y=-h_1} = 0$. It is assumed that the length of the wave is much greater than the thickness of the interface.

In this work, the initial conditions for the model are prescribed in terms of a small initial wave amplitude a/h_2, the stratification configuration, h_1/h_2 and the density difference, $\Delta\rho/\rho_2$, across the two fluid layers. Initial guesses for the particle velocities and wave speed are calculated using KdV theory. Then, at each time step, the position of the interface and the velocity potentials in the upper and lower layers are found. Further details of the model can be found in [30], [28] and [29].

In [28], experiments were performed in a two-layer fluid with $h_1/h_2 \approx 4$ and $\Delta\rho/\rho_2 = 2\%$. Amplitudes considered were between $a/h_2 \approx -0.2$ and -1.5. The model was in agreement with the experimental measurements over the whole amplitude range. For small amplitudes, the method was seen to agree well with KdV and other assymptotic theories; finite depth and deep water theories (section 2.3.4). A short review of the capability of the model to predict internal

solitary wave characteristics is given in [30], where the model also performs well. Likewise, similar experimental parameters are used in [29]. The method was compared to internal solitary waves of depression obtained both from PTV and DPIV measurement methods, a comparison pertinent to the present work. Overall, a discrepancy of 7% to 8% was found between the nonlinear predictions and the PTV and DPIV results for measurements of non-dimensional horizontal velocity, u/c_0. In addition, theoretical results were found for two other depth layer ratios, $h_1/h_2 = 10$ and $h_1/h_2 = 100$. In [34], reference experiments for a range of solitary wave amplitudes and depth layer ratios were carried out and compared to the fully nonlinear model before investigating the distortion of internal solitary waves by a finite amplitude bottom ridge. The density difference across the interface ranged from 1.25% to 2.15% and $h_1/h_2 = 4$ to $h_1/h_2 = 8$. Here too, the model provided a good fit to the experimental data.

The velocity shear, apparent on the isovelocity contours for each wave, can be identified in all four graphs of non-dimensional velocity u/c_0 against depth y/h_2, shown in figure 4.11. The velocities remain relatively constant within both the upper and lower fluid layers respectively, tending to 0 at the density interface. It can be seen that the velocities in the small amplitude waves in either stratification are smaller than their large amplitude counterparts where the velocities in the upper layer tend to the upper limit of $(u/c_0)/(a/h_2) = 1$. This concurs with findings made in previous work [44, 29].

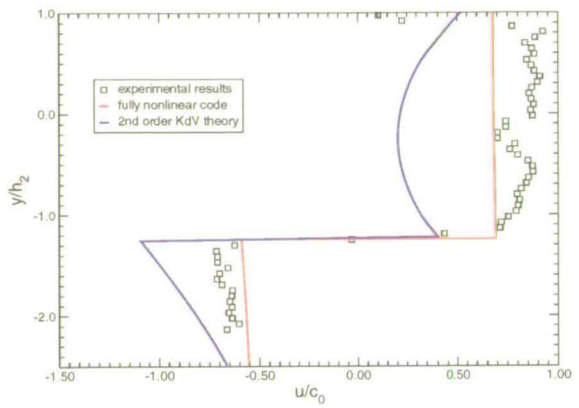

(a) $h_1/h_2 = 4.0$, $a/h_2 = -1.24$

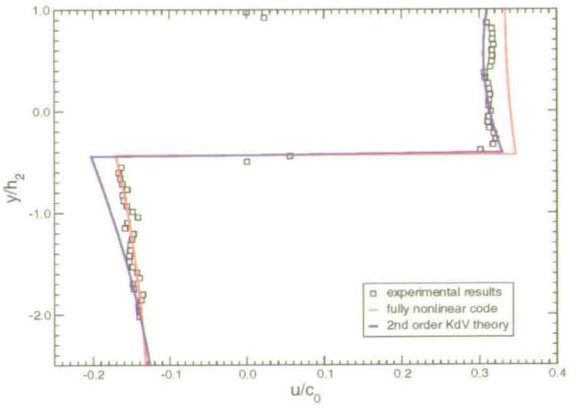

(b) $h_1/h_2 = 3.9$, $a/h_2 = -0.48$

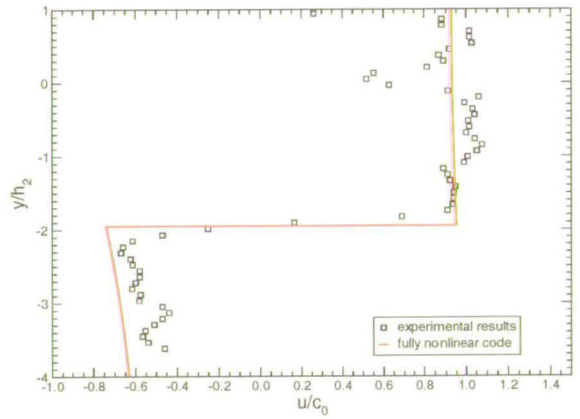

(c) $h_1/h_2 = 6.25$, $a/h_2 = -1.95$

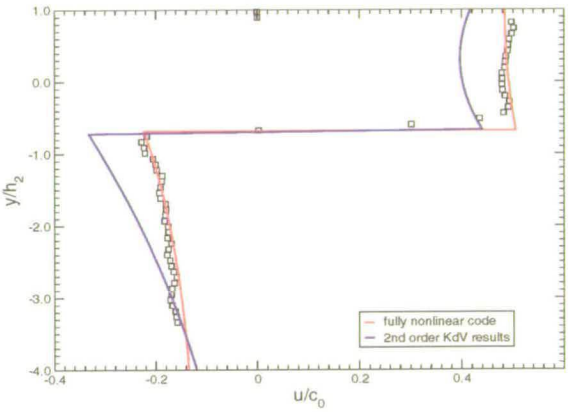

(d) $h_1/h_2 = 6.1$, $a/h_2 = -0.68$

Figure 4.11: Velocity profiles through the maximum depression of each of the solitary waves investigated. KdV (blue line) and fully nonlinear theory predictions (red line) are also shown.

In the large amplitude wave velocity plots (figure 4.11 (a) and (c)), the experimental measurements show reduced velocity values in the region of $y/h_2 \approx 0$. This is deemed to be a spurious effect, caused by pollen sticking to the glass flume sides and obscuring the cross-correlation analysis. When the fresh water layer was added initially to the free surface of the brine layer, the filling rate had to be very

slow to avoid mixing the two fluids. During this time, pollen accumulated at the free surface of the fluid and caused a smearing effect on the glass in this region. The rate of filling could be increased as the top layer increased in depth. For two reasons, the deviation is less apparent in the small amplitude wave measurements, performed using shuttering method 2. Firstly, the tank filling procedure was faster and, secondly, the seeding particle displacements between images of a pair were much greater than in the large amplitude wave investigations.

In the present work, KdV theory (blue line) fails to predict adequately the velocity profile for the large amplitude waves in either depth layer ratio regime (figure 4.11 (a) and (c)) but provides a far better estimation of the velocities in the small amplitude solitary wave $a/h_2 = -0.48$, where $h_1/h_2 = 3.9$ (figure 4.11 (b)). In contrast, the numerical model (red line) gives a better match to all experimental results, particularly in the case of the small amplitude solitary waves (figure 4.11 (b) and (d)).

Figure 4.12 shows the resulting wave shape η/h_2 against non-dimensional time, $c_{KdV}t/\lambda$, where c_{KdV} is the KdV wave speed and λ is the KdV characteristic length scale (equation (2.21)), for each of the four solitary waves. The wave shapes were obtained by finding the coordinate y/h_2 where $u/c_0 = 0$ in a specified column of each vector map in an experimental sequence. This method gives an error of $\Delta(a/h_2) = \pm 0.02$ for $h_1/h_2 \approx 4$ and an error of $\Delta(a/h_2) = \pm 0.04$ for $h_1/h_2 \approx 6$. In each graph, results have been shown for different columns in

the centre of the vector map sequences (denoted by □, △ and ◊). The column numbers have been specified in each graph legend. First order KdV theory (blue dashed line) and the fully nonlinear numerical model (red line) results are also plotted. In addition, second order KdV theory has been included in (b) and can be seen to provide a closer fit to the data than the first order approximation. In all other cases, (a), (c) and (d), it was found that the value of a/h_2 was too large to include second order terms.

The nonlinear numerical model provides a very good description of the large amplitude wave in figure 4.12 (a). The fit to the wave in (c) is less good, the laboratory generated wave being slower (the plot is wider) than that predicted. However, the stratification and amplitude of this wave are not covered in the parameter ranges in which the model has been verified previously. This observation is discussed further in section 5.2.2.

In figure 4.12 (b), the variation in the measurements at $\eta/h_2 = a/h_2$ is around $3 \times \Delta(a/h_2)$. In figure 4.12 (b) and (d), there is a greater spread in the data points in the range $-10 < ct/h_2 < 10$. It was found that when the exposure of the first image, $\Delta E_1 \sim 10$ms, as in the case of the small amplitude solitary wave experiments, the images experienced an enhanced "blooming" effect [71]. This caused a loss of greylevel information, particularly in the central area of the images, considerably reducing the contrast between the illuminated seeding particles and the black background of the wave flume. The cross-correlation of

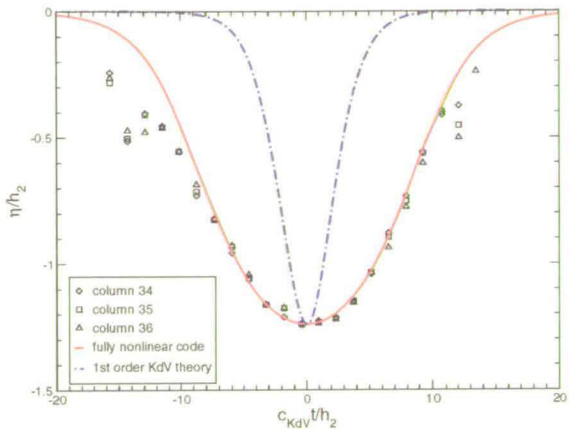

(a) $h_1/h_2 = 4.0$, $a/h_2 = -1.24$

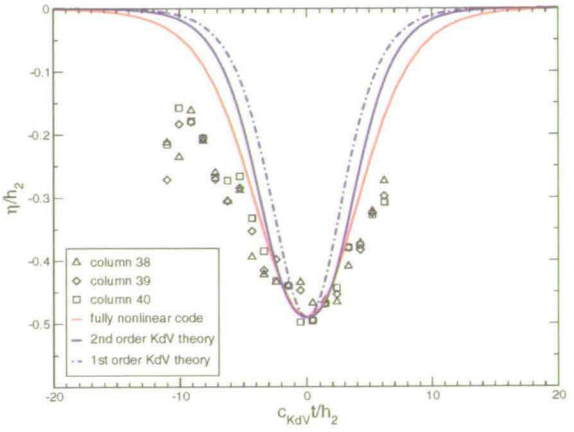

(b) $h_1/h_2 = 3.9$, $a/h_2 = -0.48$

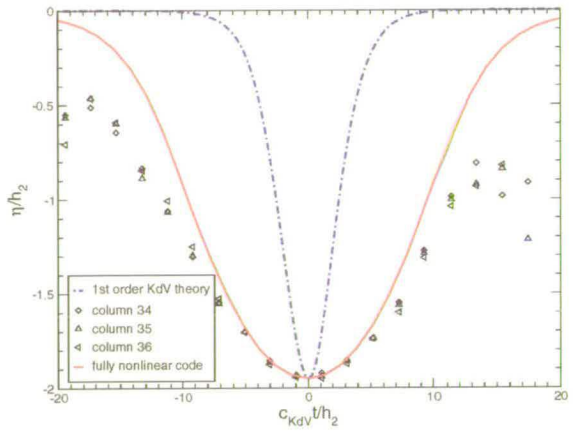

(c) $h_1/h_2 = 6.25$, $a/h_2 = -1.95$

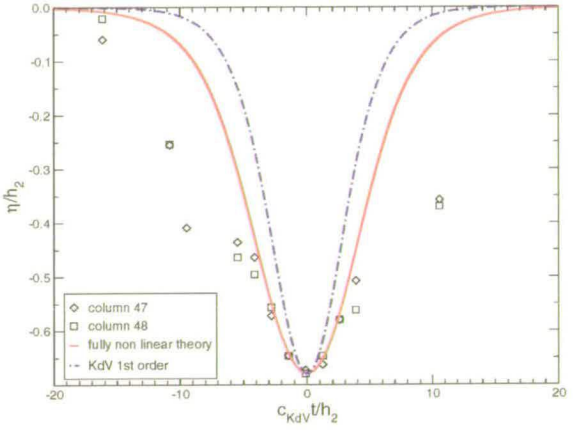

(d) $h_1/h_2 = 6.1$, $a/h_2 = -0.68$

Figure 4.12: The wave shapes of each of the solitary waves investigated. KdV theory (blue lines) and the fully nonlinear method (red line) predictions.

such image pairs produced large numbers of spurious vectors in regions of the maps corresponding to the affected areas of the images. The noise in the velocity measurements is highlighted by the irregular nature of the isovelocity contours, notably in the centre of the plots shown in figures 4.5 and 4.9. A dip in the horizontal velocity contours is apparent in the centre of the plots, particularly in figure 4.5. More than one attempt at both experiments was necessary to obtain

the vector maps shown. Given the time necessary and quantity of raw materials required for the experiments, recording the flow reliably was important. As a result of the reduced quality of the images acquired in the shuttering method 2, it was decided to use the camera in subsequent DPIV experiments using shuttering method 1 only. This imposed additional drawbacks on the camera system as the particle displacements in this latter set-up were very much smaller, reducing the accuracy and reliability of the DPIV measurements for slow flows.

One of the main consequences of using of shuttering method 1 (section 3.2.7) is that as the minimum scan period of the laser beam was 2.5ms, the particle displacements were small. The DPIV design rules set out in section 3.1.1, therefore, could not be adhered to. This increases the errors associated with the velocity measurements determined from the correlation peak detection routine. The lower signal to noise levels are reflected in the isovelocity contours plotted in figures 4.3 and 4.7 and in the horizontal velocity profiles (a) and (c) in figure 4.11. The increase in error in the estimation of the particle displacement by the DPIV analysis routine will be further discussed in section 4.4.2.

It was remarked in [29] that the guillotine-style gate generation mechanism (section 3.2.6) produced repeatable internal solitary waves. In order to verify this, a series of three DPIV experiments were performed on single internal solitary waves, with the same initial condition values, namely $V = 79\text{l}$, $D = 0.4\text{m}$, $h_1/h_2 \approx 3.9$ and $\Delta\rho/\rho_2 \approx 5\%$. The wave shape and the velocity profiles through the maxi-

mum amplitude of the waves are shown in figure 4.13. The plots show that the system does indeed produce repeatable waves, provided the variation in h_1/h_2 and $\Delta\rho/\rho_2$ is small.

In practise, eliminating variations, from experiment to experiment, in these parameter values was found to be difficult. In particular, this was true for the layer depth ratio value, h_1/h_2. The water level to which the saline fluid was filled, h_1, was the same for all experiments carried out in the same stratification configuration. It was found that even a small change in the flow rate of fresh water (held in the containers above the wave tank) from one experiment to another affected the thickness of the interface. In contrast to other work [33, 32], where $h_2 = H - h_1$, the value of h_2 here was determined from the location of the point of inflection in the plot of density versus fluid depth (figure 4.2). Consequently, the values of h_1/h_2 vary from experiment to experiment within the so-called "same" stratification regime. Both methods of calculating h_2 were used to run the nonlinear code. It was found that the speed of the solitary wave was sensitive to changes in the depth layer ratio. The nonlinear code output was found to provide a better match to the experimental results when the mid-point of the density interface was found.

The largest amplitude solitary waves investigated travelled at speeds of around 25cm.s^{-1}. The edge of the measurement area furthest from the sliding gate was situated around 2.5m from the end of the wave flume (at the surface wave pad-

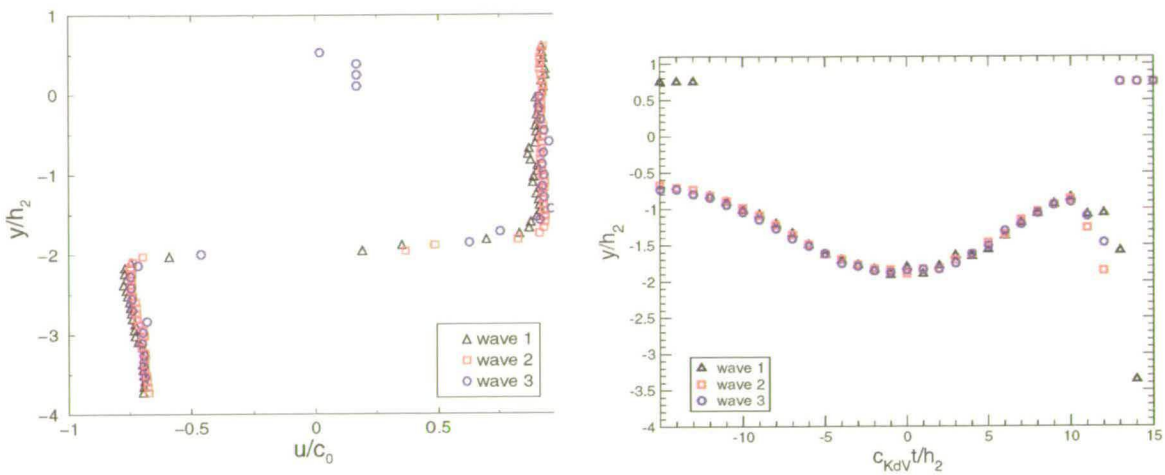

(a) Velocity profile

(b) Wave shape

Figure 4.13: Solitary wave generation: repeatability. The wave shapes and velocity profiles for three separate experiments with the same initial conditions; $V = 79$l, $D = 0.4$m, $h_1/h_2 \approx 3.9$ and $\Delta\rho/\rho_2 \sim 5\%$. The results show that the sytem does generate repeatable solitary waves.

dle) (figure 3.11). Hence, once the leading edge of the solitary wave had passed through the laser light sheet, there was a time "window" of approximately 20s before the solitary wave was reflected off the end wall of the tank and reached the measurement area once more. The time interval shown on the graph in figure 4.13 (b) covers approximately 10s. The increased scatter in the data points in the region $ct/h_2 > +10$ cannot, therefore, be attributed to reflections of the solitary wave off the end wall of the wave tank. At the leading and tailing edges of the wave, the characteristic form of the velocity profile (seen in figures 4.11 and 4.13 (a)), in which the horizontal velocity tends to 0 in the interfacial region, is no longer found. Instead, the fluid motion is less well defined and the velocities are much smaller than those near the maximum depression. The method used to

determine the wave shape relies on locating the interface by finding the depth at which the horizontal velocity is zero. At the edges of the waveform, therefore, the scatter suggests that this method is no longer suitable for determining the wave shape. Measuring the wave shape over its full extent would be best achieved by locating the interface using an alternative optical method, such as PLIF (figure 5.11).

In [29], it was noted that in some cases, Kelvin-Helmholtz instabilities could be seen along the tailing edge of the solitary wave, at the interface between the two fluids. In this study, however, no such disturbance was observed. Section 2.1.2 discussed the condition under which stratified fluid flows became unstable, namely if the gradient Richardson number, Ri_g, drops below 0.25. The buoyant forces are then no longer sufficient to maintain the structure of the stratification and turbulent mixing can occur. Table 4.5 shows the gradient Richardson number for each of the four solitary wave flows discussed above. The non-dimensional density gradient $\frac{1}{\rho_2}\frac{\partial \rho}{\partial y}$ is approximated by $\Delta\rho/\rho_2\Delta h$, where Δh, is the width of the density interface and is given by the hyperbolic tangent fit to the density profile in the quiescent stratification (section 2.1.3). The velocity gradient is given by $\partial(u/c_0)/\partial(y/h_2)$ and is estimated from the velocity profiles in figure 4.11. In all four cases, Ri_g is much greater than 0.25, indicating that the stratification is highly stabilising. This concurs with the observations made as the experiments were carried out.

depth ratio h_1/h_2	amplitude a/h_2	density gradient $\Delta\rho/(\rho_2\Delta h)$	buoyancy frequency $N(y)$ (s^{-1})	velocity gradient $\partial(u/c_0)/\partial(y/h_2)$	Ri_g
4.0	-1.24	0.055	7.34	7.1	1.06
3.9	-0.48	0.04	6.26	2.5	6.34
6.25	-1.95	0.049	6.9	4.35	2.54
6.1	-0.68	0.042	6.42	2.5	6.59

Table 4.5: The gradient Richardson numbers of the waves listed in table 4.4.

4.3.3 DPIV solitary wave investigation conclusions

In this section, a DPIV study of single internal solitary waves propagating at a brine - fresh water interface was presented. In the first instance, the parameter range of the two-layer stratification, namely the density ratio across the interface and the layer depth ratio, was assessed in the context of the limitations of the experimental facilities. Suitable initial conditions were found that would generate a single large ($a/h_2 < -1$) and a single small amplitude solitary wave ($a/h_2 \sim -0.5$) in both chosen stratification regimes.

Velocity vector maps were obtained for each wave as it passed through the measurement volume. As expected, a velocity shear was found across the interfacial region, characterised by an area of high vorticity. As the velocities for the two waves where $a/h_2 \sim -0.5$ were much smaller than those for the large amplitude waves, two different methods of shuttering the camera were employed (section 3.2.7). The velocity profiles and wave shapes, found by locating the point of zero

horizontal velocity in a sequence of velocity profiles, were compared both to KdV theory and to the results of a fully nonlinear numerical method [30, 28]. KdV theory failed to adequately predict the solitary wave characteristics in either stratification configuration for $a/h_2 \lesssim -0.5$, concurring with previous work [44, 29]. Overall, the nonlinear method provided a much better prediction of these waves' characteristics. The solitary wave generation mechanism was found to produce repeatable solitary waves, again, in accordance with findings made in previous work [29] although the interface thickness was found to be affected by the fill rate of the top fluid layer. The speed of propagation of the solitary wave was seen to be sensitive to the depth layer ratio, h_1/h_2. The stratifications in which the waves were generated were found to be highly stable, with a Richardson number, Ri, greater than 0.25 in all cases.

It was noted that the second shuttering technique (method 2), used for the small amplitude solitary wave experiments, caused a significant amount of data drop-out noise in the images obtained. This resulted in low signal to noise correlations in large areas of the vector maps. In contrast, method 1 could only be used for measuring velocities in the faster, large amplitude, internal solitary wave flows. It was decided that due to the unreliability in image and therefore measurement quality caused by method 2, it would be abandoned in favour of method 1. This imposed additional limitations on the velocity measurement range. This difficulty is further discussed in the context of the DPIV surface wave train experiments (section 4.4.2). As the apparatus was used at the limits of its operational range,

effectively the system was optimised for the study of large amplitude solitary waves.

In conclusion, single internal solitary waves were generated in a two-fluid system within the constraints of the experimental set-up. The internal solitary wave generation system has been validated. The DPIV system allowed both the wave generation parameters to be selected and the wave characteristics to be determined. To this end, the aims of this section have been met.

4.4 DPIV Measurements on Small Amplitude Monochromatic Surface Waves

In this section, the experimental set-up for the DPIV investigation of monochromatic small amplitude surface wave trains is described. As in the case of the individual solitary wave experiments (section 4.3), the aim of this investigation was to provide a reference data set against which the interaction experiments (section 4.5) could be compared.

4.4.1 Experimental set-up

All the experiments were carried out using the same experimental apparatus and facilities (section 3.2). In the first instance, limitations of the experimental pa-

rameter space for the generation of surface wave trains in the wave flume (section 3.2.1) were assessed. The two parameters used here to characterise the surface wave trains are the amplitude, a_S, and the angular frequency, ω_S. One of the key assumptions in the Longuet-Higgins theory (section 2.5.1), describing surface wave wavelength and amplitude modulation resulting from the passage of an internal solitary wave, is that the surface wavelength should be much smaller than that of the internal wave. The operative frequency range of the paddle was $f_S \sim 0.7$ to 1.4Hz. It was desirable to use wave frequencies close to these limits. The range of wave amplitudes that could be generated by the paddle was restricted by the paddle displacement. It was found that for amplitudes in excess of around $a_S \sim 3$cm, the motion of the wave paddle became unsteady. As a result, two amplitudes $a_S \approx 0.5$cm and $a_S \approx 2.5$cm were selected, again at the extremes of the range. The measured amplitude and angular frequency values from the wave trains that were generated are presented in table 4.6.

The wave paddle could not instantaneously generate waves of the required amplitude and wavelength. It was necessary for it to progressively "ramp up" to the desired wave characteristics. This ramp-up time was equal to 2s. In addition to this, due to the presence of the sliding gate for solitary wave generation, the wave flume could not accommodate a beach to damp out the surface waves reaching the far end. As a result, standing waves were rapidly set up in the flume. Consequently, as DPIV images of *travelling* surface waves were required, the operation of the experiment was designed to optimise the length of time over which the

experiment and, therefore, image grabbing could take place. The limitation of the image grabbing frequency of one image pair every 0.55s imposed by the camera system (section 3.2.7) also limited the number of DPIV images that could be taken in one experiment. For the surface waves investigated, the wave speed is the order of $1 m.s^{-1}$ (table 4.6), such that it takes around 7s for a wave to travel the full length of the tank. Surface waves of the desired amplitude arrived at the measurement area around 7s from paddle initiation (figure 4.15). This implied that there was only a short window of time in which images of travelling surface waves could be acquired. Once the first wave crest had passed the measurement area, it took in the region of 7s for it to return, having been reflected off the end wall of the flume. In order to ensure that only travelling surface waves were captured, a maximum of 10 image pairs were taken in each experimental run.

The wave paddle motion was initiated by a keyboard command to the wave paddle PC. In all experiments involving surface wave trains, the image capture was triggered from the wave paddle control software. The trigger timing, which depended on the speed of surface wave under investigation and therefore on the wavelength, was the same for all experiments involving surface waves of the same wavelength. Image acquisition was started once the first wave crests, of the correct amplitude, had reached the measurement volume, situated at a distance of approximately 2.5m from the wave paddle. Three wave gauges (section 3.2.3) were positioned at regular intervals, adjacent to and following (in the direction of the surface wave propagation) the measurement volume. The sampling of the

gauge output began at the same instant the paddle was set in motion.

The DPIV system was set up in the same way detailed in section 4.3.1, using the same lens and magnification. The fluid was uniformly seeded with pollen, introduced, in the case of the two-layer fluid experiments, in the manner described in section 4.2.1. The camera was operated using shuttering method 1 (figure 3.9). Hence, the camera timings and exposures used for the experiments described here were the same as those used in the investigation of the large amplitude solitary waves, listed in table 4.3. A schematic of the complete laboratory set-up is illustrated in figure 3.11. The DPIV analysis was performed using the same grid and interrogation area sizes as before, namely 16pxl×16pxl and 32pxl×32pxl respectively. As in the previous DPIV analyses, the resulting vector maps were median filtered and scaled using the results of the spatial calibration performed before each experiment.

Overall, four surface wave trains were investigated. Table 4.6 lists the characteristics of each. The experiments on each wave train were first carried out in a homogeneous fluid consisting of fresh water. They were repeated in both stratification configurations, $h_1/h_2 = 4.0$, where $\Delta\rho/\rho_2 = 4.67\%$, and $h_1/h_2 = 6.55$, where $\Delta\rho/\rho_2 = 4.42\%$. This was to allow a comparison to be made between the velocity fields of the waves in the stratified fluids and those in a homogeneous fluid, which appears to not have been investigated in any previous work.

Density profiles of the quiescent stratification were taken, using the microcon-

ductivity probe (section 3.2.5), before and after each wave train experiment in a two-layer fluid. The paddle motion was ceased before standing waves could develop. The generation of surface waves was seen to preserve the initial density distribution in the two-layer fluids. Two examples of the density profiles before and after different surface waves were generated are shown in figure 4.14. Consequently, 4 series of DPIV images, corresponding to the four different wave trains, were obtained in each two-layer fluid configuration without renewing the stratification. Any fluid disturbance was allowed to settle between each of the runs and the image sequences were grabbed sufficiently rapidly that the pollen seeding was still uniformly distributed through the fluid. An image of the quiescent fluid to determine the position of the still water level was taken for each experiment. The fluid depth was always $H = 0.71$m, as required for the correct operation of the paddle.

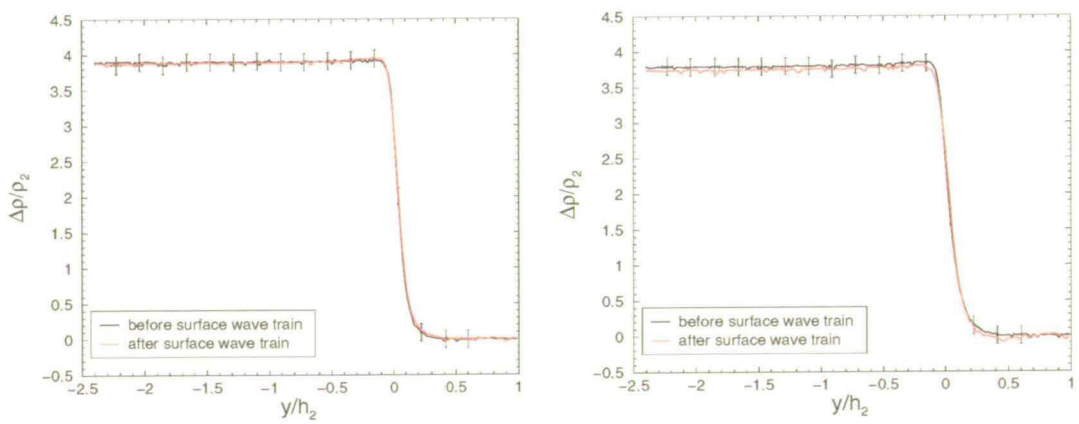

(a) $a_S = 0.87$cm, $\omega_S = 9.03$rad.s^{-1} (b) $a_S = 0.7$cm, $\omega_S = 5.87$rad.s^{-1}

Figure 4.14: Conductivity profiles before and after two wave trains were generated in the stratification configuration $h_1/h_2 = 6.55$.

4.4.2 Results of the surface wave investigation

In this section, an analysis of the DPIV surface wave investigation is presented. As in the case of the single internal solitary wave experiments, the aim of this DPIV study is, firstly, to assess the practical parameter space of the experiments in the context of the available DPIV data acquisition and the laboratory set-up, and, secondly, to provide reference data sets for comparison with the interaction results (section 4.5). The characteristics of the surface wave trains generated are verified and compared to linear surface wave theory (section 2.2). The repeatability of the surface waves generated using the hinged paddle (section 3.2.2) is also considered.

A trace of free surface elevation, $\eta_S(x,t)$, in cm, against time, t, for a wave of amplitude $a_S = 2.23$cm and frequency $\omega_S = 9.03$rad.s^{-1}, is shown in figure 4.15. The ramp-up time of the paddle can be clearly seen between $t \approx 5$s and $t \approx 7$s. First order linear surface wave theory is also plotted. It can be seen that there is good agreement between the theory and the gauge trace after $t \approx 8$s, once the wave desired amplitude and frequency have been established. In addition to providing the wave amplitude, the gauge output was also useful for verifying the frequency of the wave, either by fitting first order wave theory or by taking a Fourier transform of the portion of the trace in which the wave is well established. These frequencies and the corresponding wavelengths that are detailed in table 4.6.

In the stratified fluid experiments, it was found that the wave gauges proved

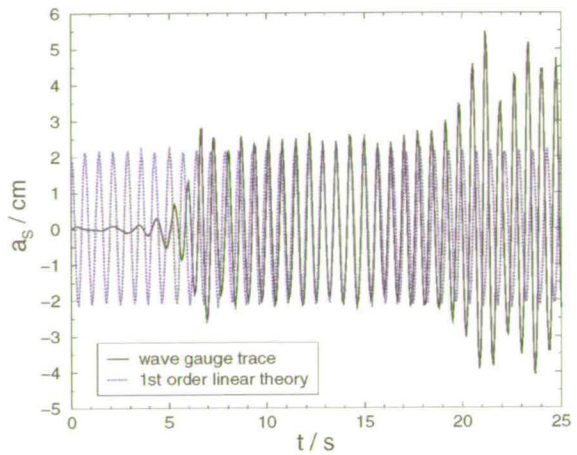

Figure 4.15: The calibrated wave gauge output for a wave train (black line), where $a_S = 2.23$cm and $\omega_S = 9.03$rad.s^{-1}. The measurements were taken in the fresh water homogeneous fluid. First order linear wave theory is also shown (dashed blue line)

to be unreliable, most probably due to the salinity of the lower fluid layer. The relationship between water level and gauge output was no longer linear or repeatable. An alternative method of determining the wave shape and amplitude was therefore devised. As the pollen at the free surface strongly reflected the laser light, the pixel intensity values in this region were greater than in other part of the image. The coordinates (i, j) of the free surface in each image were obtained by locating pixels of a given threshold greylevel.

Examples of the scaled surface wave profiles obtained using this method are shown in figure 4.16. Profiles from both the experiments performed in the homogeneous fluid and in the stratified fluid configurations can be seen. Surface wave linear theory (section 2.2) has been fitted to the plots (black line). A good fit between linear surface wave theory and the profiles is found even for the stratified fluid

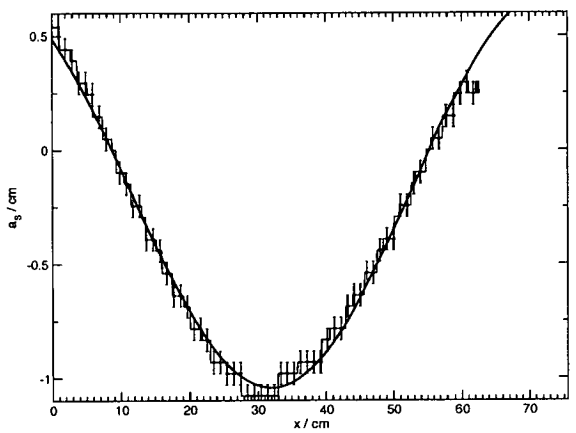

(a) Homogeneous fluid, $a_S = 0.87$cm, $\omega_S = 9.03$rad.s^{-1}

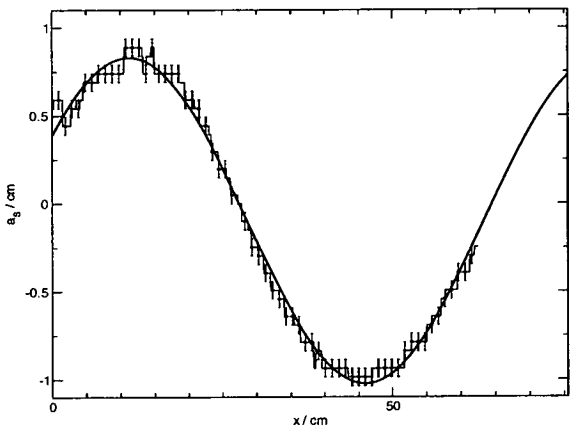

(b) $h_1/h_2 = 4.0$, $a_S = 0.87$cm, $\omega_S = 9.03$rad.s^{-1}

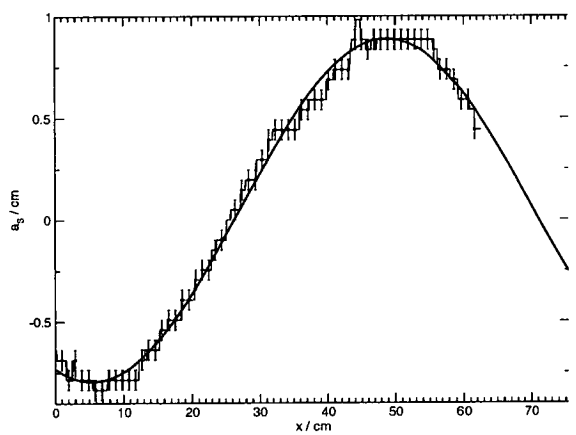

(c) $h_1/h_2 = 6.5$, $a_S = 0.87$cm, $\omega_S = 9.04$rad.s^{-1}

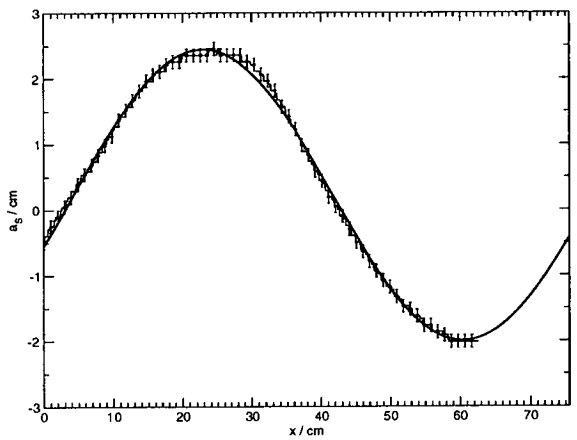

(d) $h_1/h_2 = 6.5$, $a_S = 2.23$cm, $\omega_S = 9.04$rad.s^{-1}

Figure 4.16: Examples of scaled wave profiles obtained by locating the fluid free surface in the raw DPIV images. First order linear surface wave theory is also shown (black line).

configurations. Deviations from the theory at the edges of the measured wave profiles are due to variations in laser light sheet intensity. In all plots in figure 4.16, the x-axis spans a complete wavelength, highlighting the limited field of view of the camera. In particular, only about 1/4 of a wavelength of the $a_S = 0.95$,

$\omega_S = 5.87\text{rad.s}^{-1}$ wave could be seen in the image. This made fitting linear theory to these profiles difficult. The consequences of this will be further discussed in section 4.5.1.

The fits provide a measure of both the amplitude and the frequency of the waves for all three fluid configurations. It was found that the frequency values obtained by the first order theory fit were in agreement with those obtained from the wave gauge readings. Table 4.6 summarises the amplitudes and wavelengths of the four surface wave trains generated by the wave paddle and investigated here. Although all the surface wave profiles were well described by a first order surface wave theory fit, there were small differences between consecutive profiles in the data sets obtained. This is probably a result of reflections of surface waves generated during paddle ramp-up off the far wall of the tank that altered the prescribed surface wave characteristics. This will be discussed further in the context of the measured velocity profiles seen in figures 4.19 and 4.23. Nevertheless, the good agreement found in all fluid configurations with a sinusoidal profile suggests that the shape of the surface waves is not affected by the presence of any internal wave modes set-up by the paddle motion.

It was discovered that a "bug" existed in the wave paddle software such that the trigger pulse, sent from the wave maker control box to the camera, may be randomly sent just before or just after the specified time interval. This was disappointing as for any particular time t in, say, two experimental runs using

the same wavelength, the same wave phase could not be obtained. This had implications for the interaction investigations (section 4.5) as it meant no direct comparison between surface wave profiles in the non-interacting and interacting case could be made. This matter will be further discussed in section 4.5.2.

wave amplitude a_S (cm)	angular frequency ω_S (rad.s^{-1})	deep water wavelength $\lambda_o = gT^2/(2\pi)$ (cm)	depth scaling H/λ_o	wavelength λ_S (cm)	wave speed c_S (cm.s^{-1})
0.87±0.023	9.04±0.019	75.57±0.156	0.94±0.007	75.53±0.532	108.64±0.16
0.95±0.15	5.87±0.076	177.05±1.249	0.401±0.004	176.54±1.243	164.26±0.75
2.23±0.031	9.03±0.014	75.41±0.156	0.94±0.007	75.53±0.532	108.52±0.23
2.4±0.11	5.9±0.027	178.77±3.278	0.397±0.008	174.94±1.232	164.99±2.14

Table 4.6: Table showing the surface wave amplitudes and wavelengths investigated here in the homogeneous fluid and the two-layer fluids $h_1/h_2 = 4.0$ where $\Delta\rho/\rho_2 = 4.67\%$ and $h_1/h_2 = 6.5$ where $\Delta\rho/\rho_2 = 4.45\%$.

The difficulties encountered in the analysis of the DPIV measurements in this section are caused by the very short time interval between exposures of a pair. The seeding particle displacements, particularly for the small amplitude surface waves, were effectively too small.Sub-pixel accuracy in DPIV particle displacements can be achieved by interpolation (section 3.1.1), applying a so-called "three point estimator" to the displacement correlation peak. Monte-Carlo simulations of DPIV measurements [93, 76, 94] have shown that the associated error in peak location with this estimator is between $\sim 1/10$ and $\sim 1/20$pxl when the particle image diameter, $d_t \approx 2$pxl. When the particle images are smaller than this, the estimation of the particle displacements can become biased towards integer

pixel values and is known as "peak locking". This particular problem is not encountered in this work as the particle images were optimised in the set-up.

For a wave of amplitude $a_S = 0.87$cm and $\omega_S = 9.04$rad.s^{-1}, in a DPIV system where the magnification of the camera system $M \sim 0.01$ and the time between images of a pair $\delta t = 2.5$ms, the maximum seeding particle displacements, predicted from linear theory (equations (2.12) and (2.13)), are $|\Delta i| \lesssim 0.4$pxl. In this configuration, the absolute errors associated with the displacement estimates will be of the same order, or larger, than the displacement values themselves. However, for a wave of amplitude $a_S = 2.23$cm and wavelength $\omega_S = 9.03$rad.s^{-1}, the displacements $|\Delta i| \lesssim 1$pxl, of an order similar to those measured in the large amplitude internal solitary wave flow field (figure 4.11).

Vector maps of a selection of the surface waves measured in the three different fluid configurations are shown in figure 4.17. Isovelocity contours are also shown, at intervals of 3cm.s^{-1} in (a), 2cm.s^{-1} in (b) and 1cm.s^{-1} in (c) and (d). Vectors in the region above the free surface have been removed. Small amplitude surface wave fluid flow is well known to be irrotational, as assumed by linear theory [85]. In this regime, assuming the flow is two-dimensional and incompressible, the horizontal and vertical velocity contours should intersect at right angles [19]. For $a_S = 2.23$cm and $\omega_S = 9.03$rad.s^{-1}, in figure 4.17 (a) where the particle velocities are $\sim$ 20cm.s^{-1}, the isovelocity contours are mostly perpendicular where they intersect. Where the seeding particle displacements are smaller < 0.5pxl, in the

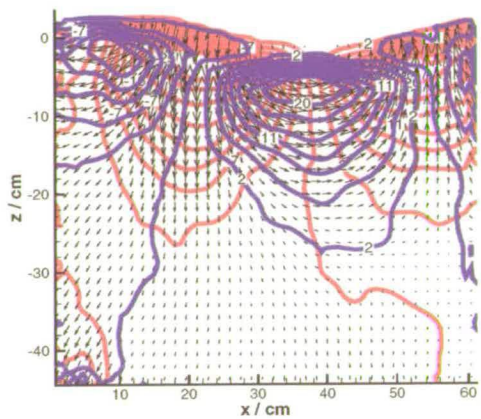

(a) Homogeneous fluid, $a_S = 2.23$cm, $\omega_S = 9.03$rad.s^{-1}

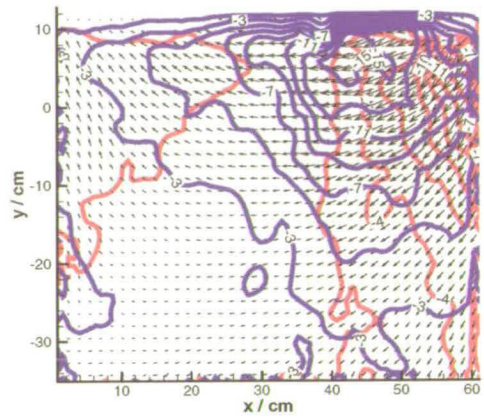

(b) $h_1/h_2 = 6.5$, $a_S = 2.23$cm, $\omega_S = 5.9$rad.s^{-1}

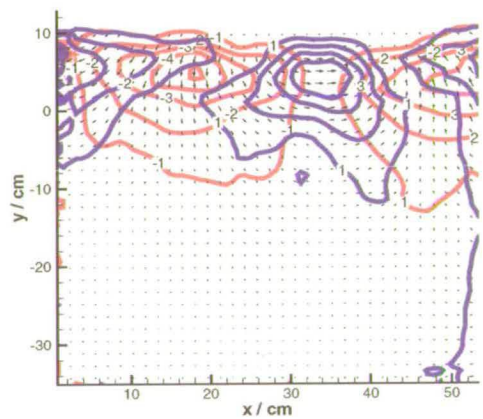

(c) $h_1/h_2 = 6.5$, $a_S = 0.87$cm, $\omega_S = 9.04$rad.s^{-1}

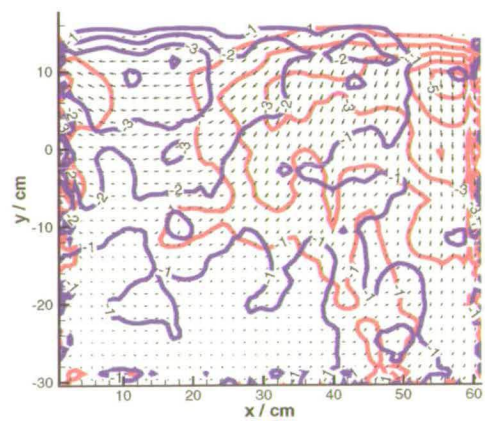

(d) $h_1/h_2 = 4.0$, $a_S = 0.95$cm, $\omega_S = 5.87$rad.s^{-1}

Figure 4.17: Vector maps showing isovelocity contours for a train of sinusoidal surface waves propagating in the homogeneous fluid and the two two-layer fluid configurations.

lower half of the plot, noise in the measurements affects the shape of the contours. This is also apparent in figure 4.17 (b) to (d). As wave amplitude decreases and wavelength increases, the plots are increasingly affected by the increasingly

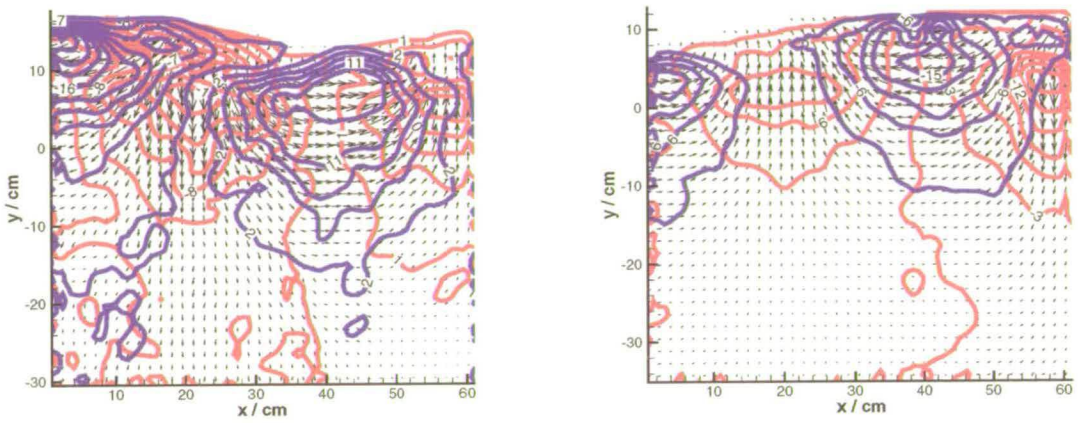

(a) $h_1/h_2 = 4.0$ (b) $h_1/h_2 = 6.5$

Figure 4.18: Isovelocity contour plots for the wave train $a_S = 2.23$cm and $\omega_S = 9.03$rad.s^{-1} in the two stratified fluid configurations, $h_1/h_2 = 4.0$ (a) and $h_1/h_2 = 6.5$ (b).

smaller particle image displacements such that in (d), the contours are very distorted. The DPIV results in this limit become meaningless. Consequently, the focus of the analysis in the remainder of this section will be placed on the DPIV analysis of the wave train where $a_S = 2.23$cm and $\omega_S = 9.03$rad.s^{-1}. The most practical way to overcome the problems encountered here, allowing a more detailed analysis of the results, would be to increase time δt, between images of a pair. With the present camera system, this would involve using an alternative shuttering method to allow short exposure times. In this way, the seeding particle images would remain in focus and the time interval between them would be sufficient to ensure the particle displacements are of the order of a few pixels (section 3.1.1).

Isovelocity contour plots are also shown for $a_S = 2.23$cm and $\omega_S = 9.03$rad.s^{-1} in the two stratification configurations, $h_1/h_2 = 4.0$ and $h_1/h_2 = 6.5$ in figures 4.18 (a) and (b) respectively. The contours are plotted at intervals of 3cm.s^{-1}. Similar features in these plots can be identified in figure 4.17 (a). A further comparison of the velocity fields for this wave train in each of the fluid configurations considered in this section is made below.

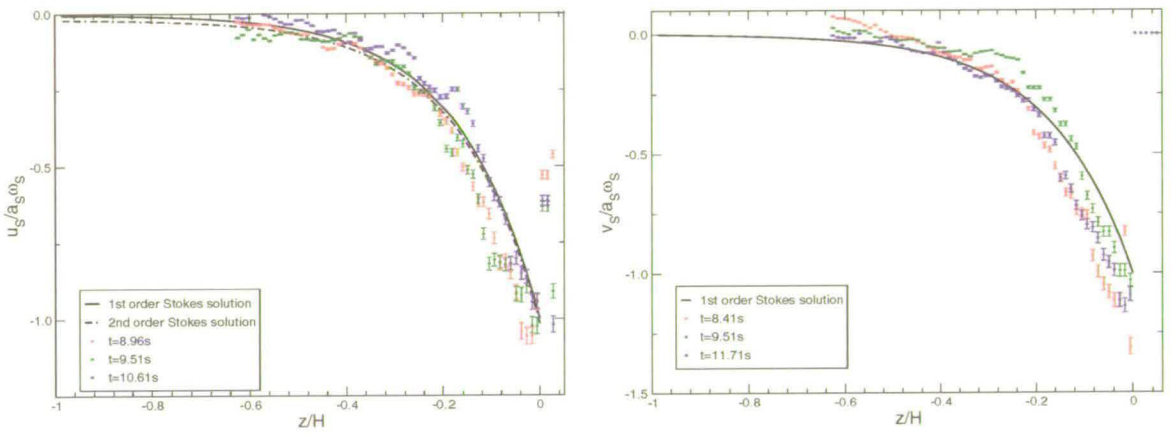

(a) $u_S/a_S\omega_S$ at $\eta_S(x,t)/a_S = 1$ (b) $v_S/a_S\omega_S$ at $\eta_S(x,t)/a_S = 0$

Figure 4.19: Surface wave maximum horizontal velocity profiles (a) and maximum vertical velocity profiles (b) scaled with $a_S\omega_S$ and plotted against non dimensional depth z/H for the wave train $a_S = 2.23$cm and $\omega_S = 9.03$rad.s^{-1}, in the homogeneous fluid. Time $t = 0$s corresponds to the instant the paddle was set in motion.

Figure 4.19 shows non-dimensional maximum horizontal and maximum vertical velocity profiles $u_S/(a_S\omega_S)$ and $v_S/(a_S\omega_S)$ for the wave train $a_S = 2.23$cm and $\omega_S = 9.03$rad.s^{-1} with non-dimensional depth z/H from the mean water level (MWL). In (a), the profiles are taken at three wave crests at times $t = 8.96$s, $t = 9.51$s and $t = 10.61$s from paddle initiation, such that $\eta_S(x,t)/a_S = 1$. In

(b), the profiles are taken from three different vector maps where $\eta_S(x,t)/a_S = 0$ at times $t = 8.41$s, $t = 9.51$s and $t = 11.71$s. The error bars show the absolute error in the velocity, calculated by considering the contributions from the displacement estimation error of ± 0.1pxl and the spatial scaling error. Both first and second order surface wave theory are also plotted (black full and dashed lines respectively).

If second order terms in the Stokes' expansion are considered, the velocities are written as

$$u_S = u_S^{(1)} + u_S^{(2)}, \tag{4.7}$$

$$v_S = v_S^{(1)} + v_S^{(2)}, \tag{4.8}$$

where $^{(1)}$ and $^{(2)}$ refer to the order in $(2a_S/\lambda)$. The first order velocity expressions were given in equations (2.12) and (2.13). The second order terms for the horizontal and vertical particle velocities are [85]

$$u_S^{(2)} = \frac{3}{4}(k_S a_S)^2 c_S \frac{\cosh[2k_S(z+H)]}{\sinh^4(k_S H)} \cos 2(\omega_S t - k_S x) - \frac{1}{8}\frac{g(2a_S)^2}{c_S H}, \tag{4.9}$$

and

$$v_S^{(2)} = -\frac{3}{4}(k_S a_S)^2 c_S \frac{\sinh[2k_S(z+H)]}{\sinh^4(k_S H)} \sin 2(\omega_S t - k_S x). \tag{4.10}$$

Second order theory provides little improvement to the fit as the wave steepness,

$2a_S/\lambda_S = 0.059$, is small. In the case of the vertical velocities in figure 4.19 (b), no difference can be seen between the two order predictions and hence only linear theory is shown.

In both figures 4.19 (a) and (b), although the measurements follow the same trend, the velocities are generally greater than those predicted by theory as $z/H \rightarrow 0$. A possible reason for this discrepancy could be due to transient wave components. These transient wave components were generated as the wave paddle "ramped up" to the required frequency and amplitude. These contained longer wavelengths that travel faster than the investigated wave train. These would therefore reflect off the end wall of the wave flume and return towards the measurement area, consequently disturbing the flow. The small differences between consecutive wave profiles, discussed previously, supports this. There appears, however, to be no consistent deviation from the theoretical curve with time. This may also be due to the effect of the reflected components providing a smaller or greater contribution to the velocities depending on their phases. In addition, the validity of the equations derived using a Stokes' expansion, as previously discussed (section 2.2), is questionable as the level of the wave trough is approached from below. Hence, deviations from the theoretical curves in the region near the free surface are not surprising. Moreover, laser light reflections and the accumulation of pollen at the free surface will have affected the DPIV cross-correlation routine in this region.

Horizontal and vertical velocity profiles of the same surface wave train $a_S =$

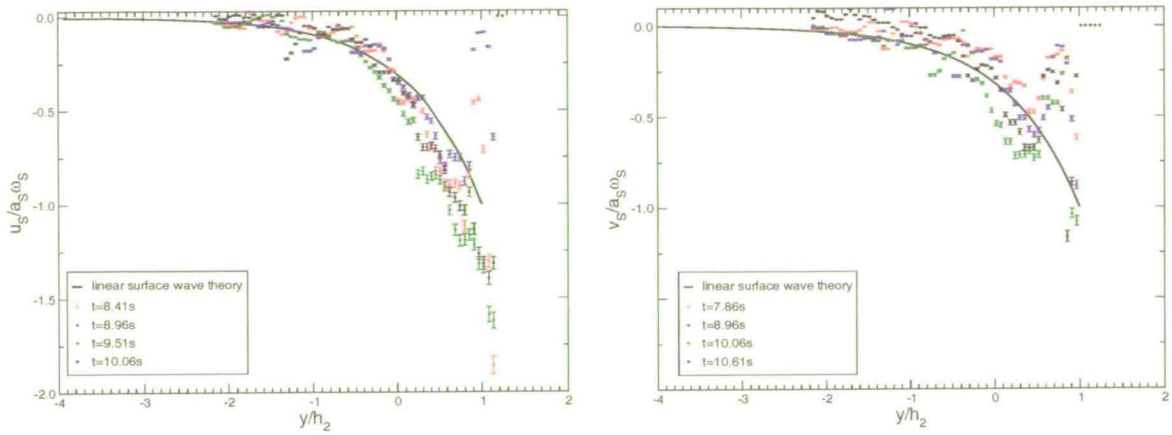

(a) $u_S/a_S\omega_S$ at $\eta_S(x,t)/a_S = 1$ (b) $v_S/a_S\omega_S$ at $\eta_S(x,t)/a_S = 0$

Figure 4.20: Profiles of surface wave horizontal velocity (a) and vertical velocity (b) in the stratification $h_1/h_2 = 4.0$ at different times t from starting the wave paddle.

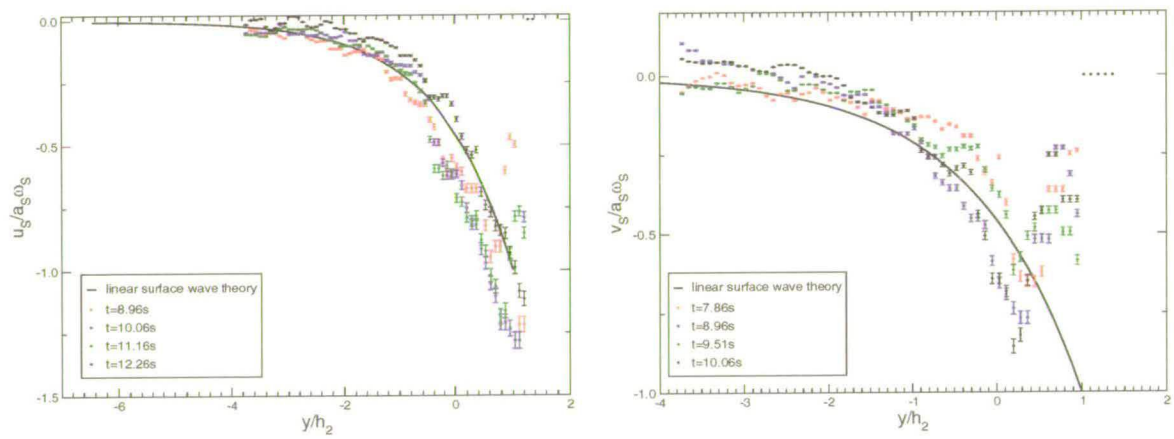

(a) $u_S/a_S\omega_S$ at $\eta_S(x,t)/a_S = 1$ (b) $v_S/a_S\omega_S$ at $\eta_S(x,t)/a_S = 0$

Figure 4.21: Profiles of surface wave horizontal velocity (a) and vertical velocity (b) in the stratification $h_1/h_2 = 6.5$ at different times t from starting the wave paddle.

2.23cm and $\omega_S = 9.03\text{rad.s}^{-1}$ in the two stratification regimes $h_1/h_2 = 4.0$ and $h_1/h_2 = 6.5$ are presented in figures 4.20 and 4.21 respectively. Each velocity profile was taken at a different time from paddle initiation. It was hoped that the effect of the sharp density gradient across the interfacial region (e.g. figure

4.14) could be identified and hence the non-dimensional velocities are now plotted against y/h_2 such that $y/h_2 = 0$ is the position of the interface in the quiescent fluid. To the authors knowledge, this aspect of this investigation has not been pursued before.

The data appear to follow the same general trend as that in figure 4.19. Linear theory appears, again, to underestimate the horizontal velocities (figures 4.20 (a) and 4.21 (a)). Light reflecting off pollen floating at, and just below, the free surface may have affected the accuracy of measurements in this region. An example of a DPIV image showing the area of the image affected by these surface reflections is shown in figure 4.22. This effect is more apparent here than in the homogeneous fluid case as substantially more pollen was present in this region, due to the additional time required to fill the top layer of fluid. This problem could probably be avoided if a longer time interval, δt, between correlated DPIV images was possible, as discussed above. Similarly to the homogeneous fluid case, variations with time in the velocities towards and away from the surface wave theory predictions can be observed. There appears to be no change in the trend in the horizontal velocity plots about $y/h_2 = 0$. In contrast, in figures 4.20 (b) and 4.21 (b), there is a peak in the vertical velocities in this region of the graph. During the experiments, the interface was seen to move with the free surface as the surface wave passed. Hence, where $\eta_S(x,t)/a_S = 0$, which is the case in the vertical velocity graphs, the interface will be found at its undisturbed position, $y/h_2 = 0$.

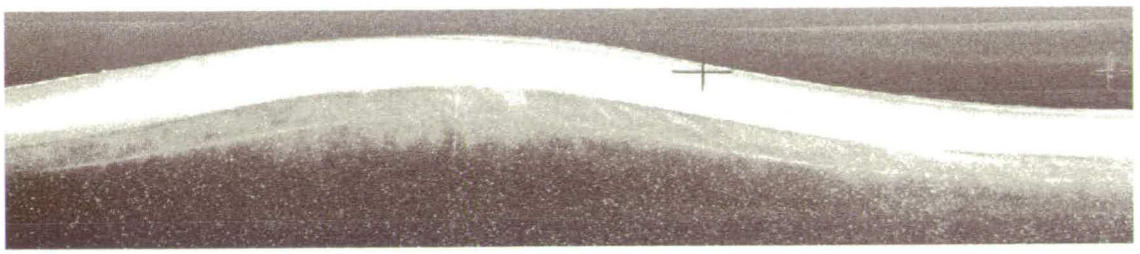

Figure 4.22: Upper section of a DPIV image taken at t=7.23s following paddle initiation. Notice the laser light reflections (broad band of white light) and the pollen in the free surface region (greyish patches).

In order to identify any changes to the velocity profiles caused by the presence of a density interface, a graph of all data sets plotted in figures 4.19 (a) and (b), 4.20 (a) and (b) and 4.21 (a) and (b) can be seen in figure 4.23 (a) and (b) respectively (red data points: $h_1/h_2 = 4.0$, blue data points: $h_1/h_2 = 6.5$, black data points: homogeneous fluid). The spread in the data points near the free surface indicates the increased uncertainty in the velocity measurements in this region. The plot of vertical velocities in (b) clearly indicates that, in the stratified fluid cases, there is a marked decrease in vertical velocity above the interfacial position. Table 4.7 shows the buoyancy frequencies associated with the stratification regimes used. The interface width is taken to be $\sim$ 1cm. The buoyancy frequency of each stratification is around 5 times larger than the surface wave frequency. As the surface wave motion imposes a forcing on the stratified fluid system, which is less than its natural frequency, the drop-off in (b) may be the result of non-resonant forcing of the vertical velocities. This matter is a subject for further work and could possibly be resolved by measuring the interfacial displacement due to the surface wave. Planar Laser Induced Fluorescence (PLIF), discussed in the next

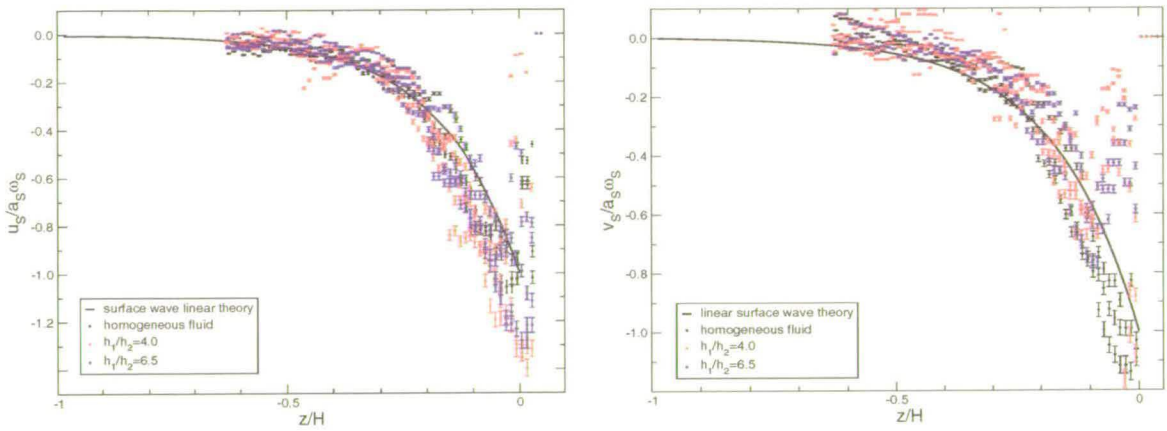

(a) $u_S/a_S\omega_S$ at $\eta_S(x,t)/a_S = 1$ (b) $v_S/a_S\omega_S$ at $\eta_S(x,t)/a_S = 0$

Figure 4.23: A comparison of horizontal and vertical velocity profiles shown in figures 4.19, 4.20, 4.23 for the three fluid configurations.

chapter, would be a suitable measurement technique for such an investigation as it would provide a non-intrusive means of visualising the interface.

depth ratio h_1/h_2	density difference $\Delta\rho/\rho_2$ (%)	buoyancy frequency $N(y)$ (s^{-1})
4.0	4.67	6.8
6.55	4.55	6.7

Table 4.7: Table showing the buoyancy frequencies for the two stratification configurations used in the surface wave train experiments.

4.4.3 DPIV Surface wave experiment conclusions

In this section, the experimental set-up for the acquisition of DPIV images of trains of progressive surface waves was described and the results were presented. DPIV experiments were carried out in a single homogeneous fluid, consisting of

fresh water, and two stratification configurations, such that $h_1/h_2 = 4.0$ and $h_1/h_2 = 6.5$. As in the case of the single internal solitary wave experiments, the aim of the non-interacting surface wave DPIV investigation was to assess the experimental parameter space in the context of the available DPIV data acquisition set-up and the laboratory facilities. It was also hoped that the experimental results would provide a basis for comparison with the interaction results presented in section 4.5.

Wave trains with amplitudes and frequencies at the two extremes of the available range were selected. The lengths of the surface waves and limited field of view of the camera and width of the laser light sheet meant that only a portion of even the smallest wavelength could be imaged at any one time. The limitations of the available DPIV camera system (section 3.2.7) had implications on the parameter range that could be measured and the accuracy of the results. Quantitative velocity information could only be realistically extracted from the larger amplitude $a_S = 2.23$cm wave train where $\omega_S = 9.03\text{rad.s}^{-1}$ where the particle velocities were large enough to be adequately resolved by DPIV analysis.

Although drawbacks to the camera - shutter system had been discovered, the DPIV images were, nevertheless, seen to provide a useful means of measuring the instantaneous free surface profile. In particular, it was shown that surface wave linear theory provided a good estimate of the surface wave profiles in all three fluid configurations investigated. This suggests that, for the amplitudes and

wavelengths investigated here, any internal fluid motion related to the disturbance of the stratified fluid column does not affect the surface wave shape. Such an observation appears to not have been reported before. This is an important consideration for the surface wave - solitary wave interaction investigation analysis where changes to the surface wave profile could be attributed to the interaction process rather than being an artefact of the surface wave generation system.

Velocity profiles for the wave train $a_S = 2.23\text{cm}$, $\omega_S = 9.03\text{rad.s}^{-1}$ were compared to linear surface wave theory. The theory was seen to slightly under-predict the velocities near the mean water level (MWL) where free surface effects must be brought into consideration. It was thought that reflections of transient wave components generated during the paddle "ramp-up" caused a deviation of the measurements from the theoretical predictions. The velocity profiles for surface waves in a homogeneous fluid were compared to profiles for the same surface wave train in the two stratified fluid configurations. It was noticed that the vertical velocities in the latter case were reduced in the regions above and below the interface position when compared to the homogeneous case. It was suggested that non-resonant forcing of the interface caused by the wave paddle motion caused a drop-off in the velocities either side of the interfacial region. In addition, a greater accumulation of pollen near the free surface in the stratified fluid experiments is thought to have reduced the accuracy of the measurements in this region.

The lack of quantitative velocity information restricted the scope of this DPIV

study. A broader investigation using a wider range of wavelengths and amplitudes would have been possible if a more appropriate time interval between DPIV images of a pair could have been used. This would be possible if an alternative shuttering method to the mechanical shutter used here was employed. This would allow the DPIV design rules to be followed, thus improving the accuracy of the DPIV measurements, and possibly reduce noise incurred by the presence of pollen near the free surface.

4.5 A DPIV Investigation of the Interaction Between an Internal Solitary Wave and a Train of Surface Waves

In this section, the interaction between a single internal solitary wave, propagating at a saline - fresh water interface, and a train of small amplitude surface waves, is investigated. To the author's knowledge, little research has been done in this field (section 2.5.2). The novelty of the present approach lies both in the investigation of large amplitude internal solitary waves and in the use of the non-intrusive DPIV technique to acquire full-field instantaneous two-dimensional velocity information.

4.5.1 DPIV experimental method for the investigation of internal solitary wave - surface wave train interactions

The experimental method for the investigation of the interaction between an internal solitary wave of depression and a progressive surface wave train is presented. The method builds upon the previous work performed using the same experimental facilities on the two waves types individually; internal solitary waves and surface wave trains. Consequently, sections 4.4.1 and 4.3.1 are referred to here. The solitary waves and surface waves were generated at the opposite ends of the wave flume, such that they travelled towards each other. The angle between the direction of propagation of the waves was therefore $\phi = \pi$.

In the experiments on surface wave trains (section 4.4.1), image capture was initiated from the paddle control software, such that the first fully developed wave crests had reached the measurement volume. Within the constraints of the experimental system, 10 DPIV image pairs following paddle ramp-up could be acquired, after which, standing waves started to develop. As a result, it was important to ensure that the paddle would only be started as the solitary wave approached the measurement region. The internal solitary wave experiments (section 4.3) established the approximate time for the solitary wave to reach the measurement volume. Hence, the wave paddle, and thus image acquisition, was

started following the sliding gate being opened, allowing for both paddle ramp-up to be completed and the solitary wave to reach the laser light sheet. The density change across the interface was around 5% as this ensured that the majority of the internal wave had passed the measurement area within the imposed time interval (section 4.2.1).

The analysis of the surface wave profiles from the DPIV images on surface wave trains (figure 4.16 (d)) demonstrated that of the two wave frequencies investigated, $\omega_S \sim 9\text{rad.s}^{-1}$ and $\omega_S \sim 5.9\text{rad.s}^{-1}$, the camera field of view could accommodate less than half a complete wavelength of the latter. In contrast, nearly a complete wavelength of the former wave train, where $\omega_S \sim 9\text{rad.s}^{-1}$, could be seen. It was also seen that the available DPIV set-up was optimised for the study of large amplitude ($a/h_2 < -1$) internal solitary waves. Consequently, this investigation centres on interaction processes that occur when a wave train of angular frequency $\omega_S \sim 9\text{rad.s}^{-1}$ rides over a large amplitude internal solitary wave of depression.

The results of four solitary wave - surface wave configurations are presented here. The two stratification regimes discussed previously (section 4.2.1), namely $h_1/h_2 \approx 4$ and $h_1/h_2 \approx 6$, were used to generate the solitary waves. The fluid was seeded with pollen in the same way as for the other stratified fluid DPIV experiments (section 4.2.2); by introducing the pollen into the lower fluid layer and letting it rise as the top layer was filled. Table 4.8 summarises the stratification,

the solitary wave and the surface wave parameters used.

surface wave parameters			stratification and solitary wave parameters				
a_S (cm)	ω_S (rad.s^{-1})	$2a_S/\lambda_S$	h_1/h_2	$\Delta\rho/\rho_2$ (%)	V (l)	D (m)	a/h_2
0.87±0.023	9.03±0.019	0.023±0.0008	3.8	4.7	79	0.4	-1.8±0.02
2.23±0.023	9.04±0.019	0.059±0.0012	3.58	4.72	79	0.4	-1.95±0.02
0.87±0.031	9.03±0.014	0.023±0.0008	5.96	4.99	80	0.4	-1.17±0.04
2.23±0.031	9.04±0.014	0.059±0.0012	6.39	4.38	80	0.4	-1.16±0.04

Table 4.8: Table summarising the parameters used in each of the DPIV internal solitary wave - surface wave train interaction experiments.

4.5.2 Results and discussion of the interaction experiments

In this section, results from the DPIV surface wave - solitary wave interaction experiments are presented. The wave parameters used are summarised in table 4.8. In the first instance, the effects of amplitude and wavelength modulation of the surface wave trains are considered. The effects of the interaction on the velocity fields are then investigated.

The series of double graphs displayed in figure 4.24 (a) to (h) show the solitary wave profile (lower graphs) and the corresponding profile of the surface wave during the interaction (upper graphs). For comparison purposes, the upper graph set also shows the undisturbed surface wave profile, obtained in the surface wave DPIV experiments (section 4.4.2). The initial surface wave steepness and angular

frequency were $2a_S/\lambda_S = 0.023$ and $\omega_S = 9.04\text{rad.s}^{-1}$ respectively. In this case, the (large amplitude) solitary wave is generated in a stratification where $h_1/h_2 = 3.8$ and $\Delta\rho/\rho_2 = 4.7\%$. Both profiles are plotted with x, the distance in cm across the measurement area. The ordinate is plotted in terms of z, the distance directed positively upwards from the MWL (also in cm). There is a change in scale for this axis between the upper and lower plots. The times indicated in the captions refer to the time from paddle initiation.

Previously (figure 4.12), the solitary wave profiles were found by determining the location of zero horizontal velocity as this was seen to mark the position of the density interface. The presence of the surface wave is an additional source of horizontal velocity within the interaction flow field. Theoretical interaction velocity profiles at surface wave crests and troughs (figure 4.32), obtained by linear superposition of the fully nonlinear solitary wave theory [30, 28] and linear surface wave theory, indicate that the surface wave contribution to this velocity field near the maximum depression of the solitary wave is positive at a surface wave trough throughout the fluid depth. Conversely, at a surface wave crest, the contribution is negative. The theoretical curve assumes an infinitely thin density interface and hence the position of zero horizontal velocity remains unaffected. In the case of the experiments performed here, the pycnocline has a finite width and hence the presence of the surface wave will alter this vertical location. However, using the maximum predicted change to the velocities at the interface, $\Delta(u/c_0) \lesssim 0.1$, and the range of non-dimensional velocity gradients over the interfacial region, given

in table 4.5, the change in vertical interfacial position of zero horizontal velocity is less than the error on the measurements themselves (section 4.3.2). Consequently, the position of zero horizontal velocity in each column of a vector map can still be used here to determine the position of the interface and hence the solitary wave profile. The error bars in the resulting plots correspond to the uncertainty in the interfacial position. The black line represents the running average over the points.

The graph sequence illustrates the progression of the internal solitary wave with time and the corresponding change in the surface wave shape. The plots also highlight the relative scales of both the surface and internal waves. Linear surface wave theory has been fitted to both surface wave profiles on each graph (black line: interaction data, red line: surface wave profile in the absence of the solitary wave, taken from the experiments discussed in section 4.4.2). In the case of the undisturbed surface wave profiles, the plots have been shifted along the x-axis in order to align either the surface wave crests or troughs. The linear theory fit (red line) has then been extrapolated over the complete x range for an easier comparison to be made between the two profiles.

Surface wave linear theory still provides a good fit to the surface wave profiles, despite the presence of the solitary wave. This provides further support for the evidence in section 4.4.2 that the surface wave profile is not disturbed by the presence of a density interface. There is, however, a noticeable change in ampli-

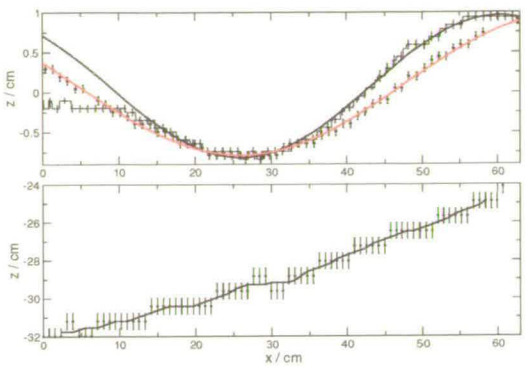

(a) $t = 7.86$s

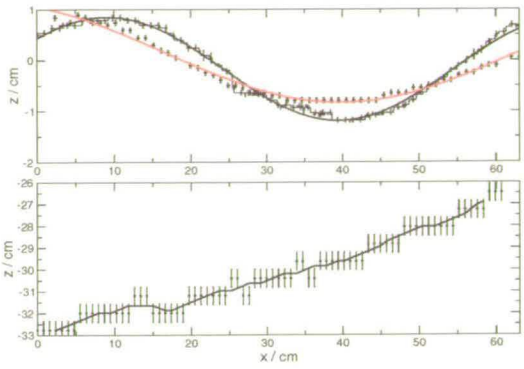

(b) $t = 8.41$s

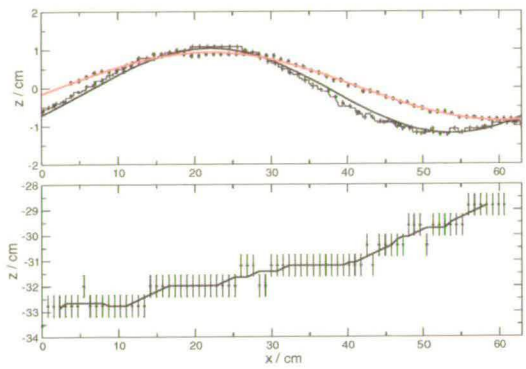

(c) $t = 8.96$s

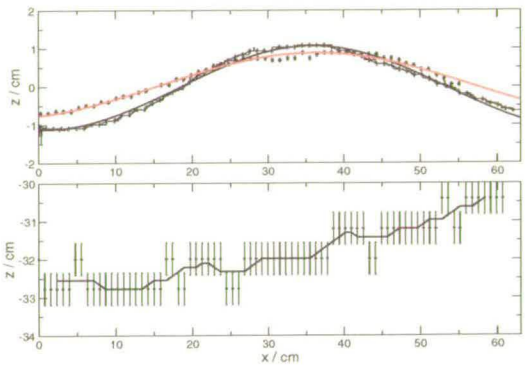

(d) $t = 9.51$s

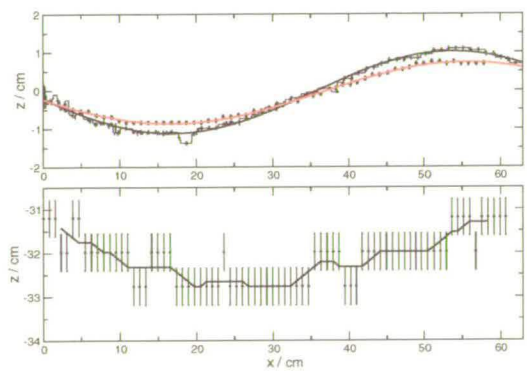

(e) $t = 10.06$s

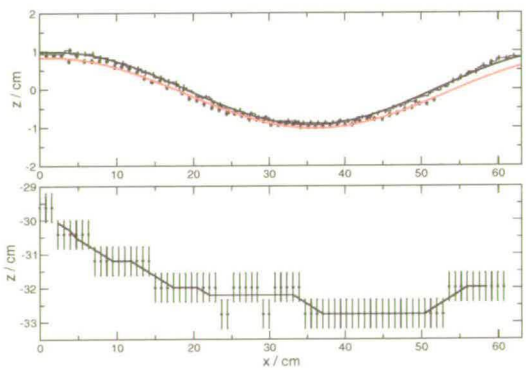

(f) $t = 10.61$s

(See caption next page)

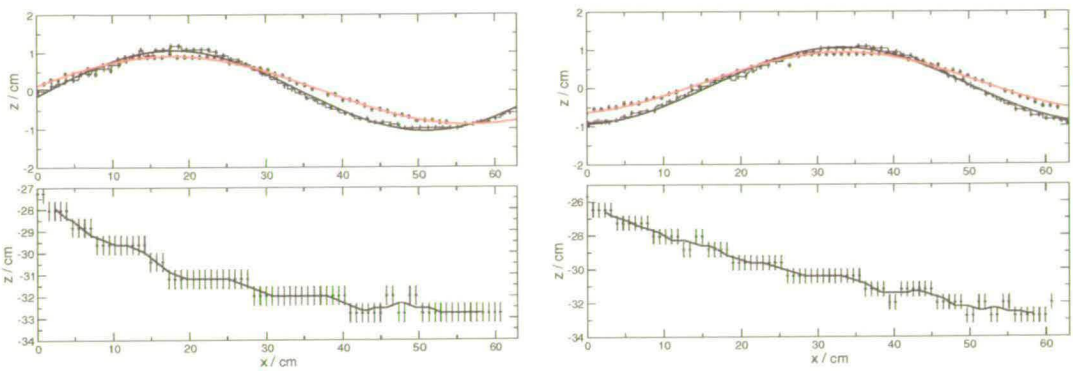

(g) $t = 11.16$s (h) $t = 11.71$s

Figure 4.24: Graphs of surface wave $2a_S/\lambda_S = 0.023$, $\omega_S = 9.04\text{rad.s}^{-1}$ profile (upper) and large amplitude internal solitary wave profile (lower) for a stratification where $h_1/h_2 = 3.8$ and $\Delta\rho/\rho_2 = 4.7\%$. Note the change in vertical axis scale between upper and lower graphs. First order linear theory is fitted to the surface wave profiles (black line: interaction data, red line: surface wave profile in the absence of the solitary wave).

tude as the solitary wave passes. This is highlighted by the comparison with the non-interacting surface wave profiles. Likewise, a modulation of the wavelength also occurs. As the solitary wave moves through the measurement volume, there is also a slight rise in the surface level, which has been accounted for in the linear theory fit. A similar change in the fluid free surface level was also noticed during the course of the single internal solitary wave experiments (section 4.3).

Similar plots of surface wave (upper graphs) and solitary wave (lower graphs) profiles with time are shown in order of increasing surface wave steepness, $2a_S/\lambda_S$, and non-dimensional solitary wave amplitude, a/h_2, in figures 4.25, 4.26 and 4.27, for the three remaining interaction cases (table 4.8). Again, surface wave linear theory has been fitted to the surface wave profiles.

The Longuet-Higgins and Stewart (LHS) theory describes the amplitude and wavelength modulation experienced by a surface wave riding over an internal solitary wave (section 2.5). The LHS theory predicts that, in a frame of reference moving with the solitary wave, the surface wave amplitude will increase and the wavelength will correspondingly decrease with distance towards the maximum depression of the soliton, or solitary wave "phase" (figure 2.7). Although the wave interactions observed here lie outwith the range of this theory (the theory assumes the wavelength of the surface waves to be very much smaller than the extent of the solitary wave and the solitary waves are described by KdV theory, which is not applicable to the large amplitude solitary waves investigated here), an increase in surface wave amplitude and a reduction in the wavelength was observed. This is substantiated by the fitted coefficient values, which are tabulated in appendix C. These coefficients can only provide a guide to the actual amplitude and wavelengths of the profiles as in most cases less than a complete wavelength is available. The fit can, therefore, slightly under- or over-estimate the values, depending on the surface wave phase. In addition, changes in the laser light sheet intensity at the edges of the measurement area and the accumulation of pollen at the water surface lead to spurious points in the plots. Amplitude increases were also noted in [33] and [32], although variations in surface wavelength were not observed (section 2.5.2).

In some of the plots, the shape of the surface wave crests and troughs show marked departures from the sinusoidal fit. This noticeable skewing implies that

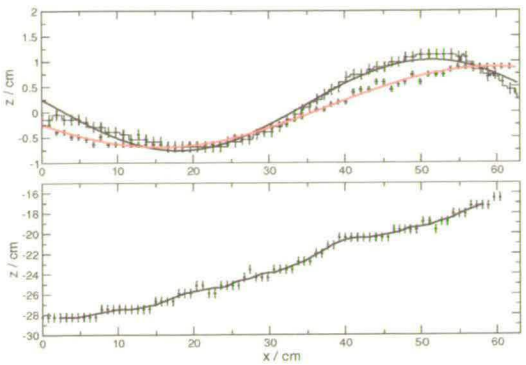

(a) $t = 7.86$s

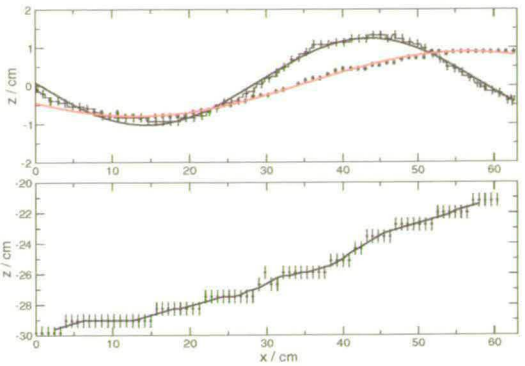

(b) $t = 8.41$s

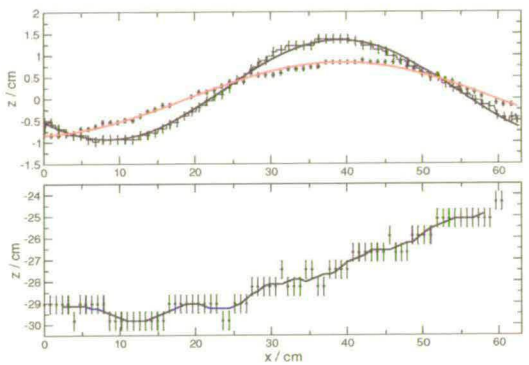

(c) $t = 8.96$s

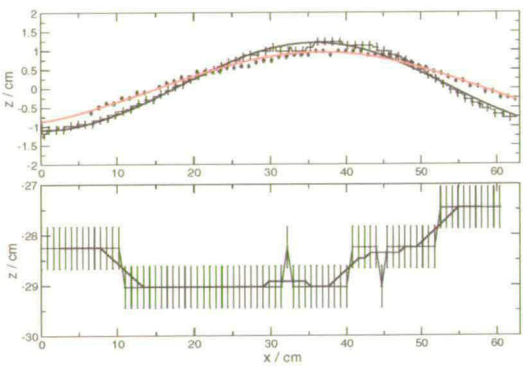

(d) $t = 9.51$s

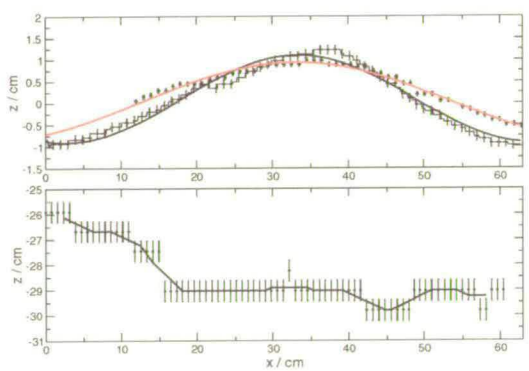

(e) $t = 10.06$s

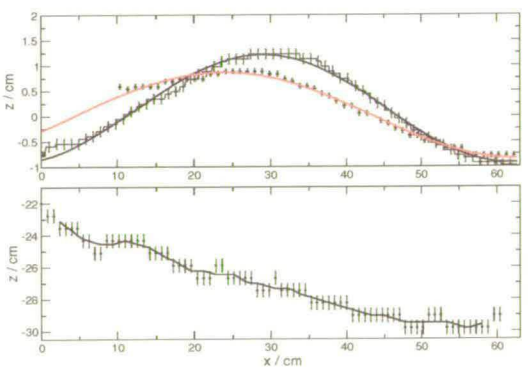

(f) $t = 10.61$s

(See caption next page)

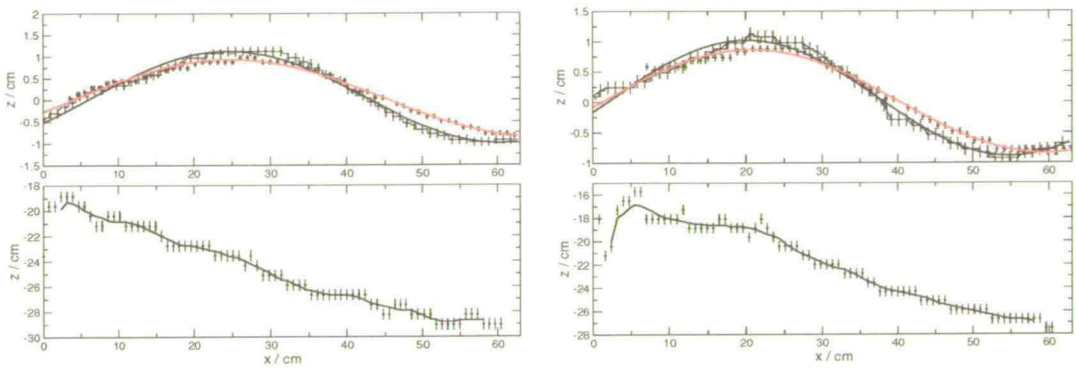

(g) $t = 11.16$s (h) $t = 11.71$s

Figure 4.25: Graphs of surface wave $2a_S/\lambda_S = 0.023$, $\omega_S = 9.04$rad.s^{-1} profile (upper graph) and large amplitude internal solitary wave profile (lower graph) for a stratification where $h_1/h_2 = 5.96$ and $\Delta\rho/\rho_2 = 4.99\%$. First order linear theory is fitted to the surface wave profiles (black line: interaction data, red line: surface wave profile in the absence of the solitary wave).

the surface waves do not experience uniform wavelength and amplitude modulation with solitary wave "phase". In contrast to the LHS theory predictions, where the dependence on solitary wave phase is symmetric about the internal wave trough (figure 2.7), the surface wave distortion seems to be most apparent when the front end of the solitary wave is visible in the measurement area and to a lesser extent when the tail end passes. In figures 4.24 (e), 4.25 (d) and 4.26 (e), where the trough of the solitary wave is visible, the effect is reduced significantly. The wave profiles become more sinusoidal.

Distortion of the surface wave shape is most noticeable where the initial surface wave steepness is largest and, in particular, in figure 4.27, for which $h_1/h_2 = 6.39$ and $a/h_2 = -1.95$. The magnitude of the solitary wave amplitude will most certainly affect the severity of the skew. For the experiment in figure 4.27, not

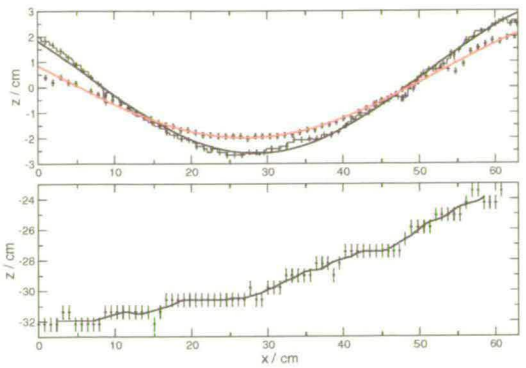

(a) $t = 7.86$s

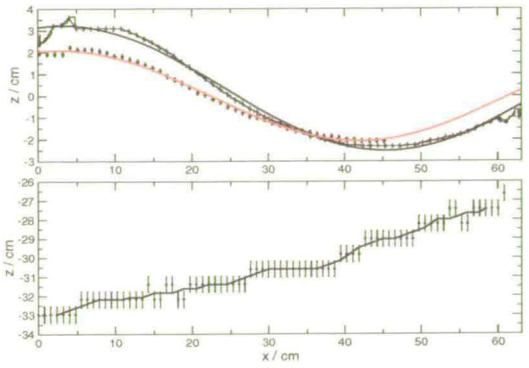

(b) $t = 8.41$s

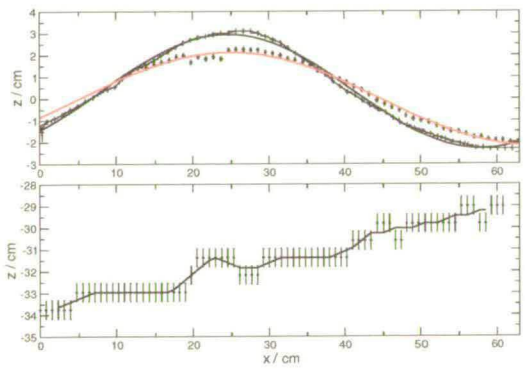

(c) $t = 8.96$s

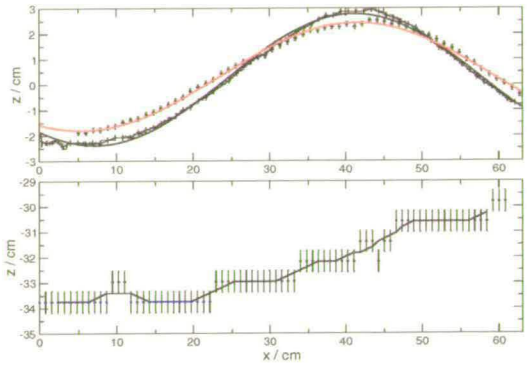

(d) $t = 9.51$s

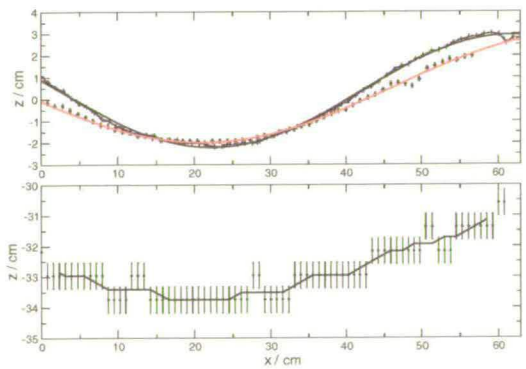

(e) $t = 10.06$s

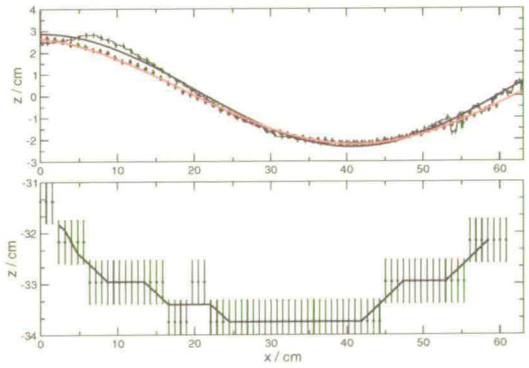

(f) $t = 10.61$s

(See caption next page)

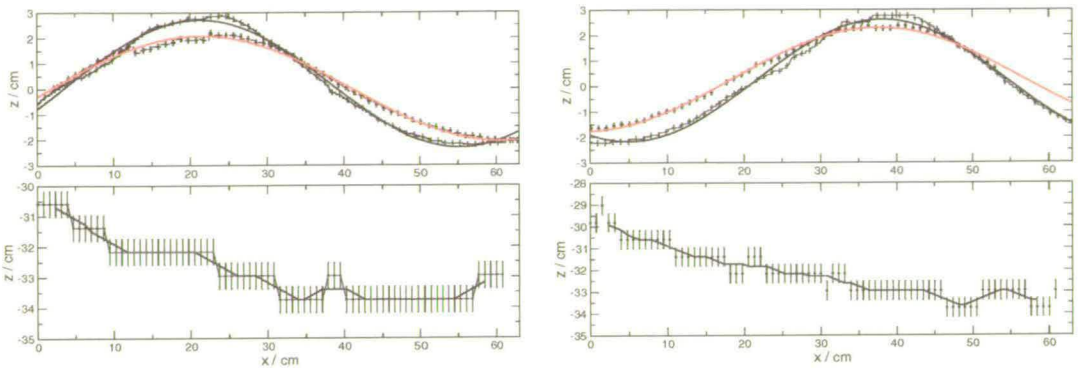

(g) $t = 11.16$s (h) $t = 11.71$s

Figure 4.26: Graphs of surface wave $2a_S/\lambda_S = 0.059$, $\omega_S = 9.03$rad.s^{-1} profile (upper) and large amplitude internal solitary wave profile (lower) for a stratification where $h_1/h_2 = 3.58$ and $\Delta\rho/\rho_2 = 4.72\%$. First order linear theory is fitted to the surface wave profiles (black line: interaction data, red line: surface wave profile in the absence of the solitary wave).

only is the non-dimensional amplitude of the solitary wave greatest but also the fluid layer depth ratio is greatest of all four experiments, such that the interface is closest to the surface. Such observations of surface wave shape distortion, resulting from the passage of the internal wave, were not reported in previous work [33, 32]. This is probably because neither the solitary wave amplitudes nor the depth layer ratio investigated were large enough (table 2.2).

Although there is a marked change in the shape of the surface wave shapes, the solitary wave profiles in the lower graphs provide little indication of any alteration to the solitary wave profiles. Though the spatial resolution of the measurement method used is limited, it does give a useful indication of the interface position as the wave passes. Solitary wave shape distortion due to the presence of the surface waves will, therefore, be left to section 5.3, where it will be discussed in

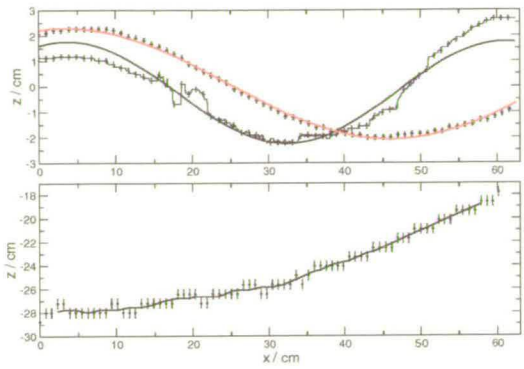

(a) $t = 7.86$s

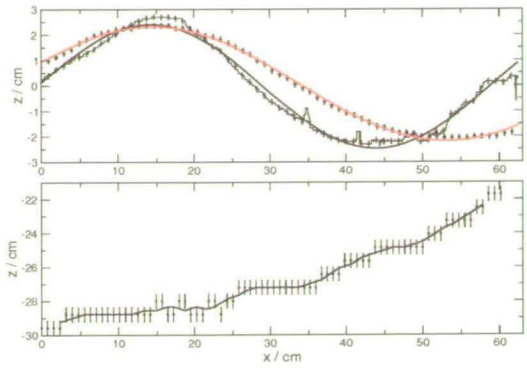

(b) $t = 8.41$s

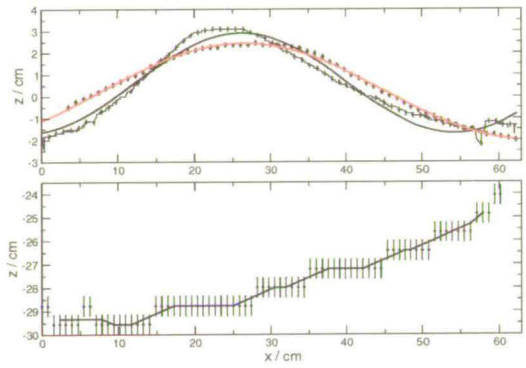

(c) $t = 8.96$s

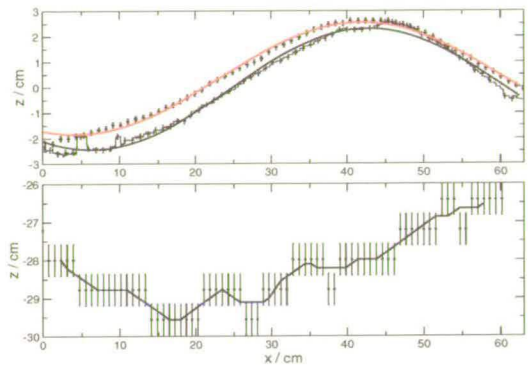

(d) $t = 9.51$s

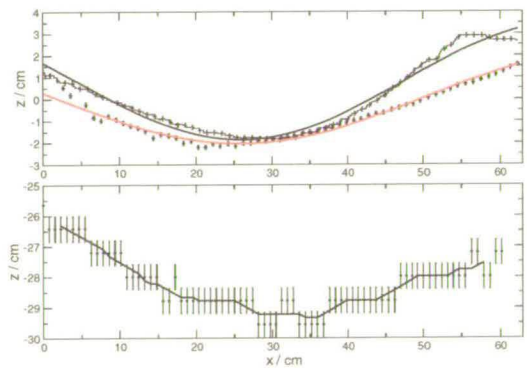

(e) $t = 10.06$s

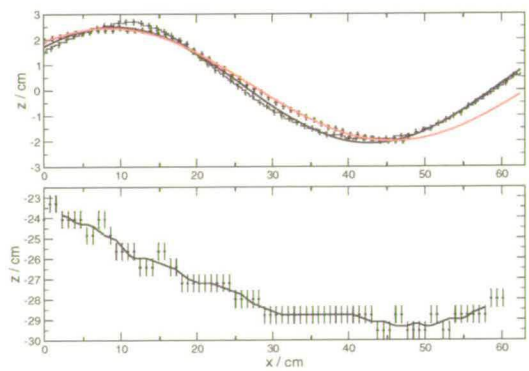

(f) $t = 10.61$s

(See caption next page)

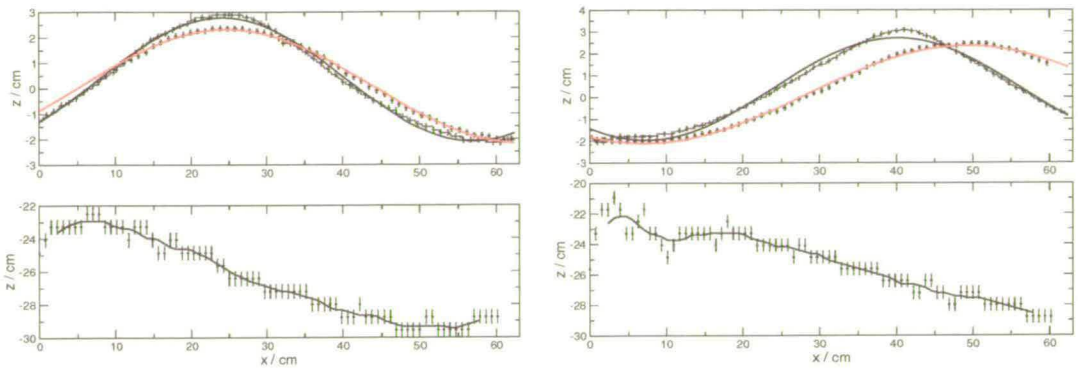

(g) $t = 11.16$s (h) $t = 11.71$s

Figure 4.27: Graphs of surface wave $2a_S/\lambda_S = 0.059$, $\omega_S = 9.03\text{rad.s}^{-1}$ profile (upper) and large amplitude internal solitary wave profile (lower) for a stratification where $h_1/h_2 = 6.39$ and $\Delta\rho/\rho_2 = 4.38\%$. First order linear theory is fitted to the surface wave profiles (black line: interaction data, red line: surface wave profile in the absence of the solitary wave).

the context of the PLIF surface wave - solitary wave interaction experiments.

Vector maps of the interaction flow fields for a surface wave train $2a_S/\lambda_S = 0.059$ and $\omega_S = 9.03\text{rad.s}^{-1}$ in each of the stratification configurations considered, $h_1/h_2 = 3.58$ and $h_1/h_2 = 6.39$, are shown in figures 4.28 and 4.29 (a) respectively. Both vector maps have been selected to show the trough of the large amplitude solitary wave. The vector maps in the adjacent figures 4.28 and 4.29 (b) show the linear superposition of the vector maps obtained from the individual DPIV experiments on both non-interacting wave types for each stratification configuration; that is the linear superposition of figures 4.3 (b) and 4.18 (a) is shown in figure 4.28 (b), whereas the linear superposition of 4.7 (b) and 4.18 (b) is shown in figure 4.29 (b). Horizontal (blue lines) and vertical (red lines)

isovelocity contours have been superimposed on each map at intervals of 7cm.s^{-1} and 4cm.s^{-1} respectively, in figure 4.28, and at intervals of 5cm.s^{-1} and 2cm.s^{-1} respectively, in figure 4.29.

For the linear superposition, both the individual solitary wave and surface wave vector maps were appropriately shifted in order to ensure that the non-interacting surface and solitary wave profiles matched, to the nearest grid unit, the position of the profiles in the interaction vector maps (figures 4.28 and 4.29 (a)). Consequently, some velocity information has been lost at the edges of the maps. This is particularly noticeable in figure 4.29(b).

Qualitatively, similar features can be seen in the maps obtained from the interaction investigation and in those of the linear superposition. In figure 4.28, the isovelocity contours indicate that in the interaction case (a), the velocities are greater than in the linear superposition case (b) both near the surface and at the interface. In figure 4.29, however, the velocities are more similar at the interface, but are greater in the interaction case (a) near the fluid surface.

To assess the magnitude of the velocity difference between the interaction and linear superposition cases, the interaction velocity field was subtracted from the corresponding linear superposition field. The resulting vector maps showing the difference in the velocity fields, illustrated in figures 4.28 and 4.29, are given in figures 4.30 and 4.31 respectively. Contours of absolute non-dimensional horizontal velocity difference, $|\Delta u/c_0|$, are superimposed on the plots in figures 4.30 and

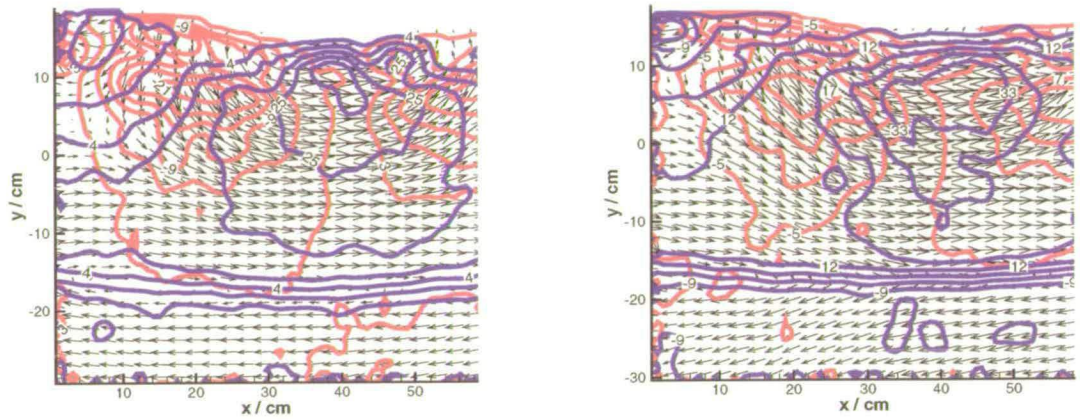

(a) Interaction (b) Linear Superposition

Figure 4.28: Vector maps showing isovelocity contours for the interaction experiment; $h_1/h_2 = 3.58$, $a/h_2 = -1.16$, $2a_S/\lambda_S = 0.059$ and $\omega_S = 9.03\text{rad.s}^{-1}$ (a) and a linear superposition of the individual surface wave and solitary wave velocity fields (b).

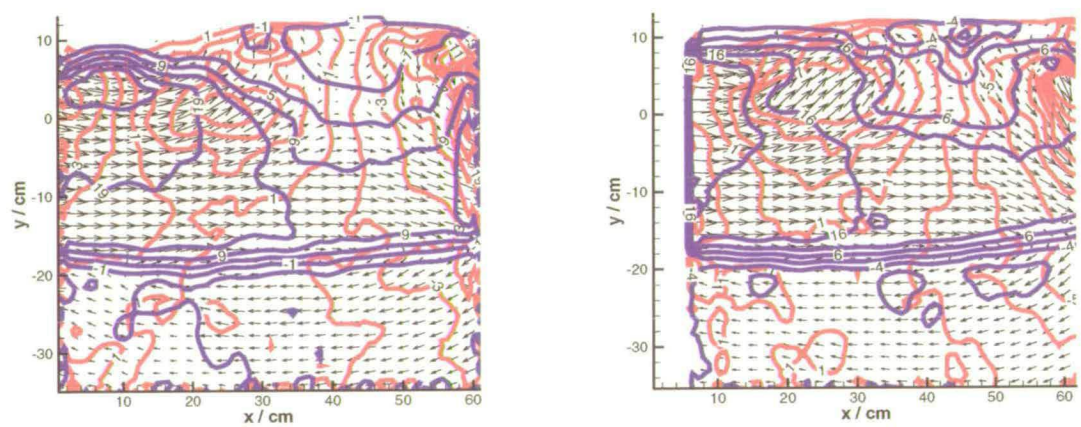

(a) Interaction (b) Linear Superposition

Figure 4.29: Vector maps showing isovelocity contours for the interaction experiment; $h_1/h_2 = 6.39$, $a/h_2 = -1.95$, $2a_S/\lambda_S = 0.059$ and $\omega_S = 9.03\text{rad.s}^{-1}$ (a) and a linear superposition of the individual surface wave and solitary wave velocity fields (b).

4.31 (a), whereas contours of absolute non-dimensional vertical velocity difference,

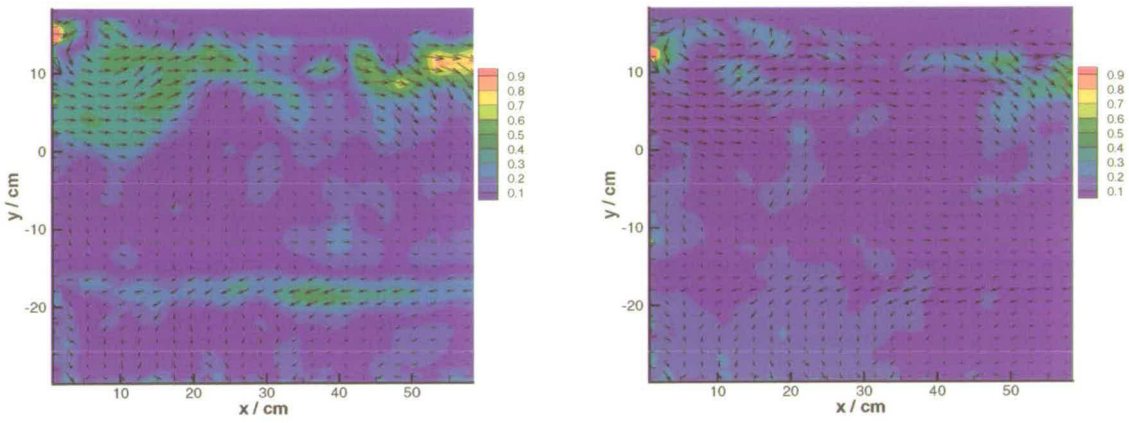

(a) $|\Delta u/c_0|$ (b) $|\Delta v/c_0|$

Figure 4.30: The difference between the measured interaction velocity field shown in figure 4.28 (a) and the linear superposition shown in figure 4.28 (b). Contours of absolute velocity difference, $|\Delta u/c_0|$ (a) and $|\Delta v/c_0|$ (b), are also shown.

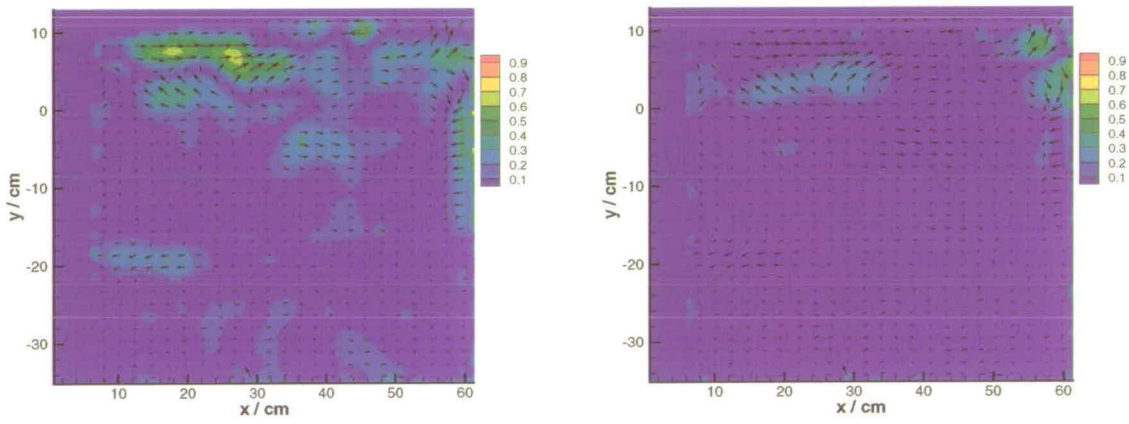

(a) $|\Delta u/c_0|$ (b) $|\Delta v/c_0|$

Figure 4.31: The difference between the measured interaction velocity field shown in figure 4.29 (a) and the linear superposition shown in figure 4.29 (b). Contours of non-dimensional absolute velocity difference, $|\Delta u/c_0|$ (a) and $|\Delta v/c_0|$ (b), are also shown.

$|\Delta v/c_0|$, are plotted in figures 4.30 and 4.31 (b).

The solitary wave generated in the interaction experiment (figure 4.28 (a)) was of smaller amplitude than that generated to produce the linear superposition plot (figure 4.28 (b)). As a result, the two wave shapes do not match exactly. Correspondingly, this difference is highlighted in the $|\Delta u/c_0|$ contours in figure 4.30 (a). In figure 4.31 (a), where the stratification characteristics in the interaction and non-interaction amplitudes were more similar, this feature is not apparent. Instead, however, bands of higher absolute horizontal and vertical velocity difference can be seen at the right and left edges of the vector maps. These are caused by a larger shift in the individual surface wave and solitary wave vector maps used to generate figure 4.29 (b). Despite the larger horizontal velocity difference seen in 4.30 (a) in the interfacial region, overall, the difference in the velocity fields is small in both stratification set-ups. The greatest changes appear to be associated with the horizontal velocity field, most particularly in the upper fluid layer. The largest horizontal velocity differences are found just below the fluid free surface. The vertical velocity differences appear to be more uniform over the fluid depth, again with the largest differences occurring just below the free surface.

Figure 4.32 shows the horizontal velocity profiles versus non-dimensional depth, y/h_2, taken at a wave crest (red data points) and/or at a wave trough (blue data points) for the four interaction cases investigated (table 4.8). The crests and troughs selected are those closest to the maximum depression of the solitary wave. For figure 4.32 (b) and (c), both a wave crest and trough were not available.

The initial conditions listed in table 4.8 are used in the fully nonlinear numerical method [30, 28] to obtain the theoretical velocity profile (black line) for a non-interacting single solitary wave (section 4.3.2, figure 4.11). In each graph, the linear superposition of the numerical method prediction and surface wave linear theory (section 2.2) is also plotted, for both a wave crest (red line) and a wave trough (blue line).

As it is not clear from the wave profiles whether the solitary wave shapes undergo any distortion, the amplitude values listed in table 4.8 are, in effect, only an approximation to the real amplitude of the solitary wave. A comparison of the amplitude values of the solitary waves generated here (table 4.8) with the amplitudes of the solitary waves previously discussed (section 4.3.2, table 4.4) reveals that, in figure 4.32 (a), (b) and (c), the interacting solitary wave non-dimensional amplitudes are smaller than their non-interacting internal wave counterparts. This is probably caused by differences in the initial stratification parameters (tables 4.4 and 4.8), which although similar were not identical, rather than modulations of solitary wave amplitude. In particular, the depth layer ratios, h_1/h_2, for the velocity profiles in figure 4.32 (a), (b) and (c) were smaller. This was due to a slightly faster fill-rate of the fresh water fluid layer. Consequently, the top layer depth was larger, yielding a smaller non-dimensional amplitude, a/h_2, for the same volume of water, V, added behind the sliding gate. A comparison between the percentage change in the values of h_1/h_2 in both experiment sets and the corresponding change in the values of a/h_2 verifies this.

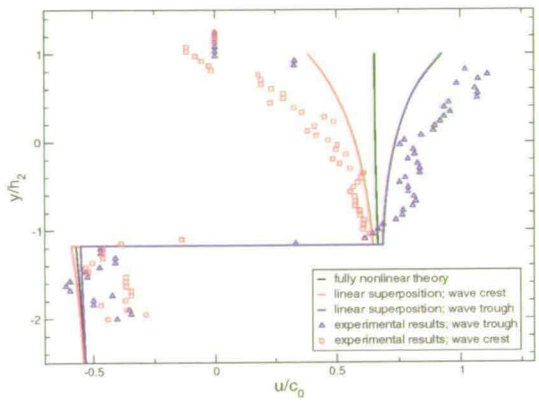

(a) $h_1/h_2 = 3.8$, $a/h_2 = -1.17$, $2a_S/\lambda_S = 0.023$

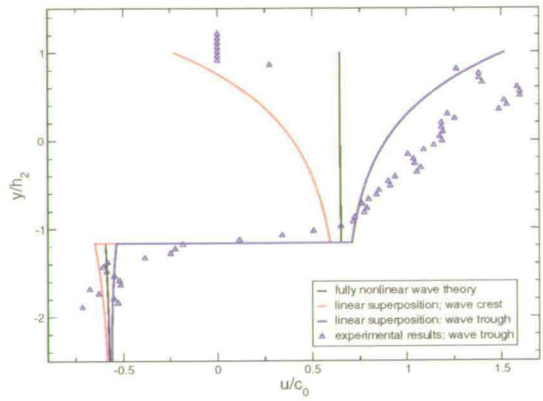

(b) $h_1/h_2 = 3.58$, $a/h_2 = -1.16$, $2a_S/\lambda_S = 0.059$

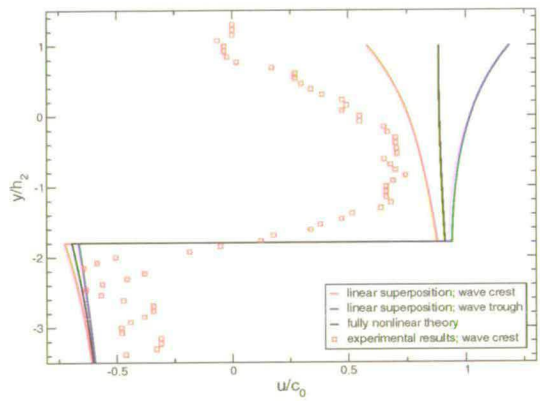

(c) $h_1/h_2 = 5.96$, $a/h_2 = -1.8$, $2a_S/\lambda_S = 0.023$

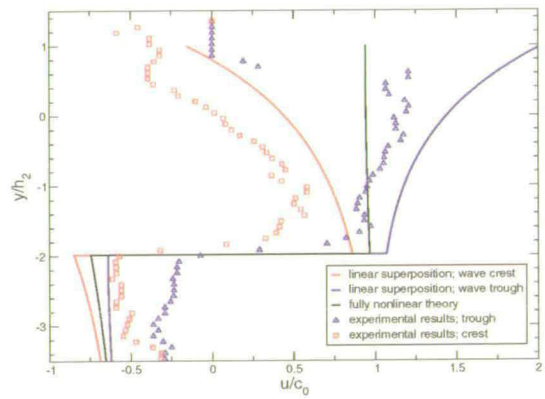

(d) $h_1/h_2 = 6.4$, $a/h_2 = -1.95$, $2a_S/\lambda_S = 0.059$

Figure 4.32: Horizontal velocity profiles at a wave crest (red data points) and/or trough (blue data points) closest to the maximum depression of the solitary wave. The fully nonlinear theory for the single non-interacting solitary wave case is plotted (black line). The linear superposition of linear surface wave theory and the fully nonlinear method is shown for both a wave crest (red line) and trough (blue line).

Furthermore, it was found that, for the errors on the amplitude measure quoted for this work, the maximum change in the non-dimensional horizontal velocity prediction is $\Delta(u/c_0)|_{y>a/h_2} \approx 1\%$ for the velocities in the top layer for all four solitary waves. The change in horizontal velocity in the lower layer, $\Delta(u/c_0)|_{y<a/h_2}$,

is slightly larger, between 2% and 4%. Nevertheless, as all the velocity measurements show a much greater difference from the theoretical linear superposition predictions than these error bounds, the accuracy of the amplitude measurement is not considered to affect the outcome of the comparisons made here.

Whereas the fully nonlinear theory [30, 28] assumes a step-like density profile between the two fluids (section 4.3.2), the finite width of the interface in the experiments is highlighted in the measurements by the velocity gradient across it. Nevertheless, qualitatively, the plots follow the same form as the theoretical linear superposition. In concurrence with the observations made above (figures 4.30 and 4.31), there exists an increase in the fluid velocities near the free surface for both the experimental and theoretical results. The magnitude of the velocities with depth are systematically greater than the linear superposition predictions in all but one case (figure 4.32 (d), surface wave trough). It was for this solitary wave - surface wave interaction configuration (figure 4.27) that the maximum deformation of the surface wave profile was found, namely where the surface wave steepness, the depth layer ratio and the non-dimensional amplitude of the solitary wave were greatest. It could be, therefore, that this particular profile highlights nonlinearities in the velocity field, manifested at the free surface as a surface wave shape skewing.

4.5.3 Conclusions of the surface wave - internal wave interaction DPIV study

The interaction between an internal solitary wave of depression and a small amplitude progressive surface wave train was investigated using DPIV. The literature review (section 2.5.2) indicated that little work has previously been undertaken in this field. In particular, the novelty of this study lay in the investigation of large amplitude solitary waves ($a/h_2 < -1$) and the use of a non-intrusive full-field measuring technique (DPIV).

The work followed on from the initial DPIV investigations on single internal solitary waves and small amplitude surface waves (sections 4.3 and 4.4). The same experimental facilities were used. In this way, considering differences in the stratification initial set-ups and their effects on the resulting velocity fields, the interaction experimental results could be compared to those obtained in the individual solitary wave and surface wave investigations.

The waves approached each other from opposite ends of the tank, such that the angle between their direction of propagation was $\phi = \pi$. Single solitary waves were generated in two different stratification regimes, $h_1/h_2 \approx 4$ and $h_1/h_2 \approx 6$. Two surface wave amplitudes of the same wavelength were employed, such that $2a_S/\lambda_S = 0.023$ and 0.059. The wave profiles, in particular, were seen previously (section 4.4.2) to be described well by surface wave linear theory.

Progression of the solitary wave through the measurement area was tracked by determining the position of zero horizontal velocity within the interfacial region. Surface wave profiles were also obtained. In all cases, amplitude and wavelength modulation of the surface waves were observed.

Quantitative comparison with predictions from the Longuet-Higgins and Stewart (LHS) theory (section 2.5.1) was not possible for two reasons. Firstly, the theory relies on first order KdV theory for the determination of the solitary wave characteristics. It was seen (section 4.3.2) that this approximation did not provide a good description of the solitary waves investigated in this work. Secondly, the LHS theory requires that the length scales of the surface waves be much smaller than that of the solitary wave. This was not the case in the experiments performed here. Nevertheless, analysis of the surface wave modulation showed that the LHS predictions were met qualitatively. That is, the amplitude of the surface wave increased and its wavelength decreased. Where the initial wave steepness was smallest, the surface wave shapes were found to be well described by surface wave linear theory, despite the modulation effects. In contrast, for the larger wave steepness, distortion of the wave shape from a sinusoidal profile was evident, being most pronounced for the largest non-dimensional solitary wave amplitude and layer depth ratio. The skewing experienced by the surface wave train may depend on the solitary wave "phase" or, equivalently, with distance from the maximum depression of the wave. No reports of this observation seem to have been made by previous authors [33, 32]. Difficulties in detecting any distortion

of the solitary wave shape will be further discussed in section 5.3. A larger data sample would be required to parameterise the results and establish the relationship between surface wave amplitude or wavelength modulation and solitary wave "phase". Possible extensions to the present case studies will be discussed further in section 6.4.

Vector maps and velocity profiles of the interaction flow field were compared to the linear superposition of solitary wave and surface wave velocity field measurements (sections 4.3 and 4.4) and to a linear superposition of solitary and surface wave theoretical predictions, respectively. Similar features were identified in both velocity fields, although the horizontal velocities in the region below the fluid free surface were larger in the interaction cases. This was reflected in the plots of velocity profile, where qualitative agreement between experiment and theory was found except where the greatest surface wave shape skewing was observed. These differences were attributed to nonlinearities in the velocity field, which were manifested at the fluid free surface as a distortion to the surface wave profile. Further investigation of this is needed.

4.6 Summary

The aim of the work presented here was to investigate the interaction between a single internal solitary wave of depression, propagating in a two-layer stratifi-

cation, and a train of progressive monochromatic small amplitude surface waves using Digital Particle Image Velocimetry (DPIV). To the author's knowledge, such an investigation using this particular measuring technique has not been performed before. Previous work on the subject [33, 32] has been done using small amplitude solitary waves. In contrast, in the present study, large amplitude solitary waves, that is waves with amplitudes greater than the depth of the top fluid layer, are investigated.

The goal of the work presented in the first half of this chapter was to obtain characteristic velocity data for both internal solitary waves (section 4.2) and surface wave trains (section 4.4), within the constraints imposed by the experimental facilities. This provided a set of reference measurements, which could be compared to the subsequent interaction data sets, where solitary waves and surface waves with similar characteristics were employed. The second half of the chapter (section 4.5) focussed on the DPIV investigation of interaction processes resulting from a progressive surface wave train passing over a large amplitude internal solitary wave, whose direction of propagation was opposed to that of the surface wave. In all the experiments, the results were compared to the appropriate theory. In particular, the interaction investigation yielded a number of interesting phenomena, which, to date, have not been reported.

Hence, DPIV studies were performed separately on

- large and small amplitude internal solitary waves of depression, propagat-

ing in a brine - fresh water two-layer fluid, generated by a sliding gate mechanism [44, 29]

- small amplitude progressive surface wave trains, generated by a computer controlled hinged wave paddle
- a small amplitude progressive surface wave train passing over a single large amplitude solitary wave in a brine - fresh water two-layer fluid

Overall this study has demonstrated that DPIV can be successfully applied to the study of two-layer (brine - fresh water) fluid flow. Even within the limitations of the available data acquisition system, which were in the first instance identified and subsequently overcome, the technique was seen to yield quantitative and qualitative velocity information. This provided encouraging initial results, which indicates that it would be worthwhile extending the present study in future investigations. This will be discussed further in chapter 6.

Chapter 5

The Interaction of a Surface Wave Train and an Internal Solitary Wave: A PLIF Investigation

5.1 Introduction

In this chapter, Planar Laser Induced Fluorescence (PLIF) experiments, performed on single internal solitary waves propagating at a brine - fresh water interface, are presented. As in chapter 4, the study is extended then to look at

internal solitary wave - small amplitude wave train interactions. It appears, from a review of the literature (sections 2.3.4 and 2.6), that work has yet to be done in this field.

The investigation of single internal solitary waves of depression in a brine - fresh water two-layer stratification is presented in section 5.2. The consequences of various drawbacks of the experimental apparatus, such as variations in intensity across the width of the laser light sheet, are identified and their effect on the raw images of the flow is discussed. An assessment of the most suitable analysis approach is made in the light of these drawbacks (section 5.2.2). The solitary wave amplitudes and wave shapes are determined from the post-processed images. The density profile and a measure of the density interface width, within the soliton waveform, is obtained. The suitability of the PLIF technique to accurately measure density variations in the internal solitary wave flow field in a brine - fresh water stratification is also considered.

A PLIF investigation into the interaction between a single internal solitary wave of depression with a small amplitude progressive surface wave train is presented (section 5.3). The image analysis techniques follow the same principle as those developed in the PLIF work on single internal solitary waves (section 5.2.2). Analysis of the results (section 5.3.2) focusses on assessing changes to the density structure of the stratification, with depth through the fluid, within the solitary waveform.

The aims of this chapter can thus be summarised as follows:

- to assess the ability of the PLIF technique to provide quantitative density information on internal solitary wave flow in a brine - fresh water stratification
- to provide a reference data set against which PLIF solitary wave - surface wave interaction data may be compared
- to assess the instantaneous effect of the solitary - surface wave interaction on the structure of the stratification
- to assess any mixing processes that may occur as a result of the interaction

5.2 Investigations of Single Internal Solitary Waves using Planar Laser Induced Fluorescence

As little, if any, work appears to have been done in this area of research, the primary motivation of the work presented in this section is to assess the ability of Planar Laser Induced Fluorescence (PLIF) technique to be used as a quantitative investigative tool in the study of single internal solitary wave flow in a brine - fresh water stratification. As remarked in [29], the structure of the interface

within the soliton waveform remains unknown. The use of PLIF may reveal the density structure and thickness within the internal wave. The suitability of the PLIF technique to the study of internal solitary waves is therefore considered.

All the PLIF experiments performed throughout this work follow the principles outlined in section 3.1.2. The experimental set-up and method are presented (section 5.2.1). A discussion of the analysis approach and the experimental results then follows (section 5.2.2).

5.2.1 The PLIF Setup and Experimental Method

In this section, the PLIF experimental set-up is presented. The camera settings and timings are outlined and the method involved in performing the experiments is discussed in general terms. The description and discussion of the experimental analysis, involving image post-processing techniques and calibration of the resulting data, however, is left until section 5.2.2.

Two separate experiments were performed on one single large amplitude ($a/h_2 < -1$) and one single small amplitude ($a/h_2 \sim -0.5$) internal solitary wave in a stratification configuration where $h_1/h_2 \sim 6$. The upper layer depth, h_2, was determined, as described in section 4.3.2, using the density profile of the stratification. The wave flume set-up remained as before (section 3.2). Table 5.1 summarises the parameters used.

	small amplitude wave $a/h_2 \sim -0.5$	large amplitude wave $a/h_2 < -1$
H (m)	0.71	0.71
h_1/h_2	6.24	5.82
V (l)	20	80
D (m)	0.4	0.4
$\Delta\rho/\rho_2$	3.57	4.11

Table 5.1: Table summarising the parameters used for each of the two PLIF internal solitary wave experiments.

The basic camera and wave flume set-up of these single solitary wave PLIF experiments remained as for the DPIV solitary wave measurements (section 4.3). The PLIF theory, presented in section 3.1.2 is referred to here. As previously, the PCO Sensicam camera was triggered on the opening of the sliding gate and image pairs were grabbed at the maximum possible frequency (one image every 0.55s). Again, this ensured that as many images as possible were captured as the wave passed the measurement volume. A cut-out filter was placed in front of the lens in order to remove the green laser light and reflections (section 3.1.2). Unlike in the case of the DPIV experiments, here, the ability of the PCO Sensicam camera to grab pairs of images was not important. As the first exposure could be more accurately controlled than the second, only the first image of every pair was used and the timings and shutter set up were selected to optimise the greylevel range of the first image. Care was taken to ensure that the first image was exposed for long enough to obtain the maximum contrast between the dyed saline layer and the upper fresh water layer without blurring.

In the first instance, a stock solution of dye (0.7g of rhodamine powder per litre of brine) was prepared. A known volume of this solution, according to the amplitude of the solitary wave generated, was mixed into the bottom layer of the stratification using the submersible pumps. In all cases, the initial concentration was around 0.01% of the stock solution. Following considerable mixing, the stratification was completed, in the manner described in 3.2.5. Care was taken in the preparation of the stock solution and when adding it to the brine in tank, as the substance is extremely toxic.

In order to assess the relationship between fluorescence intensity, or equivalently, image pixel greylevel, and dye concentration a calibration was performed. In each of the individual solitary wave PLIF experiments, a sample of the initial concentration of dye in the salt water layer was removed from the tank and diluted in 10% increments. The samples were placed in a series of sealed vessels in order of increasing concentration and were then suspended in a supporting cage in the path of the laser light sheet. The flume was filled with brine of the same density as in the experiment, such that the attenuation of the laser light with distance from the source could be taken into account. Care was taken to ensure that the vessels were positioned in the lower region of the measurement volume, which, during the experiment, would contain dyed fluid rather than fresh water. The resulting fluorescence intensity from the samples was recorded using the same exposure timings, camera position and set-up as for the wave experiments.

On completion of each experimental run, the dye in the tank was mixed, again using the submersible pumps, into both fluid layers so as to obtain a uniform concentration of dye across the measurement volume. Multiple images of this uniform dye concentration were then taken with the same camera exposure settings as used for the main experiment. The resulting images were then smoothed and averaged in order to obtain a representative background intensity. A graph of average background intensity with j, image depth, where $(i, j) = (0, 0)$ is the top left hand corner of the picture, is shown in figure 5.1. The reflections at the water surface are characterised by a large increase in pixel greylevel at around $j = 200$pxl, such that the region $0 \leq j \leq 200$pxl is above the water surface (in air). A second order fit to the data for $j > 200$pxl is also shown (red line) and has been extrapolated to $j = 0$pxl. Using the quadratic coefficients, the pixel values in the image, in the region above the water surface, were recalculated to remove the artificial brightness. This technique is particularly useful for the analysis of the PLIF surface wave - internal solitary wave interaction experiments where the position of water surface changes from image to image due to the surface wave train (section 5.3). The interpolated background image was then used to normalise the raw images from both the experiment and the calibration following the regime outlined in section 3.1.2.

The normalised calibration images yield a series of "patches" of increasing greylevel, corresponding to increasing dye concentration on a background of small and constant greylevel. The intensity of each pixel within each of these patches,

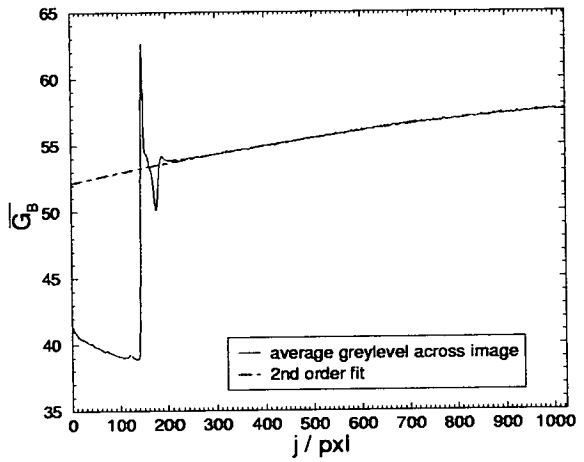

Figure 5.1: An example of a plot of average background greylevel, $\overline{G_B}$, with image width, j. The quadratic fit to the data for $j > 200$pxl and the extrapolation to $j = 0$pxl (red line) is also shown.

once the images had been normalised, was averaged to yield a representative greylevel for each concentration value. The relationship between concentration and recorded fluorescence intensity could then be determined by plotting greylevel against concentration. This will be discussed further in the next section.

5.2.2 PLIF Image Post Processing and Discussion of the Results

The results from the Planar Laser Induced Fluorescence experiments performed on two individual internal solitary waves, one of large amplitude ($a/h_2 < -1$) and one of small amplitude ($a/h_2 \sim -0.5$), in a layer depth ratio of $h_1/h_2 \approx 6$, are presented. As no work appears to have yet been reported in this field, the experimental results are first considered for their ability to produce reliable and

quantitative information about the density distribution within the solitary waveforms. The second goal of these experiments, as in the case of the DPIV experiments presented in section 4.3.2, is to provide a set of reference measurements for the PLIF surface wave - internal solitary wave interaction experiments, presented in section 4.5.2. In particular, the investigation focusses on the accuracy with which the density interface can be measured as the wave passes the measurement volume and the structure of the interface within the depression of the solitary wave. Throughout the discussion of the results, when images are referred to, they are assumed to be normalised with respect to the interpolated background image unless otherwise stated.

For each of the two solitary wave experiments discussed here, a reference image of the still interface was taken, prior to the sliding gate being removed. Figure 5.2 shows a graph of the average pixel greylevel, $\overline{G_N}(j)$, where N refers to the fact that the pixel intensities have been normalised, at two different positions in the reference image, $i_1 = 300$pxl and $i_2 = 1065$pxl, for the large amplitude wave experiment. The averages were performed over a section of the images, equivalent to a distance of ~ 2.5cm, from i_1 and i_2 respectively. Averaging over a section of this width was adequate to remove the noise from spurious pixel greylevel values whilst remaining much smaller than the wavelength of either the small or large amplitude solitary wave. Running averages of each profile are also shown (black lines) and can be seen to follow closely the shape of the mean intensity profiles, whilst reducing the noise in them. As a result, running average plots of

the intensity profiles will be used throughout the PLIF studies.

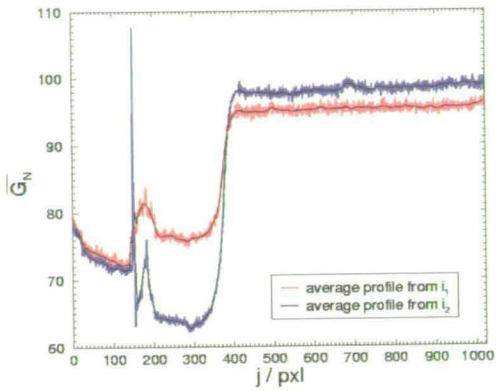

Figure 5.2: Average pixel intensity profiles with image depth, j, for the reference image of the large amplitude solitary wave experiment. The profiles were found by averaging the normalised greylevels at two different horizontal image locations, i_1 and i_2. Running averages (black lines) over each plot are also shown.

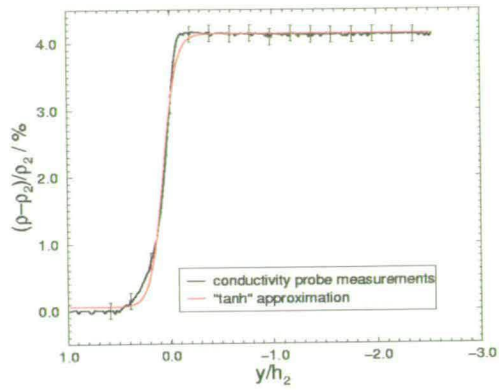

Figure 5.3: Density profile of relative change in density in percent from fresh water for the stratification used in the large amplitude solitary wave PLIF experiment. The "tanh" approximation is also shown.

Both profiles in figure 5.2 follow the same form and clearly show the two layers of fluid of different density in the stratification, separated by a sharp interface. The water surface can be located by the sharp peak in the graphs at $j \sim 150$pxl. Secondary reflections of the free surface are also apparent between $j \approx 150$pxl and $j \approx 200$pxl.

In each profile, the saline layer is characterised by a higher greylevel $\gtrsim 90$ for $j >$ 450pxl. It can be seen, however, that the greylevel in this region is not constant but increases slightly with increasing j, or equivalently with depth through the fluid. This implies that the dye concentration was not constant but increased slightly with depth. It could be inferred from this therefore, that the salinity is

also increasing with depth.

The plot of non-dimensional density, $(\rho - \rho_2)/\rho_2$, in percent, versus y/h_2, non-dimensional depth, in figure 5.3, was obtained from the micro-conductivity probe measurements, prior to removing the gate and at a location within the measurement area. The graph shows that the density in the lower layer is constant within the depth of fluid considered in the image, around 35cm below the density interface, such that the increase in dye in this region cannot be attributed to an increase in density. Instead, the intensity increase in the lower region of fluid demonstrates the difficulty encountered in uniformly mixing even a small quantity of a high concentration tracer dye solution into a large volume of fluid (of the order of 2000l). As one of the aims in this work was to assess the thickness of the interface, it was important that the dye was as homogeneously mixed as possible throughout the depth of the saline fluid prior to the experiment. This is because if any mixing occurred during the experimental run, it would cause changes to the initial vertical distribution of dye. A significant gradient in the intensity profile over the saline layer before mixing would result in a greater uncertainty in the estimation of the interfacial width. This would render comparisons with measurements of the interfacial width post-mixing more difficult to interpret. Even though the raw images were corrected for the horizontal variations in intensity across the laser light sheet and attenuation of the laser light through the fluid depth, this background correction procedure could not account for vertical changes in intensity caused by non-uniform initial dye distribution.

Although no dye was mixed into the top layer of fluid during the stratification preparations, not only is the average greylevel in this region not close to 0, but it is also not the same at the two image locations (figure 5.2). The average pixel greylevel in the top layer was not constant over the image width. The two profiles shown were taken in the lightest and darkest regions of the image respectively. The non-zero greylevel values in this region can be explained by the filling method (section 3.2.5). Floating sponges were used to slowly drip-feed the fresh water layer onto the dyed saline solution. It is likely that a very small amount of dye was drawn up from the bottom fluid as the top layer was filling. Thus, the top layer of the stratification, although consisting of fresh water, was not dye-free prior to the opening of the sliding gate.

In the raw images, the non-uniformities in the laser light sheet, caused by dust and variations in the silvered coating on the parabolic mirror, are particularly apparent in the saline layer, where the dye concentration is strongest. They are visible across the raw images as vertical bands of higher or lesser greylevel such that for a constant dye concentration, the intensity of light recorded by the camera was not constant. The image normalisation process, described in the previous section 5.2.1, is relatively effective at removing these variations in light intensity in the saline layer, $j \gtrsim 450$pxl. In this region, the difference in pixel contrast between the profiles is only 2-3 levels. In contrast, in the upper fluid layer where the concentration of dye is much less, the normalisation process tends to reinforce the light sheet fluctuations, rather than reduce them. Thus,

for any fixed vertical coordinate $j \lesssim 350$pxl, there exists variations in average pixel brightness of around 10 or so greylevels across the width of the normalised images. Reference to the density profile in figure 5.3 indicates that the upper layer of the stratification was constant in density and was equal that of fresh (tap) water. Hence, the top layer of fluid was neither saline nor non-uniform in density prior to the wave generation.

The intensity variations in the top layer of fluid in the normalised images were reduced by linearly scaling them. If the brightness of a normalised pixel within a column i was less than the average brightness of the whole image, then the greylevel of the pixel was scaled by this value. The new greylevel of the pixel is denoted $G'(i,j,t)$ and the subscript N, indicating that the pixel was previously normalised, has now been dropped. Figure 5.4 shows both the original intensity profile, $\overline{G_N}(j)$, from location i_2 in figure 5.2, and the recalculated intensity profile, $\overline{G'}(j)$. The graph shows that although the greylevel in the lower layer of fluid and the profile over the density interface remain the same, the greylevel in the fresh water layer has been increased. Thus, the scaling effectively removes some of the variations in greylevel in the top layer of fluid by collapsing the intensity profiles onto a representative greylevel of this layer. This process nevertheless preserves the characteristic shape of the intensity change across the interface and the greylevel value of the saline layer. Although the variation in greylevel across the normalised images was not removed completely by this transformation, it was improved significantly, reducing the variation to 3 or 4 greylevels. It was therefore

applied systematically to all images.

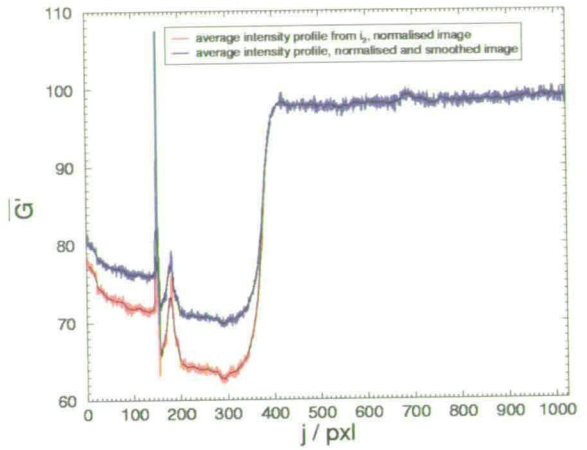

Figure 5.4: Graph showing the average intensity profile over an image width of 50pxl at $i_2 = 1065$pxl in the reference image of the large amplitude wave, before and after linearly scaling the image greylevels. The running averages of both profiles are also shown (black lines).

The horizontal variations in greylevel across the normalised images demonstrate the drawback of using a scanning mirror - parabolic mirror laser light sheet generation system (section 3.2.4) when a light sheet of constant intensity across the entire measurement area is required. As the parabolic mirror is a silvered perspex strip, it cannot be cleaned and is damaged easily. A light sheet perfectly uniform in intensity is, therefore, hard to achieve. Where a large measurement area is necessary, this drawback could be avoided in future by using a set-up similar to that used by Schlicke [81] where a rotating octagonal mirror is used to sweep a collimated laser beam through a fan-shaped 90^o arc.

The calibration described in the previous section was repeated for every PLIF experiment, as the initial dye concentration in the bottom layer could not be

guaranteed to be identical each time. The initial sample was taken from the dyed saline layer as far as possible from the surface, before the fresh water layer of the stratification was added. The calibrations were all carried out under similar conditions, without altering the magnification of the camera system, the laser power or the position of the supporting cage within the measurement area. Figure 5.5 shows the calibration results for both the large amplitude (a) and small amplitude (b) solitary wave experiments. Average greylevel is plotted against concentration of the initial dye solution in the lower layer of the stratification. As only five calibration vessels could fit across the width of the measurement area, the samples were thus imaged in two parts; from 100% to 60% and 50% to 10% of the initial concentration in the lower layer. The graph in figure 5.5 (a) follows a linear trend, whereas in (b) this trend is not apparent. Instead, the trend appears to be linear over both concentration ranges imaged seperately (100% to 60% and 50% to 10%).

Contrary to the theory, neither graph goes through the origin. However, this can be explained by the high sensitivity of the PCO Sensicam camera which is designed specifically to work in low light levels. The error bars are representative of the variation found over multiple calibration images of an experiment, grabbed consecutively within a time period of a few seconds and subsequently normalised by the background image (5.2.1). It had been noted [87], in recent PLIF experiments involving surface films, that the use of tap water, as opposed to distilled water, lead to discrepancies in the fluorescence - dye concentration

relationship, disturbing the linearity of the plot. It is evident that in this work, the use of distilled water in the preparation of the stratification was not possible, due to the large volume of fluid involved. In each experiment, the calibration vessels were always placed in the same order within the support. The nonlinearity could therefore be an artefact of the horizontal intensity variations in the laser light sheet. The recorded fluorescence could be artificially enhanced or reduced by these defects as image normalisation did not wholly remove the intensity non-uniformities.

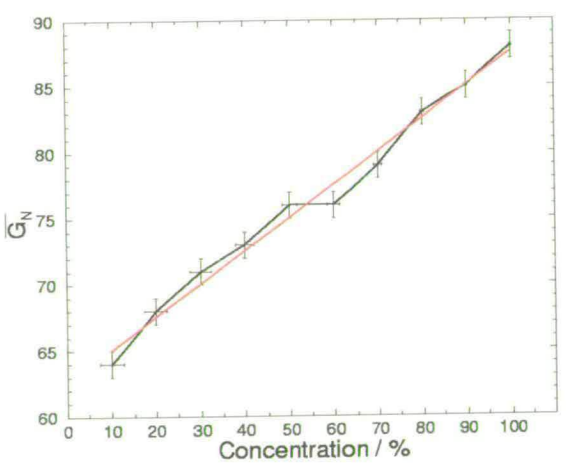

(a) Large amplitude solitary wave experiment

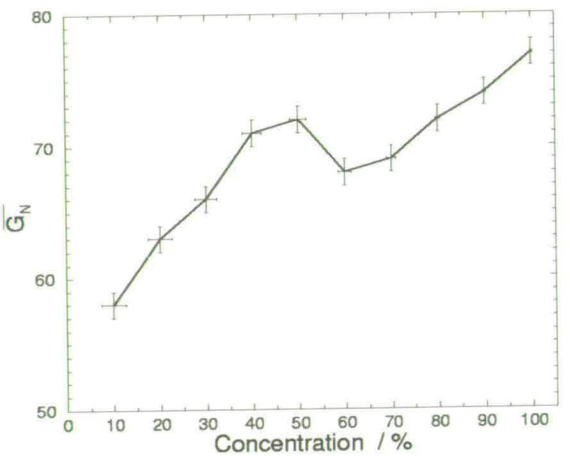

(b) Small amplitude solitary wave experiment

Figure 5.5: PLIF Calibration: graphs of average greylevel, $\overline{G_N}$, versus concentration of the initial dye solution in the lower layer of fluid in the stratification for each of the large and small amplitude internal solitary wave PLIF experiments respectively

A common characteristic of both calibration graphs in figure 5.5 is the limited greylevel range over the concentration values. The pixel intensity range covers around 20 greylevels from a possible 256 and the pixel intensity jump between

each 10% increment in concentration is around 3 to 4 greylevels. This limited range reduces the resolution of the PLIF images such that small changes in fluorescence intensity cannot be detected. The salinity of the lower fluid layer resulted in strong attenuation of the laser light through the fluid, resulting in a reduction in fluorescence. The attenuation could have been decreased by using a smaller amount of salt in the preparation of the saline solution. This would yield a smaller density difference, $\Delta\rho/\rho_2$, across the interface. The solitary - surface wave interaction experiments (section 5.3), however, required a density difference of the order of that considered here.

In general, the density profile of a two-layer stratification can be approximated well by a hyperbolic tangent, or "tanh", fit (section 2.1.3). Figure 2.1 demonstrated that the typical density profiles encountered in this work do indeed follow this trend. The equivalent "tanh" fit, following equation (2.5) and corresponding to the density profile for the initial stratification for the large amplitude internal solitary wave, is shown in figure 5.3. Again, the approximation can be seen to follow the density profile. Figure 5.6 shows the hyperbolic tangent fit to the running average plots of the two profiles previously shown in figure 5.2 above. In this instance, the ideal "tanh" profile is expressed as:

$$\overline{G'(j)} = \frac{\Delta G'}{2}\left[\tanh\left(\frac{j + J_I}{\Delta j}\right)\right] + G'_{\text{mid}}, \tag{5.1}$$

The fit is applied to the area of the intensity profile about the interfacial region.

The coefficients $\Delta G' = G'_{\max} - G'_{\min}$ and $G'_{\text{mid}} = \frac{G'_{\max}+G'_{\min}}{2}$ such that $G'_{\max}$ is a greylevel value representative of the pixel intensity in the saline fluid layer and $G'_{\min}$ is a greylevel value representative of the pixel intensity in the fresh water layer. Both $G'_{\max}$ and $G'_{\min}$ are derived from the curve fitting process. The coefficient J_I is the displacement of the "tanh" profile in pixels from $j = 0$pxl. The distance in pixels over which there exists an intensity gradient is given by Δj.

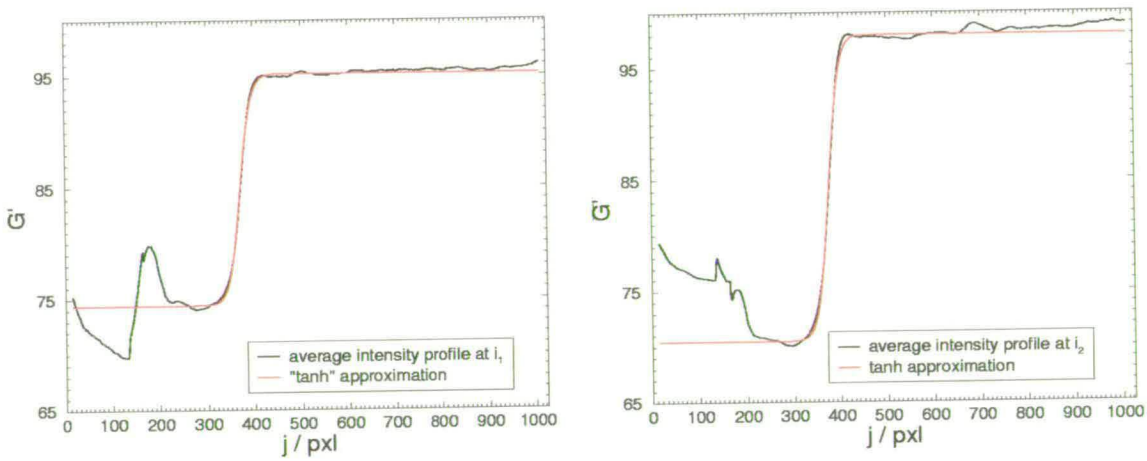

(a) Image location i_1

(b) Image location i_2

Figure 5.6: Intensity profiles $\overline{G'(j)}$ and the corresponding hyperbolic tangent fit given by equation (5.1) for the two images locations in the reference image of the stratification for the large amplitude wave experiment.

In the graphs in figure 5.6, the surface reflections in the fresh water layer, are characterised by a marked increase in greylevel at $j \approx 200$pxl. Similarly, for $j \gtrsim 600$pxl there is a deviation from the tanh fit caused by the increase in dye concentration in the lower layer. Despite the difference in average greylevel in the upper fluid layer, the "tanh" approximation provides a good match to both.

All the intensity profiles shown in the figures above and discussed so far are taken from the large amplitude solitary wave experiment reference image. They are, however, characteristic of all the PLIF experiments performed in this work. It has been shown that some of the variations in greylevel within the PLIF images cannot necessarily be attributed to variations in dye concentration and thus to variations in density. Nevertheless, it is important to be able to relate changes in pixel intensity to changes in salinity quantitatively.

The background fluorescence, present in the upper layer and attributed to the stratification filling technique, not only affected the dynamic range of the pixel intensities in the images, reducing it to 20 to 30 greylevels out of a possible 256, but also inhibited effective mapping of the pixel intensities to dye concentration using the calibration results. The good match between the "tanh" fits (equation (5.1)) and the intensity profiles across the density interface, in both solitary wave experiments, suggests that the relationship between fluorescence and salinity can be assumed to be linear. So long as this is true, changes in greylevel in the post-processed images can be related directly to changes in density via the conductivity profile results, which, taken throughout both the DPIV and PLIF experiments, have been shown to be repeatable.

By matching G'_{min}, the representative greylevel in the upper layer, to ρ_2, the density of fresh water, and G'_{max}, the representative greylevel in the lower layer of the stratification, to ρ_1, the density determined by the micro-conductivity probe

calibration, the intermediate greylevels can be linearly mapped to the intermediate density values across the interface. Equation (2.5) can thus be rewritten in terms of y/h_2, the non-dimensional vertical coordinate, and $(\rho(y/h_2) - \rho_2)/\rho_2$, the non-dimensional density difference, to give

$$\frac{\rho(y/h_2) - \rho_2}{\rho_2} = \frac{\Delta\rho}{2\rho_2} \tanh\left[\frac{(y/h_2 + \eta/h_2)}{\Delta h/h_2}\right] + \frac{\Delta\rho}{2\rho_2}. \tag{5.2}$$

Here, an additional term η/h_2 has been included to describe the depression of the interface due to the amplitude of the solitary wave.

Figure 5.7 (a) and (b) show the non-dimensional density profiles with non-dimensional fluid depth, resulting from scaling the intensity plots presented in figures 5.6 with the micro-conductivity probe measurements. The corresponding "tanh" fits, given by equation (5.2), are also plotted. By matching the greylevels in the upper and lower fluid layers to the appropriate densities, the intensity profiles from figures 5.6 have been successfully collapsed onto a representative density profile. The "tanh" approximations provide a good description of the density plots. Figures 5.8 (a) and (b) show the two equivalent density profiles, calculated under the same conditions, from the same locations i_1 and i_2 in the small amplitude solitary wave experiment reference image. As the camera was not moved between the two experiments, both positions still correspond to areas in the image between which there exists a maximum contrast in greylevel. The same characteristics; surface reflections and slight increase in fluorescence inten-

sity in the bottom layer, can be distinguished here. Nevertheless, in this case also, the "tanh" profile provides a good approximation to the density change over the interfacial region. Moreover, a comparison between the resulting density profiles and the corresponding calibrated conductivity profile (figures 5.7 and 5.8 (c)) shows the shapes of the plots are well matched.

It has been shown that the intensity profiles, taken over two locations, i_1 and i_2, in a reference image of the initial stratification, where there exists a noticeable contrast in greylevel, particularly in the upper fluid layer, result in similar density plots with fluid depth. It has also been seen that these density profiles can be well approximated by a hyperbolic tangent fit given by equation (5.2). The coefficient $\Delta h/h_2$ in the "tanh" approximation can therefore be used as a measure of the interfacial width. If it can be assumed that, for the reference image of the stratification, the interface width is constant over the width of the images, then the variation in width between these two locations provides an estimate of the accuracy of the measure. The variation in the measure of the width between areas of maximum contrast in the images, i_1 and i_2, was found to be 11.9% for the large amplitude solitary wave and 8.7% for the small amplitude solitary wave. This assessment will be useful for the analyses of the PLIF surface wave - internal solition interaction experiments discussed in the next section where the compression and expansion of the interface with surface wave phase will be investigated. It can also be applied to different images within the same experiment to assess the variation in interface width from one image to another.

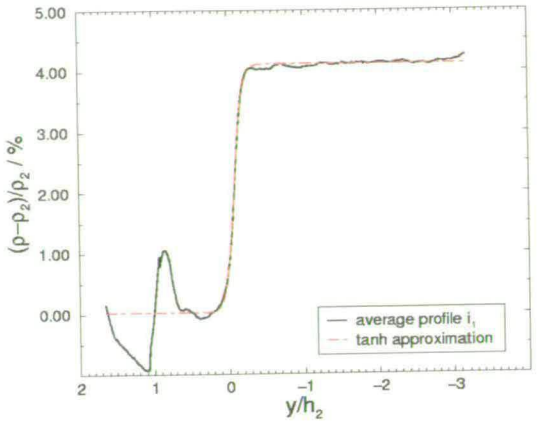

(a) Image location i_1

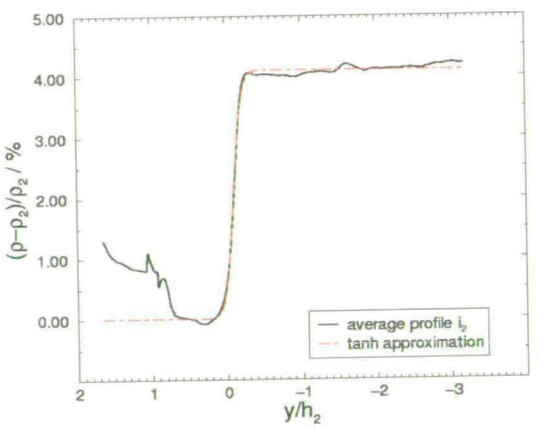

(b) Image location i_2

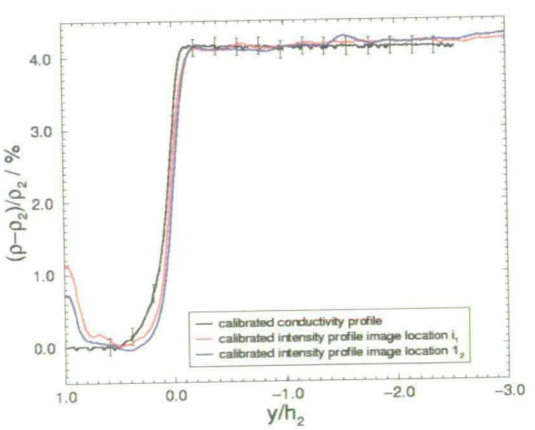

(c) Comparison with the calibrated conductivity measurements

Figure 5.7: Large amplitude wave experiment, quiescent stratification.

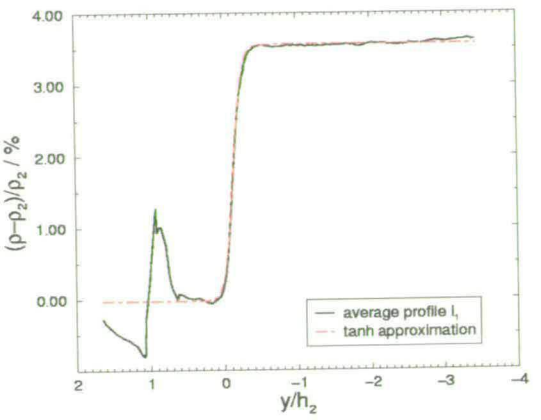

(a) Image location i_1

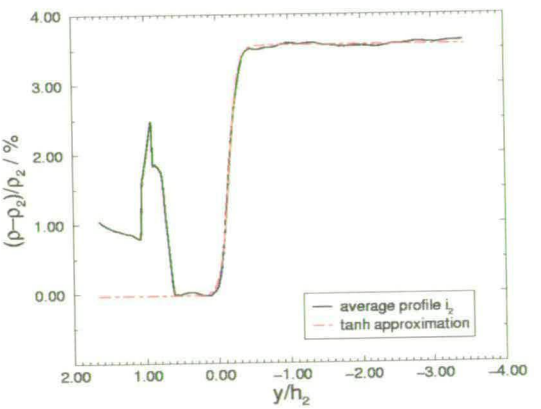

(b) Image location i_2

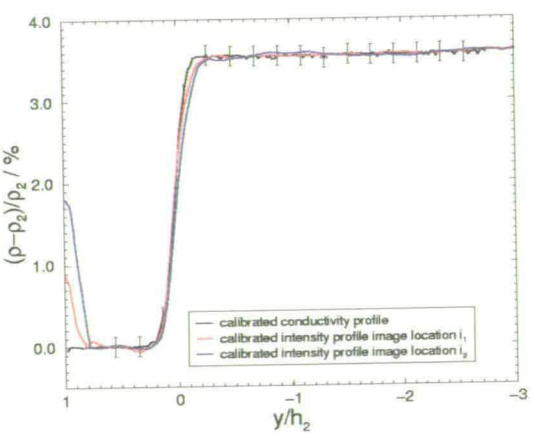

(c) Comparison with the calibrated conductivity measurements

Figure 5.8: Small amplitude wave experiment, quiescent stratification.

The graphs in figures 5.9 and 5.10 are calibrated intensity profiles taken through the maximum depression of the large and small amplitude internal solitary waves, respectively. The images were selected such that the wave trough was located over the locations i_1 at time t_1 and i_2 at time t_2, such that calibrated intensity profiles from two images, between which there exists a maximum contrast in pixel greylevel, could be compared. It was assumed that there was no significant amplitude attenuation over the measurement volume imaged (a distance of < 60cm) [29] and also that the width of the interface through the maximum amplitude of the wave remained unchanged as the wave passed the measurement volume, a reasonable assumption as no mixing between the stratified layers was observed.

The plots show that the interface is no longer centred about $y/h_2 = 0$ but has been pushed down, providing a measure of the solitary wave amplitude. This will be further discussed below. The hyperbolic tangent fits to both profiles are also shown. The sliding gate mechanism does not seem to alter the structure of the interfacial region as the "tanh" curves still provide a good fit to the profiles. This could be indicative of the stable nature of the stratification configurations used in this study (table 4.5) rather than a feature of the solitary wave generation method. For the large amplitude solitary wave, the variation in the estimation of the width from the "tanh" fits to each profile is 27.7%. In this instance, the fit provides a less useful measure of the variation in the width as the profiles are more curved near the fresh water layer and less curved near the saline layer. Nevertheless, the gradient of the "tanh" curve across the interface still provides

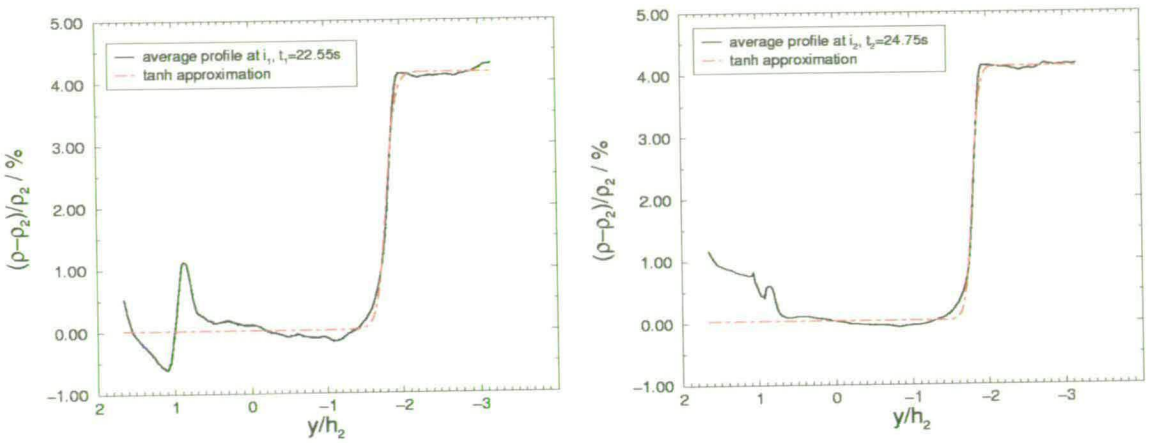

(a) Image location i_1, $t_1 = 22.55$s

(b) Image location i_2, $t_2 = 24.75$s

Figure 5.9: Non-dimensional density plots with depth, y/h_2, obtained from calibrating the intensity profiles from the conductivity probe measurements, for the large amplitude solitary wave. The profiles are obtained from two separate images taken at times $t_1 = 22.55$s and $t_2 = 24.75$s after the gate is opened, through the maximum depression of the wave at positions i_1 and i_2 respectively. The "tanh" fits, from which the width of the interface can be estimated, are also shown.

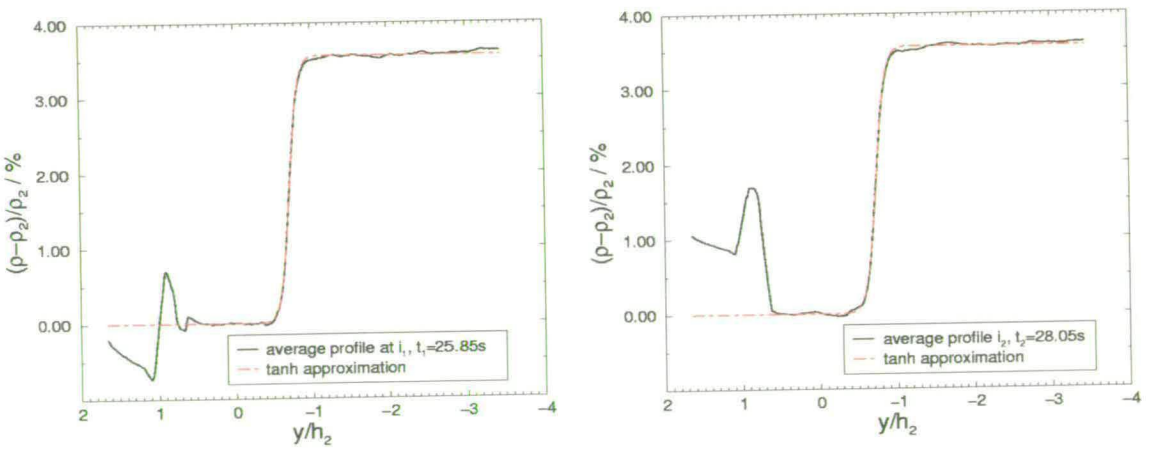

(a) Image location i_1, $t_1 = 25.85$s

(b) Image location i_2, $t_2 = 28.05$s

Figure 5.10: Non-dimensional density plots with non-dimensional depth , y/h_2, obtained from calibrating the intensity profiles from the conductivity probe measurements, for the small amplitude solitary wave. The profiles are taken from two images 2.2s apart through the maximum depression of the wave. The "tanh" fits, from which the width of the interface can be estimated, are also shown.

a measure of the density gradient in this region. The equivalent variation in interface width for the small amplitude solitary wave is more reasonable, being 8.1%.

Table 5.2 summarises the measures of the interfacial widths, $\Delta h/h_2$, for the reference stratification image and through the maximum amplitude of the wave at locations i_1 and i_2 for both the large and small amplitude solitary waves. The larger amplitude wave stratification is associated with a thicker interface than is the small amplitude wave. In all cases, however, it can be seen that the density interface thickness is very small, such that $\Delta h/h_2 \sim 0.1$. Similar analysis of profiles taken at various points across the solitary waveform did not suggest, for the stratification parameters investigated here and within the accuracy of the technique, that there existed any variation in interfacial thickness with solitary wave "phase" (or distance from the solitary wave trough).

wave amplitude a/h_2	reference image $\Delta h/h_2$ i_1	i_2	change in %	maximum amplitude $\Delta h/h_2$ i_1	i_2	change in %	calibrated conductivity $\Delta h/h_2$
-1.8	0.099	0.091	8.8	0.12	0.094	27.7	0.125
-0.64	0.113	0.124	9.7	0.11	0.12	9.1	0.0961

Table 5.2: Table showing the interface widths at the two image locations i_1 and i_2, chosen to obtain the greatest contrast in pixel intensity, in the reference image and through the maximum depression of the wave, for each solitary wave. As the camera position was not changed between the two experiments, i_1 and i_2 are the same in each.

Two other methods of quantifying the interface width were also considered (sec-

tion 2.1.3). These were namely finding the derivative of the profile in the interfacial region and measuring the width at half height, and finding the distance between the coordinates, j, in the profiles where, for instance, $\rho(j) - \rho_2)/\rho_2 = 1.2 \times \Delta\rho/2\rho_2$ and $(\rho(j) - \rho_2)/\rho_2 = 0.8 \times \Delta\rho/2\rho_2$. Both approaches, however, were found to provide no better a measure of the width due to the inherent noise in the intensity profiles. Overall, the smallest discrepancy in the width approximations for each image was achieved using the "tanh" fit approach.

When suitably calibrated, the normalised and scaled image intensity distribution, $G'(i, j, t)$, which characterises the change in density over the interfacial region seen in figures 5.7, 5.8, 5.9 and 5.10 can yield density maps of the flow field. In both experiments discussed here, the PLIF images are composed of pixel intensities spanning a 20 to 30 greylevel range, depending on the pixel location within the laser light sheet. The dynamic greylevel range in the image was divided into discrete bands, each spanning an equal number of greylevels. Each band was mapped to a single greylevel value, which corresponds to the appropriate density range. Table 5.3 shows the banding scheme for the large amplitude solitary wave experiment. The contrast between each band was maximised by using the full dynamic range of the banded images. Effectively, the banding scheme serves as a look-up table to obtain density maps of the flow.

The banded greylevel associated with the mid-density difference $(\rho - \rho_2)/\Delta\rho = 1/2$ is $G_3 = 127$, in the case of the large amplitude wave images. The location of

band number n	original greylevel range $G'(i,j,t)$	banded greylevel $G_n(i,j,t)$	non-dimensional density range $\frac{\rho(i,j)-\rho_2}{\Delta\rho}$
1	$0 \leq G'(i,j,t) < 77$	0	$0 \leq \frac{\rho(i,j)-\rho_2}{\Delta\rho} < \frac{1}{5}$
2	$77 \leq G'(i,j,t) < 82$	63	$\frac{1}{5} \leq \frac{\rho(i,j)-\rho_2}{\Delta\rho} < \frac{2}{5}$
3	$82 \leq G'(i,j,t) < 87$	127	$\frac{2}{5} \leq \frac{\rho(i,j)-\rho_2}{\Delta\rho} < \frac{3}{5}$
4	$87 \leq G'(i,j,t) < 94$	191	$\frac{3}{5} \leq \frac{\rho(i,j)-\rho_2}{\Delta\rho} < \frac{4}{5}$
5	$94 \leq G'(i,j,t) \leq 255$	255	$\frac{4}{5} \leq \frac{\rho(i,j)-\rho_2}{\Delta\rho} \leq 1$

Table 5.3: Table showing the PLIF banding scheme for the large amplitude solitary wave experiment.

this density contour was picked out for each image in the experiment sequence. Following a smoothing routine, the result was a series of (i,j) plots of interface position. The shift, in pixels, between two consecutive plots of interface position where a portion of the wave was visible in the image, could be found using a least squares difference technique. The average shift over a sequence of interface profiles gave an estimation of the speed of the solitary wave. The error in the measure is given by the standard deviation from the mean shift value.

Figure 5.11 shows the resulting scaled large amplitude wave profile, η/h_2 against x/λ, the non-dimensional distance from the maximum amplitude of the wave. Although spurious points, which weren't removed by the filtering process can be seen in the region $|x| > 5$, the waveform is clearly defined. The equivalent plot for the small amplitude wave is also shown (figure 5.12). The irregularities in this graph are surprising. A slightly nonlinear relationship between dye fluores-

cence and concentration cannot be ruled out, particularly given the nature of the calibration results (figure 5.5 (b)). However, it would imply that a similar relationship existed for the large amplitude experiment as the initial dye concentration was the same. There is no evidence from the large amplitude wave calibration or other results that this was the case, particularly given the good match between the theoretical "tanh" fits and the intensity profiles across the density interface. If, on the other hand, the laser intensity had not been constant over time, but very slightly varying, consecutive images may not have received the same level of illumination.

Both the solitary wave profiles (figures 5.11 and 5.12) and the calibrated density profiles through the maximum depression of each wave (figures 5.9 and 5.10) provide an measure of the internal wave amplitude (table 5.4). As remarked in the DPIV surface wave - internal solitary wave interaction investigation (section 4.5), differences in the values of wave amplitudes between the amplitudes of the two waves investigated here and solitary waves generated in similar stratification configurations in the previous DPIV studies (table 4.4). These differences could be a result of slight differences in the initial stratification set ups, although it is possible that the locations of zero horizontal velocity, $u(x,y)/c_0 = 0$, used to characterise interfacial position in the DPIV investigations and that of the average density across the interface used here, are not the same. Simultaneous velocity and density visualisation techniques, such as DPIV and PLIF would be required in order to investigate this further.

depth ratio h_1/h_2	amplitude a/h_2	density difference $\Delta\rho/\rho_2$ (%)	KdV linear wave speed c_0 (cm.s^{-1})	shift wave speed c_{shift} (cm.s^{-1})	nonlinear wave speed c (cm.s^{-1})
5.82	-1.77	4.11	18.86	21.34 ±0.94	26.01
6.24	-0.62	3.57	17.16	17.71 ±0.89	20.6

Table 5.4: Table showing the characteristics of the 2 solitary waves investigated. The wave speeds found from the shift between consecutive wave profiles plots and the nonlinear method prediction are both shown.

The average shifts, found between consecutive wave profile portions to obtain the graphs in figures 5.11 and 5.12, provided a measure of the speed of each wave, c_{shift}. The predictions of the wave speed, c, from the nonlinear method (section 4.3.2) [30, 28], were also obtained (table 5.4). The nonlinear theory predicts a much greater wave celerity than that calculated from the PLIF images. A discrepancy of around 20% exists between the large amplitude wave speed prediction and measurement and 16% for the small amplitude wave. It was seen in section 4.3.2 that the nonlinear code also overestimated the wave speed for the equivalent wave in the DPIV measurements. In [29], a comparison is made between the measured wave speed and the nonlinear method predictions for solitary waves of depression of amplitudes $-1.55 < -a/h_2 < -0.4$ for a density difference of $\Delta\rho/\rho_2 \sim 2\%$. A deviation of around 5% from the theory at for larger wave amplitudes is seen. The large amplitude wave investigated here is around 20% larger than that in [29]. In addition, as the density difference and depth layer ratio are greater in the present work, a more detailed investigation of this discrepancy needs to be made. The clarity of the wave shape obtained (figure 5.11) by finding the mean

shift would indicate that the speed, c_{shift}, had been suitably estimated.

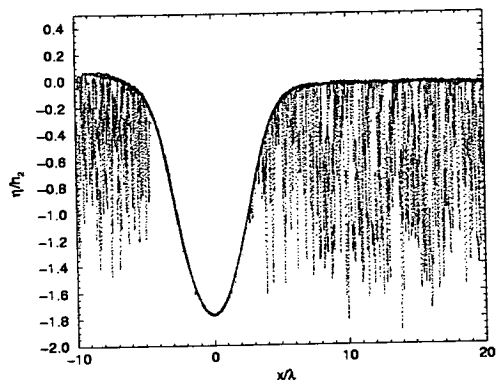

Figure 5.11: Large amplitude solitary wave: scaled wave profile η/h_2 against non-dimensional distance from the maximum amplitude of the wave, x/λ.

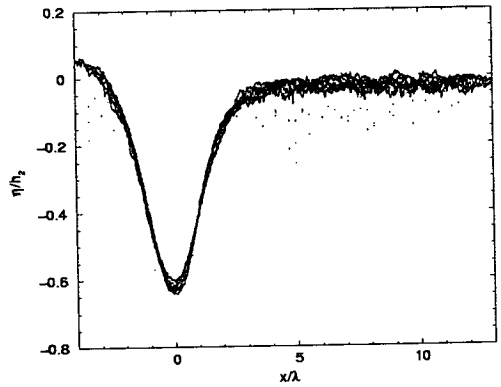

Figure 5.12: Small amplitude solitary wave: scaled wave profile η/h_2 against non-dimensional distance from the maximum amplitude of the wave, x/λ.

Using the average shift found from the interface profile analysis, the images in each wave sequence were joined together, so as to obtain a picture of the whole wave. The banded images were false-coloured, each greylevel band being assigned a particular RGB (red-green-blue) value. This enhances the difference between each density level, making them easier to distinguish. The resulting density map for the large amplitude solitary wave is shown in figure 5.13 where purple corresponds to the maximum density difference, $(\rho(i,j) - \rho_2)/\Delta\rho = 1$, and red to corresponds to fresh water, $(\rho(i,j) - \rho_2)/\Delta\rho = 0$. The image has been cropped such that only the area below the free surface is displayed. The noise, caused by the variations in the light sheet, is particularly visible on the left hand side of the map where the laser intensity in the light sheet was greatest. The concatenated

series of image sections in the right of the picture, each 232pxl in width, can be easily distinguished. Observation of the calibrated intensity profiles above showed that both the high density of the saline layer and the method of adding the upper fluid layer in this investigation generated a thin density interface. Despite this and the small number of density bands, the variation in density across the interface can still be seen. However, using a wider interface and reducing the salinity of the bottom layer, in future investigations, would improve both the spatial resolution within the interfacial region and the intensity resolution (and hence density resolution) across the entire image.

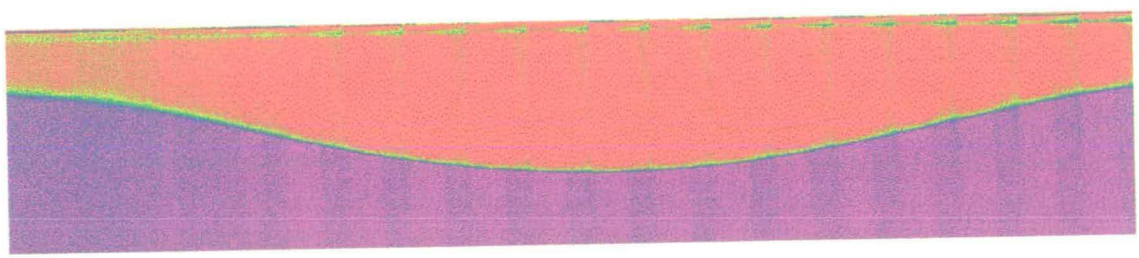

Figure 5.13: The density map for the large amplitude solitary wave. The image was produced by joining the banded PLIF images together using the shift, found by matching successive interface profiles. The resulting image was then false coloured to highlight the different density levels.

5.2.3 Conclusions from the single solitary wave PLIF experiments

Planar Laser Induced Fluorescence (PLIF) experiments were performed on two internal solitary waves, one of large and one of small amplitude, in a two-layer stratification where $h_1/h_2 \approx 6$. To date, it seems that such an investigation had

yet to be completed (section 2.6). The density difference across the interface, as in the previous experiments was of the order of 5%.

It was found that changes in image greylevel were not necessarily linked to changes in salinity. Variations in intensity caused by a non-uniform laser light sheet were found to be exacerbated in the top layer by image normalisation and were reduced subsequently by linear scaling. The stratification filling method (section 3.2.5), although providing a sharp interface, reduced the dynamic range of the pixel greylevels by drawing up dye from the saline layer as the top fluid layer was filling. In addition, there had been insufficient mixing of the dye in the saline layer, despite using submersible pumps to mix the fluid, causing an increase in pixel intensity with fluid depth. These two considerations hindered the usefulness of the fluorescence intensity to fluid concentration calibrations. The images were calibrated using the micro-conductivity probe measurements (section 3.2.5), taken in the quiescent stratification and shown, in previous experiments performed in this study, to be repeatable.

Hyperbolic tangent ("tanh") fits (equation (5.1)) to the calibrated profiles provided a measure of both the width of the density interface and also the accuracy with which such a measurement could be made in the post-processed PLIF images. The widths obtained by this method were comparable with those obtained by applying a "tanh" fit to the calibrated micro-conductivity probe output and were found to be around 0.1 times the width of the top fluid layer. The accu-

racy of this measure depended largely on the noise and defects in the raw images caused by surface reflections, variations in light sheet intensity across its width and a small pixel greylevel range. Overall, the margin of error associated with the method was in the region of 10%. Any changes in interfacial width as a result of a solitary wave - surface wavetrain interaction will be investigated in section 5.3.

Profiles of both solitary waves and density maps of the flow were obtained. The wave amplitudes were also determined. These were found to be smaller than those for waves with similar initial conditions, determined from the DPIV measurements. The discrepancy could be a result of slight differences in stratification initial conditions or could be caused by a difference between the vertical position of the zero horizontal velocity contour and that of the mid-density contour. It was found that the fully nonlinear method [30, 28] predicted faster wave speeds, by around 20%, for both waves than that calculated by determining the shift between two consecutive portions of the wave profile and used subsequently to generate the complete wave profiles. A discrepancy in the predicted and measured wave speeds at larger wave amplitudes had been noted already [29], for a different stratification configuration. This could be further investigated. In addition, an investigation into the effect of initial interfacial width could help to determine the effect of interface width on the solitary wave characteristics.

Overall, PLIF was successfully applied to internal solitary wave flow where the

stratification consisted of a two-layer brine - fresh water fluid. Quantitative information was obtained. A more extensive study, varying stratification initial conditions, h_1/h_2 and Δh, should be made. In addition, a reduction in laser intensity variations across the width of the light sheet would increase raw image quality. Likewise, a decrease in the salinity of the brine would reduce laser light attenuation through the fluid. This would provide increased fluorescence intensity, and therefore density, resolution. The relationship between dye concentration and fluorescence intensity in saline solutions also needs further investigation.

5.3 A PLIF Study of the Interaction between a Small Amplitude Surface Wave Train and an Internal Solitary Wave

In section 4.5, an investigation of the interaction of an internal solitary wave of depression and a train of small amplitude surface waves was presented. Here, a study of the same interaction process is made using PLIF. As in the case of the PLIF work on single solitary wave flow in section 5.2, it seems that, to date, no work has been done in this field.

5.3.1 The PLIF experimental set-up and method for the interaction investigation

In this section, the experimental method for the PLIF study of the interaction between an internal solitary wave of depression and a train of small amplitude surface waves is presented. As in the previous investigations (chapter 4 and section 5.2), the same experimental facilities and apparatus are used. Consequently, the method brings together elements of both the previous work on the same interaction process using DPIV (section 4.5) and the work performed using PLIF on single solitary waves (section 5.2).

As before, the waves approach each other from opposite ends of the wave flume and thus the angle between the directions of wave propagation $\phi = \pi$. The solitary waves were generated using the same sliding gate mechanism (section 3.2.6). The surface wave trains were generated using the built-in surface wave paddle (section 3.2.2). Image acquisition was initiated in the same way as in the previous interaction experiments (section 4.5).

Rhodamine dye was introduced into the saline fluid layer in the same manner as before, such that the initial concentration was around 0.01% of the stock solution. The intensity fluorescence was again calibrated using a series of known dye concentrations for each experimental run. The density difference across the interface was similar to that used previously.

The interaction was investigated in two experiments, using a large and a small amplitude solitary wave respectively. The DPIV study (section 4.5) used a single surface wave angular frequency, $\omega_S = 9.04\text{rad.s}^{-1}$ and two values of surface wave steepness, $2a_S/\lambda_S$. The greatest surface wave shape distortion from a sinusoidal profile was seen when the surface wave steepness was largest, that is $2a_S/\lambda_S = 0.059$. It was therefore this particular set of surface wave characteristics ($\omega_S = 9.04\text{rad.s}^{-1}$, $2a_S/\lambda_S = 0.059$) that were used here. The experimental parameters are detailed in table 5.5.

surface wave parameters			**solitary wave parameters**			
a_S (cm)	ω_S (rad.s^{-1})	$2a_S/\lambda_S$	h_1/h_2	$\Delta\rho/\rho_2$ (%)	V (l)	D (m)
2.23±0.023	9.04±0.019	0.059±0.0012	6.4	3.95	20	0.4
2.23±0.031	9.04±0.014	0.059±0.0012	5.83	3.87	80	0.4

Table 5.5: Table summarising the parameters used in each of the PLIF internal solitary wave - surface wave train interaction experiments.

Digital processing of the raw PLIF images followed the procedure outlined in section 5.2.1. The artificial brightness in the vicinity of the (quiescent) free surface in the background intensity reference image was removed by extrapolation (figure 5.1), before normalising the intensity distributions in the raw images. This ensured that the areas in the raw images above and below the SWL were normalised in the same regime (the position of the free surface in the raw images changed with the passage of the surface wave). Lastly, both experiment image sequences were greylevel-banded following a similar scheme to that described for the single

large amplitude solitary wave experiment (table 5.3).

5.3.2 Results of the PLIF interaction investigation

In this section, the results of the PLIF investigation into the interaction between an internal solitary wave and a small amplitude surface wave train are presented and discussed. The analysis of the results centres on the assessment of how the interaction process affects both the structure of the density interface within the solitary waveform and its shape.

In the same vein as figures 4.24, 4.25, 4.26 and 4.27 for the DPIV investigations of solitary wave - surface wave interactions, figures 5.14 and 5.15 show the sequence of surface wave profiles (upper graphs) and solitary wave profiles (lower graphs) for each of the two PLIF interaction experiments. In both cases, the initial surface wave characteristics were the same. The times correspond to the time from wave paddle initiation. The vertical axis is again plotted in terms of z, the distance in cm from the MWL, directed positively upwards. The horizontal axis is plotted in terms of x, the distance in cm across the measurement volume. It must again be noted that the scale of the z axis changes between the upper and lower graphs. Surface wave linear theory has been fitted to the surface wave profiles (blue line). Unlike in the DPIV experiments, the free surface was not always well illuminated as the upper fluid layer was dark. Hence, in some cases, the profiles are rather noisy.

The solitary wave profiles shown in (solid) black are obtained directly from the banded PLIF images. The profiles correspond to the position of the mid-density contour, $(\rho(i,j) - \rho_2)/\Delta\rho = 1/2$. As the smaller amplitude solitary wave passes under the surface wave train (figure 5.14), both the surface and solitary wave shapes are altered. This is in contrast to the observations made in the (large amplitude solitary wave) DPIV interaction investigation, where no alteration to the solitary wave profile was measured. The interface can be seen to move with the free surface, being pulled up at a wave crest and pushed down at a trough. Although previous work [33, 32] has investigated small amplitude solitary wave - surface wave interactions, this phenomenon has not been remarked before. A possible reason for this is that the layer depth ratios used previously were smaller, such that the top fluid layer was deeper. The pycnocline was thus further away from the free surface. In addition, the ratio of the solitary wave to surface wave length scales used previously was larger than in the current work.

It is possible, however, to correct for the distortion to the position of the density interface due to the presence of the surface waves. In deep water, an assumption which is valid in these experiments (table 4.6), the radius of the fluid particle orbits, α, decay exponentially with depth following [85]

$$\alpha_S = a_S\, e^{(k_S z)}. \tag{5.3}$$

For an initial surface wave profile of $a_S \cos(k_S x - \omega_S t)$, an amount $\alpha_S \cos(k_S x -$

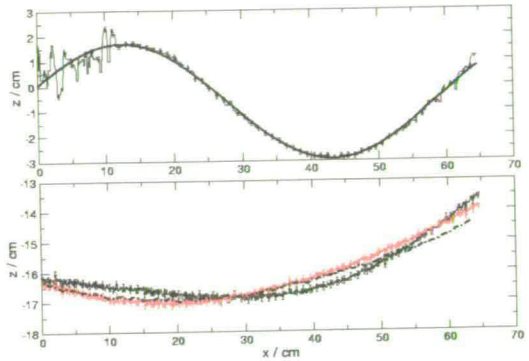

(a) $t = 7.31$s

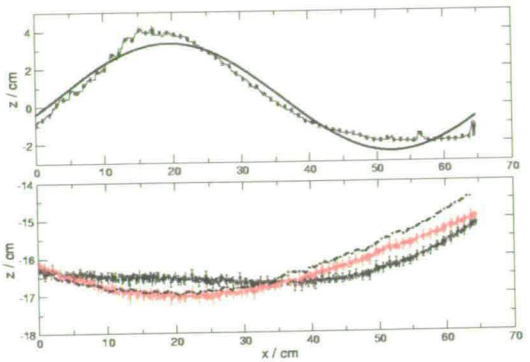

(b) $t = 7.86$s

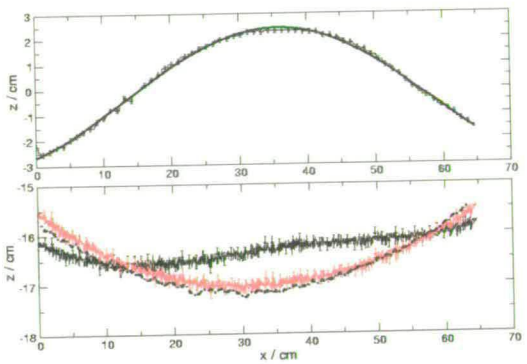

(c) $t = 8.41$s

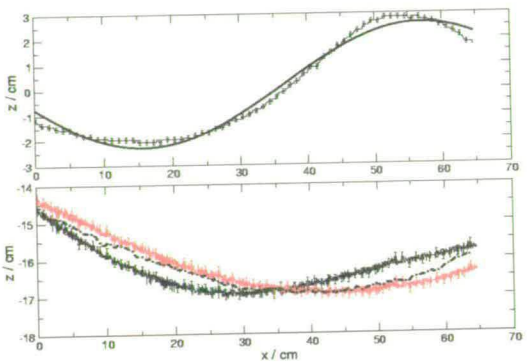

(d) $t = 8.96$s

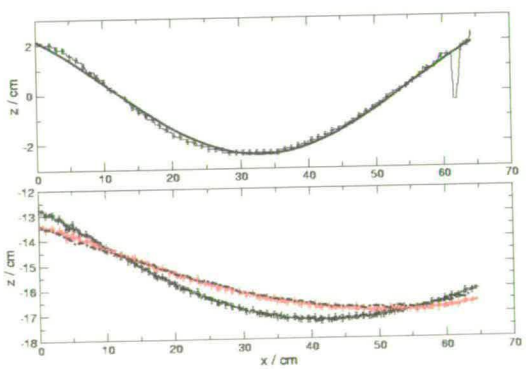

(e) $t = 9.51$s

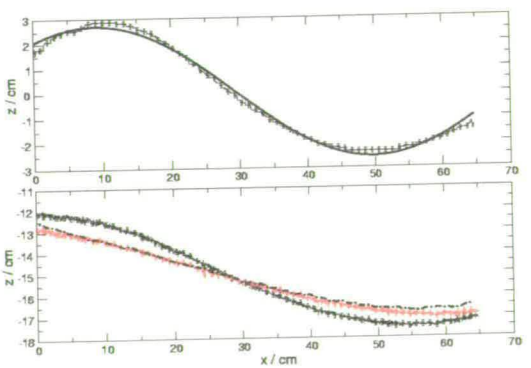

(f) $t = 10.06$s

(See caption next page)

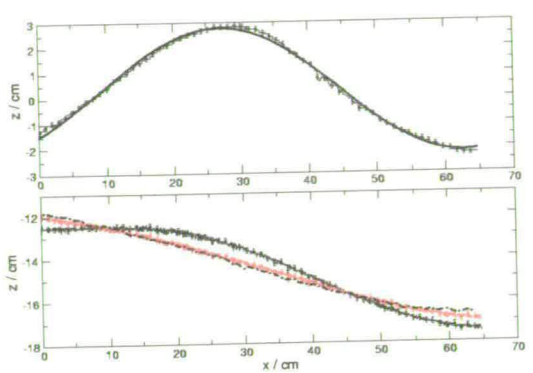

(g) $t = 10.61$s

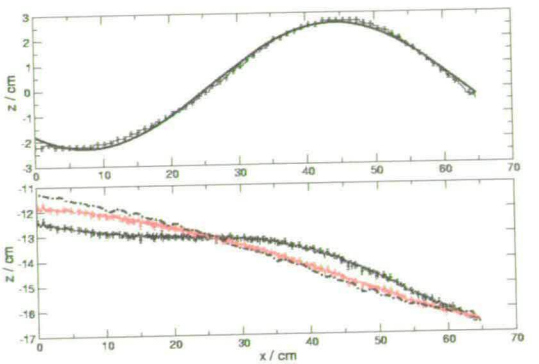

(h) $t = 11.16$s

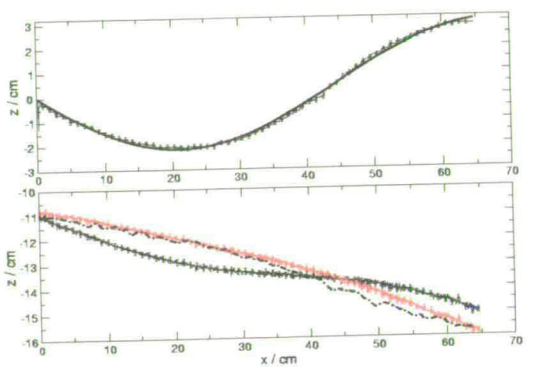

(i) $t = 11.71$s

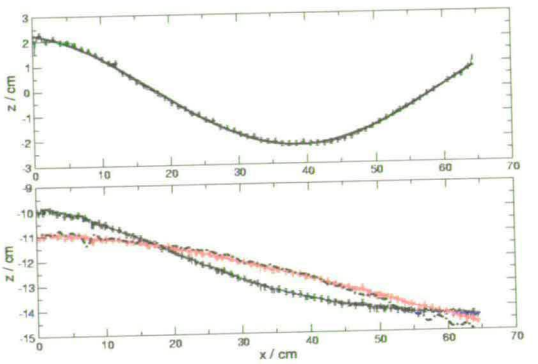

(j) $t = 12.26$s

Figure 5.14: Graphs of surface wave $2a_S/\lambda_S = 0.059$, $\omega_S = 9.04\text{rad.s}^{-1}$ profile (upper) and small amplitude internal solitary wave profile (lower) for a stratification where $h_1/h_2 = 6.4$ and $\Delta\rho/\rho_2 = 3.95\%$. First order linear theory (upper graph, black line) is fitted to the surface wave profiles. The solitary wave profiles have been corrected for the presence of the surface waves following equation (5.3) (lower graph, red line). The measured profiles are also shown for the interaction (lower graph, solid black line) and the equivalent non-interacting solitary wave (lower graph, black dot-dashed line).

$\omega_S t$) is subtracted from the measured interface profiles to allow for the surface wave motion at the interface. These corrected solitary wave interfacial profiles are also shown on the lower set of graphs (red line).

For the initial surface wave characteristics used in these experiments, the fluid

particle orbits have decayed to around 1/4 of their original value at the interfacial position of the small amplitude solitary wave. For comparison, the running average profile of the solitary wave, generated in the absence of surface waves and previously discussed in section 5.2.2, is plotted on the lower graphs in figure 5.14 (black dot-dashed line). It can be seen that, once the motion of the fluid at the interface due to the surface waves is taken into account, the undisturbed solitary wave shape is retrieved, such that the movement of the interface (noticeable on the solid black line plots) is due only to the surface wave propagation. Discrepancies between the corrected interfacial profile and that of the non-interacting solitary wave can be accounted for by the slight differences in the stratification initial conditions and the non-linearities apparent in figure 5.12.

In contrast, for the large amplitude wave, at the interfacial depths seen in figure 5.15, the particle orbits have decayed to around 1/10 of their free surface value. Consequently, little change is seen between the corrected and measured profiles. In section 4.5.2, the solitary wave profiles found from locating the point of zero horizontal velocity had not been corrected for the fluid motion due to the surface wave train only. In fact, the change in position of the interface due to the surface waves is smaller than the resolution of this method.

In both solitary wave cases, the surface wave linear fits show that the surface wave amplitude increases; a result which concurs both with previous work [33, 32] and with the findings of the DPIV investigation (section 4.5). They also indicate that

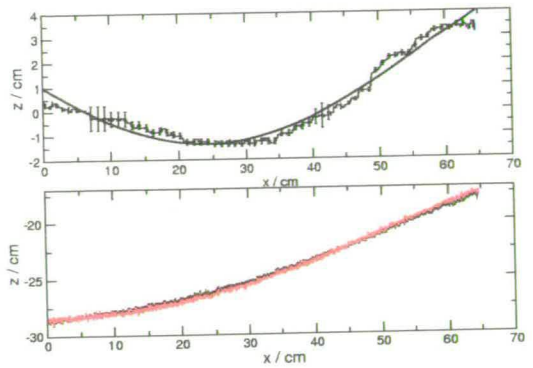

(a) $t = 7.31$s

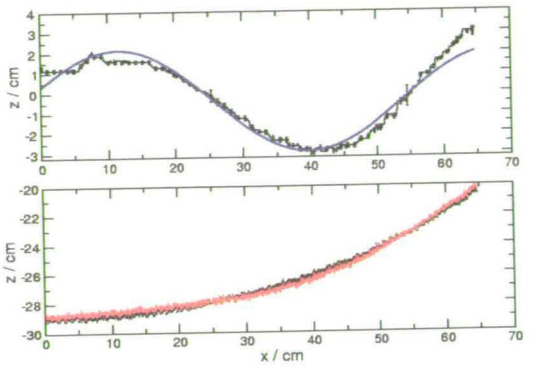

(b) $t = 7.86$s

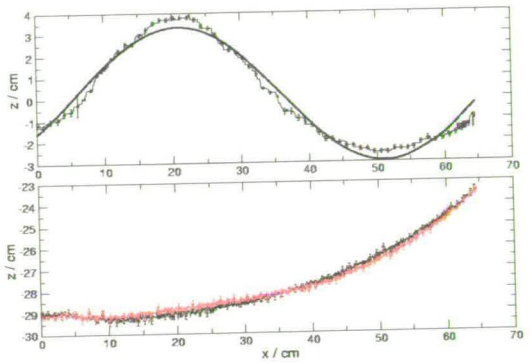

(c) $t = 8.41$s

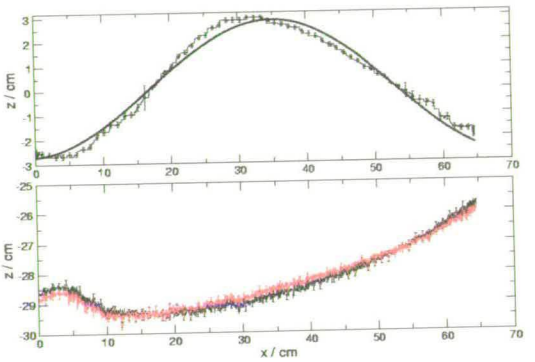

(d) $t = 8.96$s

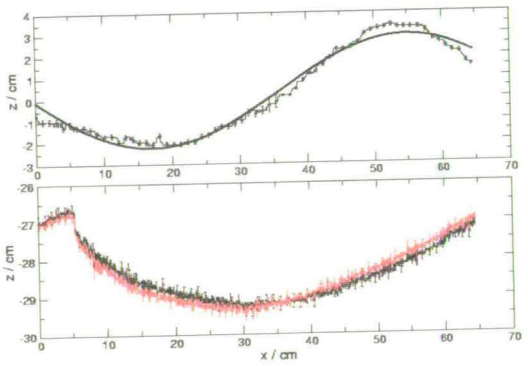

(e) $t = 9.51$s

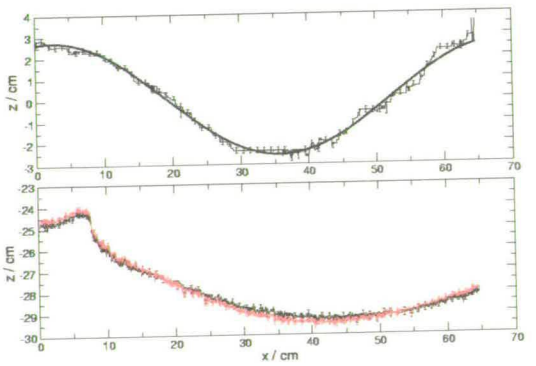

(f) $t = 10.06$s

(See caption next page)

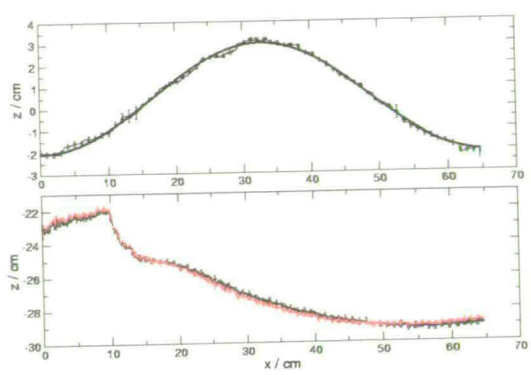

(g) $t = 10.61$s

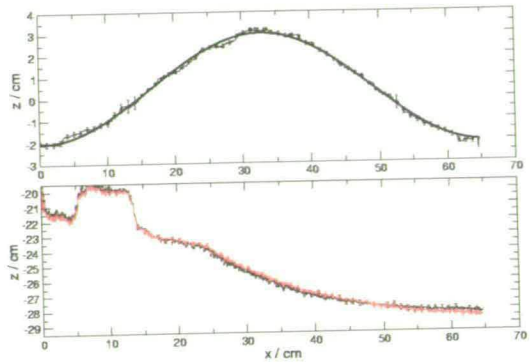

(h) $t = 11.16$s

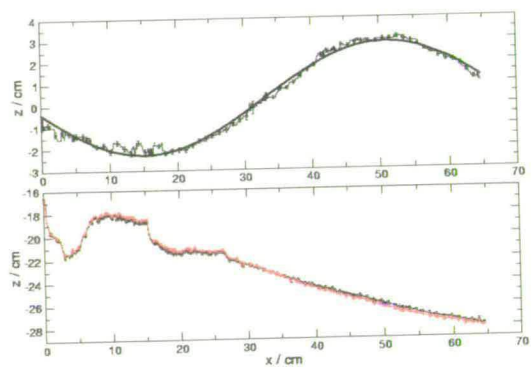

(i) $t = 11.71$s

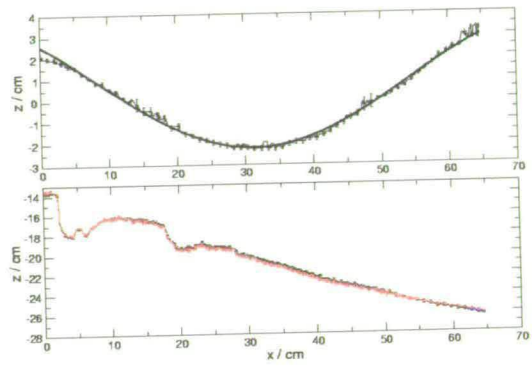

(j) $t = 12.26$s

Figure 5.15: Graphs of surface wave $2a_S/\lambda_S = 0.059$, $\omega_S = 9.04\text{rad.s}^{-1}$ profile (upper) and large amplitude internal solitary wave profile (lower) for a stratification where $h_1/h_2 = 5.83$ and $\Delta\rho/\rho_2 = 3.87\%$. Note the change in vertical axis scale between upper and lower graphs. First order linear theory (upper graph, black line) is fitted to the surface wave profiles. The solitary wave profiles have been corrected for the presence of the surface waves following equation (5.3)(lower graph, red line). The measured profiles are also shown (lower graph, black line).

the wavelength is also modulated. It appears that even for the small amplitude solitary wave, some skewing of the surface wave profile occurs. Skewing was also seen for the large amplitude solitary wave interactions with the same initial surface wave characteristics in the DPIV investigation (figures 4.26 and 4.27). Again, the phenomenon appears to be most pronounced as the solitary wave

trough moves through the measurement area and in particular under the leading edge of the internal wave.

As the amplitude of this solitary wave is large, the solitary wave profile initially remains undisturbed and the trough is more easily discernible than in the smaller amplitude solitary wave interface measurements (figure 5.14, solid black line). As the wave moves through the volume, however, a disturbance develops towards the tail end of the wave (figure 5.15 (d)). This continues to develop as the wave moves through the measurement volume (figure 5.15 (d) to (j)) but remains fairly localised, moving with the wave.

The interfacial disturbance is best seen in the time series of concentration maps in figure 5.16. These maps are the result of false-colouring the processed and greylevel-banded PLIF images from the experiment. The density levels are colour-coded such that purple represents areas where the fluid is most dense, that is where $(\rho(i,j) - \rho_2)/\Delta\rho = 1$, and red represents fresh water, such that $(\rho(i,j) - \rho_2)/\Delta\rho = 0$. The same colour coding was used in figure 5.13. The light reflected at the free surface appears as a thin, mostly blue, "curvy" strip at the top of the map. The interface is characterised by another thin strip of blue, followed by green and yellow, between the saline (purple) layer and the fresh water (red/yellow) layer above. Variations in the laser light sheet intensity are apparent, particularly in the left of the images. These appear as yellow patches within the predominantly red background in the fresh water region.

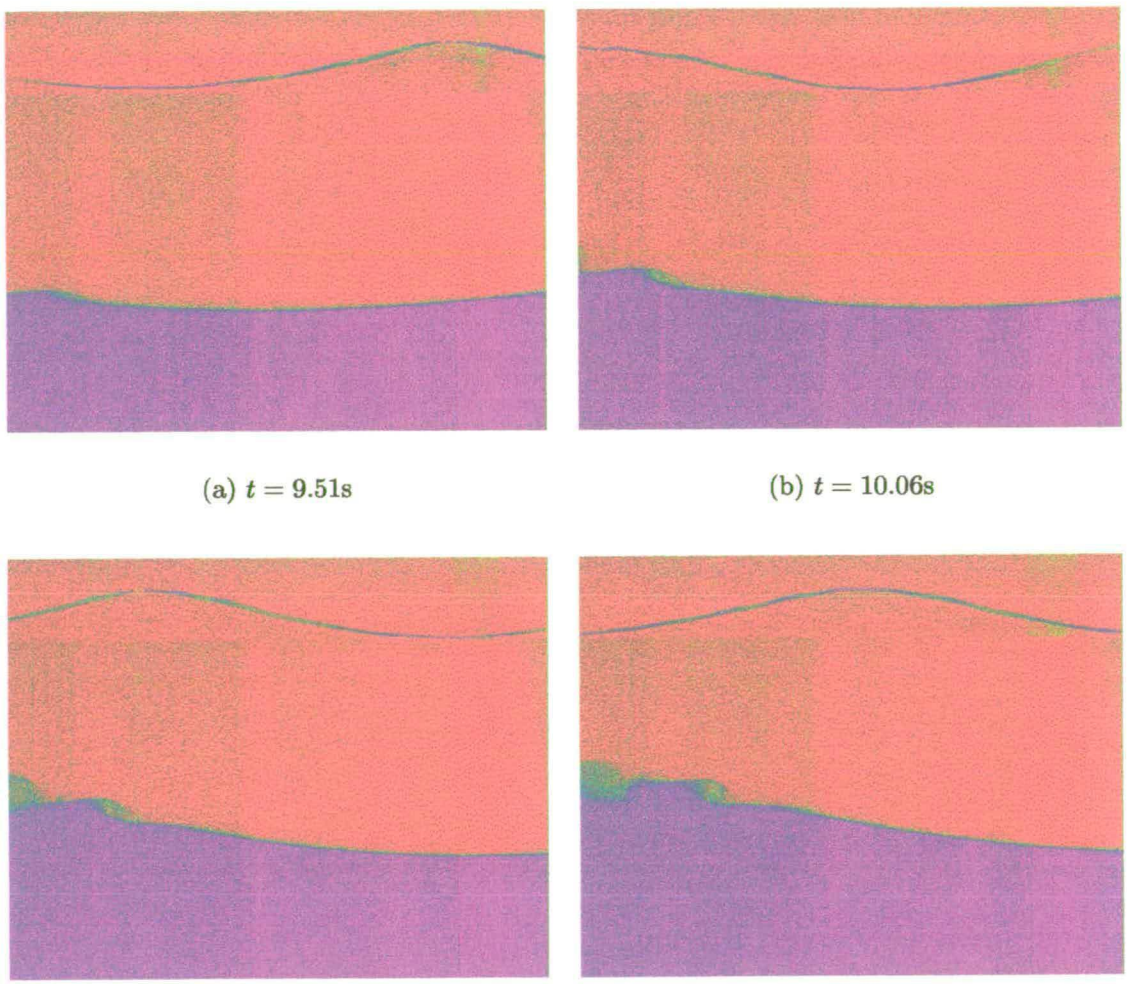

(a) $t = 9.51$s

(b) $t = 10.06$s

(c) $t = 10.61$s

(d) $t = 11.16$s

(See caption next page)

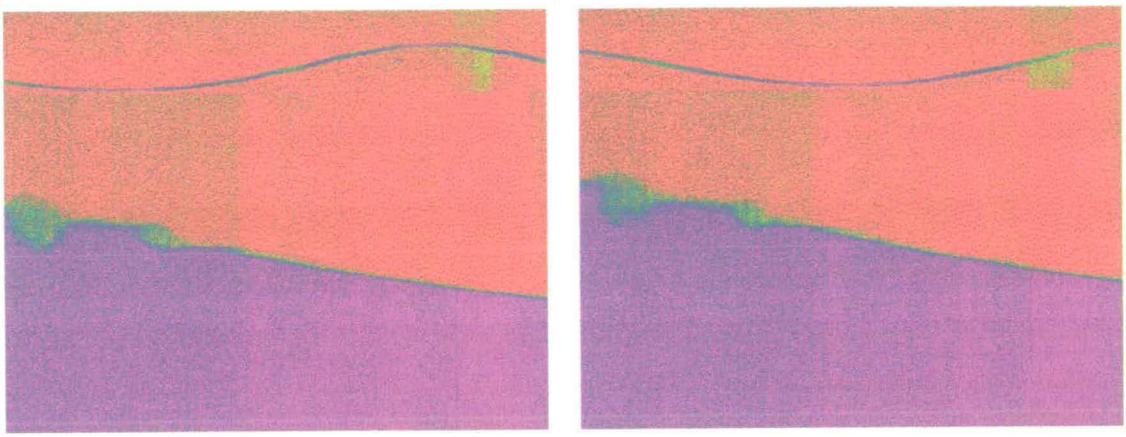

(e) $t = 11.71$s (f) $t = 12.26$s

Figure 5.16: Times series of concentration maps for the large amplitude solitary wave ($h_1/h_2 = 5.83$, $\Delta\rho/\rho_2 = 3.95\%$) - surface wave ($2a_S/\lambda_S = 0.059$, $\omega_S = 9.04\text{rad.s}^{-1}$) interaction experiment.

Although the resolution of the map is limited, it can be seen that as the wave moves through the measurement area, a disturbance develops at the interface in the left-most area of the maps. The disturbance slowly grows into a series of rolls but remains localised about the tail end of the solitary wave. Table 4.5 summarised the buoyancy frequencies and gradient Richardson numbers calculated using velocity gradients approximated from the DPIV single solitary wave measurements. In each case, the gradient Richardson number was found to be greater than 0.25 and, in accordance with the theoretical predictions [40], the interface remained stable within the entire waveform; Kelvin-Helmholtz instabilities were not observed along the interface, behind the maximum depression of the solitary wave. Likewise, in the case of the PLIF study, there was no evidence of such instability formation. This was corroborated by the smooth appearance

of the large amplitude solitary wave shape (figure 5.11). As this particular solitary wave was generated in very similar conditions to the large amplitude solitary wave studied here, it would be expected that similar features should be seen in each. The observed disturbances must therefore be a result of the presence of the surface wave train.

In the analysis of the DPIV interaction experiments, the horizontal velocities in the upper fluid layer were seen to increase as a consequence of the combined flow fields associated with the solitary and surface waves (figure 4.32). The disturbances observed at the interface are probably a consequence of this increase. The velocity profile behind the solitary wave trough becomes unstable as a result of the interaction. Thus, the stabilising effect of the density profile is no longer sufficient to maintain the well-defined step-like interfacial structure observed within the solitary waveform in the non-interacting case (figure 5.9) and mixing occurs.

Reference to figure 5.17 (a), showing graph 4.27 (h), reveals that the tail end of the solitary wave shape exhibits increased scatter in the data points close to $x = 0$cm. This DPIV experiment was performed in a stratification configuration with a sharper interface and slightly larger density difference ($h_1/h_2 = 6.39$, $\Delta\rho = 4.38\%$) than that in the PLIF experiment discussed here (table 5.5). Nevertheless, in both experiments, the same initial surface wave parameters were employed. As the profiles in the DPIV measurements were obtained by locating the point of zero horizontal velocity within the interfacial layer, the scatter could be an indication

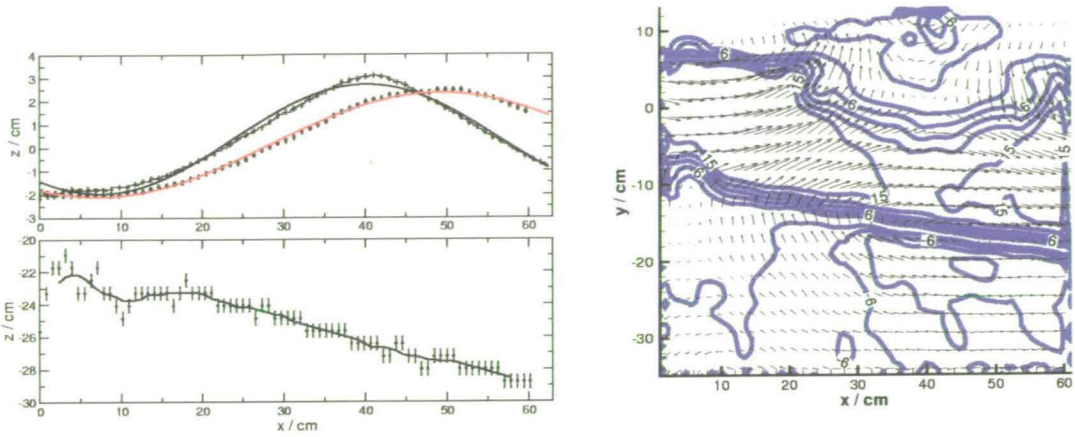

(a) Wave profiles

(b) Vector map

Figure 5.17: Surface wave and solitary wave profiles (as seen in figure 4.27 (h)) with similar initial characteristics to those in the equivalent PLIF experiment. The vector map from which the solitary wave profile was obtained is also shown (b).

that instability rolls also developed during this interaction. This observation is corroborated by the rise in the horizontal velocity contours, plotted at intervals of 3cm.s^{-1}, at the left hand edge of the vector map shown in figure 5.17 (b). This is the map from which the solitary wave shape shown in figure 5.17 (a) was obtained. The horizontal velocity contours highlight the position of the interface. The rise in the contours from their undisturbed position is of the order of 2cm. This is comparable with the radius of the area of mixing seen at the left of figure 5.16 (e) and (f), or equivalently figure 5.15 (i) and (j) where the scale of the disturbance can be measured on the z axis. The area of small velocity vectors in the region $-15 < y < -10$cm also suggests that the disturbance extends into the saline fluid, as indicated in the PLIF data. Further work is required to measure

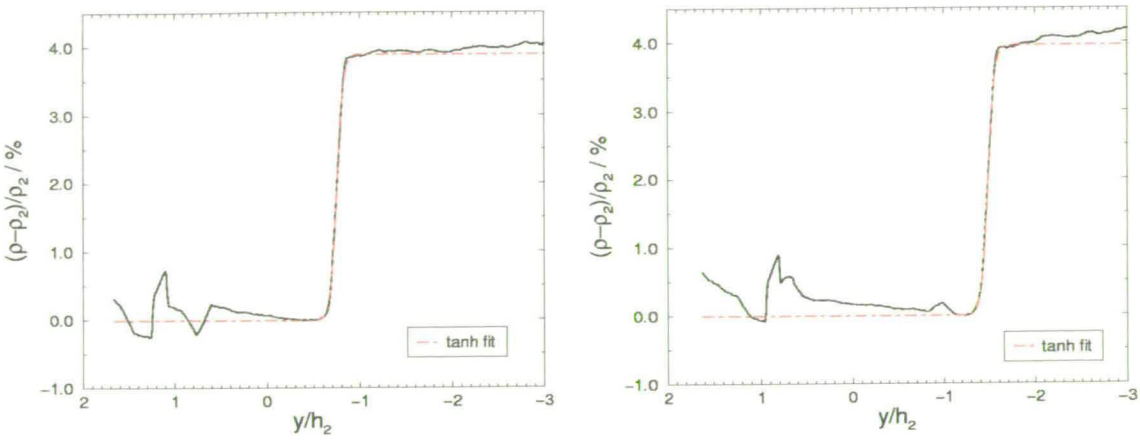

(a) Wave crest

(b) Wave trough

Figure 5.18: Non-dimensional density plots with depth, y/h_2, obtained from calibrating the intensity profiles from the conductivity probe measurements for the small amplitude solitary wave - surface wave interaction. The profiles are taken at the surface wave crest and trough shown in figure 5.14 (a).

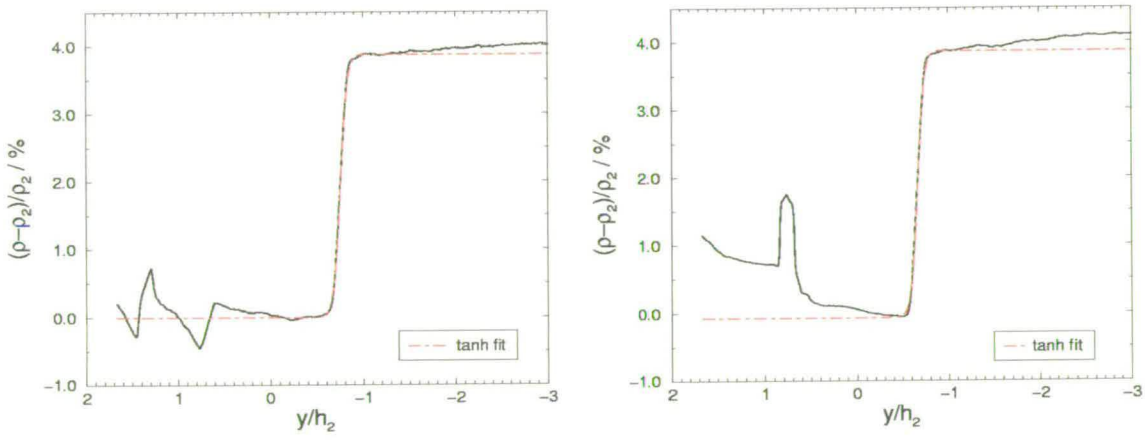

(a) Wave crest

(b) Wave trough

Figure 5.19: Calibrated intensity plots with non-dimensional depth , y/h_2, taken at the surface wave crest and trough shown in figure 5.14 (b).

and investigate the velocity fields in this region of the solitary wave waveform. It would be useful to ensure that equivalent stratification parameters are used in both sets of measurements.

Figures 5.18 and 5.19 show plots of non-dimensional density versus non-dimensional depth at the surface wave crests (a) and troughs (b) shown in figure 5.15 (a) and (b), respectively. The density plots were obtained in the same way as before (section 5.2.2), by calibrating intensity profiles from the processed PLIF images with the calibrated output from the micro-conductivity probe. Hyperbolic tangent fits, satisfying equation (5.2), are also plotted (red line). The profiles have been selected to be as close to the maximum depression of the solitary wave as possible. The same features, identified in similar plots obtained for the non-interacting solitary waves, (e.g. figures 5.7 and 5.8) can be seen here. The increase in rhodamine dye intensity with depth through the fluid in the bottom layer, caused by non-uniform mixing of the dye with the brine before adding the top fresh water layer, is indicated on the graph as an increase in fluid density. This is also true in the top layer, where dye has been drawn up through the top fresh water layer during the filling process. The laser light reflections at the fluid free surface are also shown as a pronounced density increase in this region. Similar plots of calibrated intensity profile with depth at a surface wave crest and trough, for the large amplitude solitary wave case, are shown in figures 5.20 and 5.21. The plots are obtained from the crests and troughs in figures 5.15 (b) and (c).

As in the case of the single solitary wave study (figures 5.9 and 5.10), the "tanh" fits show good agreement with the calibrated intensity profiles across the interfacial region for both the large and small amplitude solitary wave experiments.

In addition, the micro-conductivity probe outputs, obtained by sampling each quiescent stratification configuration prior to the internal wave generation, were also found to be well-described by a "tanh" curve. This demonstrates that, despite the presence of the surface wave train, the shape of the stratification is not disturbed. Although the graphs shown here (figures 5.18, 5.19, 5.20 and 5.21) are taken from positions within the solitary waveform close to its maximum depression, intensity profiles at surface wave crests and troughs above the leading and tailing sections of the internal wave are were also found to be adequately described by the "tanh" fits.

A comparison of the interfacial widths below both a surface wave crest and trough was made to assess the maximum compression or expansion of the interface. The minimum change in interfacial width that could be determined from the intensity profiles was around 10% (table 5.2). This limited accuracy was, in part, caused by the restricted resolution of the PLIF raw images and accounted for the horizontal variations in laser light sheet intensity. It was found that, where no interfacial mixing was observed, the interfacial width under a wave crest or trough changed by less than around 5% over each waveform. Consequently, if any compression or expansion did occur, the present PLIF set-up was not capable of measuring it.

For the large amplitude solitary wave interaction, where rolls developed along the interface, behind the maximum depression of the internal wave (figure 5.16), an intensity profile taken at the wave trough shown in the upper plot of figure 5.15

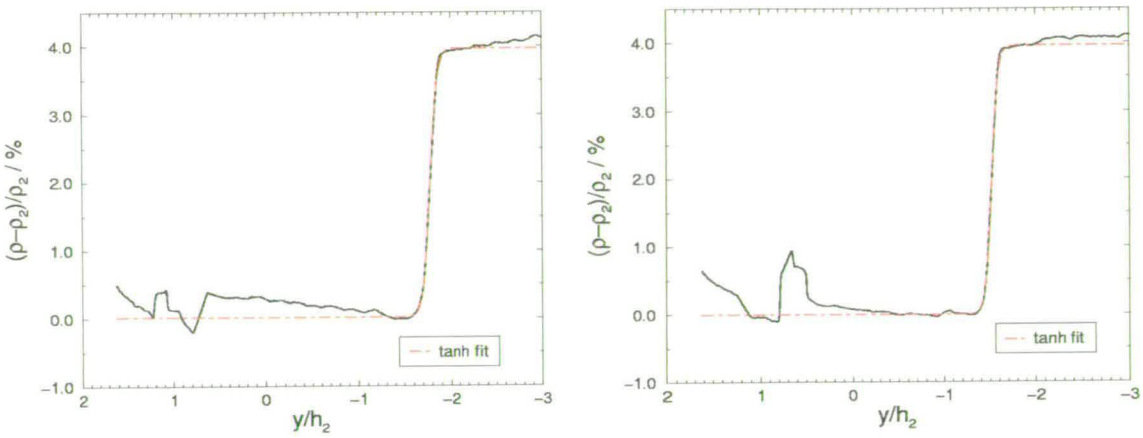

(a) Wave crest

(b) Wave trough

Figure 5.20: Non-dimensional density plots with depth, y/h_2, obtained from calibrating the intensity profiles from the conductivity probe measurements for the large amplitude solitary wave - surface wave interaction. The profiles are taken at the surface wave crest and trough shown in figure 5.15 (b).

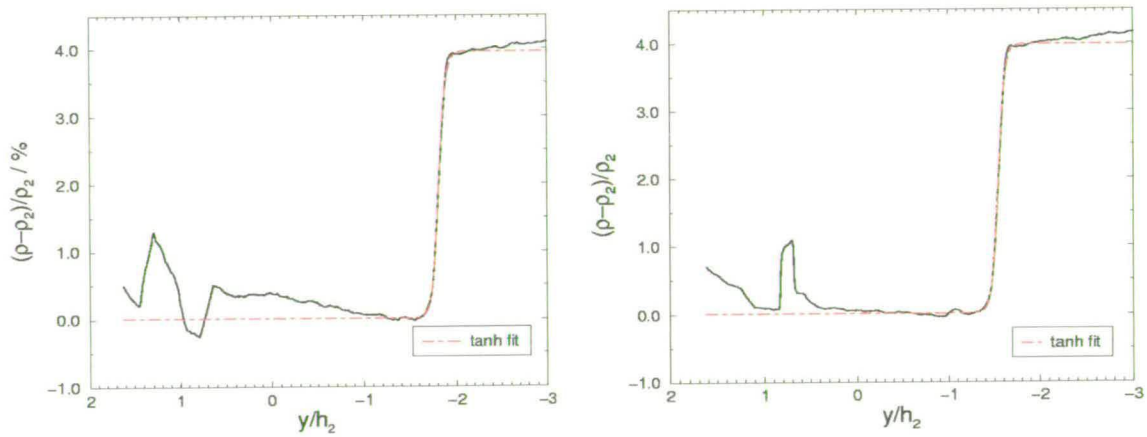

(a) Wave crest

(b) Wave trough

Figure 5.21: Calibrated intensity plots with non-dimensional depth , y/h_2, taken at the surface wave crest and trough shown in figure 5.15 (c).

(i) (corresponding density map: figure 5.16 (e)), indicated that the interface had been thickened by the observed mixing processes. Nevertheless, the profile still followed the shape of a hyperbolic tangent curve across the interfacial region. In

contrast, at the wave crest, in the same figure, the profile was of a similar width to that at other locations within the waveform. This suggests that the observed mixing remains very localised within the tailing edge of the solitary wave shape.

In these experiments, the interfacial width was of the order of 1cm, that is around one tenth of the top fluid layer depth. In addition, the density difference between the two fluid layers was large. Overall, this, as demonstrated by the values of gradient Richardson number calculated in the previous chapter (table 4.5), yielded a highly stable stratification. Performing a similar PLIF investigation using stratifications characterised by a smaller buoyancy frequency (and therefore a reduced gradient Richardson number) may give rise to other mixing processes and changes to the density structure of the stratification, which could not be observed here.

5.3.3 Conclusions of the PLIF interaction investigation

In this section, the interaction between an internal solitary wave and a train of small amplitude surface waves was investigated using PLIF. The experimental set-up and data acquisition method closely followed that described in the previous chapter for the investigation of the same interaction processes using DPIV (section 4.5). The solitary and surface waves approached each other from opposite ends of the wave flume, such that the angle between their directions of propagation was $\phi = \pi$. In contrast to the DPIV experiments however, both a large ($a/h_2 <$

-1) and a small ($a/h_2 \sim 0.5$) amplitude solitary waves were generated in two separate surface wave interaction experiments. To the author's knowledge, such an investigation had not been performed before.

Simultaneous surface wave shape and solitary wave shape profiles with distance across the measurement area were obtained from the processed PLIF image sequences. The profiles indicated that both the surface wave and solitary wave shapes underwent distortion throughout the interaction. Solitary wave deformation had not been detected either in the previous DPIV experiments (section 4.5) or in previous work [33, 32]. In the small amplitude solitary wave - surface wave interaction, the interface moved with the free surface as the surface wave passed. In the case of the large amplitude solitary wave interaction, some distortion of the wave shape took place and Kelvin-Helmholtz type rolls were seen to develop behind the maximum depression of the wave. These were not observed in the previous non-interacting solitary wave experiments (section 4.3 and 5.2). It was suggested that the velocity gradient across the interface became unstable in this region of the waveform due to the interaction and thus lead to interfacial mixing. Surface wave amplitude and wavelength modulation was observed, as in the DPIV investigation. In addition, surface wave skewing was identified in both cases.

Calibrated intensity profiles, taken at surface wave crests and troughs as the solitary wave progressed through the measurement area, were seen to be described well by a hyperbolic tangent fit across the interfacial region. Within the accu-

racy of the interfacial width measure, neither compression nor expansion of the interface with surface wave phase was observed. This could be due to the highly stable density stratifications employed in this study. Further work in this field needs to be performed to assess whether changing the stratification parameters would affect the structure of the interface in wave interactions of this type.

5.4 Summary of Chapter 5

An investigation of internal solitary wave flow was made using Planar Laser Induced Fluorescence (PLIF), a non-intrusive full-field laser measuring technique. This flow visualisation technique relies on digitally recording the flow and subsequently post processing the resulting images. It appears, from a review of the literature, that no work with this particular investigative method has yet been done in this field.

Single internal solitary waves were generated in a brine - fresh water stratification by means of a sliding gate system (section 3.2.6). The first goal of the work was to assess the ability of PLIF to be employed as a quantitative investigative tool in internal solitary wave flow. Secondly, as in the case of the DPIV investigations, the aim was to obtain reference data sets for the equivalent experiments performed for the interaction investigations (section 5.3). The work was then extended to investigate the interaction between a small amplitude surface wave train and an

internal solitary wave (section 5.3). As in the DPIV investigation of the interaction (section 4.5), the two wave types had opposite directions of propagation, being generated at opposite ends of the laboratory wave flume. Previous investigations of internal solitary wave flow have focused mainly on obtaining velocity and wave shape information [92, 51, 44, 29] and consequently, the exact structure of the interface within the waveform remained unknown. These considerations provided the main motivation for this study.

Further to the DPIV investigation (chapter 4), this PLIF study has revealed additional interesting processes that occur during the solitary wave - surface wave interaction process. In particular, in addition to surface wave modulation, distortion of the solitary wave shape was observed. It was also found that for the parameters employed in the study, there was no change in interfacial density structure with surface wave phase, except where interfacial mixing was observed. These phenomena would merit further attention in any subsequent investigation.

The aims of this chapter (section 5.1) have been met overall. The present study was inhibited by the low intensity resolution of the raw PLIF images. Nevertheless, even given the difficulties, which were identified throughout the course of the analysis (section 5.2.2), this PLIF investigation has shown that the technique can provide quantitative concentration, and therefore density, information about two-layer solitary wave flows. Any subsequent study would yield more far-reaching conclusions about the processes that occur in a solitary wave - surface wave train

interaction if a wider parameter space was utilised and if the disadvantages of the present set-up were reduced, if not removed.

Chapter 6

Conclusions and Further Work

6.1 Review of the subject

Internal solitary waves are a common and important oceanic phenomenon. They have been measured to have large amplitudes, in some cases in excess of 100m, and also to have large associated currents. Both *in situ* observations and, more recently, satellite imaging have shown that the passage of an internal wave modulates the sea surface roughness. Little laboratory work, however, appears to have been done on the subject. This provided the main motivation for the present work. The interaction between an internal solitary wave of depression and a progressive, small amplitude surface wave train was investigated. In previous studies, measurements were performed using capacitative and resistive probes at single points in the flow. In contrast, here, non-intrusive quantitative flow visual-

isation techniques were employed, yielding two dimensional velocity and density information within a plane of the fluid.

This chapter is intended as a summary of the investigation. A brief overview of the experimental measuring techniques and the experimental set-up is given. The main conclusions of the study are presented and suggestions for further work are outlined.

6.2 Summary of the Experimental Set-Up, Measuring Techniques and Methods

This laboratory investigation considered the interaction between small amplitude surface waves and a single internal solitary wave of depression. Two non-intrusive planar measurement techniques were applied to the study, namely Digital Particle Image Velocimetry (DPIV) and Planar Laser Induced Fluorescence (PLIF). These are both optical measurement techniques and rely on imaging a plane of the flow, illuminated by a laser light sheet. This yielded velocity and concentration (or density) maps of the flow respectively.

Overall, two main groups of experiments were performed. DPIV and PLIF experiments were first carried out on large and small amplitude single non-interacting internal solitary waves. In this work, a large amplitude solitary wave was defined

as a wave with an amplitude greater than the depth of the top fluid layer. In addition, DPIV experiments were performed on a set of small amplitude surface waves in a homogeneous (fresh water) fluid and two stratified fluid regimes. DPIV and PLIF experiments were then performed on the interaction case, where a single internal solitary wave passed under a small amplitude progressive surface wave train.

All experiments were carried out in the same laboratory wave flume. The solitary waves were generated at a brine - fresh water interface over which the density varied continuously. The two fluid layers were separated by a thin density interface, approximately one tenth of the upper fluid layer. The corresponding density profile was found to be step-like in structure and represented well by a hyperbolic tangent fit. The total density change across the interface was around 5%. The top layer was filled by slowly feeding fresh (tap) water through floating sponges onto the saline fluid surface. A built-in hinged paddle at one end of the glass-walled tank generated the surface waves. This provided a limited range of both surface wave amplitudes and frequencies. The solitary waves were generated from the opposite end of the tank using a sliding gate mechanism, such that, for the interaction experiments, the two wave types travelled towards each other.

In the case of the DPIV experiments, the flow was seeded with conifer pollen. For the PLIF experiments, a low concentration of rhodamime dye was mixed into the saline layer of the fluid. A scanning beam set-up produced a "pseudo" laser

light sheet that was directed upwards through the glass base of the wave flume, thus illuminating a plane of the fluid. In all experiments, the flow was recorded using a digital camera system.

The relatively short wave flume (7.5m) caused standing surface waves to be set up shortly after paddle initiation. In addition, the frequency of image capture was limited by the camera system. Within these constraints, the system was optimised to acquire a maximum amount of data. The camera field of view was also maximised so as to image as much of the solitary wave in one exposure as possible. A mechanical shutter, placed behind the camera lens, fixed the exposure length of the images. In the case of the DPIV experiments, the time between exposures of an image pair was defined by the scan rate of the laser beam. This resulted in a short time interval that optimised the system for the study of large amplitude solitary wave flows. The salinity of the lower fluid layer, chosen to optimise the solitary wave speed for the interaction experiments, caused strong attenuation of the laser light. This reduced the intensity resolution of the PLIF images.

6.3 Summary of the Main Results

The application of each measuring technique, DPIV and PLIF, and the corresponding data analyses were discussed separately (chapters 4 and 5 respectively).

First, results from the non-interacting solitary wave cases were presented. In addition, in the case of the DPIV investigation, experiments on small amplitude surface wave trains were performed. A discussion of the interaction experiments followed. This section brings together the main conclusions drawn from these.

The present work has, in effect, presented a series of case studies of internal solitary wave - surface wave interactions. It has helped to establish the limits on the properties of both wave types for which such modifications can be both qualitatively and quantitatively observed. First and foremost, the study has shown that when a train of small amplitude surface waves rides over an internal solitary wave, not only does the internal solitary wave have a measurable effect on the surface wave flow and characteristics, but also that the converse is true; a progressive surface wave train also affects the internal solitary wave flow field. This latter observation, in particular, does not appear to have been mentioned in previous studies of solitary - surface wave interactions [33, 32].

The flow visualisation techniques used in the present work have confirmed previous reports [33, 32] that the presence of a solitary wave modulates the amplitude of a surface wave. Furthermore, it has shown that the surface wavelength is also modulated, which in the previous studies [33, 32] had not been detected. The observed modulation of these surface wave characteristics also concurs qualitatively with the theoretical predictions proposed by Longuet-Higgins and Stewart [61] (section 2.5.1). Significantly, the modified surface wave profiles, initially sinu-

soidal in shape, become skewed. This skewness appears to increase with surface wave steepness and solitary wave amplitude.

The PLIF study has, in addition, revealed that the solitary wave shape also undergoes some distortion. This was seen to be irrespective of the internal wave amplitude for large enough surface wave steepness. The application of PLIF also allowed observation of interfacial mixing processes, which were seen to develop along the tailing edge of the large amplitude internal waveform. The instabilities remained localised, but caused interfacial thickening in this region. Elsewhere, the density structure of the interface remained undisturbed from its initial profile and no change in interfacial width was observed with surface wave phase.

This preliminary application of both DPIV and PLIF to the investigation of internal wave - surface wave interactions has revealed a number of interesting phenomena. It has shown that both DPIV and PLIF can be applied to internal wave - surface wave problems. Velocity and concentration maps of the flow were obtained and interesting features in both fields were identified. In addition, the present study has indicated how the two measuring techniques can complement each other such that together, they can provide a good description of two-layer fluid flow properties. Further development of the methods would be needed to extend the study undertaken here. This would increase their range of applicability within the presently available parameter space and allow parameterisation of any future results. Possible improvements to the measuring techniques and extensions

to the present study are discussed in the following section (section 6.4).

Moreover, the results presented here may be of importance to other fields of research, specifically, to future oceanographic studies. In particular, the observed surface wave shape skewing may have implications for the use of satellite imaging to detect and track internal solitary waves.

Overall, therefore, the present work has shown that:

- DPIV and PLIF can be successfully applied to internal wave - surface wave interaction studies.
- the interaction causes not only distortions to the surface wave profile but also to the solitary wave shape.
- surface wave modulation observations were in accordance with theoretical predictions
- the modulated surface wave profile exhibits some skewness, from an initially sinusoidal profile, for increased surface wave steepness and solitary wave amplitude.
- for an initially thin, stable density interface, the interfacial width within the solitary wave waveform does not vary with surface wave phase.
- the initially stable solitary wave velocity field, behind the maximum depression, becomes unstable along the interface, during the surface wave

interaction, for the large amplitude solitary wave case.

- further developments to increase the range of applicability of the measuring techniques would enable parameterisation of future results.

6.4 Suggestions for Further Work

The case studies presented here have provided necessary and extensive groundwork for future internal solitary wave - surface wave interaction investigations. The work has identified many aspects of the experimental set-up that could be refined. Many of these improvements could not have been known *a priori*. Were these issues to be addressed in future studies, the scope of the present work could be significantly extended. Some of these are now considered.

From one experiment to another, the layer depth ratio and the density of the saline layer varied. It was found that, as long as the variations were kept to a minimum, the solitary wave generation system produced repeatable waves. In practice, this proved difficult, in part due to the scale of the experimental facilities. Nevertheless, eliminating, or at least reducing, these differences would enable clearer conclusions to be drawn when comparing, for example, non-interaction and interaction solitary wave cases, using either the same or different measurement techniques.

It must be emphasised that the limited velocity resolution, and hence accuracy,

encountered during the DPIV experiments were a consequence of the exposure-control system used, rather than of the DPIV technique and analysis method themselves. Were the same camera system to be used in further work, these difficulties could be overcome by using an alternative shuttering method, such as an opto-acoustic light modulator. This would significantly enhance the range of fluid velocities and hence solitary wave amplitudes that could be accurately determined.

An alternative scanning beam method, which does not rely on a parabolic mirror [81] would reduce the horizontal variations in laser light sheet intensity observed in the current work and thus increase the accuracy of the technique. The reduced intensity resolution of the PLIF images was also inhibited by the (unintentional) presence of dye in the upper fluid layer. This could be resolved best by dyeing the upper, fresh water, layer rather than the lower saline one. In order to do this, the dyed fresh water must be stored. This option, although considered, was not adopted because the rhodamine dye is toxic and leaves a stubborn residue.

In the current study, the length scales of each wave type were of the same order. Evidently, this does not mimic even closely oceanic conditions, where the surface waves would be of considerably smaller wavelength than the characteristic length of any solitary wave. Although the experiments presented here showed some surface wave modulation, it would be interesting to extend the work to cover configurations in which the solitary wave to surface wave length scale ratio is

greater.

Although not possible within the framework of the present experimental set-up, it would be interesting to investigate the case where the two wave types propagate in the same direction. The previous work in this field [33, 32] has already investigated, within a limited parameter range, this situation. Differences between the case where the wave propagation directions were the same and opposite were observed. Measuring velocity and density fields in this alternative flow configuration would complement the present study.

This work, in particular, has revealed that, although there are significant advantages to using non-intrusive measuring techniques because they do not disturb the fluid flow, they do bring with them certain drawbacks. The low frequency of image capture, as well as the relative extent of the camera field of view to the internal and surface wave length scales, constrained the scope of the data analysis. In contrast, both continuous surface wave train wavelength and amplitude modulations in addition to solitary wave modulations could have been quantitatively obtained with time, using probe measuring techniques. Although such techniques only provide information at a single point in the flow, they would allow not only quantitative comparisons with surface wave amplitude and wavelength modulation predictions to be made but also any change in the solitary wave speed to be measured. Perhaps, therefore, future studies should consider the possibility of using both probe and non-intrusive techniques to investigate surface and internal

wave interaction phenomena.

This initial work on solitary - surface wave interactions provides many opportunities to develop the experimental set-up and procedures to yield more accurate and more quantitative results than those presented. In addition, there is plenty of scope to extend the parameter space of the investigation and further investigate the interesting phenomena observed here.

Appendix A

Notation

Δh	interfacial width
$\Delta \rho$	density difference between fluid layers 1 and 2
Δt	time between images
δt	time between exposures of an image pair
δZ	out-of-plane displacement
ϕ	angle between wave propagation directions
η	solitary wave elevation
η_S	surface wave elevation
λ	solitary wave characteristic length scale
λ_S	surface wave wavelength
λ'_S	modulated surface wave wavelength
μ	dynamic viscosity

ν	kinematic viscosity
ρ	fluid density
$\overline{\rho}$	mean density
ρ_0	reference density
ρ_1	density of the lower fluid layer
ρ_2	density of the upper fluid layer
ω_S	surface wave angular frequency
A	fit coefficient for surface wave profiles
a	solitary wave amplitude
a_S	surface wave amplitude
a'_S	modulated surface wave amplitude
B	fit coefficient for surface wave profiles
c	solitary wave speed from nonlinear theory
c_0	solitary wave KdV linear long wave speed
c_{KdV}	solitary wave KdV speed
$c_{\mathcal{L}}$	long wave speed
$c_{\mathcal{S}}$	short wave speed
c_S	surface wave speed
$c_{g\mathcal{S}}$	short wave group velocity
c_{gS}	surface wave group velocity
c_{shift}	approximation to the solitary wave speed from PLIF measurements

D	distance to sliding gate
d_t	particle image diameter
d_r	dimension of pixel
E	rate of transfer of short wave energy
E_S	energy density of short waves
f_S	surface wave frequency
f_s	spatial frequency
F_I	in-plane displacement
F_O	out-of-plane displacement
G_B	background greylevel value
G_N	normalised greylevel value
G_r	raw greylevel value
G'	linearly scaled greylevel
g	gravitational acceleration
H	total water depth
h_1	lower layer depth
h_2	upper fluid depth
$I_O(Z)$	intensity distribution of the laser light sheet
$I_1(\mathbf{X})$	intensity over the interrogation area centred at $\mathbf{X}$
k_S	surface wavenumber
L	length scale

M	magnification of the camera system
N	dimension of DPIV interrogation area
$N(y)$	buoyancy frequency as a function of vertical coordinate y
$N(z)$	buoyancy frequency as a function of vertical coordinate z
$\mathcal{N}$	overall seeding particle density
S	PLIF normalisation scaling factor
$\mathbf{s}$	spatial frequency coordinate in the Fourier transform plane of the image
T	time scale
t	time
U	velocity scale
$u_{\mathcal{L}}$	horizontal component of particle velocity of long waves
u_S	horizontal component of surface wave particle velocity
$u_{\mathcal{S}}$	horizontal component of particle velocity of short waves
u_1	horizontal component of solitary wave particle velocity in the lower fluid layer
u_2	horizontal component of solitary wave particle velocity in the upper fluid layer
V	additional volume of fresh water for solitary wave generation
$v_{\mathcal{L}}$	vertical component of particle velocity of long waves
v_S	vertical component of surface wave particle velocity
w	z-component of vorticity
$\mathbf{X}$	$= (X, Y)$ in image plane
X	horizontal coordinate in image plane

x	horizontal coordinate
Y	vertical coordinate in image plane
y	vertical coordinate from the centre of the density interface
Z	DPIV coordinate perpendicular to the plane of the light sheet
z	vertical coordinate from the mean water level

Appendix B

The Second Order KdV Equation

Following [51], the second order KdV equation in section 2.3.3 is given in terms of the elevation $\eta(x,t)$ of a wave propagating in a two fluid system where the upper and lower layers have depths h_2 and h_1 and densities ρ_2 and ρ_1 respectively, such that

$$\eta_t + c_0\,\eta_x + c_1\eta\eta_x + c_2\eta_{xxx} + c_3\eta_{5x} + c_4(\eta\eta_{xx})_x + c_5(\eta^3)_x + c_6(\eta_x^2)_x = 0, \quad \text{(B.1)}$$

where the constants c_0, c_1 and c_2 are defined in equations (2.17), (2.18) and (2.19) such that c_1 and c_2 can be written as

$$c_1 = (c_0/h_2)\tilde{c_1}, \quad \text{(B.2)}$$

and

$$c_2 = (c_0 h_2^2)\tilde{c}_2. \tag{B.3}$$

The constants c_3, c_4, c_5 and c_6 are given by

$$\begin{aligned} c_3 &= (c_0 h_2^4) \times \left(\frac{h_1}{h_2}\right)^3 \left[\frac{\rho_1/\rho_2 + \frac{1}{(h_1/h_2)^3}}{90\left(1 + \frac{\rho_1/\rho_2}{h_1/h_2}\right)}\right] + \frac{3\tilde{c}_2{}^2}{2} \\ &= (c_0 h_2^4)\tilde{c}_3, \end{aligned} \tag{B.4}$$

$$\begin{aligned} c_4 &= (c_0 h_2) \times \left[\frac{\rho_1/\rho_2 - 1}{6\left(1 + \frac{\rho_1/\rho_2}{h_1/h_2}\right)} + \frac{7\tilde{c}_1\tilde{c}_2}{3}\right] \\ &= (c_0 h_2)\tilde{c}_4, \end{aligned} \tag{B.5}$$

$$\begin{aligned} c_5 &= (c_0/h_2^2) \times \left[-\frac{1 + \frac{\rho_1/\rho_2}{(h_1/h_2)^3}}{1 + \frac{\rho_1/\rho_2}{h_1/h_2}} + \frac{7\tilde{c}_1{}^2}{18}\right] \\ &= (c_0/h_2^2)\tilde{c}_5, \end{aligned} \tag{B.6}$$

$$\begin{aligned} c_6 &= (c_0 h_2) \times \left[\frac{\rho_1/\rho_2 - 1}{12\left(1 + \frac{\rho_1/\rho_2}{h_1/h_2}\right)} + \frac{17\tilde{c}_1\tilde{c}_2}{12}\right] \\ &= (c_0 h_2)\tilde{c}_6. \end{aligned} \tag{B.7}$$

The corresponding solitary wave solution to this equation is

$$\frac{\eta(x,t)}{h_2} = \frac{a}{h_2}\operatorname{sech}^2[(x - ct)/\lambda]\left\{1 + \frac{a}{h_2} C \tanh^2[(x - ct)/\lambda]\right\} + O\left[\left(\frac{a}{h_2}\right)^3\right], \tag{B.8}$$

where the constant C is given by

$$C = 3\tilde{c}_4/4\tilde{c}_2 - 5\tilde{c}_3\tilde{c}_1/4\tilde{c}_2{}^2 - 3\tilde{c}_5/2\tilde{c}_1 + \tilde{c}_6/2\tilde{c}_2. \tag{B.9}$$

Appendix C

Surface Wave Fit Coefficients

The coefficients a_S, k_S, A and B were found by fitting the curve

$$z = a_S \cos(k_S(A + x)) + B \tag{C.1}$$

to the surface wave profiles obtained from digital post-processing of the DPIV images.

C.1 Figure 4.24

Figure	**Interaction/No interaction**	a_s	k_S	A	B
(a)	Interaction	0.887	0.09148	-25.996	-0.049
	No interaction	0.88034	0.07297	99.626	0.0941

(b)	Interaction	-1.0167	0.1034	-39.446	-0.170
	No interaction	0.99332	0.06747	102.275	0.1628
(c)	Interaction	-1.1151	0.09885	-53.831	0.0737
	No interaction	0.8977	0.08157	59.044	0.0398
(d)	Interaction	-1.093	0.08876	-71.291	-0.0283
	No interaction	0.85473	0.07624	122.014	0.0329
(e)	Interaction	-1.0674	0.08496	90.732	-0.0552
	No interaction	0.79964	0.08096	95.844	-0.0678
(f)	Interaction	-0.9592	0.0936	-1.9711	0.0255
	No interaction	-0.9261	0.09046	92.934	-0.097
(g)	Interaction	-1.057	0.09479	-117.411	0.004
	No interaction	0.899897	0.0804	130.693	0.0124
(h)	Interaction	0.995	0.09283	-134.68	0.0652
	No interaction	0.79509	0.0864	112.042	0.1423

C.2 Figure 4.25

Figure	**Interaction/No interaction**	a_s	k_S	A	B
(a)	Interaction	0.893	0.09452	-18.042	0.1323
	No interaction	0.78909	0.07178	115.616	0.098
(b)	Interaction	-1.1321	0.1078	-14.431	0.0107

	No interaction	0.84146	0.07258	124.44	0.0469
(c)	Interaction	-1.1433	0.10274	-8.4465	0.2091
	No interaction	0.83802	0.07717	123.597	0.0003
(d)	Interaction	-1.1495	0.08783	-0.11809	0.0536
	No interaction	0.97249	0.07208	144.274	-0.0171
(e)	Interaction	-1.0034	0.10241	-2.61581	0.09715
	No interaction	0.89254	0.07778	140.458	0.04589
(f)	Interaction	-1.0674	0.09562	-28.941	0.14387
	No interaction	0.852694	0.08077	142.045	0.01364
(g)	Interaction	1.0622	0.08778	-24.511	0.066
	No interaction	0.89254	0.07778	140.458	0.04589
(h)	Interaction	-0.9719	0.09475	12.1236	0.065
	No interaction	0.89254	0.07778	140.458	0.04589

C.3 Figure 4.26

Figure	**Interaction/No interaction**	a_s	k_S	A	B
(a)	Interaction	3.11627	0.07049	105.279	0.5184
	No interaction	2.52619	0.06247	124.752	0.5439
(b)	Interaction	2.86862	0.07426	81.4615	0.3561
	No interaction	2.07274	0.08022	59.0795	0.0111

(c)	Interaction	2.61874	0.09414	42.1448	0.3275
	No interaction	2.14227	0.07911	68.4427	-0.014
(d)	Interaction	2.58173	0.09255	26.74	0.1946
	No interaction	-2.11355	0.08712	71.733	0.3149
(e)	Interaction	2.57392	0.07964	17.155	0.36255
	No interaction	2.52619	0.06247	124.752	0.5439
(f)	Interaction	2.60492	0.07924	0.13921	0.26757
	No interaction	2.46433	0.07047	90.6215	0.2524
(g)	Interaction	2.51235	0.09247	80.63	0.1958
	No interaction	2.07274	0.08022	59.0795	0.0111
(h)	Interaction	-2.39161	0.09481	61.2621	0.224
	No interaction	-2.32258	0.05411	110.134	0.113

C.4 Figure 4.27

Figure	**Interaction/No interaction**	a_s (cm)	k_S	A	B
(a)	Interaction	-1.99883	0.1093	-3.676	-0.242
	No interaction	2.1833	0.07367	81.8324	0.1082
(b)	Interaction	-2.43593	0.1058	-14.255	0.0337
	No interaction	2.24808	0.08117	62.8634	0.0687
(c)	Interaction	-2.2937	0.1119	-26.1966	0.6123

	No interaction	2.21988	0.08395	51.9097	0.2248
(d)	Interaction	-2.375	0.08619	-42.748	-0.069
	No interaction	2.19681	0.08356	34.667	0.3494
(e)	Interaction	-2.6831	0.07279	-69.092	0.829
	No interaction	2.0914	0.06499	25.09	0.0567
(f)	Interaction	-2.2917	0.09311	-76.619	0.207
	No interaction	2.21988	0.08395	51.9097	0.2248
(g)	Interaction	2.43511	0.09569	-89.798	0.338
	No interaction	2.24808	0.08117	62.8634	0.0687
(h)	Interaction	-2.3399	0.09574	-105.78	0.372
	No interaction	2.23465	0.07452	33.0192	0.123

Bibliography

[1] Web Site: http://www.dropbears.com/brough/images.htm.

[2] R. J. Adrian. Particle imaging techniques for experimental fluid mechanics. *Ann. Rev. Fluid Mech.*, 23:261–304, 1991.

[3] R. J. Adrian. Dynamic ranges of velocity and spatial resolution of particle image velocimetry. *Meas. Sci. Technol.*, 8:1393–1398, 1997.

[4] W. Alpers and I. Hennings. A theory of the imaging mechanism of underwater bottom topography by real and synthetic aperture radar. *J. Geophysical Research*, 89(C6):10,529–10,546, 1984.

[5] W. Alpers and E. Salusti. Scylla and charybdis observed from space. *J. Geophysical Research*, 88:1800–1808, 1983.

[6] J. R. Apel. *Principles of Ocean Physics*, volume 38 of *International Geophysics Series*. Academic Press, 1990.

[7] J. R. Apel, R. F. Gasparovic, D. R. Thompson, and B. L. Gotwols. Signatures of surface wave / internal wave interactions: experiment and theory. *Dynamics of Atmospheres and Oceans*, 12:89–106, 1988.

[8] C. Arcoumanis, J. J. McGuirk, and J. M. L . M. Palma. On the use of fluorescent dyes for concentration measurements in water flows. *Experiments in Fluids*, 10:177–180, 1990.

[9] T. K. Barrett and C. W. Van Atta. Experiments on the inhibition of mixing in stably stratified decaying turbulence using Laser Doppler Annemometry and Laser Induced Fluorescence. *Physics of Fluids A*, 3, May 1991.

[10] T. Brooke Benjamin. Internal waves of permanent form in fluids of great depth. *J. Fluid Mech.*, 29:559–592, 1967.

[11] J. B. Bole. Soliton currents in the South China Sea: measurements and theoretical modelling. In *26th Offshore Technology Conf.*, pages 367–376, May 1994.

[12] Borzelli, Marullo, Ligi, and Cannizzaro. Solitary waves in the Gulf of Quasano revealed by Landsat Thermatic Mapper. *Il Nuovo Cimento*, 17, 1994.

[13] P. Brandt, R. Romeiser, and A. Rubino. On the determination of characteristics of the interior ocean dynamics from radar signatures of internal solitary waves. *J. Geophysical Research*, 104(C12):30,039–30,045, 1999.

[14] D. Christie and R. White. The Morning Glory of the Gulf of Carpentaria. *AOPA*, January 1995.

[15] R. E. Davis and A. Acrivos. The stability of oscillatory internal waves. *J. Fluid Mech.*, 30:723–736, 1967.

[16] I. P. D. de Silva, J. Imberger, and G. N. Ivey. Localized mixing due to a breaking internal wave ray at a sloping bed. *J. Fluid Mech.*, 350:1–27, 1997.

[17] Lokenath Debnath. *Non-linear Water Waves.* Academic Press USA, 1994.

[18] T. P. Dewhirst. *Multiple CCD Array Digital Particle Image Velocimetry.* PhD thesis, University of Edinburgh, 1998.

[19] N. Emarat. *Particle image velocimetry on surf-zone breaking waves.* PhD thesis, University of Edinburgh, 2000.

[20] H. J. S. Fernando. Turbulent mixing in stratified fluids. *Ann. Rev. Fluid Mech.*, 23:455–493, 1991.

[21] H. J. S. Fernando and J. C. R. Hunt. Turbulence, waves and mixing at shear free density interfaces. Parts 1 and 2. *J. Fluid Mech.*, 347:197–261, 1997.

[22] D. I. M. Forehand. *Numerical prediction of free-surface flows caused by body/fluid interaction.* PhD thesis, University of Edinburgh, 1998.

[23] A. E. Gargett and B. A. Hughes. On the interaction of surface and internal waves. *J. Fluid Mech.*, 52:179–191, 1972.

[24] S. Gaskey, P. Vacus, R. David, and J. Villermaux. A method for the study of turbulent mixing using fluorescence spectroscopy. *Experiments in Fluids*, 9:137–147, 1990.

[25] A. E. Gill. *Atmosphere - Ocean Dynamics*, volume 30 of *International Geophysics Series.* Academic Press, 1982.

[26] R. J. Goldstein. *Fluid Mechanics Measurements.* Taylor and Francis, second edition, 19.

[27] R. Grimshaw. Internal solitary waves. *Advances in Coastal and Ocean Engineering*, 3:1–30, 1997.

[28] J. Grue, H. A. Fris, E. Palm, and P. O. Rusås. A method for computing unsteady fully non-linear interfacial waves. *J. Fluid Mech.*, 351:223–252, 1997.

[29] J. Grue, A. Jensen, P. Rusås, and J. K. Sveen. Properties of large amplitude internal waves. *J. Fluid Mech.*, 159:19–53, 1985.

[30] J. Grue and E. Palm. Modelling of fully non-linear internal waves and their generation in transcritical flow at a geometry. Abstract for the 12th international workshop on water waves and floating bodies, Marseilles, March 1997.

[31] Guilbault. *Practical fluorescence: theory, methods and techniques.* Marcel Dekker Inc., 1973.

[32] K. Guizien. *Les ondes longues internes: généraction et interaction avec la houle.* PhD thesis, Université Joseph Fourier Grenoble I Sciences et Géographie, 1998.

[33] K. Guizien and E. Barthelemy. Amplitude modulation in the internal solitary wave - surface wave interaction. Experiments. *C. R. Acad. Sci. Paris Mécanique des Fluides*, 327:1325–1330, 1999.

[34] Y. Guo, P. A. Davies, K. Sveen, J. Grue, and P. Dong. Laboratory modelling of the motion of an internal solitary wave over a finite amplitude bottom ridge. In *Stratified Flows*, pages 761–766, 2000.

[35] K. Hasselmann. Ocean circulation and climate change. *Tellus Series A - Dynamic Meterology and Oceanography*, 43:82–103, 1991.

[36] M. J. Head. *The use of miniature four-electrode conductivity probes for high resolution measurement of turbulent density or temperature variations in salt stratified water flow.* PhD thesis, University of California, 1983.

[37] K. R. Helfrich. Internal solitary wave breaking and run-up on a uniform slope. *J. Fluid Mech.*, 243:133–154, 1992.

[38] Honji, Matsunaga, Sugihara, and Sakai. Experimental observation of internal symmetric solitary waves in a two layer fluid. *Fluid Dynamics Research*, 15:89–102, 1995.

[39] I. Houcine, H. Vivier, E. Plasari, R. David, and J. Villermaux. Planar laser induced fluorescence technique for measurements of concentration fields in continuous stirred tank reactors. *Experiments in Fluids*, 22:95–102, 1996.

[40] L. N. Howard. Note on a paper of John W. Miles. *J. Fluid Mech.*, 10:509–512, 1961.

[41] H. Segur J. L. Hammack. The Korteweg - de Vries equation and water waves. Part 2: Comparison with experiments. *J. Fluid Mech.*, 65:289–314, 1974.

[42] F. F. Jin. A theory of interdecadal climate vairability of the North Pacific ocean-atmosphere system. *Journal of Climate*, 10:1821–1835, 1997.

[43] R. I. Joseph. Solitary waves in a finite depth fluid. *J. Phys. A: Math Gen.*, 10(12):L225–227, 1977.

[44] T. W. Kao, F. Pan, and D. Renouard. Internal solitons on the pycnocline; generation, propagation and shoaling and breaking over a slope. *J. Fluid Mech.*, 159:19–53, 1985.

[45] R. D. Keane and R. J. Adrian. Optimization of particle image velocimetry: part 1. Double pulsed systems. *Meas. Sci. Technol.*, 1:1202–1215, 1990.

[46] R. D. Keane and R. J. Adrian. Theory of cross-correlation analysis of PIV images. *App. Sci. Res.*, 49:191–215, 1992.

[47] G. H. Keulegan. Gradual damping of solitary waves. *Journal of Research of the National Bureau of Standards*, 40(3), June 1948.

[48] G. H. Keulegan. Characteristics of internal solitary waves. *Journal of Research of the National Bureau of Standards*, 51(3), September 1953.

[49] G. Konokova and K. V. Pokazeyev. Experimental study of the interaction between surface and internal waves. *Oceanology*, 20(6):660–663, 1980.

[50] M. M. Koochesfahani and P. E. Dimotakis. Laser induced fluorescence measurements of mixed fluid concentration in a liquid plane shear. *AIAA*, 23(11):1700–1707, 1985.

[51] C. G. Koop and G. Butler. An investigation of internal solitary waves in a two fluid system. *J. Fluid Mech.*, 112:225–251, 1981.

[52] C. G. Koop and L. G. Redekopp. The interaction of long and short internal gravity waves: theory and experiment. *J. Fluid Mech.*, 111:367–409, 1981.

[53] D. J. Korteweg and G. de Vries. On the change of form of long waves advancing in a rectangular canal and on a new type of long stationary waves. *London, Edinburgh and Dublin Philosophical Magazine and Journal of Science*, 39:422–443, 1895.

[54] T. Kubota, D. R. S. Ko, and L. D. Dobbs. Propagation of weakly nonlinear internal waves in stratified fluids of finite depth. *AIAA Journal of Hydronautics*, 12:157–165, 1978.

[55] G. Kychakoff, R. D. Howe, and R. K. Hanson. Quantitive flow visualization technique for measurements in combustion gases. *Applied Optics*, 23(5):704–711, March 1984.

[56] M. Lakshamaran, editor. *Solitons: Introduction and Applications.* Springer series in Non-linear Dynamics Proceedings. Springer - Verlag, 1988.

[57] C. Leone, H. Segur, and J. L. Hammack. Viscous decay of long solitary waves. *Physics of Fluids*, 25(6):942–944, 1982.

[58] J. E. Lewis, B. M. Lake, and D. R. S. Ko. On the interaction of internal waves and gravity waves. *J. Fluid Mech.*, 63:775–800, 1974.

[59] J. Lighthill. *Waves in fluids.* Cambridge University Press, 1978.

[60] R. R. Long. Solitary waves in one and two fluid systems. *Tellus*, 8:460–471, 1956.

[61] M. S. Longuet-Higgins and R. W. Stewart. Changes in the form of short gravity waves on long waves and tidal currents. *J. Fluid Mech.*, 8:565–583, 1960.

[62] M. S. Longuet-Higgins and R. W. Stewart. The changes in amplitude of short gravity waves on steady non-uniform currents. *J. Fluid Mech.*, 10:529–549, 1961.

[63] M. S. Longuet-Higgins and R. W. Stewart. Radiation stresses in water waves; a physical discussion with applications. *Deep Sea Res.*, 11:529–562, 1964.

[64] A. J. Martin and W. J. Easson. Non-linear internal wave kinematics. In *Proceedings of the 7th International Offshore and Polar Engineering Conference*, pages 123–129, Honolulu, USA, May 1997.

[65] H. Michallet and E. Barthelemy. Experimental study of interfacial solitary waves. *J. Fluid Mech.*, 366:159–177, 1998.

[66] J. W. Miles. The KdV equation: a historical essay. *J. Fluid Mech.*, 106:131–147, 1981.

[67] A. B. Neal, I. J. Butterworth, and K. M. Murphy. The Morning Glory. *Weather*, 32:176–183, 1977.

[68] D. J. Olbers and K. Herterich. The spectral energy transfer from surface waves to internal waves. *J. Fluid Mech.*, 92:349–379, 1979.

[69] A. R. Osborne and T. L. Burch. Internal solitons in the Andaman Sea. *Science*, 208:451–460, 1980.

[70] L. A. Ostrovsky and A. Stepanyants. Do internal waves exist in the ocean? *Reviews of Geophysics*, 27:293–310, 1989.

[71] PCO Optics GmbH. *PCO CCD Imaging*, 1998.

[72] G. L. Pickard. *Descriptive Physical Ocenaography.* Pergammon Press, third (SI) edition, 19.

[73] R. R. Prasad and K. R. Sreenivasan. The measurement and interpretation of fractal dimensions of the scalar interface in turbulent flows. *Physics of Fluids A*, 2(5):792–807, May 1990.

[74] J. Pullen. *Particle image velocimetry applied to waves with surface films.* PhD thesis, University of Edinburgh, 1998.

[75] P. A. Quinn. *Breaking waves on beaches.* PhD thesis, University of Edinburgh, 1995.

[76] M. Raffel, C. Wilert, and J. Kompenhans. *Particle Image Velocimetry - A Practical Guide.* Springer, 1998.

[77] Matiur Rahman. *Water Waves: Relating Modern Theory to Advanced Engineering Practice.* Oxford Science Publications, 1995.

[78] J. S. Russel. Report on waves. *Report of the 14th British Associaton Meeting for the Advancement of Science*, pages 311–390, 1845.

[79] J. Sakakibara, K. Hishida, and M. Maeba. Measurements of thermally stratified pipe flow using image processing techniques. *Experiments in Fluids*, 16:82–96, 1993.

[80] J. Sander and K. Hutter. On the development of the theory of the solitary wave. A historical essay. *Acta Mechanica*, 86:111–152, 1991.

[81] T. Schlicke. *Breaking Waves and the Dispersion of Surface Films.* PhD thesis, University of Edinburgh, 2001.

[82] H. Segur and J. L. Hammack. Soliton models of long internal waves. *J. Fluid Mech.*, 118:285–304, 1982.

[83] D. Skyner. *The mechanics of extreme water waves.* PhD thesis, University of Edinburgh, 1992.

[84] R. K. Smith and J. Goodfield. The 1979 Morning Glory expedition. *Weather*, 36:130–136, 1981.

[85] I. B. A. Svendsen and Ivar G. Jonsson. *Hydrodynamics of Coastal Regions.* Den Private Ingeniørfond, Technical University of Denmark, DK 2800 Lyngby, 1980.

[86] I. J. Svendsen. Mixed boundary value problem for Laplace's equation in domain of arbitrary shape, 1971.

[87] University of Edinburgh T. Schlicke. Private communication.

[88] S. Tett. Simulation of El Niño - Southern Oscillation-like variability in a global AOGCM and its response to CO2 increase. *Journal of Climate*, 8:1473–1502, 1995.

[89] P. J. Unna. Sea waves. *Nature*, 159:239–42, 1947.

[90] I. van Cruyningen, A. Lozano, and R. K. Hanson. Quantitive imaging of concentration by planar laser induced fluorescence. *Experiments in Fluids*, 10:41–49, 1990.

[91] D. A. Walker. A fluorescence technique for measurement of concentration in mixing fluids. *J. Phys. E. Sci. Instrum.*, 20:217–223, 1987.

[92] L. R. Walker. Interfacial solitary waves in a two fluid medium. *Physics of Fluids*, 16:1796–1804, 1973.

[93] J. Westerweel. *Digital Particle Image Velocimetry - Theory and Applications.* PhD thesis, Delft University, 1993.

[94] J. Westerweel. Fundamentals of digital particle image velocimetry. *Meas. Sci. Technol.*, 8:1379–1392, 1997.

[95] H. U. Widdel. Experimental evidence for solitary waves in the middle atmosphere. *Journal of Geophysical Research*, 96:15931–15942, 1991.

[96] University of Dundee Y. Guo. Private communication.

[97] N. J. Zabusky and M. D. Kruskal. Interaction of "solitons" in a collisionless plasma and the recurrence of initial states. *Physical Review Letters*, 15(6):240–243, 1965.